

**Roman Trattnig**

# **Solution Processed Organic Multilayer Devices for Light Emitting and Photovoltaic Applications**

## **DOCTORAL THESIS**

For obtaining the academic degree of  
Doktor der technischen Wissenschaften

Doctoral Programme of Technical Sciences  
Technical Physics



**Graz University of Technology**

Supervisor:

Ao.Univ.-Prof. Dipl.-Ing. Dr.techn. Emil J.W. List  
Institute of Solid State Physics

Graz, February 2013

“There are in fact two things, science and opinion;  
the former begets knowledge, the latter ignorance.”

Hippocrates

## Acknowledgement

“Alone we can do so little; together we can do so much” is a famous quote from Helen Keller. Looking back at these last few years of my doctoral studies, I’m only able to add: so true! The thesis at hand could not have been realized without all those people, who contributed a mite, be it as colleagues or as friends. Thus, it is time to say “Thank You”!

First of all, I want to express my gratitude to my supervisor Emil J. W. List, who gave me the opportunity to work in a team of extraordinary people, for his scientific support, for his patient explanations and above all, for him challenging me to improve my work from topic to topic.

Furthermore I would like to thank Gernot Mauthner who guided me through my beginnings in the field of organic solar cells, who let me find my own ways to gain a deeper insight into scientific topics but who was always there to give a good advice during a cup of coffee.

I also want to express my gratitude to those people with whom I worked on the development of nanocomposite solar cells at NTC Weiz and who spent loads of hours in the labs with me in order to enhance solar cell efficiencies as much as we could. I’m especially indebted to Monika Jäger, for the collaborative realization of a vast amount of solar cells, for fruitful and inspiring discussions and for a competing, yet overall pleasant collaboration. Further thanks go to Markus Postl for setting up and programming the solar measuring setup and for not losing his nerves, when I was close to losing my patience; to Conny Ranz for her assistance in the chemistry lab as well as to Markus Seidl for patiently and accurately fulfilling his tasks, no matter how much it was. I also want to thank my former OLED group members Sebastian Schuh and Sebastian Nau for inspiring discussions, challenging questions and for the exchange of experience.

Moreover, I want to thank Gregor Trimmel and all the former members of the “*Christian Doppler Laboratory for Nanocomposite Solar Cells*” at the “*Institute for Chemistry and Technology of Materials*” at the “*Graz, University of Technology*” for their collaboration, in particular Thomas Rath, Michael Edler, Achim Fischereeder, Sebastian Dunst and Christopher Fradler.

Special thanks go to Klaus Müllen and his group of chemists at “*Max Planck Institute for Polymer Research, Mainz, Germany*” and there especially to Teresa Figueira Duarte, Tianshi Qin, Matthias Schwab and Leonid Pevzner for providing ever new compounds in the field of blue light emitting materials. Concerning materials, another “thank you” goes to Bilal Kaafarani at the “*American University of Beirut, Lebanon*” for providing the pyrene-carbazole compounds.

This thesis would not have been possible without some measurements “on the road”. Therefore I want to express my gratitude to Maria-Antonietta Loi and her group, in particular Marianna Manca, from the “*Zernike Institute for Advanced Materials of the University of Groningen, Netherlands*” for performing time resolved photoluminescence measurements. Moreover, I want to thank Norbert Koch and coworkers at the “*Institute for Physics at the Humboldt-Universität zu Berlin*” for their photoelectron spectroscopy measurements and in particular, Raphael Schlesinger for teaching me how to evaluate the respective spectra and for showing me that a full nightshift of measurements does not have to be boring. I also want to thank Roland Resel and Birgit Kunert for their XRD-measurements as well as Wernfried Haas for performing the TEM investigations.

I am especially indebted to all current and former members of the NTC Weiz for their collaboration, encouraging discussions and great support, in particular Helmut Wiedenhofer, Sonja Stessl-Mühlbacher, Renée Hirschmann, Sonja Larissegger, Bianca Lembacher, Rita Eckhard, Hannes Holl, Josef Harrer, Kerstin Schmoltner, Johannes Kofler, Peter Krabb, Karl Popovic, Patrick Hierzer and Christoph Bauer. Special thanks in this regard go to the NTC Weiz version of “*Statler and Waldorf*”, Andres Klug and Stefan Sax, for their usually open ears when I had a question and for giving a good advice whenever it was necessary.

A huge amount of gratitude goes to Alexander Blümel, who not only taught me how to operate an AFM but also how to use a base cap, who shares the passion for my favorite sports and who made me burst into laughter for several times, not only at the office but also in the middle of San Francisco.

I definitely will not forget Manfred Gruber, Manuel Auer and Katrin Koren who assisted me and stood by my side during the final stage of this thesis and my last exams.

None of this work, however, would be possible without the personal backup of some good and close friends. Thus, I want to express my gratitude to Martina Tschuden, Matthias König, Rene Plasser, Ingo Oberrauner and Katja Streit, who were always there for me when I needed help, who cheered me up or just snatched me off my work when I felt completely drained. Thank you all for not forgetting me even when I did not call for several weeks.

My hugest gratitude goes to those people, who are closest. First of all to Yvonne, who constitutes the bright light in my life, that is always able to lighten my mood, especially when I'm completely down, who gives me a smile just to expel my sorrows and who kept her patience during these last few months when I had almost had no time.

Finally yet most importantly, I want to thank those people whom I honestly will never be able to thank enough: my Mum and Dad. Thank you for being here, for guiding and supporting me whenever I ask and for always providing me with the security that as long as you are there, there will be someone for me to lean on.

## List of Publications

### Journal Articles:

- Kappaun S., Scheiber H., Trattnig R., Zojer E., List, E., Slugovc C.; “Defect chemistry of polyfluorenes: Identification of the origin of “interface defects” in polyfluorene based light-emitting devices” *Chemical Communications* **2008**, 0, 5170 - 5172.
- Niedermair F., Trattnig R., Mereiter K., Schmuck M., Sax S., List E., Slugovc C.; “Red Electrophosphorescent Platinum(II) Quinolinolate Complexes” *Monatshefte für Chemie – Chemical monthly* **2010**, 141, 847 - 858.
- Figueira-Duarte T. M., Del Rosso P. G., Trattnig R., Sax S., List E., Müllen K.; “Designed Suppression of Aggregation in Polypyrene: Toward High-Performance Blue-Light-Emitting Diodes” *Advanced materials* **2010**, 22, 990 - 993.
- Schwab M. G., Qin T., Pisula W., Mavrinsky A., Feng X., Baumgarten M., Kim H., Laquai F., Schuh S., Trattnig R., List E., Müllen K.; “Molecular Triangles: Synthesis, Self-Assembly, and Blue Emission of Cyclo-7,10-tris-triphenylenyl Macrocycles” *Chemistry - an Asian journal* **2011**, 6, 3001 - 3010.
- Trattnig R., Figueira-Duarte T. M., Lorbach D., Wiedemair W., Sax S., Winkler S., Vollmer A., Koch N., Manca M., Loi M.-A., Baumgarten M., List E., Müllen K.; “Deep blue polymer light emitting diodes based on easy to synthesize, non-aggregating polypyrene” *Optics Express* **2011**, 19, A1281 - A1293.
- Qin T., Wiedemair W., Nau S., Trattnig R., Sax S., Winkler S., Vollmer A., Koch N., Baumgarten M., List E., Müllen K.; “Core, shell, and surface-optimized dendrimers for blue light-emitting diodes” *Journal of the American Chemical Society* **2011**, 133, 1301 - 1303.
- Rath T., Edler M., Haas W., Fischereeder A., Moscher S., Schenk A., Trattnig R., Sezen M., Mauthner G., Pein A., Meischler D., Bartl K., Saf R., Bansal N., Haque S. A., Hofer F., List E. J. W., Trimmel G.; “A Direct Route Towards Polymer/Copper Indium Sulfide Nanocomposite Solar Cells” *Advanced Energy Materials* **2011**, 1, 1046–1050.
- Kaafarani B. R., El-Ballouli A. O., Trattnig R., Fonari A., Sax S., Wex B., Risko C., Khnayzer R. S., Barlow S., Patra D., Timofeeva T. V., List E. J. W., Brédas J.-L., Marder S. R.; “Bis(carbazolyl) derivatives of pyrene and tetrahydropyrene: synthesis, structures, optical properties, electrochemistry, and electroluminescence” *Journal of Materials Chemistry C* **2013**, 1, 1638 - 1650.
- Trattnig R., Pevzner L., Jäger M., Schlesinger R., Nardi M. V., Ligorio G., Christodoulou C., Koch N., Baumgarten M., Müllen K., and List E. J. W.; “Bright blue solution processed triple-layer polymer light emitting diodes realized by thermal layer stabilization and orthogonal solvents” accepted in *Advanced Functional Materials* **2013**.
- Schmoltner K., Schlütter F., Kivala M., Baumgarten M., Winkler S., Trattnig R., Koch N., Klug A., List E. J. W., Müllen K.; “A Heterotriangulene Polymer for Air-stable Organic Field-Effect Transistors” accepted in *Polymer Chemistry* **2013**.

### Talks:

- Rath T., Fischereeder A., Edler M., Moscher S., Trattnig R., Mauthner G., List E., Haas W., Hofer F., Trimmel G.; “Preparation of metal-sulfide – polymer nanocomposites for photovoltaic applications” 14. Österreichische Chemietage, Linz am 28.09.2011.
- Fradler, C.; Rath, T.; Edler, M.; Fischereeder, A.; Moscher, S.; Pein, A.; Trattnig, R.; Mauthner, G.; List, E.; Haas, W.; Hofer, F.; Trimmel, G.; “Polymer Nanocomposite Solar Cells based on in-situ formed CuInS<sub>2</sub>” SPIE Optics + Photonics: Organic Photovoltaics, San Diego, CA, am 23.08.2011.

- Rath T., Arar M., Pein A., Fradler C., Kaltenhauser V., Edler M., Moscher S., Trattnig R., List E., Haas W., Dunst S., Hofer F., Trimmel G.; *“Copper Indium Sulphide / Polymer Nanocomposite Solar Cells”* 27th European PV Solar Energy Conference and Exhibition, Frankfurt am 25.09.2012.
- Trattnig R.; *“Pyrene as emitter: New material concepts enabling for stable deep blue light emitting devices”* Physikalisches Oberseminar für DissertantInnen, Graz am 21.06.2012.
- Maier E., Edler M., Fischereeder A., Fradler C., Haas W., Hofer F., Larissegger S., Mauthner G., Meischler D., Pein A., Rath T., Saf R., Santis Alvarez A., Trattnig R., Stelzer F., List E., Trimmel G.; *“Hybrid Photovoltaic Cells via a Novel Direct Route”* NAWI Graz Workshop 2009, Graz am 26.06.2009.

### **Poster Presentations:**

- Niedermair F., Trattnig R., Schmuck M., Sax S., List E., Slugovc C.; *“Heteroleptic Platinum(II) Complexes of 8-Quinolinolates Bearing Electron Withdrawing Groups in 5 Position”* COST D35 Workshop – Dithiolenes and non-innocent redox-active ligands, Vravrona, Griechenland am 17.06.2009.
- Trattnig R.; Figueira-Duarte, T. M.; Del Rosso, P. G.; Sax, S.; List, E.; Müllen, K.: *“Investigations on a novel, highly emissive, non-aggregating Pyrene-based Polymer for Blue Light Emitting Devices”* 2010 MRS Spring Meeting, San Francisco, USA am 05.04.2010.
- Rath T., Fischereeder A., Edler M., Moscher S., Trattnig R., Mauthner G., Haas W., Dunst S., Hofer F., List E., Trimmel G.; *“Metal xanthates as precursors for efficient solution processed CuInS<sub>2</sub>-polymer nanocomposite solar cells”* MRS Fall Meeting 2011, Boston, USA am 28.11.2011.
- Trimmel G., Fischereeder A., Edler M., Moscher S., Trattnig R., Mauthner G., List E., Haas W., Hofer F., Rath, T.; *“CuInS<sub>2</sub>-Polymer nanocomposite solar cells prepared via metal xanthate precursors”* EMRS Spring Meeting 2011, Nizza, Frankreich am 09.05.2011.
- Trattnig R., Qin T., Wiedemair W., Nau S., Sax S., Winkler S., Vollmer A., Koch N., Baumgarten M., List E., Müllen K.; *“Blue Dendrimer Light-Emitting Diodes Based on Core, Shell, and Surface-Optimized Dendrimers”* E-MRS ICAM IUMRS 2011 Spring Meeting, Nizza, Frankreich am 09.05.2011.
- Rath T., Edler M., Haas W., Moscher S., Pein A., Kaltenhauser V., Dunst S., Arar M., Fradler C., Saf R., Trattnig R., Jäger M., Postl M., Seidl M., Bansal N., Haque S. A., Hofer F., List E., Trimmel G.; *“A Direct In Situ-Preparation Route for Organic-Inorganic Hybrid Solar Cells Based on Metal Sulfides and Conjugated Polymers”* Plastic Electronics 2012, Dresden am 09.10.2012.
- Rath T., Edler M., Haas W., Moscher S., Trattnig R., Jäger M., Pein A., Kaltenhauser V., Dunst S., Arar M., Fradler C., Saf R., Postl M., Seidl M., Bansal N., Haque S. A., Hofer F., List E., Trimmel G.; *“Polymer / copper indium sulphide hybrid solar cells”* EMRS Spring Meeting 2012, Straßburg am 14.05.2012.

### **Patents:**

- Müllen K., Figueira-Duarte T. M., Del Rosso P. G., List E., Trattnig R.; *“Pyrene-Based Polymers for Organic Light Emitting Diodes (OLEDs)”* WO/2010/145726 filed: 20.04.10.
- Trimmel G., Trattnig R., Schenk A., Rath T., Mauthner G., Haas, W., Fischereeder A., Edler M.; *“Solutions for the production of homogeneous large-area photoactive layers consisting of an electroactive polymer and semiconductor nanoparticles and use thereof in photovoltaics and optoelectronics”* WO/2011/085425, filed: 13.01.11.

## Abstract

Organic light emitting devices belong to the most promising candidates for the lighting revolution of the 21<sup>st</sup> century with the potential to save hundreds of GWh/year if put in place. Yet, while research and development in this field has already led to commercial products, the lifetime and stability of OLEDs are still issues to be addressed in order to allow for an entire commercialization. In particular, while well-established active emitters can be found for the red and green region of visible light there is still a quest for stable, highly efficient and easy to synthesize molecules emitting light in the deep blue wavelength range. Furthermore, device-assembling strategies that allow for a cost effective production of devices on the industrial scale are still topics that need development.

Among possible compounds for blue light emitting chromophores, pyrene is one of the most thoroughly investigated candidates. In particular, pyrene is known for its high fluorescence lifetime, but also for its liability to form light emitting excimers shifting the blue molecular emission into the green spectral region. The first part of this thesis shows that this intrinsic drawback of the pyrene molecule can be overcome by implementing pyrene via proper molecular engineering for semiconducting polymers, dendrimers and small molecules leading to bright deep blue emitting OLEDs. Moreover, a solution based device assembling strategy is presented, which leads to highly efficient blue emitting PLEDs and bears the potential to act as a starting point for future large scale device fabrication.

Today the worldwide photovoltaic market is dominated by inorganic silicon based mono- and polycrystalline solar cells. Yet, due to their complex and often high temperature fabrication processes these solar cells prove to be expensive, resulting in a large payback time. Among new emerging thin film photovoltaic devices, organic (polymer) based solar cells showed to be a promising alternative technology which holds potential for the fabrication of inexpensive and flexible photovoltaic cells. The reason OSCs do not yet play a significant role on the market, however, results from the still rather low efficiencies of these organic devices, which – due to their larger bandgap – show a lower Shockley-Queisser limit than their inorganic counterparts.

Precisely this issue is addressed in the second part of the thesis by nanocomposite solar cells in which the light absorbing photoactive layer consists of both, an organic conjugated polymer and an inorganic semiconductor. Thereby the light harvesting properties are expanded from the visible part of the spectrum down to the near-infrared region. In particular, the thesis shows that polymer:CIS NCSCs can be assembled by solution based processes. This assembling strategy is facilitated by soluble precursor materials for the inorganic phase, which are blended into a polymer solution and in situ form nanocrystals within the polymer matrix during a mild thermal annealing step with temperatures in the range of 200°C. Furthermore it is shown that the power conversion efficiency of the NCSCs can be raised considerably by the utilization of low-bandgap polymers, which enable a further broadening of the solar cells' light absorption characteristics.

## Kurzfassung

Organische Leuchtdioden gehören zu den aussichtsreichsten Kandidaten für die Beleuchtungsrevolution des 21. Jahrhunderts mit dem Potenzial durch ihren Einsatz Hunderte von GWh/Jahr einzusparen. Doch während Forschung und Entwicklung in diesem Bereich zwar bereits zu kommerziellen Produkten geführt haben, stellen die Lebensdauer und Stabilität der OLEDs noch immer Herausforderungen dar, die in Angriff genommen werden müssen, um eine vollständige Kommerzialisierung zu ermöglichen. Insbesondere gibt es noch immer einen Mangel an stabilen, hoch effizienten und einfach zu synthetisierenden Molekülen, die Licht im tief-blauen Wellenlängenbereich emittieren, während für den roten und grünen Bereich des sichtbaren Lichts bereits etablierte emittierende Materialien verwendet werden. Darüber hinaus bedürfen auch Bauteil-Fabrikationsprozesse einer weiteren Entwicklung um letztendlich eine kostengünstige Produktion von Geräten im industriellen Maßstab zu ermöglichen.

Unter den möglichen Molekülen, die sich als blaues Licht emittierende Farbstoffe eignen, ist Pyren eines der am gründlichsten untersuchten Materialien. Pyren ist insbesondere für seine hohe Fluoreszenz-Lebensdauer bekannt, aber auch für seine Anfälligkeit in Leuchtdioden Exzimeren zu bilden welche zu einer Verschiebung der blauen molekularen Emission in den grünen Spektralbereich führen. Der erste Teil dieser Arbeit zeigt, dass dieser intrinsische Nachteil des Pyren-Moleküls, durch einen geeigneten molekularen Aufbau, für halbleitende Polymere, Dendrimere sowie für kleine Moleküle überwunden werden kann, und damit helle blau emittierende OLEDs realisiert werden können. Darüber hinaus wird eine Lösungsmittel basierte Bauteilfabrikationsstrategie vorgestellt, mit der hocheffiziente, blau emittierende PLEDs hergestellt werden können und welche möglicherweise das Potenzial hat, als Ausgangspunkt für eine zukünftige, industrielle Bauelementherstellung zu dienen.

In der heutigen Zeit wird der weltweite Photovoltaik-Markt vollständig von anorganischen Silizium-basierten mono- und polykristallinen Solarzellen dominiert. Doch aufgrund ihrer komplexen und oft hohe Temperaturen erfordernden Herstellungsprozesse erweisen sich diese Solarzellen als teuer, was zu einer hohen Amortisationszeit führt. Unter den neuen, aufstrebenden Dünnschicht-Fotovoltaik Zellen erweisen sich organische (Polymer-) Solarzellen als eine vielversprechende, alternative Technologie die das Potenzial zur Herstellung von kostengünstigen und flexiblen Solarzellen in sich birgt. Der Grund warum OSCs noch keine bedeutende Rolle auf dem Markt spielen, ergibt sich jedoch aus den immer noch recht geringen Wirkungsgraden für diese organischen Bauteile, die – aufgrund ihrer größeren Bandlücke – nicht zuletzt ein geringeres Shockley-Queisser Limit aufweisen als die meisten anorganischen Solarzellen. Gerade dieses Problem adressieren die Nanokompositsolarzellen im zweiten Teil der Dissertation. In NKSZ besteht die Licht absorbierende, fotoaktive Schicht sowohl aus einem organischen konjugierten Polymer als auch aus einem anorganischen Halbleiter, wodurch die Absorptionsfähigkeit der Solarzelle vom sichtbaren Bereich des Spektrums bis in den nahen Infrarot-Bereich erweitert wird. Insbesondere zeigt die Arbeit, dass Polymer:CIS Nanokomposit Solarzellen durch lösungsbasierte Prozesse hergestellt werden können. Diese Strategie wird durch lösliche Ausgangsstoffe für die anorganische Phase ermöglicht, die in eine Polymerlösung gemischt werden und während eines milden thermischen Ausheizenschrittes, im Bereich von 200°C, in situ Nanokristalle innerhalb der Polymermatrix bilden. Darüber hinaus wird gezeigt, dass der Wirkungsgrad von Nanokomposit Solarzellen durch den Einsatz von Low-Bandgap Polymeren, die eine weitere Verbreiterung der Absorptionscharakteristik der Solarzellen ermöglichen, erheblich angehoben wird.



Deutsche Fassung:  
Beschluss der Curricula-Kommission für Bachelor-, Master- und Diplomstudien vom 10.11.2008  
Genehmigung des Senates am 1.12.2008

## EIDESSTÄTTLICHE ERKLÄRUNG

Ich erkläre an Eides statt, dass ich die vorliegende Arbeit selbstständig verfasst, andere als die angegebenen Quellen/Hilfsmittel nicht benutzt, und die den benutzten Quellen wörtlich und inhaltlich entnommene Stellen als solche kenntlich gemacht habe.

Graz, am ..28..02..2013.....



.....  
(Unterschrift)

Englische Fassung:

## STATUTORY DECLARATION

I declare that I have authored this thesis independently, that I have not used other than the declared sources / resources, and that I have explicitly marked all material which has been quoted either literally or by content from the used sources.

.....28.02.2013.....  
date



.....  
(signature)

## Table of Contents

1	Introduction.....	1
1.1	History.....	1
1.2	Motivation and Outline .....	2
2	Fundamentals.....	4
2.1	Organic Semiconductors .....	4
2.1.1	Small Molecules.....	5
2.1.2	Conjugated Polymers .....	6
2.2	Excited States .....	8
2.2.1	Polarons.....	8
2.2.2	Excitons.....	9
2.3	Basic Optical Properties and Frank-Condon-Principle .....	10
2.3.1	Photoluminescence and Electroluminescence.....	13
2.4	Charge Transport.....	14
2.5	Energy Transfer.....	15
2.5.1	Förster Transfer.....	16
2.5.2	Dexter Transfer .....	18
2.6	Interfaces and Energy Level Alignment.....	18
2.6.1	Metal-Organic Interfaces .....	19
2.6.2	Organic-Organic interfaces .....	21
2.7	Charge Injection .....	21
2.7.1	Ohmic Contacts.....	22
2.7.2	Injection Limited or Schottky Contact.....	22
2.7.3	Charge Injection Mechanisms.....	23
2.8	Fundamentals on Organic Light Emitting Devices .....	24
2.8.1	OLED – Architecture .....	24
2.8.2	OLED – Working Principle .....	25
2.9	Fundamentals on Organic Solar Cells.....	29
2.9.1	OSC – Architectures .....	29
2.9.2	OSC – Working Principle .....	30
2.9.3	Characterization of OSCs.....	32
2.9.4	Standard Test Conditions for Solar Cells.....	33
3	Experimental Methodology .....	35
3.1	Solution and Film Preparation.....	35
3.2	Absorption Measurements.....	35
3.3	Photoluminescence Measurements .....	36
3.4	Photoluminescence Quantum Yield.....	36
3.5	Time Resolved Photoluminescence.....	37
3.6	Photoinduced Absorption.....	37
3.7	Photoelectron Spectroscopy .....	40
3.8	X-ray Diffraction.....	42
3.9	Atomic Force Microscopy.....	43
3.10	OLED Preparation and Characterization.....	45
3.10.1	OLED Fabrication.....	45
3.10.2	OLED Characterization.....	45
3.11	OSC Preparation and Characterization.....	45
3.11.1	OSC Fabrication.....	45
3.11.2	OSC Characterization.....	46

3.11.3	Incident Photon to Current Efficiency .....	46
3.12	Statistical Relevance of the Device Results .....	47
4	Organic Light Emitting Devices .....	48
4.1	Introduction .....	48
4.2	Pyrene based Emitters .....	50
4.2.1	Introduction on Pyrene .....	50
4.3	Designed Suppression of Aggregation in Polypyrene: Toward High-Performance Blue-Light-Emitting Diodes .....	51
4.3.1	Introduction .....	51
4.3.2	Synthesis of PPyr .....	52
4.3.3	Photophysical Properties of PPyr .....	53
4.3.4	Surface Morphology and Thermal Stability of PPyr Thin Films .....	55
4.3.5	PPyr – Device Characterization .....	56
4.3.6	Conclusion .....	58
4.4	Deep Blue Polymer Light Emitting Diodes Based on Easy to Synthesize, Non- aggregating Polypyrenes .....	59
4.4.1	Introduction .....	59
4.4.2	Synthesis of PPyrTPA .....	60
4.4.3	Dependence of Absorption and Emission Characteristics on Solvent Polarity .....	61
4.4.4	Photophysical Properties of PPyrTPA .....	62
4.4.5	Surface Morphology and Thermal Stability of PPyrTPA Thin Films .....	63
4.4.6	Exciton Lifetime in PPyr .....	64
4.4.7	UPS-studies on PPyr and PPyrTPA .....	67
4.4.8	Modified PPyr-based Devices .....	69
4.4.9	Conclusion .....	71
4.5	Bright Blue Solution Processed Triple-Layer Polymer Light Emitting Devices realized by Thermal Layer Stabilization and Orthogonal Solvents .....	73
4.5.1	Introduction .....	73
4.5.2	Synthesis of PEGPF .....	75
4.5.3	Optical and Morphological Characteristics of PEGPF .....	76
4.5.4	Optical and Morphological Characteristics of TFB .....	77
4.5.5	Morphological Stability of Solution Processed Polymeric Multilayers .....	78
4.5.6	Energy-Level Alignment across the Multilayer Assembly .....	80
4.5.7	Electroluminescent Properties and Device Performance of Single- and Multilayer PLEDs .....	84
4.5.8	Conclusion .....	89
4.6	Blue Dendrimer Light-Emitting Diodes Based on Core, Shell and Surface- Optimized Dendrimers .....	91
4.6.1	Introduction .....	91
4.6.2	Dendrimer Synthesis .....	92
4.6.3	Photophysics of Pyrene-cored Dendrimers .....	93
4.6.4	Surface Morphology and Thermal Stability of PYGx Thin Films .....	97
4.6.5	UPS-Studies on Pyrene-cored Dendrimers .....	99
4.6.6	Electroluminescent Properties and Device Performance of Single Layer DLEDs .....	100
4.6.7	PYGTPA Multilayer DLEDs .....	102
4.6.8	Conclusion .....	105

4.7	Photophysics and Electroluminescent Properties of Bis(Carbazolyl) Derivatives of Pyrene and Tetrahydropyrene in Small Molecule Organic Light Emitting Devices.....	106
4.7.1	Introduction.....	106
4.7.2	Synthesis of Carbazole-Pyrene Small Molecules.....	107
4.7.3	Photophysical Properties of Carbazole-Pyrene Molecules.....	108
4.7.4	Thin Film Surface Morphology.....	109
4.7.5	Electroluminescent Properties of Pyrene-Carbazole Derivatives.....	111
4.7.6	Conclusion.....	112
4.8	Molecular Triangles: Blue Emission of Cyclic Triphenylene Trimers.....	114
4.8.1	Introduction.....	114
4.8.2	Synthesis of Macrocycles.....	115
4.8.3	Liquid Crystallinity of CTP1.....	117
4.8.4	Photophysics of CTP1, CTP2 and CTP3.....	118
4.8.5	Electroluminescent Characteristics of CTP1, CTP2 and CTP3.....	119
4.8.6	Conclusion.....	121
4.9	Conclusions – Organic Light Emitting Devices.....	122
5	Organic Photovoltaics.....	124
5.1	Introduction.....	124
5.2	Nanocomposite Solar Cells – In-situ Formation of Inorganic Nanoparticles and their Potential in MDMO-PPV:CIS Hybrid Cells.....	127
5.2.1	Introduction to Nanocomposite Solar Cells.....	127
5.2.2	Experimental.....	128
5.2.3	Nanoparticle Formation Approaches.....	128
5.2.4	Synthesis of Precursor Xanthates.....	128
5.2.5	Photophysical Properties of MDMO-PPV.....	129
5.2.6	MDMO-PPV:CIS Morphology Investigations.....	130
5.2.7	Photophysical Properties of MDMO-PPV:CIS Nanocomposite Films.....	132
5.2.8	MDMO-PPV:CIS Nanocomposite Solar Cells.....	134
5.2.9	IPCE Characteristics.....	135
5.2.10	Conclusion.....	136
5.3	Influence of the Bridging Atom in Donor-Acceptor Fluorene-Analogue Low-Bandgap Polymers on Morphology and Efficiency of Polymer:CIS-Nanocomposite Solar Cells.....	137
5.3.1	Introduction.....	137
5.3.2	Experimental.....	138
5.3.3	Morphology Studies on PCDTBT:CIS and PSiF-DBT:CIS Nanocomposite Films.....	139
5.3.4	X-Ray Diffraction.....	141
5.3.5	Photophysical properties of PCDTBT:CIS and PSiF-DBT:CIS Nanocomposite Films.....	142
5.3.6	Field Effect Charge Carrier Mobility.....	145
5.3.7	PCDTBT:CIS and PSiF-DBT:CIS Nanocomposite Solar Cells.....	146
5.3.8	Conclusion.....	148
5.4	Conclusions – Organic Photovoltaics.....	150
6	Outlook.....	151
7	References.....	152

# 1 Introduction

## 1.1 History

The tremendous scientific and technological progress in the field of solid state electronics, achieved from the middle of the last century until today, resulting in ever new electronic applications and devices, without any doubt plays one of the major roles in the changes and developments of society and way of living in that time.

In the beginning the key role in this development was exclusively held by inorganic electronics, not at least based on the invention of the first bipolar transistor by Bardeen, Brattain and Shockley in 1947,<sup>[1-3]</sup> which was awarded with the Nobel prize in 1956. Remarkable progress in inorganic electronics followed, resulting nowadays in high-complex electronic circuits and devices with critical device dimensions in the sub-micron length scale.

Yet, in the last two decades a completely different type of technology, namely “plastic electronics” based on organic semiconducting materials – as there are conjugated small molecules, conjugated oligomers and polymers – emerged and plays more and more an important role in the field of electronic devices. In contrast to their inorganic counterparts, organic semiconducting materials exhibit considerable advantages concerning their production and processability. In particular, this means that an adequate synthetic route can properly tune the physical, chemical, electrical, and optical properties of these materials. Moreover, most of these materials are lightweight, are able to form thin flexible structures, are easy to synthesize and can be applied on various substrates at comparably low temperatures. This is particularly valid for conjugated polymers, which are processed from solution and thus enable low cost and large scale processing.

The cornerstone for the vast development in academic and industrial research and development, however, was already laid in the middle of the last century by the spadework of M. Pope,<sup>[4]</sup> W. Helfrich and W.G. Schneider<sup>[5]</sup> in the 1960’s, which discovered electroluminescence (EL) in anthracene crystals as well as by the work of H. Shirakawa, A.J. Heeger, A.G. Mac Diarmid et al.<sup>[6]</sup> in 1977 about electrical conductivity in doped polyacetylene. Since then, various different classes of electronic devices using organic semiconducting compounds as active materials were realized, including organic light emitting devices (OLEDs),<sup>[7]</sup> organic thin film transistors (OFETs),<sup>[8,9]</sup> organic solar cells (OSCs),<sup>[10-12]</sup> organic photo detectors,<sup>[13]</sup> organic based sensors,<sup>[14,15]</sup> organic memory devices (OMDs)<sup>[16,17]</sup> and many more.

The start for the rapid development of OLEDs was triggered by the first report on a thin film OLED based on small molecules presented by C.W. Tang and S. VanSlyke<sup>[18]</sup> at Kodak followed only three years later by the first polymer light emitting diode (PLED) described by Burroughes et al.<sup>[19]</sup> From that point on both technologies – OLEDs based on organic small molecules as well as PLEDs based on conjugated polymers – attracted increasing attention, above all because of their potential as emitting components for flat panel displays<sup>[20,21]</sup> as well as for signage and lighting applications.<sup>[22,23]</sup>

Research and development of organic photovoltaic devices started and happened almost simultaneous to that of OLEDs, however, the first observation of a photovoltaic effect in an organic material was already reported in 1906 by Pochettino.<sup>[24]</sup> Yet, the actual start of growing interest in the scientific community can be traced back to 1958 when Kearns and Calvin reported on a photovoltaic effect of magnesium phtalocyanine between two glass electrodes.<sup>[25]</sup> With the reports on the first heterojunction, bulk heterojunction and polymer/fullerene organic solar cells between 1986 and 1993, wherein the latter already exhibited a power conversion efficiency (PCE) of around 1%, the major

breakthrough in science for this technology was achieved.<sup>[26–28]</sup> Since then many different classes of heterojunction as well as bulk heterojunction OSCs were investigated including dye/dye solar cells,<sup>[29]</sup> polymer/polymer solar cells,<sup>[30,31]</sup> polymer/fullerene solar cells<sup>[32]</sup> and hybrid solar cells,<sup>[33,34]</sup> whereas in the latter a combination of organic as well as of inorganic semiconducting materials is used. Until today record PCEs already in the range of 10-12%<sup>[35–38]</sup> could be realized and first organic based photovoltaic products can be found on the market.<sup>[39]</sup>

## 1.2 Motivation and Outline

Organic light emitting devices constitute a new emerging and exciting technology with great potential for lighting and display applications. This is primarily caused by their prospective advantages of exhibiting low power consumption, high luminous efficiency, a wide viewing angle, high switching speed as well as the possibility for the fabrication of flexible devices. Yet, for both device applications the realization of highly efficient and stable electroluminescent materials and devices in the three primary colors red, green and blue is imperative. While devices satisfying the particular prerequisites allowing for a commercial application could already be realized for all three colors, blue materials and devices still lag behind with respect to their operational lifetime and stability.<sup>[40,41]</sup>

Nevertheless, a huge interest lies in the realization of OLEDs based on polymers, thus more precisely PLEDs, since their applicability from solution in common solvents in principle allows for an easy scale up of lab-scale devices to industrial mass production via solution based low-cost and low-waste processes like ink-jet printing or roll-to-roll slot dye coating. Concerning this matter a major challenge poses the development of assembling strategies for multilayer PLED-structures, which allow for the fabrication of highly efficient and highly luminescent polymer light emitting devices, exhibiting efficiencies in the same range as achieved for OLEDs based on small molecules.

In general, the field of photovoltaic technology is still dominated primarily by crystalline silicon wafer based solar cells. Even if some workgroups were already able to present lab-scale devices with PCEs in the range of 10%, OSCs basically suffer from low efficiencies undoing their principle advantages of low-cost and low-temperature processability or their potential fabrication on large scale and flexible substrates. These low efficiencies are typically caused either by imbalanced charge carrier mobility in polymer/polymer solar cells or by only low contribution of fullerenes to the photocurrent generation in typical polymer/fullerene bulk heterojunction (BHJ) solar cells. One possible way to enhance the PCE of organic based solar cells significantly might be found in the realization of hybrid-cells comprising conjugated polymers and inorganic nanoparticles as components of a bulk heterojunction layer. Hybrid solar cells consequently have the potential to exploit the electrical and optical properties of both material classes and still are able to profit from the general advantages of organic based devices with respect to production processes, production cost and substrate customization.

The outline of this thesis is given in the following: After providing some fundamental knowledge about basic properties of organic semiconducting materials and organic electronic devices in chapter 2 and after explaining the experimental methodology in chapter 3, the thesis divides itself into two major parts. The first part (chapter 4) is dealing with the realization of organic blue light emitting devices. Various different organic materials (polymers, dendrimers and small molecules) based on pyrene as emissive unit are presented in the chapters 4.2-4.7. All these materials were investigated by several different measurement techniques including optical absorption and photoluminescence emission and their suitability as light emitting materials in simple single layer light emitting devices is examined in detail.

Moreover, the device related results achieved for pyrene-based polymers provide the basis for a conceptual work on blue emitting multilayer polymer light emitting devices fabricated by a proper combination of solution-based fabrication processes. The resulting multilayer PLEDs show considerably improved luminous efficiencies and maximum luminance values (chapter 4.5).

Photophysical characterizations are presented as well for a novel class of blue emitting organic compounds based on a cyclic combination of triphenylene units. Additionally, OLEDs with these cyclic molecules are fabricated in order to assess their potential as blue light emitting materials serving as an alternative to already well established small molecules and polymers for blue light emission (chapter 4.8).

The second part of this thesis (chapter 5) deals with the realization of hybrid polymer:copper indium sulfide (CIS) solar cells. The active layer for these nanocomposite solar cells (NCSCs) is fabricated from a solution containing the active polymer as well as indium and copper xanthates. During a thermal annealing step CIS nanoparticles are formed in situ from the xanthates as precursor materials. The electro-optical as well as the film formation properties of such produced polymer:CIS films using a well known poly(phenylene vinylene) polymer are investigated at first to test the suitability of this approach (chapter 5.2). Subsequently, two different fluorene-thiophene based so called “low-bandgap” polymers are utilized as organic components for hybrid solar cells and the dependence of the composite film morphology as well the dependence of the PCE on the bridging atom at the 9-position of the fluorene analog unit is thoroughly investigated (chapter 5.3).

## 2 Fundamentals

### 2.1 Organic Semiconductors

As for all materials referred to as “organic”, the basic component for organic semiconductors is carbon. The electronic shell of one carbon atom bears six electrons; two in the inner K-shell and four electrons in the outer L-shell. When the carbon atom is in its electronic ground state, according to *Hund's rule* and *Pauli's exclusion principle* two paired electrons of the L-shell occupy the 2s atomic orbital and two electrons are located in the  $p_x$  and  $p_y$  atomic orbitals leading to the electron configuration  $1s^2 2s^2 2p_x^1 2p_y^1$ .

The energy difference between the s- and p-orbitals, however, is low and only a small amount of energy is sufficient to promote one electron from the 2s-orbital to the unoccupied  $p_z$ -orbital. This amount of energy can for example be provided by an interaction with another carbon atom. The promotion of the 2s electron leads to the formation of four new electron orbitals, so called  $sp^3$ -hybrid orbitals. These hybrid orbitals are energetically equal, each exhibiting a stretched drop like shape, and are arranged symmetrically around the atomic core thereby forming a tetrahedral structure. In quantum mechanics hybrid orbitals can be derived by a linear combination of the principle 2s and all three 2p electron orbitals, which was presented first by Linus Pauling, based on the molecular orbital theory (*MO-theory*) of Heitler and London,<sup>[42]</sup> which described qualitatively the bonding and structure properties of methane ( $CH_4$ ).<sup>[43]</sup> In addition to the  $sp^3$ -hybridization, also  $sp^2$ - and  $sp^1$ -hybridized orbitals can be generated if two ( $p_x$  and  $p_y$ ) or only one ( $p_x$ ) of the 2p-orbitals are involved in the linear combination, respectively. In the former case the hybridized  $sp^2$ -orbitals are arranged symmetrically in one plane, enclosing an angle of  $120^\circ$ , with the  $p_z$ -orbital perpendicular to them, while in the latter case two  $sp^1$ -orbitals are aligned along the x-axis and the remaining p-orbitals orient along the y- and z-axis (c.f. Figure 2-1). In both cases, the hybridized orbitals again are energetically equal.

In that context, however, it is important to note, that hybridization can only be found in molecules and not in a single atom, since the necessary energy for the formation of the hybridized orbitals is gained in general from a very strong and directed bond with other atoms.

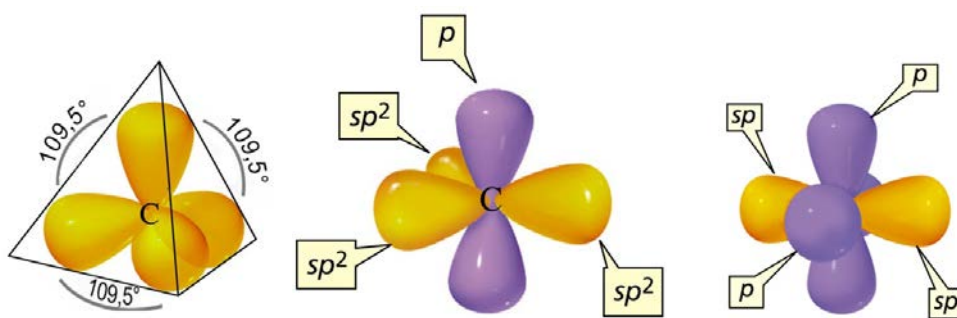


**Figure 2-1: Spatial charge density distribution of  $sp^3$  (left),  $sp^2$  (center) and  $sp^1$ -hybridized (right) orbitals and the remaining p-orbitals. (modified from [44])**

When talking about plastics in a general linguistic usage one usually refers to organic hydrocarbon materials such as polyethylene, which belongs to the group of polyalkanes with their characteristic formula  $C_nH_{2n+2}$ . In these compounds all carbon atoms are  $sp^3$ -hybridized and form strong directed  $\sigma$ -bonds with four adjacent atoms. In contrast to that, carbon atoms in conjugated small molecules and conjugated polymers are  $sp^2$ -hybridized which results in the formation of  $\sigma$ -bonds with only three neighbouring atoms in one plane. Due to the small distance between the atoms taking part in these  $\sigma$ -



bonds the remaining  $p_z$ -orbitals, which are located perpendicular to the  $sp^2$ -hybridization plane, overlap and are able to form  $\pi$ -bonds with the  $p_z$ -orbitals of the neighboring atoms. Due to these additional  $\pi$ -bonds, which are parallel to the plane of the  $\sigma$ -bonds, in a chain of carbon atoms a regular alteration of single and double bonds is established. Quantum mechanically, however, in this chain of equivalently bound carbon atoms it is not possible to assign each  $\pi$ -bond to two specific atoms. In contrary, (ideally) the spatial probability density for the  $\pi$ -electrons is extended over the whole chain forming the so-called  $\pi$ -electron system, where the participating electrons are delocalized over the whole chain. The extension and delocalization of the  $\pi$ -electron system, finally, leads to a lowering of the total system energy in the molecule compared to the molecule with localized  $\sigma$ - and  $\pi$ -bonds resulting in an enhanced stability of the molecular bonds. The as described formation of alternating single and double bonds ( $\sigma$ - and  $\pi$ -bonds) between the participating molecules, as well as the generation of the  $\pi$ -electron system is called *conjugation*.

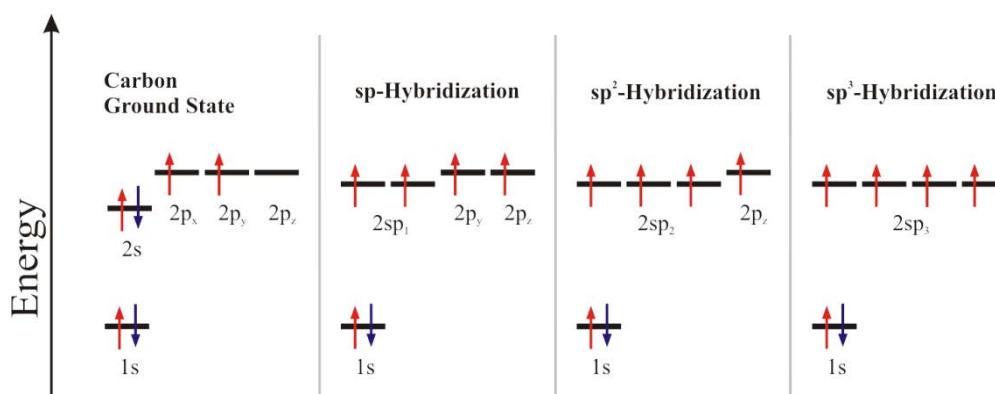


Figure 2-2: Schematic illustration of carbon ground state,  $sp$ -,  $sp^2$ - and  $sp^3$ -hybridized state energy levels (left to right).

### 2.1.1 Small Molecules

In order to understand the optical and electronic properties of *conjugated small molecules* (or just: *small molecules*), benzene is perfectly suitable to act as an example. Benzene, which consists of six carbon atoms in a ring-shaped arrangement, is the best known representative of the group of aromatic hydrocarbons or acenes, which are planar cyclic molecules formed by carbon atoms that are bound by alternating single- and unsaturated double bonds stemming from  $sp^2$ -hybridization. As mentioned in the previous section, this alternation leads to the formation of a delocalized  $\pi$ -electron system. According to the MO-theory, the particular molecular orbitals (MOs) can be expressed by a linear combination of the respective atomic orbitals. The combination of carbon's s- and  $p_z$ -orbitals consequently leads to the formation of bonding ( $\sigma$ ,  $\pi$ ) and antibonding ( $\sigma^*$ ,  $\pi^*$ ) orbitals (Figure 2-3). Corresponding to Pauli's law two electrons with antiparallel spin direction can populate each atomic orbital. This law is also valid for the population of MOs. Since every carbon atom in benzene contributes three electrons to form  $\sigma$ -bonds and one electron to form  $\pi$ -bonds one ends up with 12 completely filled  $\sigma$ -orbitals (C-H orbitals included) and 3  $\pi$ -orbitals completely filled as well. In contrast the respective antibonding  $\sigma^*$ - and  $\pi^*$ -orbitals remain unpopulated. Energetically  $\pi$ -orbitals show a lower binding energy and can be found at higher absolute energy values than  $\sigma$ -orbitals while in return  $\sigma^*$ -orbitals show higher absolute energy values than  $\pi^*$ -orbitals. Thus the highest occupied molecular orbital (HOMO) and the lowest unoccupied molecular orbital (LUMO) are formed by the  $\pi$ - and  $\pi^*$ -orbitals. As also depicted in Figure 2-3 the individual  $\pi$ -orbitals are not all located at the same energy. For bigger molecular systems this results in the development of band like structures for the bonding and antibonding  $\pi$ - and  $\pi^*$ -bands which can be pictured similar to the band structures in

inorganic semiconductors. Now, since the  $\pi$ -band is completely filled and the  $\pi^*$ -band is empty, which means there are no partially filled bands, and due to the delocalization of the  $\pi$ -electrons on the molecule, benzene shows semiconducting properties.<sup>[45]</sup> The height of the bandgap, i.e. the distance of the bonding and antibonding orbitals, is defined by the extent of the delocalization of the  $\pi$ -electrons. In particular, the stronger delocalized the electrons get, the closer are the bonding and antibonding orbitals and the lower is the bandgap. Thus, one way to alter the bandgap of conjugated small molecules can be achieved for example by linking two benzene rings covalently. Due to the low distance between the two molecules, their  $\pi$ -systems start to overlap. This leads to a splitting of the orbital energies and to an extension of the  $\pi$ -system over both benzene rings finally resulting in a reduction of the bandgap (Figure 2-3).

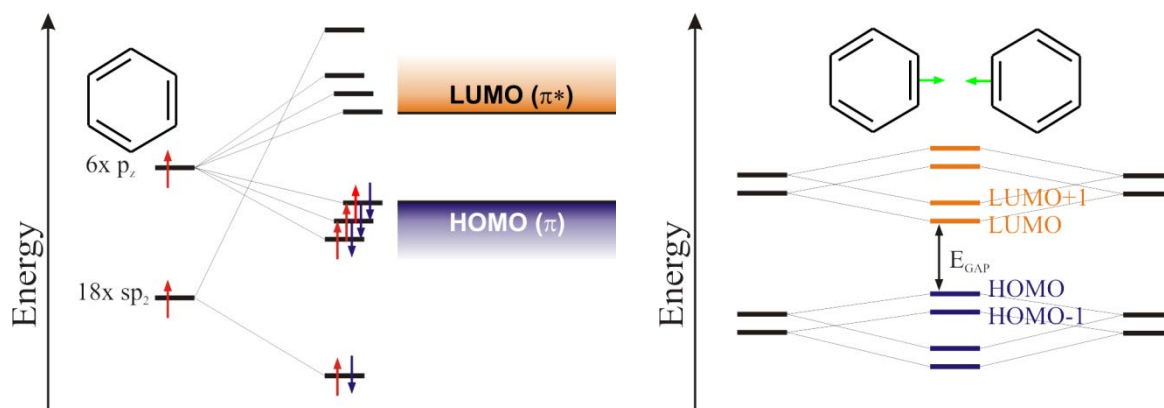


Figure 2-3: Energy structure of benzene (left, modified from [46]) and symbolic change in molecular energy levels due to interaction of  $\pi$ -orbitals of two benzene rings (right, modified from [47]).

### 2.1.2 Conjugated Polymers

The situation for conjugated polymers is similar to that present in small molecules. In typical conjugated polymers, strong directed chemical bonds are formed by the overlap of the respective  $sp^2$ -orbitals. The remaining  $p_z$ -orbitals of every carbon atom form  $\pi$ -bonds between the successive carbon atoms thus leading to an electron delocalization along the whole chain. In polymers the high amount of carbon atoms and the strong extension of delocalized electrons over the polymer chain lead to a decrease of the bandgap caused by the splitting of the orbitals upon approximation. As a general rule in that context it can be stated that the higher the extent of the electron delocalization gets, i.e., the greater the conjugation length, the lower is the bandgap. Additionally, because of the high amount of electrons involved, the structure of discrete energy levels for the  $\pi$ - and  $\pi^*$ -orbitals more or less vanishes and, analogously to small molecules, a band like structure develops.<sup>[48,49]</sup>

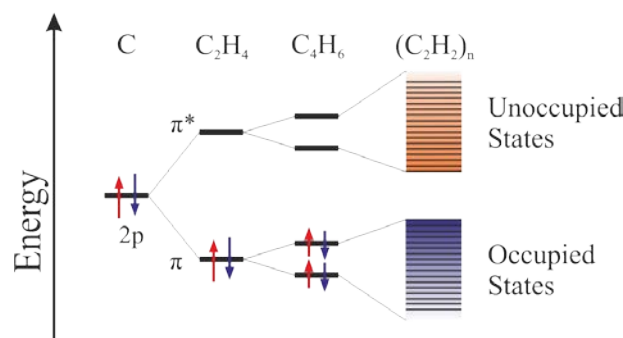


Figure 2-4: Evolution of HOMO and LUMO energy levels from discrete values to band-like structure for conjugated polymers in dependence of the number of carbon atoms involved in the formation of the  $\pi$ -electron system.

In theory the simplest way to describe the electronic properties of conjugated polymers is given by the *free electron molecular orbital model*.<sup>[50]</sup> In this theory, the  $\pi$ -electrons in a conjugated molecule are treated as independent particles in a one-dimensional box, leading to an energy value for the bandgap that is inversely proportional to the number of  $\pi$ -electrons. In the case of long conjugated chains consisting of  $N$  carbon atoms, like in polyacetylene ( $[\text{CH}]_x$ ),  $N$  electrons have to be considered. However, if  $N$  is big enough theory states that the bandgap actually vanishes, leading to a half filled energy band and metallic properties of the polymer.

A similar result is achieved according to the *Hückel-molecular orbital theory* using a simple band-picture for the  $\pi$ -electron system: each of the  $N$  carbon atoms in the polymer chain provides one unpaired electron in the  $2p_z$ -orbital, which leads to the formation of  $N$   $\pi$ -molecular orbitals. The overlap of the participating orbitals, however, leads to a delocalization of  $\pi$ -system wavefunction over the whole molecule, resulting in only one  $\pi$ -band. Since this band is only half filled, because every atom is providing just one unpaired electron to the  $\pi$ -system, metallic properties are expected for the polymer.

Yet, this outcome is in strong contradiction to experimental data achieved for polyacetylene and other conjugated polymers, which present semiconducting or even insulating properties.<sup>[51,52]</sup>

The discrepancy between theory and experiment can be explained by the *Peierls-instability*,<sup>[53,54]</sup> which accounts for the fact that single and double bonds in the polymer exhibit different lengths. Since double bonds exhibit a smaller atom-atom distance than single bonds, the structure of the polymer is dimerized leading to the formation of  $\pi$ - and  $\pi^*$ -bands, separated by an energy gap, instead of one half filled  $\pi$ -band as expected from the theories described above.<sup>[45]</sup>

As first successful model describing the electronic properties of conjugated organic materials was developed by Su, Schrieffer and Heeger (*SSH-model*).<sup>[55,56]</sup> The SSH-model presents an independent electron tight binding model describing the dimerized ground-state configuration of polyacetylene. Even when the results are able to explain that a molecular configuration with alternating bond-lengths is energetically more favorable than a configuration with equal length, thereby affirming the results obtained by Peierls, the model fails when describing the lowest excited state in polyenes.<sup>[57,58]</sup> This failure occurs because as the main parameter for the SSH-model a single-particle approximation accounting for the electron-lattice interaction is investigated, the electron-electron interaction, however, is neglected. A theory that advances beyond any single-particle formalism is presented by the *Peierls-Hubbard-model* which takes into account both, the electron-lattice as well as the electron-electron interaction.<sup>[59-61]</sup>

In the recent years, due to ever more powerful computing capacity of modern computer systems, the modeling of electronic properties of large molecular systems is based on *ab-initio* approaches like (*time dependent*)-*density-functional-theory*,<sup>[62,63]</sup> *Hartree-Fock theory*,<sup>[64,65]</sup> *Post-Hartree-Fock*,<sup>[48]</sup> and many more.

It is important to note, that the considerations presented above are theoretical approximations, trying to evaluate and interpret the electronic properties of “ideal” polymers. In real conjugated polymers and materials, however, the bandgap is determined by various different factors. The chemical configuration of the molecule for example might include heteroatoms in the polymer structure, implemented on purpose or due to contamination during the synthesis, which interrupt the conjugation. In addition, electrostatic repulsion between different molecular segments can lead to steric hindrances thus inducing a considerable deviation from the theoretical spatial arrangement of the molecule. Moreover, real polymers contain kinks, twists, and bends, which potentially cause an interruption of the conjugation. These factors give rise to a situation where the delocalization of  $\pi$ -electrons does not extend over the whole molecule but is divided into series of several conjugated segments with different conjugation lengths all over the polymer strand. As a result, the so called effective conjugation length characterizing a polymer is determined on the one hand by the extension

of the  $\pi$ -electron conjugation and on the other hand by the degree of overlap of the participating  $p_z$ -orbitals, which is depending on geometrical issues. For a pyrene based polymer, which will be presented in the course of this thesis, these influences for example cause a dihedral angle of  $70^\circ$  between different monomer units and the conjugation stays more or less confined to the individual pyrene units.<sup>[66]</sup>

## 2.2 Excited States

In general electronic semiconductor systems need to be promoted from the electronic ground state into an energetically higher located excited state in order to execute electrical and electro-optical processes like charge transport, charge transfer or the emission of light. Inorganic semiconductors with their rigid three-dimensional lattice structure do not show any considerable structural reaction upon excitation. Conjugated organic materials, in contrast, are considered as one-dimensional and exhibit a strong electron-lattice coupling. An excitation of any kind constitutes a change of the electronic configuration and the electronic potential, respectively, and thus triggers a structural relaxation of the atoms in the molecule, in order to achieve an energetically more favorable configuration. As a consequence, an excited state in conjugated materials, in contrary to their counterparts in inorganic semiconductors which are highly delocalized, show a more or less pronounced localization and are not able to move freely throughout the molecule.<sup>[67]</sup> Consequently, excited states in organic semiconductors can be described as quasi-particles consisting of the localized excitation itself in conjunction with the resulting structural distortion.

Two kinds of these quasiparticles can be found in the focal point of this thesis: singly charged polarons and bound electron-hole pairs called excitons.

### 2.2.1 Polarons

The creation of an excess charge in an organic semiconducting material by removing an electron from the HOMO (creating a hole) or by adding an electron to its LUMO is accompanied by a deformation of the molecular structure near the charge at the cost of elastic energy. Simultaneously the electronic energy of the excess charge is lowered. The interaction between the increased deformation energy and the lowered electronic energy results in a reduction of the overall system energy and determines the extent of the molecule's lattice deformation that normally has the dimension of some monomer units. The created excess charge and its resulting structural distortion as an entity are termed a *positive polaron* in case of a hole or *negative polaron* in case of an electron, respectively. These polarons, in contrast to free electrons or holes in inorganic semiconductors, are quasi-particles localized by the electron-lattice coupling in the material. Moreover, due to shift of the electronic energy, new states, called *intra-band-states*, are generated which are situated in the  $\pi$ - $\pi^*$  energy gap between the HOMO and the LUMO of the undistorted system.

For the sake of completeness, please note that doubly charged excess charges can be generated as well and are called *bipolarons*. Figure 2-5 depicts the different types of polarons and their respective energy levels. Following Pauli's law each level is able to accommodate two charge carriers of the same electronic charge but with different spin direction.

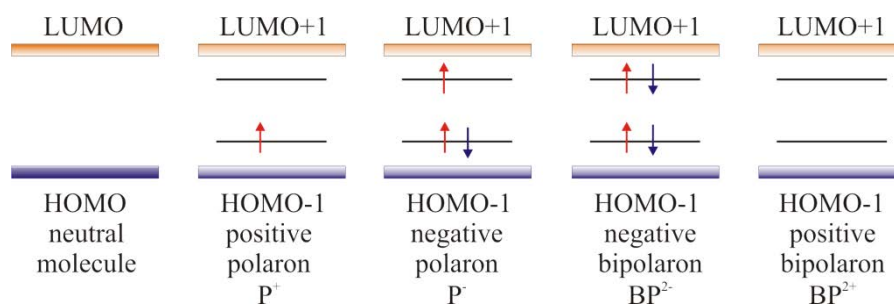


Figure 2-5: Schematic picture of the energy levels and their charges including spin directions of a neutral molecule, a positive polaron, a negative polaron, a negative bipolaron and a positive bipolaron.

### 2.2.2 Excitons

Neutral excited states that appear in the electronic system of a conjugated organic material are called *excitons*. They consist of an electron-hole pair bound due to Coulomb interaction (Coulomb-correlated electron-hole pair) thereby forming a neutral entity.<sup>[68]</sup>

Exciton formation can basically be induced by two processes: Firstly an electron can be excited upon photon-absorption promoting the electron from the HOMO to the LUMO and at the same time creating a hole in the LUMO. Due to the Coulombic force both charge carriers are bound together thus forming an electrically neutral quasi-particle, the exciton. Secondly, positively and negatively charged polarons can form electron-hole pairs due to Coulomb interaction after injection from electrodes and subsequent charge carrier transport. As for all excited states in organic semiconducting materials the excitation is accompanied by a modification of the molecular structure surrounding it. In combination with the Coulomb interaction, the structural relaxation again leads to the formation of intra-band-states with an energy difference between the ground state and the excitonic state that is lower than expected from the difference of the ionization potential (IP) and the electron affinity (EA) of the material. Excitons in organic polymers exhibit a typical localization within the range of one monomer unit or 1.5-2 nm in not very dense matter and display binding energies in the range of 0.3-0.5 eV. Their binding energy and localization classifies them as *Frenkel-excitons*. *Wannier-excitons*, in contrast, typically appear in inorganic semiconductors. They show an extent of several unit cells in denser materials caused by a screening of the electron-hole attraction by the atoms, and exhibit a binding energy of about 0.1 eV.<sup>[69-71]</sup>

Excitons can be classified further according to the overall spin state of the electron-hole pair. Both charge carriers belong to the class of fermions thus exhibiting a spin of  $\pm \frac{1}{2}$  that can be added to a total spin of zero or one. Furthermore, in quantum mechanics quasi-particles are described by wavefunctions and consequently a wavefunction can be derived for excitons, with a spatial and a spin part that has to obey Pauli's principle of antisymmetry with respect to particle exchange. Following these principles there are four different combinations to form the neutral state of an exciton: If the spatial part of the wavefunction is supposed to be symmetric, the spin part has to be antisymmetric with a total spin of zero and the configuration  $2^{-1/2} [(\uparrow\downarrow) - (\downarrow\uparrow)]$ . The corresponding exciton is termed *singlet-exciton*. If, on the other hand, the spatial part of the wavefunction is supposed to be antisymmetric, the spin part has to be symmetric with a total spin of one. In accordance with quantum mechanics this yields three possibilities for the spin configurations:  $(\uparrow\uparrow)$ ,  $(\downarrow\downarrow)$  and  $2^{-1/2} [(\uparrow\downarrow) + (\downarrow\uparrow)]$ . Evidently, all three configurations are energetically equal which means that they constitute a three-fold degenerated state and therefore are called *triplet-excitons*. Since in the triplet state the electrons are not paired, they have to occupy different orbitals, which is in contrast to the singlet state where the pairing of the electrons allows for the occupation of the same orbital. Consequently, triplet excitons show decreased electron-electron repulsion which results in lower triplet energy in comparison to the singlet state.

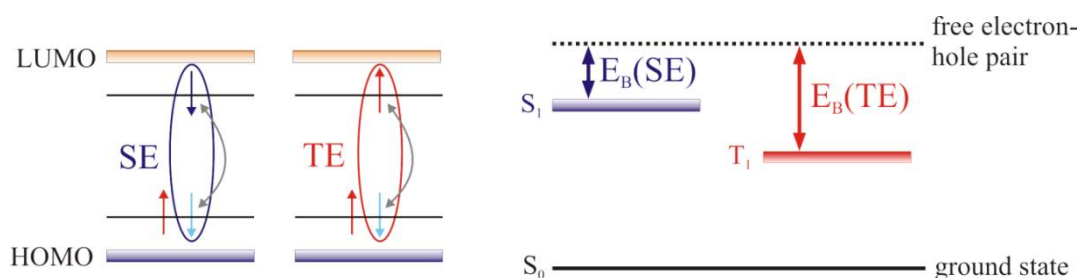


Figure 2-6: Schematic picture of singlet (SE) and triplet excitons (TE) regarding the spin directions of electrons and holes (left); Energy level schematics of first excited singlet and triplet states (right).

## 2.3 Basic Optical Properties and Frank-Condon-Principle

As it is known, electronic transitions between the  $\pi$ - $\pi^*$  gap like excitation of a molecule or the deactivation of the excited state back to the ground state – e.g. absorption or emission of a photon, respectively – in organic semiconductors are accompanied by a change in the structural order of the atoms. Thereby, electronic transitions usually take place within a timescale of femtoseconds ( $10^{-15}$  s), while the atomic structure needs about  $10^{-13}$  s to respond to the change of the electronic state. In quantum mechanics the *Born-Oppenheimer approximation* is used to describe such a process by expressing the multi-particle wavefunction as the product of an electronic and an atomic wavefunction. Hence, an electronic transition is considered as a two-step process: At first, the electronic wavefunction is determined under the condition that the atomic nuclei of the molecule are fixed around their equilibrium position. Subsequently the atomic wavefunction and thus the change of the atoms' positions is evaluated by using the average potential of the electron distribution.

According to the fundamental principles presented so far, transitions between the electronic ground state and an electronic excited state, i.e. HOMO-LUMO transitions, always involve  $\pi^*$ -states, which due to their antibonding character display an increased bond length in comparison to the  $\pi$ -states, which results in elevated equilibrium distances ( $Q'_A$ ) for the nuclei. Thus, the potential energy curves for the ground state and an excited state display a specific offset with respect to their spatial position (Figure 2-7).

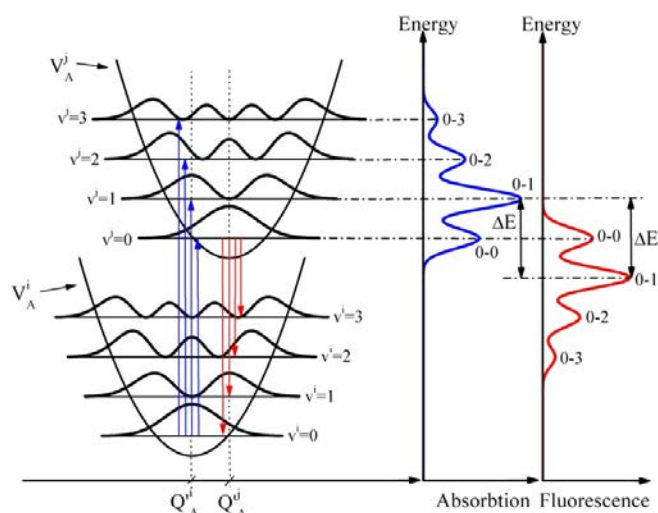


Figure 2-7: Potential characteristic with additional vibrational levels of a molecule in ground and excited state. Red and blue arrows indicate the possible electronic transition paths and the corresponding absorption and emission spectra are depicted on the right side.

The excitation or deactivation process can further be described according to the *Franck-Condon-principle*<sup>[72,73]</sup> which takes into account the different equilibrium atomic distances as well as the difference in timescales for excitation and atomic rearrangement. It yields that electronic transitions in most cases are coupled to vibrational modes of the molecule.<sup>[74]</sup> Therefore in the schematic energy diagram of Figure 2-7 the electronic transitions are depicted as vertical transitions.

Two vibrational levels of a certain electronic state are separated by an energy difference usually in the range of 0.1 eV. Since this amount of energy via  $E = k_B T$ , where  $E$  is the energy,  $k_B$  is the Boltzmann constant and  $T$  is the temperature, corresponds to a temperature of  $\approx 1200$  K, the preferred vibrational state  $v$  at room temperature (293 K) is the lowest state ( $v = 0$ ;  $E = 0.025$  eV). Consequently, electronic transitions of an electron starting at the lowest vibrational state do not necessarily result in the population of the lowest vibrational level of the final state. In fact, transition processes typically exhibit a transition from the zero vibrational state to higher vibrational levels. Depending on the vibrational levels involved such transitions are referred to as  $0-0$ -,  $0-1$ -,  $0-2$ -...transitions which appear as corresponding side-bands in absorption and emission spectra. The intensity of the individual transitions is described by the *Franck-Condon factor*, which is proportional to the absolute square of the overlap integral of the participating vibrational wavefunctions. In any case the coupling between the electronic and vibrational transitions is dependent on the displacement of the atoms in the beginning compared to the final state and can be described by the *Huang-Rhys factor*  $S$ .<sup>[75]</sup>

$$S = \frac{1}{2} \frac{M \omega^2}{\hbar \omega} (Q_A^i - Q_A^j)^2 = \frac{\Delta E}{\hbar \omega} \quad (2.1)$$

where  $M$  denotes the effective mass,  $\hbar \omega$  is the corresponding transition energy,  $Q_A^i$  and  $Q_A^j$  denote the corresponding coordinates of the starting and the final states and  $\Delta E$  is the energy difference between the main vibrational final state and the lowest vibrational state of the starting state. From this formula, which characterizes the prevailing transition, it is obvious that  $0-0$  transitions are strongest in the case when the molecule shows no structural rearrangement since the factor is zero. For significant displacements, however, oscillator strength is shifted from this transition towards higher located vibrational states leading to pronounced sidebands in the spectra. Consequently, this means that  $S$  is large for molecules exhibiting high degrees of freedom concerning deformation as can be found in small non-rigid molecules.

After the transition, according to *Kasha's rule*,<sup>[76]</sup> finally, the molecule relaxes down to the lowest vibrational state, a process which is termed *internal conversion (IC)*. As an example for these processes a molecule should be considered in the lowest vibrational state of the ground state. A photon with an energy above the bandgap is absorbed and promotes an electron from an occupied  $\pi$ -orbital to an unoccupied  $\pi^*$ -orbital, thereby lifting the molecule to a higher vibrational level of the excited state. In that context please note that, since the ground state is a singlet state with an overall spin  $S_{tot}$  of zero, due to the population of all corresponding orbitals with paired electrons, and since spin selection rules for optical transitions dictate that  $\Delta S = 0$ , only singlet excitonic states can be generated by direct absorption of a photon. Following the excitation, the molecule will relax to the lowest vibrational state via internal conversion typically in the timescale of  $10^{-12}$ - $10^{-13}$  s. After remaining in this excitonic state with an average lifetime in the lower nanoseconds ( $10^{-9}$  s) range, the molecule relaxes back to one of the vibrational levels of the ground state, either by emitting the excess energy as a photon (fluorescence), or through a non-radiative decay path where the excess energy is dispensed as phonons. Yet, the emitted photon, due to the internal conversion processes, obviously has a lower energy in comparison to the first photon used for the excitation. In absorption and emission spectra this leads to a more or less pronounced difference in the positions of the absorption and emission

maxima of the material which is called *Stokes-shift*.<sup>[77]</sup> From all the processes so far, it can be expected that molecules with predominating 0-0 transitions do not show a Stokes-shift. However, in addition to the stretching vibrations which can be resolved well, torsional vibrations may occur which, even when they cannot be detected as features in the spectrum, frequently cause a distinct Stokes-shift for 0-0 transitions. Because of the low difference between the corresponding vibrational levels of the excited state and the ground state for many organic semiconductors, a kind of mirror symmetry with respect to the 0-0 transition can be observed qualitatively between the absorption and the emission spectra. Yet, if for example a conjugated polymer exhibits considerable torsional freedom between the monomer units, the mirror symmetry can be strongly disturbed or even break down completely.<sup>[78]</sup>

In addition to the aforementioned transition processes of excitation and photon-emission in the singlet-manifold, which are in accordance with the spin selection rules for optical transitions, also triplet excitons may be formed from singlet excitons by a transition to the triplet-manifold *via intersystem crossing (ISC)*. Basically, this transition requires a flip or rephasing of the spin and according to the selection rules for dipole radiation is highly forbidden. Nevertheless, since the transition probability is not zero, triplet excitons may be formed as well, but their deactivation usually happens non-radiatively by the formation of phonons since a radiative decay back to the ground state again is forbidden by spin selection rules. However, in the case of strong spin-orbit coupling in the molecule the selection rules can be alleviated and singlet-triplet transitions are facilitated. In organic semiconducting materials a strong spin-orbit coupling and a resulting high transition probability can be induced by the incorporation of heavy metal atoms like iridium, platinum or bromine to the molecule.<sup>[79-81]</sup> Such materials are able to show significant radiative decay from the triplet- to the ground state (phosphorescence), yet, due to the occurring ban of triplet-singlet recombination the lifetime of triplet states in general is much higher and can be found typically in the range of microseconds to milliseconds ( $10^{-6}$ - $10^{-3}$  s).

Apart from the basic processes of fluorescence and phosphorescence, *delayed fluorescence* may occur in organic semiconductors. This term describes a radiative singlet recombination, which was delayed for example due to an energetic trapping of a singlet excited state at a particular site in the material. Another possibility causing a delayed singlet recombination is raised by triplet-triplet annihilation, where two triplet excitons interact, thereby forming one singlet exciton which recombines subsequently.<sup>[82,83]</sup>

In contrast to radiative or non-radiative recombination, an exciton can also dissociate forming two oppositely charged polarons. This polaron formation requires a charge transfer from one molecule to another and often occurs after a preceding generation of a charge transfer exciton, for example at the interface of two different materials or due to an electric field. Under these conditions, a dissociation of the exciton into two polarons displays an energetically more favorable configuration than the exciton. A graphic presentation of possible excitation and recombination processes in a material can be given by the *Jablonski* diagram.<sup>[84]</sup> As shown below, this diagram schematically depicts the energetic and vibrational levels of the different states – singlets and triplets – as well as possible transition processes. The characters S and T stand for singlet and triplet excitonic states and the indices label their order in the respective manifold (Figure 2-8).



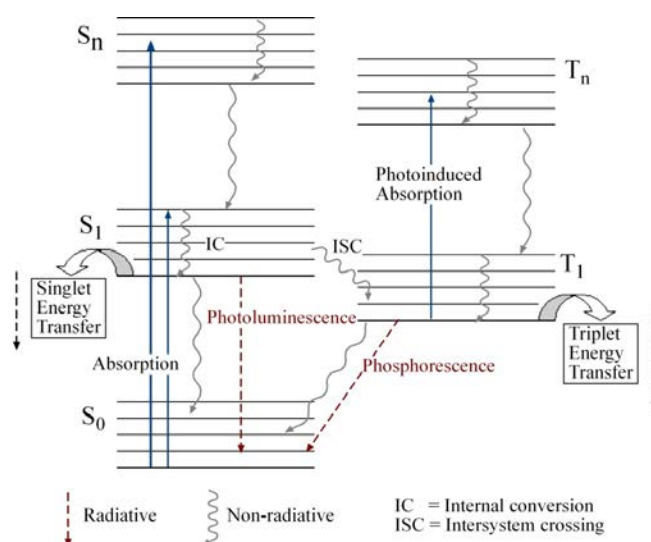


Figure 2-8: Jablonski diagram of radiative and non-radiative processes in an organic semiconductor.

- **Excimer and Exciplex**

Another type of emissive states occasionally appearing in conjugated molecules are excimers or exciplexes. Under specific conditions it is possible that a molecule in an excited state interacts with another molecule, either in an excited or in the ground state, thereby forming a completely new excited state involving both molecules. This new state constitutes a kind of a charge transfer complex and is called *excited dimer* or short *excimer* if both parts exhibit the same chemical structure or *exciplexes* if the two molecules have a different chemical configuration. Because in general the formed excimeric state is situated at a considerable lower energy level, the luminous emission characteristically emitted by these complexes is considerably shifted to higher wavelengths in comparison to the characteristic emission of the individual molecules taking part in the interaction. Furthermore, the emission characteristic shows no vibrational structure due to the mixing of vibrations and rotations of both components involved. It is important to note, that excimers as well as exciplexes do not exhibit a stable groundstate configuration, thus they exist only in their excited form.

### 2.3.1 Photoluminescence and Electroluminescence

In chapter 2.2.2 two basic processes were mentioned to generate excitons: Photo-absorption and recombination of two injected and oppositely charged polarons. Depending on the kind of generation, the emission of light by recombination of electronically excited states, which in general terms *luminescence*, can be divided in *photoluminescence* and *electroluminescence*.

- **Photoluminescence:**

In case excitons are generated upon absorption of light a subsequent photon emission is called *photoluminescence (PL)*. As noted, only singlet excitons are generated due to the spin selection rules for optically induced transitions. The amount of excitons that recombine radiatively is depending on the availability and probability of non-radiative deactivation pathways, which cause a decrease of light emission. In addition, since in regular conjugated organic materials spin-orbit coupling is negligible, also triplet excitons generated by ISC will not contribute to luminescent exciton decay due to the absence of a radiative recombination channel. The ratio of the number of photons emitted  $N_e$  to the number of photons absorbed  $N_a$  is called *photoluminescence quantum yield*  $\eta_{PL}$  and can be expressed as

$$\eta_{PL} = \frac{N_e}{N_a} = \frac{k_r}{k_r - k_{nr}} \quad (2.2)$$

where  $k_r$  and  $k_{nr}$  denote the radiative and non-radiative rate constants.

- **Electroluminescence:**

Radiative recombination of excitons generated by previously injected charge carriers is called *electroluminescence*. In contrast to PL, the electronic excitation is not limited to the generation of singlet excitons but also triplets excitons are formed. Moreover, according to quantum mechanical spin statistics the ratio of triplet excitons amounts to 75%, due to the three-fold degeneration of the triplet state, in comparison to 25% for singlet excitons. The singlet-triplet ratio, however, is still a widely discussed topic among the scientific community.<sup>[79,85,86]</sup> The maximum efficiency achievable for electroluminescence in the case of organic semiconducting materials without enhanced spin orbit coupling consequently is limited to 25%. The ratio of photons created per injected electron thus defines the internal quantum efficiency for electroluminescence  $\eta_{EL}$  and is given by the formula:

$$\eta_{EL} \propto \eta_{PL} \cdot r_{st} \cdot \gamma_{cap} \cdot k \quad (2.3)$$

with  $r_{st}$  representing the ratio of singlets formed per exciton,  $\gamma_{cap}$  denotes the number of excitons formed per injected electron and  $k$  is a proportionality factor regarding various losses like quenching effects.

## 2.4 Charge Transport

Charge carriers, i.e. polarons, in organic semiconductors exhibit considerable lower charge carrier mobility (from  $10^{-5} \text{ cm}^2/\text{Vs}$  to  $10^{-1} \text{ cm}^2/\text{Vs}$ )<sup>[87]</sup> compared to charge carriers in inorganic semiconducting materials ( $10^3 \text{ cm}^2/\text{Vs}$  to  $10^5 \text{ cm}^2/\text{Vs}$ ).<sup>[88]</sup> The main reasons for this discrepancy can be found on the one hand in the nature of the polaron itself, causing highly localized structural and energetic disorder. The distortion of the molecular conformation combined with the altered electronic potential, in this way, act as shallow traps for the charge carriers. On the other hand, the greater majority of organic semiconductors, small molecules as well as conjugated materials, show impurities stemming from synthesis or incorporated during the assembly. In addition, semiconducting polymers usually manifest a distinctive disorder between the different monomer units, and kinks and twists of the polymer backbone give rise to low charge carrier mobility as well. Even though HOMO and LUMO in organic materials can often be visualized and described as band-like structures, similar to those in inorganic semiconductors, the energy values for these orbitals exhibit a Gaussian distribution of discrete HOMO and LUMO levels around theoretical values (Figure 2-9).

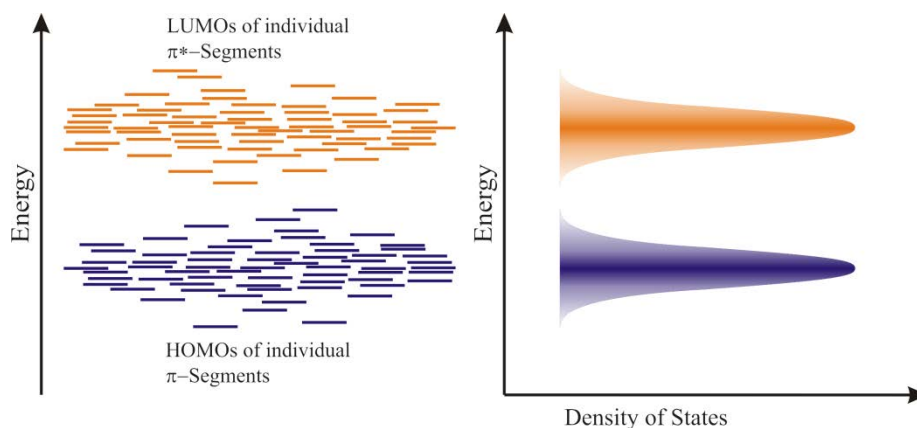


**Figure 2-9: HOMO and LUMO levels within real organic semiconductors following a Gaussian distribution. (from [89])**

As a consequence, the charge carriers are not able to move freely through the material and their movement can be characterized by a thermally activated (phonon-assisted) hopping process from one position to the next. Yet, a theoretical description of the charge transfer rates of electron-transfer reactions can be given by the *Marcus theory* developed by R.A. Marcus in the middle of the last century.<sup>[90]</sup> The following formula, which is valid over a wide range of temperatures, in a first approximation, specifies the hopping process in an organic semiconductor:

$$k_{et} = \left(\frac{4\pi}{h}\right) t^2 \left(\frac{1}{\sqrt{4\pi\lambda RT}}\right) e^{\frac{\lambda}{4RT}}. \quad (2.4)$$

In this formula  $h$  denotes the Planck constant,  $t$  stands for interchain transfer integral regarding the dependence of the charge mobility on the electronic coupling between the HOMO and the LUMO,  $\lambda$  describes the term of internal reorganization, thus the degree of structural reorganization, and  $T$ , finally, is the temperature.

## 2.5 Energy Transfer

Excited energy transfer processes in organic semiconductors, thus exciton transfers, basically can be described as an energy exchange between an excited donor ( $D^*$ ), which relaxes to the ground state by emitting the excess energy and an acceptor ( $A$ ) in the ground state, which gets excited by absorbing the energy.

The most trivial process in this regard constitutes a radiative energy exchange. In this process, an excited donor emits the energy as a photon that is absorbed by the acceptor. The corresponding energy transfer rate depends on the extinction coefficient of  $A$ , the number of molecules in the path of the photon (the thickness of the sample), the spectral overlap of the emission and the absorption spectrum and finally on the quantum yield of  $D^*$ .

Yet, for organic semiconductors two non-radiative energy exchange processes are of main importance: the first one is known as *Förster-transfer* and is induced by a dipole-dipole coupling of the interacting  $D^*$  and  $A$  molecules. The second non-radiative energy transfer, called *Dexter-transfer*, is based on the exchange of an excited electron between  $D^*$  and  $A$ . This process represents a quantum mechanical exchange process between the participating molecules and requires a non-vanishing overlap of the spatial part of the wavefunctions.

A general expression for the non-radiative excitonic energy transfer rate is given by

$$k_{DA} = \frac{2\pi}{\hbar} |U_{DA}|^2 J_{DA}. \quad (2.5)$$

Here  $U_{DA}$  denotes the electronic coupling between donor and acceptor while  $J_{DA}$  represents the spectral overlap integral of the emission spectrum of the donor and the absorption spectrum of the acceptor

$$J_{DA} = \int S_D(E) S_A(E) dE \quad (2.6)$$

where  $S_D(E)$  and  $S_A(E)$  constitute the normalized emission and absorption spectra. Initial and final electronic states participating in the excitation energy transfer are assumed to be products of intermolecular donor and acceptor ground and excited states  $|\psi_D\rangle, |\psi_D^*\rangle, |\psi_A\rangle, |\psi_A^*\rangle$  and thus can be expressed as

$$\begin{aligned} |init\rangle &= |\psi_D^*\rangle \otimes |\psi_A\rangle \\ |final\rangle &= |\psi_D\rangle \otimes |\psi_A^*\rangle \end{aligned} \quad (2.7)$$

The electronic coupling  $U_{DA}$  between D and A can further be split in two parts, the first ( $U_{DA}^C$ ) accounting for the Coulombic interaction between donor and acceptor and the second ( $U_{DA}^{Ex}$ ) considering the exchange interaction of the D-A pair:

$$U_{DA} = U_{DA}^C + U_{DA}^{Ex} \quad (2.8)$$

Quantum mechanically the particular terms can be expressed as:

$$U_{DA}^C = \sum_{i,j \in I_D} \sum_{R,S \in I_A} (\phi_i \phi_j | \phi_R \phi_S) \left\langle \psi_D^* \left| \sum_{\sigma} c_{i\sigma}^{\dagger} c_{i\sigma} \right| \psi_D \right\rangle \times \left\langle \psi_A \left| \sum_{\sigma^{\dagger}} c_{R\sigma^{\dagger}}^{\dagger} c_{S\sigma^{\dagger}} \right| \psi_A^* \right\rangle \quad (2.9)$$

and

$$U_{DA}^{Ex} = \sum_{i,j \in I_D} \sum_{R,S \in I_A} \sum_{\sigma, \sigma'} (\phi_i \phi_S | \phi_R \phi_j) \left\langle \psi_D^* \left| \sum_{\sigma} c_{i\sigma}^{\dagger} c_{i\sigma'} \right| \psi_D \right\rangle \times \left\langle \psi_A \left| \sum_{\sigma^{\dagger}} c_{R\sigma^{\dagger}}^{\dagger} c_{S\sigma} \right| \psi_A^* \right\rangle. \quad (2.10)$$

Here the characters  $i, j$  and  $R, S$  represent the interacting molecular orbitals of the donor and the acceptor molecule, respectively;  $c_{i\sigma}^{\dagger}$  and  $c_{i\sigma'}$  denote the fermionic creation and annihilation operators for electrons with spin  $\sigma$  or  $\sigma'$  in the mutually orthogonal orbitals  $\phi_i$  and  $\phi_j$ .

### 2.5.1 Förster Transfer

The first term of equation (2.8),  $U_{DA}^C$  represents the energy transfer mechanism known as *Förster-transfer*. It refers to a Coulomb mechanism firstly described by Förster<sup>[91]</sup> under the condition that donor and acceptor are separated sufficiently. In such a case, the transfer process can be understood as an emission and subsequent absorption of a virtual photon, thus only the leading dipole-dipole contributions have to be considered whereas interaction contributions can be neglected. Because of

$U_{DA}^C$  being zero unless the spin is conserved for each, the donor as well as the acceptor molecule, Förster-transfer can only occur for singlet excitons (Figure 2-10).

Thus, two key-factors are playing the main role for the efficiency of the Förster-transfer: The first one is represented by the spectral overlap  $J_{DA}$  for the dipole-dipole interaction and is defined as:

$$J_{DA} = \int_0^{\infty} \epsilon_A(\lambda) f_D(\lambda) \lambda^4 d\lambda \quad (2.11)$$

where  $\lambda$  denotes the wavelength,  $f_D$  represents the normalized emission spectrum of the donor and  $\epsilon_A$  is the molar decadic extinction coefficient of the acceptor.

As the second important factor the acceptor-donor spacing is decisive. Since Förster-transfer, which is also called *Fluorescent Resonant Energy Transfer (FRET)*, is strictly applicable for sufficiently high distances – in general much higher than the molecules' dimensions – an approximation can be used for  $U_{DA}^C$ :

$$U_{DA}^C = \frac{1}{4\pi\epsilon_0} \frac{\kappa \vec{\mu}_D \vec{\mu}_A}{R^3} \quad (2.12)$$

Here  $R$  is the distance between the two molecules,  $\kappa$  is an orientation factor and  $\vec{\mu}_D$ ,  $\vec{\mu}_A$  are the transition dipole moments for donor and acceptor. Additionally, it needs to be considered that the moment of an induced dipole is proportional to the inducing force thus an interaction involving an induced dipole is a second order effect. As a consequence a proportionality to the donor-acceptor spacing of  $R^{-6}$  arises for the energy transfer rate  $k_{ET}$  yielding the relation:

$$k_{ET} = \frac{1}{\tau_0} \left( \frac{R_0}{R} \right)^6 \quad (2.13)$$

where  $\tau_0^{-1}$  denotes the sum of radiative and non-radiative decay constants of the donor,  $R$  is the distance between donor and acceptor and  $R_0$  is the *Förster-radius*. This radius is defined as the distance between donor and acceptor where the probabilities for a radiative decay of the donor or a transfer of the excitation energy to the acceptor are equal and its definition is given by:

$$R_0 = \frac{9000 \ln 10 f^2 \eta_{PL} J_{DA}}{128\pi^2 N_A n^4} \quad (2.14)$$

where  $N_A$  is the Avogadro number,  $f$  represents an orientation factor,  $\eta_{PL}$  denotes the photoluminescence yield,  $J_{DA}$  stands for the spectral overlap integral and finally  $n$  is the refractive index.

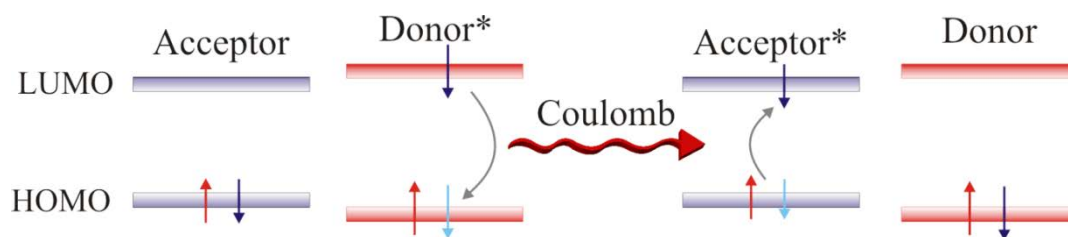


Figure 2-10: Schematic picture of the non-radiative Förster energy transfer mechanism between an excited donor molecule and an acceptor molecule. Due to spin selection rules, this transfer process is restricted to singlet-excitons.

### 2.5.2 Dexter Transfer

The second term of equation (2.8) refers to the electronic coupling due to an exchange interaction. It regards the *Dexter-transfer*<sup>[92]</sup> mechanism which can be understood as an exchange of an excited electron from the donor with a non-excited one from the acceptor. Quantum mechanically this transfer constitutes a tunneling process of an exciton from the donor to the acceptor that does not demand a spin conservation for the particular molecules but requires conservation of the total spin for the interacting donor-acceptor pair. Hence, Dexter transfer is permitted for singlet- as well as for triplet-excitons. Since quantum mechanical tunneling demands for a high overlap of the wavefunctions of both molecules the spatial distance needs to be sufficiently small to allow for an efficient energy transfer. The energy transfer rate  $k_{ET,Dexter}$  accordingly shows an exponential dependence on the distance between the donor and the acceptor molecule:

$$k_{ET,Dexter} = KJ_{DA}e^{-\frac{2R_{DA}}{L}}. \quad (2.15)$$

In this formula  $K$  is related to specific orbital interactions,  $J_{DA}$  again represents the normalized spectral overlap integral,  $R_{DA}$  denotes the donor-acceptor distance and  $L$  is the van der Waals radius.

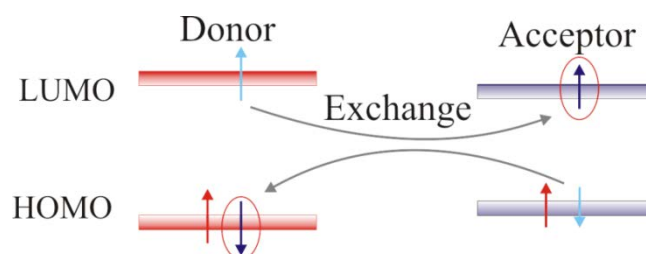


Figure 2-11: Schematic picture of an electron exchange via Dexter type energy transfer between donor and acceptor for a triplet exciton.

Since the intermolecular overlap between the donor and acceptor molecular orbitals depends strongly on the molecular distance, it is clear that the transfer probability from equation (2.15) decreases fast with increasing distance and thus Dexter energy transfer is only significant for distances up to 1 nm.<sup>[93,94]</sup>

## 2.6 Interfaces and Energy Level Alignment

Even though the electronic properties of an organic electronic device, be it an OLED or an OSC, are for the most part governed by the basic properties of the respective organic materials it is imperative to investigate the specific processes at the interfaces between particular materials. Basically there are two types of interfaces occurring most commonly in organic electronic devices: metal-organic interfaces

(e.g. between metal electrodes and active semiconducting organic material) and organic-organic interfaces (e.g. between different electro-active materials performing specific tasks within the device). In any case, the interface properties of the particular material combinations bear the potential to influence considerably the device function due to a probable formation of charge carrier blocking energy barriers and thus are of utmost importance in order to ensure optimized functional capability.

An appropriate way to describe the conditions at any interface, and thus qualitatively or quantitatively the interaction between the materials, is to analyze the alignment of the respective energy levels as there are the *vacuum level* ( $E_{VAC}$ ), the *Fermi level* ( $E_F$ ), the work function ( $\phi$ ) as well as the HOMO and the LUMO.

### 2.6.1 Metal-Organic Interfaces

A first approach frequently applied earlier to characterize the energy level alignment between metals and organic semiconductors was performed by treating the particular levels according to the *Mott-Schottky-rule*.<sup>[95,96]</sup> In this idealized model, the vacuum levels of the participating materials align and all other energy levels are considered as constants of the particular materials. This theory assumes that the organic semiconducting material constitutes an amorphous van der Waals solid exhibiting closed shell properties and that are linked to other solids just by weak van der Waals forces. Moreover it is the assumption that charge carriers are highly localized and charge transport only occurs by site-to-site hopping.<sup>[97]</sup> Thus, it is presumed that the participating materials do not interact, i.e. no interface states are created with energy values differing from those determined separately for the individual materials (Figure 2-12). While in general a description in that way might enable a vague estimation that is helpful for the characterization of conditions occurring at the interface (offsets between the work function and the HOMO/LUMO levels), it is strictly only applicable for interfaces which are completely free from any interface states. Even though the validity of the Mott-Schottky rule in case of metal-organic interfaces could be shown for highly purified conjugated materials,<sup>[98]</sup> considerable discrepancies between the theoretical model and experimental data frequently occur. In particular, experimentally determined energy barriers at the interface are often distinctively (up to 1 eV) higher or lower than those predicted by the Mott-Schottky model.

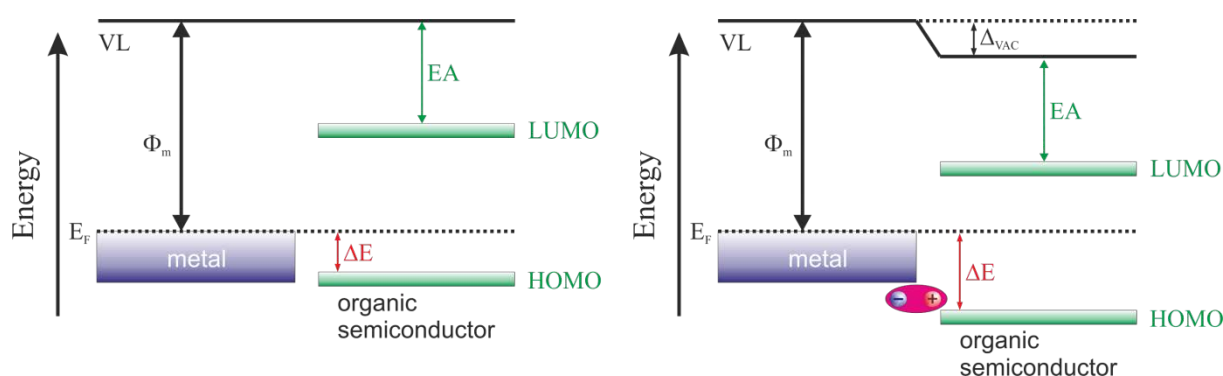


**Figure 2-12: Energy level alignment according to the Mott-Schottky model (left) and considering the formation of interface dipoles (right). (modified from [99])**

To explain the differences and to develop an understanding of the metal-organic interface significant efforts have been done and a variety of measuring methods such as *ultraviolet photoelectron spectroscopy* (UPS), *inverse photoelectron spectroscopy* (IPES), *x-ray photoelectron spectroscopy* (XPS) and *Kelvin probe* (KP) measurements were employed to probe the interfaces. One of the most important conclusions was that the Mott-Schottky model for the greater majority of metal and organic semiconductor combinations does not apply. In contrary, an abrupt change of the work function of a

clean metal could be detected upon layer by layer deposition of organic molecules within the first 2 nm. This effect, occurring closely to the interface, is often accompanied by a further slight change of the work function for thicknesses of the organic material up to several hundred nanometers. This phenomenon, which is commonly termed as *vacuum level shift* ( $\Delta_{VAC}$ ) can be explained by a modification of the surface dipole of the metal due to a rearrangement of the electron density distribution of the surface of the metal as well as of the organic material, which leads to a modification of the electrical potential above the surface.<sup>[99,100]</sup>

A qualitative picture of the formation of  $\Delta_{VAC}$  between a clean metal and an organic material is shown in Figure 2-13. As depicted on the left hand side of the scheme the work function  $\phi_m$  of the metal consists of two parts: the *bulk chemical potential* ( $\mu_{bulk}$ ) and the *surface dipole* (*SD*), caused by electrons protruding from the metal's free surface into the vacuum. For the organic material HOMO and LUMO levels are depicted as they are appearing at a distance sufficiently large to exclude interaction (Figure 2-13). Yet, upon contact between the materials, i.e. material deposition onto the metal, a reduction of  $\phi_m$  to  $\phi'_m$  can be detected which is referred to as *interface dipole* (*ID*). However, this ID is a virtual dipole since it results from a pushing back of the electrons spilling out of the metal surface thus effectively just lowering SD (Figure 2-13, right). The consequences for the energy level alignment and the resulting energy level offsets can perfectly be observed by comparing the schematic alignment of the energy levels according to the Mott-Shockley rule (Figure 2-12, left) and by adjusting the work function via accounting for the ID-formation (Figure 2-12, right). While in the former case no energy difference can be found between  $\phi_m$  and the HOMO, in the latter case a distinct blocking barrier is formed due to the downward-shift of the vacuum level and the corresponding mismatch between the metal's work function and the HOMO of the organic material.

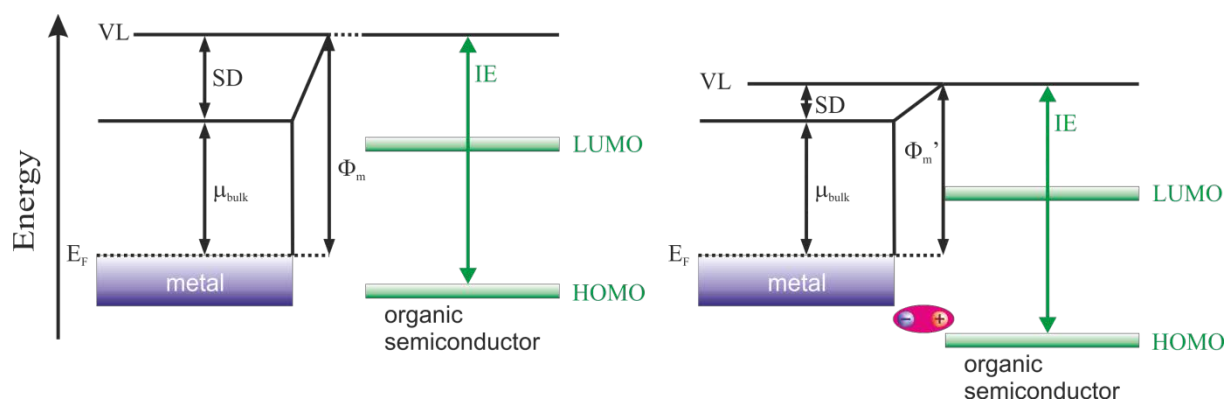


**Figure 2-13: Schematic picture of the energy levels before (left) and after the formation of a vacuum-level shift due to an interface dipole at a metal-organic interface (right). (modified from [99])**

In the situation described above, the formation of an ID only because of pushing back of electrons strictly speaking assumes only a weak metal-organic interaction and the assumption of vacuum alignment still holds as long as the change of  $\phi_m$  upon contact with the organic is considered. However, several mechanisms may form a “real” interface dipole between the two materials caused by strong interactions that demand to omit the vacuum level alignment completely. In these cases, a stepwise alignment of the vacuum levels of the different materials can be detected. As sources for the ID formation the following mechanisms or conditions can be specified:<sup>[89,100]</sup>

- Charge transfer between the metal and the organic material resulting in a completely ionized first molecular layer of the organic material
- Polarization of the electron cloud of the organic molecules adjacent to the metal surface due to image charges in the metal



- Chemical reactions leading to a rearrangement or the formation of new bonds in the organic material as well as between the organic material and the metal
- Interfacial electronic states caused by the mixing of the energy states of the metal and the organic material
- Permanent dipoles in the organic material caused by intrinsic dipoles of the molecules, especially when forming highly ordered structures on the metal's surface.

### 2.6.2 Organic-Organic interfaces

To enhance functionality and efficiency in modern design concepts for organic electronic devices, frequently so called multilayer structures are used where the organic part comprises of a layer-by-layer assembly of several different organic semiconducting materials. Consequently, not only the alignment of the energy levels between a metal and an organic material is important but also the energetic states of organic-organic interfaces need to be examined accurately. It has to be noted that for organic-organic interfaces distinct values of  $\Delta_{\text{VAC}}$  could be obtained as well, however a neglect of the shift does by far not lead to such large discrepancies regarding energy level alignment as in the case of metal-organic interfaces. From the reasons mentioned above for the formation of ID at a metal-organic interface, in the case of an interface between two different organic components primarily charge transfer, interfacial electronic states and permanent dipoles seem to be of higher importance.

Summing up this section, it has to be noted that, even if in some particular cases a simple estimation of the energetic structure at a specific interface from the energy levels of the separate materials might be successful, only a thorough experimental analysis of the energy levels of the actual material combination is able to provide the required data in order to understand the contribution of each of the particular materials to the functionality of an organic electronic device. More detailed information about metal-organic as well as organic-organic interface energetics and some fundamental discussions about the occurring processes upon interface formation in organic electronic devices are presented in references [100–103].

## 2.7 Charge Injection

In organic electronics the very well most important role concerning metal-organic interface formation is played by metal electrodes providing charge injection into or charge extraction from the organic semiconducting material, respectively. In that context, one has to keep in mind that organic semiconductors constitute amorphous van der Waals solids exhibiting highly localized charge carrier (polaronic) states on individual molecules or conjugated segments of the polymer. As a result of the strong localization, where an excess charge is accompanied by a local distortion of the molecule structure, charge transport consists of a phonon-assisted hopping process (c.f. chapter 2.4). Metals in contrast display completely delocalized charge carriers which quantum mechanically can be described by an electron density that is distributed equally over the whole metal. As a consequence of this basic difference of localization on the one hand and completely delocalization on the other, a charge transfer from a metal to an organic semiconducting material represents a transition from an extended band-like state in the metal to a highly localized polaronic state on the organic molecule or polymer segment and vice versa.<sup>[104]</sup>

In accordance with the interface energetics at metal-organic interfaces explained in chapter 2.6 two kinds of contacts can be formed between a metal and an organic semiconductor: an *ohmic contact* or an *injection limited contact*. The decisive factor in this context is the energy difference between the

workfunction (Fermi-level) of the metal and the HOMO or LUMO-level of the semiconductor, respectively (Figure 2-12).

### 2.7.1 Ohmic Contacts

From the charge carriers point of view an ohmic contact for electron injection ideally is formed when  $\phi_m < E_{LUMO}$ . Under these conditions, electrons are transferred from the metal to the semiconductor, thereby enhancing  $\phi_m$  until it lines out with the LUMO. This effect is termed as *Fermi-level pinning*.<sup>[105]</sup> Therefore, the electron density in the semiconductor is enhanced and the contact resistance is negligible small. For hole injection an ohmic contact is established when  $\phi_m > E_{HOMO}$ . Also in this case, a charge carrier transfer occurs, leading to an alignment of  $\phi_m$  and the HOMO of the organic material, which finally results in a positively doped semiconductor and the formation of a low resistance contact.

### 2.7.2 Injection Limited or Schottky Contact

The contact between a metal and an organic semiconductor is called injection limited or rectifying for electrons when  $\phi_m > E_{LUMO}$ . In this case electrons move from the semiconductor to the metal or at least are transferred to the interface, forming an interface dipole within the first few molecular layers of the semiconductor. Upon the displacement of the electrons, the interface will be charged positively at the semiconductors side and negatively at the metals side. This situation, however, was already depicted in Figure 2-12 and a vacuum level shift between the two materials arises. Consequently, an electrostatic potential barrier  $\Delta E_B$  is formed at the metal-organic interface, which results in an electric field that repels electrons from the junction and prevents transitions from the organic to the metal. In a first approximation the height of  $\Delta E_B$  can be calculated by

$$\Delta E_B = \phi_m - E_{LUMO} \quad (2.16)$$

The metal-organic junction acts like a rectifying contact (Schottky diode), thus in order to inject electrons from the metal to the organic semiconductor  $\Delta E_B$  has to be overcome. In organic semiconductor devices, this can be achieved by applying a bias in forward direction. Thereby, a triangular potential characteristic is formed which enables an injection of the charge carriers.

For hole injection the formation of an injection limited contact and the processes at the junction can be explained analogously and these contact are formed when  $\phi_m < E_{HOMO}$ .

Equation (2.16) describes the energy barrier in case of an ideal contact. However, in real devices the potential actually shows to be slightly smaller. This can be explained by taking into account the potential of the electric field, which is applied in order to overcome the barrier and the potential of an image charge. The image charge is induced within the metal upon injection and possesses an inverse polarity to the injected charge carrier thus lowering the effective barrier height. The resulting potential can be described by the following formula:

$$\phi(E, x) = \Delta E_B - eEx - \frac{e^2}{16\pi\epsilon\epsilon_0 x}. \quad (2.17)$$

Here  $\Delta E_B$  denotes again the difference between  $\phi_m$  and the electron affinity  $\chi$  of the semiconductor, the second term accounts for the potential of the applied electric field  $E$  and the last term represents the potential of image charges in the metal caused by injected charges close to the interface. The variable  $x$  is the distance of the injected charge to the interface.

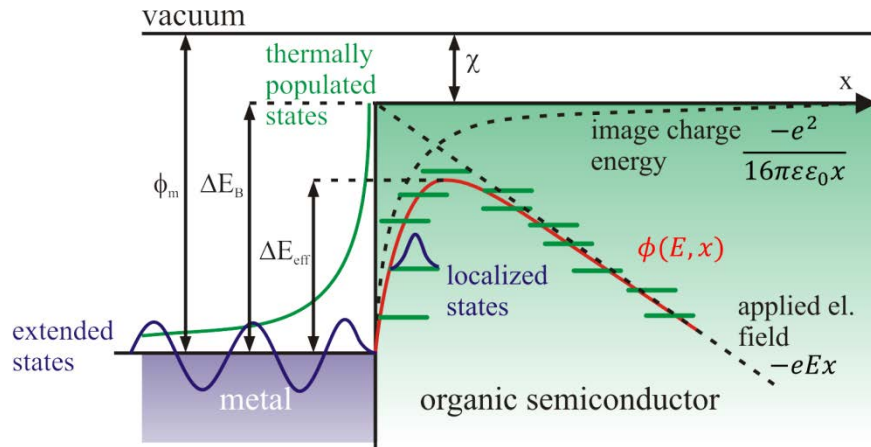


**Figure 2-14:** Electronic potential  $\Phi$  at a metal-organic interface in dependence of the distance  $x$ . The scheme shows the development of the effective energy potential barrier  $\Delta E_B$  as a combination of the potential of an applied electric field and of image charges generated in the metal upon charge carrier injection.

### 2.7.3 Charge Injection Mechanisms

There are basically two classical mechanisms which can be used to describe the process of charge carriers overcoming the potential barrier. The first one describes a thermionic emission process at low applied fields, where the probability to surmount an energetic barrier increases with temperature. This process is mainly observed for charge carriers emitted from a hot metal surface. According to a model derived by Richardson<sup>[106]</sup> and Dushman<sup>[107]</sup> the current density  $J$  caused by thermionic injection of charge carriers into an inorganic semiconductor can be described by the famous *Richardson-Dushman-equation*:

$$J = \frac{4\pi k^2 m^*}{h^3} T^2 \exp\left(-\frac{q\phi}{kT}\right) = A^* T^2 \exp\left(-\frac{q\phi}{kT}\right) \quad (2.18)$$

with  $\phi$  representing the potential barrier,  $k$  is the Boltzmann-constant,  $m^*$  denotes the effective mass of the charge,  $h$  is the Planck constant,  $T$  represents the absolute temperature and  $A^*$  stands for the material dependent effective Richardson-constant. However, since generally the temperatures in organic semiconducting devices are rather low, the thermal contribution only gets significant for low barrier heights.

The second mechanism enabling to overcome a potential barrier constitutes of a tunneling effect induced by field emission and was presented by Fowler and Nordheim.<sup>[108]</sup> Their model is based on a quantum mechanical tunneling effect through a triangular barrier and has to be considered when strong electric fields are applied. In this case the current density is expressed by the *Fowler-Nordheim-equation*:

$$J = \alpha \frac{E^2}{\phi} \exp\left(-\frac{8\pi\sqrt{2m^*}\phi^{\frac{3}{2}}}{3eEh}\right). \quad (2.19)$$

In this formula  $E$  represents the applied electric field,  $\alpha$  is a material constant,  $m^*$  denotes the effective mass of the charge,  $\phi$  represents the potential barrier,  $e$  is the elementary charge and finally  $h$  is again the Planck constant.

Both models, the Richardson-Dushman- as well as the Fowler-Nordheim model, allow for a qualitative description the charge injection process. Yet, in terms of a correct quantitative description for the injection of charges from a metal into organic semiconductors both fail. This is caused on the one hand by the negligence of possible recombination due to backflow of charge carriers to the metal. On the other hand, the energetic disorder, due to randomly distributed polaronic states, is ignored as well. Models accounting for both effects, as for example presented by Arkhipov,<sup>[109,110]</sup> describe the injection as thermally assisted tunneling injection. Monte-Carlo simulations were conducted for this model and its validity could be experimentally verified for small molecules as well as for polymers.<sup>[109,111,112]</sup>

## 2.8 Fundamentals on Organic Light Emitting Devices

### 2.8.1 OLED – Architecture

Despite remarkable efforts have been made in the last decades in the field of research and development on organic light emitting devices and polymer light emitting devices, today's state-of-the-art devices in principle still exhibit more or less the same device architecture as the first practical OLEDs and PLEDs presented by Tang and Burroughes about 30 years ago.<sup>[18,19]</sup> This simple architecture is called “*Sandwich-structure*” and consists of one or more active organic layers situated (sandwiched) between two electrodes, one of which is transparent in the spectral region of visible light in order to enable light outcoupling (Figure 2-15). In detail, the basis for the simplest device setup, a single layer OLED, is represented by a glass substrate which is covered by a very thin layer of indium-tin-oxide (ITO) which constitutes the bottom electrode. On top of this bottom electrode, the active light emitting organic layer is deposited either via a solution based deposition process, which is typically the case for conjugated polymers, or by thermal evaporation under high vacuum which is usually done for small molecules. The evaporation of a metal layer on top of the organic semiconductor finally finishes the assembly. It is important to note that this simple single layer structure generally leads to low overall device efficiencies, thus the device assembly is frequently modified by additional layers exhibiting for example specific charge carrier transporting or blocking properties in order to improve the device performance.

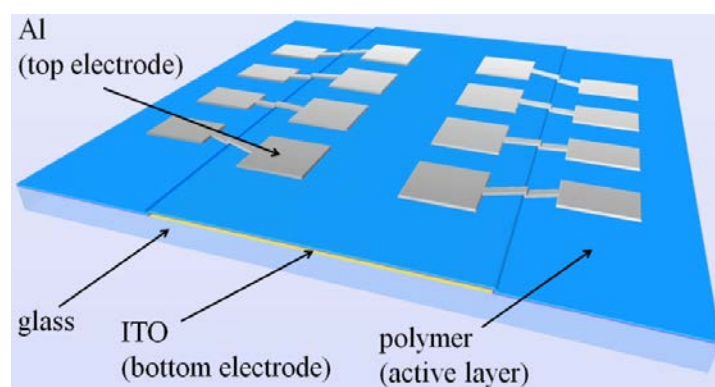


Figure 2-15: Schematic structure of a single layer OLED substrate containing eight devices.

## 2.8.2 OLED – Working Principle

Basically, in order to generate electroluminescence emission in an OLED three main processes take place:

- charge carrier injection from the electrodes into the active layer
- polaron formation in the organic semiconductor and polaron transport driven by an applied external electric field and finally
- exciton formation, migration and radiative recombination in the organic material.

The relevant fundamental mechanisms forming the basis for these processes were already discussed in the previous sections. Thus, in order to provide a basic understanding, a schematic description of an OLED's working principle is given in the following.

Figure 2-16 shows the energy schematics of a single layer device structure under the assumption that no external electric field is applied.  $\phi_A$  and  $\phi_C$  denote the Fermi levels of the electrode metals and  $\Delta E_e$  and  $\Delta E_h$  are the injection barrier for electrons and holes, respectively. As described in chapter 2.7 the formation of energy barriers, resulting from an unfavorable alignment of the electrodes' work functions and the HOMO/LUMO levels of the organic semiconductor, can considerably limit the amount of charge carriers that can be injected into the device. Thus, in order to maximize the device performance, it is necessary to select the electrode materials in such a way that energy barriers are as small as possible or at best vanish completely. In practice, the latter case is seldom achieved, however a minimization of energy loss can be realized by the utilization of electrode materials, which at least exhibit work functions that are close to the organic semiconductor's HOMO and LUMO level, respectively.

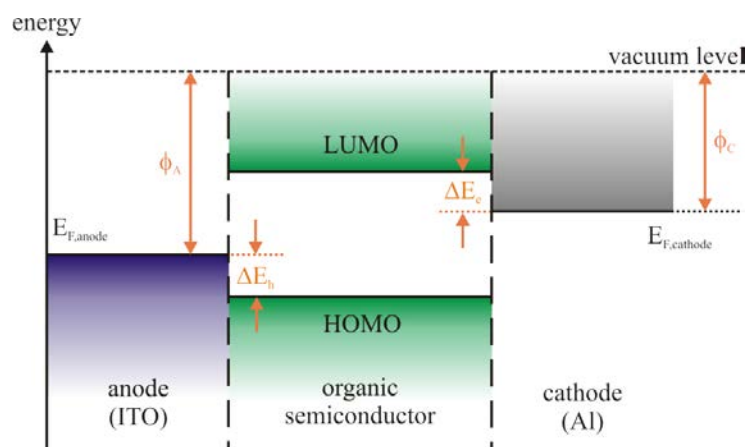


**Figure 2-16: Energy levels of the organic semiconductor and Fermi levels of anode and cathode materials in a single layer device without applied voltage.**

If an external bias in forward direction  $U_{\text{ext}}$  is applied to the presented device, which means that the low work function metal acts as a cathode, a tilting of the HOMO and LUMO levels occurs (cf. Figure 2-17). This effect results in the formation of a triangular shaped potential barrier at the electrodes, which can be overcome by charge carriers, as described in chapter 2.7. In the organic semiconductor, the charge carriers form polarons that move through the material driven by the applied electric field. If two oppositely charged carriers meet, they are able to generate excitons and finally relaxation occurs via one of the possible decay paths. From Figure 2-17 it is immediately clear that the formation of rather high injection barriers is effectively blocking the injection of charge carriers when a bias in reverse direction is applied. Thus, the rectifying behavior of an OLED is caused by the difference

between the work functions of the electrodes, in contrast to inorganic diodes, where the rectifying behavior is caused by p- and n-doped regions of the semiconductor.

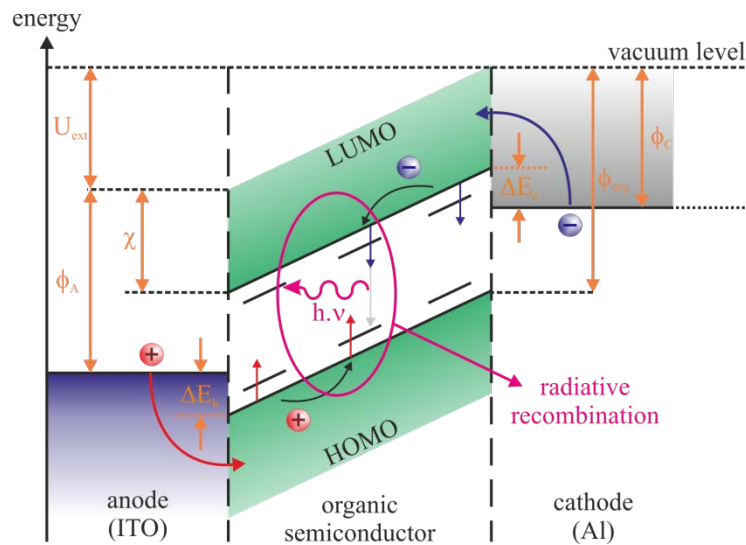


**Figure 2-17: Working principle and energy levels of an OLED biased in forward direction.**

It was already stated in the beginning of chapter 2.8 that in order to enhance the OLED's efficiency, frequently additional layers exhibiting enhanced charge carrier transport properties modify the assembly. Figure 2-18 exemplifies the working principle for an OLED bearing a hole transport layer (HTL) at the anode's side of the emitting layer (EML) as well as an electron transport layer (ETL) at the cathode's side of the EML. From the flat-band model in Figure 2-18 (left) it can be seen that again an energy-barrier is formed between the cathode and the ETL. However, this barrier is clearly lower than it would be at an EML-cathode-interface. Since the injection probability scales inversely proportional to the height of the barrier, the electron injection into the first layer is enhanced. The same is valid for the second barrier, which is formed at the ETL-EML interface. Also in this case, the energy difference needs to be surmounted by the negative polarons in the ETL in order to be injected into the EML. At the EML-HTL interface the conditions need to be contrary. In the ideal case, which is realized by the proper selection of hole- and electron transporting materials, respectively, here a large blocking barrier should be formed for negative polarons. When the device is biased in forward direction, this high barrier should be able to significantly reduce the extraction of negative polarons from the EML, which leads to a strong enhancement of the electron density within the EML (Figure 2-18, right). For positive charge carriers, the conditions can be described equally. After surmounting two lower energy barriers at the anode-HTL and the HTL-EML interface, an accumulation of positive polarons in the EML occurs caused by a blocking at the EML-ETL interface. The combination of both enhancement processes, for positive and negative polarons in the EML, consequently leads to an enhanced exciton formation probability and thus the amount of emitted light as well as the device efficiency should be increased.

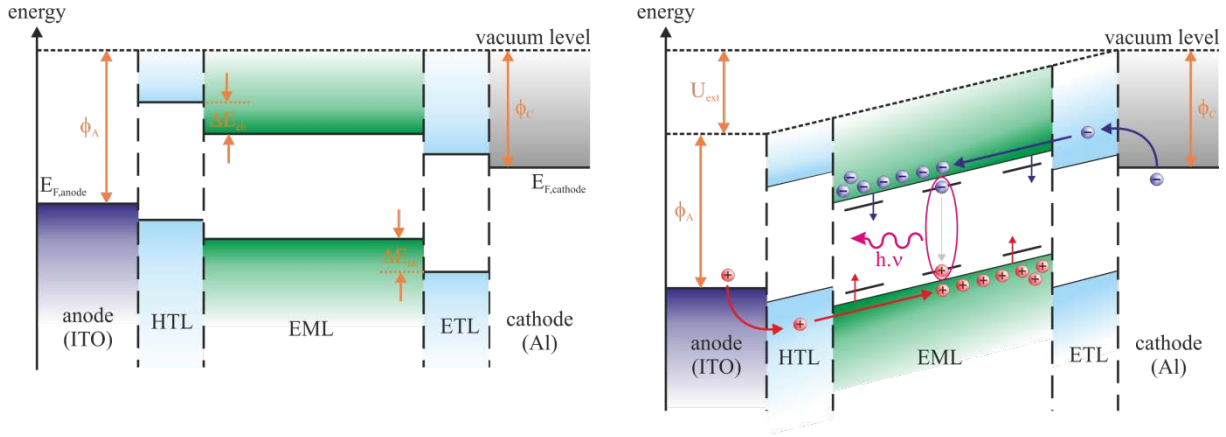


**Figure 2-18: Flat band model (left) and working principle (right) of a multilayer OLED biased in forward direction.**

Based on equation (2.3) and considering the given geometry of a state-of-the-art OLED, thus only accounting for photons leaving the device through the front glass surface, the external quantum efficiency  $\eta_{ext}$  of an OLED commonly is defined as:

$$\eta_{ext} = \eta_{PL} \cdot r_{st} \cdot \gamma_{cap} \cdot k \cdot g \quad (2.20)$$

where  $\eta_{PL}$  again is the photoluminescence quantum efficiency,  $r_{st}$  is the ratio of singlet excitons formed per exciton,  $\gamma_{cap}$  denotes the amount of excitons formed per injected electron,  $k$  accounts for various loss effects like quenching and  $g$  represents a factor considering losses caused by the assembly design like substrate-absorption, waveguiding or plasmon-generation. However, recently several workgroups presented more sophisticated examinations of that topic.<sup>[113–115]</sup> One of the main conclusions on that topic is represented by the fact, that due to active layer thicknesses of OLEDs in the wavelength or sub-wavelength range of the emitted light, respectively, and due to the encapsulation of the organic layers between two metal electrodes, the devices have to be treated as *microcavity* structures. In microcavity or resonant cavity structures, however, the photoluminescence emission quantum yield  $\eta_{PL}$ , which depends on the rate of spontaneous emission  $k_r$ , is not any longer a material constant, but highly depends on the surrounding environment (*Purcell-effect*).<sup>[116]</sup> Consequently, instead of  $\eta_{PL}$ , an effective efficiency  $\eta_{eff}$  is introduced, which is specific for every OLED-stack and which is influenced by the layer thickness as well as by the position of the recombination zone within the organic layer. Since the microcavity only has influence on the radiative decay rate  $k_r$  while  $k_{nr}$  stays unchanged  $\eta_{eff}$  can be expressed as:

$$\eta_{eff} = \frac{k_r^*}{k_r^* - k_{nr}} \quad (2.21)$$

Where  $0 \leq \eta_{eff} \leq 1$ ,  $k_r^*$  represents the altered radiative recombination rate and  $k_{nr}$  denotes the recombination rate for non-radiative decays.  $k_r^*$  is defined as

$$k_r^* = \frac{p_{tot}^{cav}}{p_{tot}^{hom}} k_r \quad (2.22)$$

Here  $p_{tot}^{cav}$  and  $p_{tot}^{hom}$  denote the total radiated power in the microcavity system and in the homogeneous medium.<sup>[113]</sup>

As already discussed in chapter 2.3, in regular fluorescent materials only singlet excitons are allowed to recombine radiatively yielding  $r_{st} \approx 0.25$ . However, in small molecular organometallic complexes, containing for example Pt, Ir or Eu atoms, radiative triplet decay is facilitated and  $r_{st} \approx 1$  can be achieved.

Regarding  $\gamma_{cap}$  it has to be noted that, while simple single layer structures show values significantly lower than 1 due to imbalanced charge injection and transport, for multilayer structures a value close to 1 can be realized based on a proper utilization of hole- and electron transport layers.

The factor  $k$  in equation (2.20) refers to various loss mechanisms, which are also termed as luminescence quenching. Quenching of singlet excitons can occur for example due to extrinsic effects like impurities in the material, due to field induced dissociation for example at high bias voltages in the device or by singlet-triplet annihilation, where a triplet exciton absorbs the excess energy of a singlet exciton and is transferred to a higher level in the triplet manifold. The latter case is especially important for materials exhibiting exceptionally long fluorescence lifetimes like in pyrene-based compounds,<sup>[117]</sup> however, it could be shown that an adequate tailoring of the molecule is able to reduce the singlet exciton lifetimes considerably.

The factor  $g$  in the equation takes accounts for all losses connected to the particular device assembly like absorption of light in the materials, the generation of plasmons at the organic-metal interfaces by emitted photons, total reflection at interfaces between materials with different refractive indices as well as waveguiding of the emitted light in the device. Among these effects absorption can almost be neglected with respect to the other effects. In order to minimize the loss due to the creation of polarons it is necessary to move the recombination zone away from the metal interfaces which for example can be achieved by a variation of the thickness of the transporting layers.<sup>[113]</sup> The extraction of waveguided modes can be accomplished finally for example by the application of grating foils to the substrate or simply by using a substrate material with a high refractive index thereby reducing total reflection at the organic-substrate interface.<sup>[118]</sup> The influence of the different loss mechanisms on the external quantum efficiency is depicted in Figure 2-19. Nevertheless, until today a maximum of 40-50% of the radiation generated inside an OLED can be extracted even in an optimized structure.<sup>[114,115]</sup>

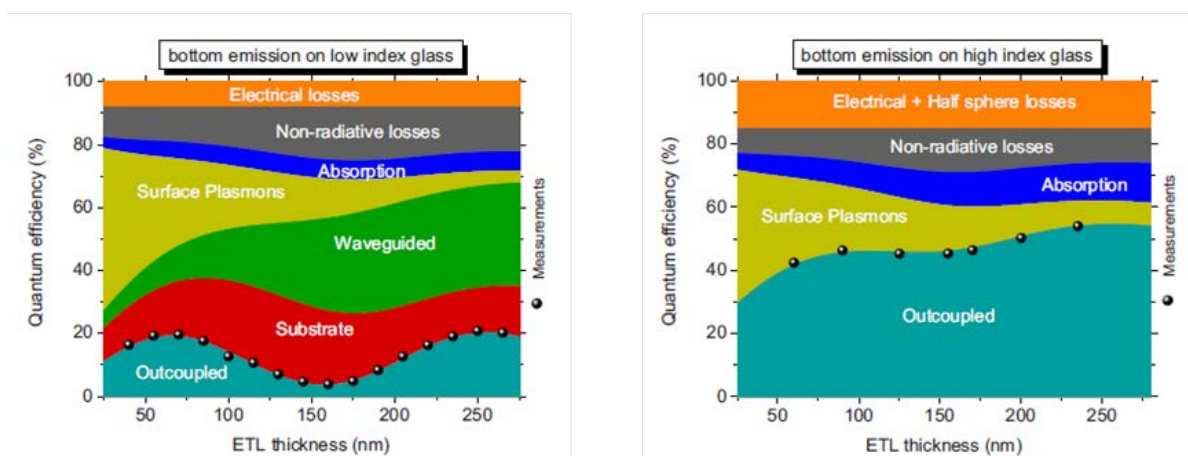


Figure 2-19: Influence of the different loss mechanisms on the amount of the extracted light from an OLED as a function of the thickness of an ETL, and thus on the dimension of the microcavity, on glass with a low refractive index (left) and on a glass with a high refractive index (right). (from [115])



## 2.9 Fundamentals on Organic Solar Cells

### 2.9.1 OSC – Architectures

The device architecture of organic solar cells can be described analogously to that of OLEDs. OSCs basically consist of one or more photoactive organic layers sandwiched between two metallic electrodes, one of which needs to be transparent in order to allow light to enter the device. However, for OSCs in the early years which consisted of only one organic layer it showed that such devices were rather inefficient with respect to the generation of photocurrent.<sup>[119,120]</sup> This is based on the fact that excitons generated by the incoming light in these single layer OSCs do not readily dissociate into free charge carriers. As explained in chapter 2.2.2 these excitons exhibit rather high binding energies and cannot be broken up by the external field that is established due to the difference in the workfunctions of the metal electrodes under short circuit conditions between anode and cathode. However, within the organic layer excitons diffuse within a typical range of 10 nm. If during such a diffusion process the exciton reaches one of the electrodes it may dissociate into separate charge carriers. Yet, since the diffusion length is short compared to the device thickness the majority of created excitons recombines (radiatively or non-radiatively) in the bulk of the polymer and thus is lost for photocurrent generation.

In contrast to such single-organic solar cells, heterojunction devices constitute a much more efficient alternative.<sup>[121]</sup> The idea behind these devices is to combine two organic materials comprising different electron affinities and ionization potentials, which may favor exciton dissociation at the heterojunction interface. Provided that the potential differences are higher than the exciton binding energy, thereby the material with the higher electron affinity will act as electron acceptor (A), while the material with the lower ionization potential will accept the hole and is termed as donor (D). In planar bilayer heterostructures the D-A interface is able to separate charge carriers more efficiently than the metal-organic interface in a single layer assembly. However, the efficiency in these bilayer devices is still limited, since only the region close to the D-A interface, where diffusing excitons are able to reach the heterojunction, contributes to photocurrent generation in the device.

Even higher photon-to-electron efficiencies can be achieved by so called bulk heterojunction structures.<sup>[122]</sup> For the realization of these structures, donor and acceptor materials are blended together in a single layer. By doing so it is possible to form nanomorphologies between D and A with a length scale in the range of the exciton diffusion length. Under such conditions, however, every photogenerated exciton should be able to reach the D-A interface and is split up into two different charge carriers. Provided that continuous pathways of the donor material and the acceptor material exist, leading from the interface to the respective electrode, ideally all generated charge carriers can be extracted from the solar cell and thus contribute to photocurrent generation.

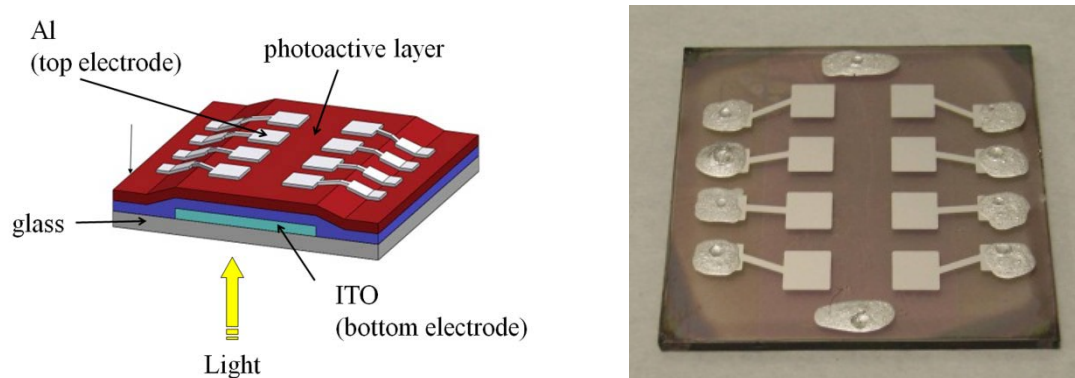


**Figure 2-20:** Schematic structure of an OSC substrate containing eight devices (left) and picture of a PCDTBT:CIS nanocomposite solar cell substrate (right).

### 2.9.2 OSC – Working Principle

In order to convert incident photons to free charge carriers that are extracted from the device, i.e. to photocurrent, five fundamental processes take place:

- exciton formation by photon absorption
- exciton diffusion (migration) and exciton dissociation at an interface
- charge carrier pair dissociation
- charge carrier transport in the semiconductor and finally
- charge carrier extraction at the respective electrodes.

Figure 2-21 shows the energy level schematics as well as the mentioned processes for a bulk-heterojunction solar cell under short circuit conditions, where the respective electrodes are brought into contact. At first an exciton is generated in the donor by the absorption of a photon according to the fundamentals described in chapter 2.3. After this generation excitons are able to move randomly within a radius in the range of 10 nm in the organic material, which is described by an exciton diffusion process.<sup>[123,124]</sup> When the exciton reaches the donor-acceptor interface the electron can be transferred to the acceptor, while the hole stays on the donor's side, thus forming a charge transfer state if the energy gained by this transition is bigger than the exciton's binding energy. Roughly this energy gain can be estimated from the LUMO-LUMO distance between D and A. Yet, the positive and negative charges located forming the charge transfer state are still Coulomb-bound. Under the influence of the existent electric field, which is induced by the Fermi-level alignment of the electrode metals when they are brought into contact, the bound polarons finally can dissociate into separated charge carriers. This process can be described by the *Braun-Onsager* model.<sup>[125]</sup> This model is based on a theory derived by Onsager which deals with the separation probability of Coulomb-bound and oppositely charged ion pairs under the influence of an applied electric field.<sup>[126]</sup> The theory was extended by Braun with respect to the limited lifetime of the charge transfer state in D-A systems.<sup>[125]</sup> According to this model the field dependent polaron pair dissociation probability  $P(F)$  can be expressed by the formula:

$$P(F) = \frac{k_d(F)}{k_d(F) - k_f} \quad (2.23)$$

where  $k_d(F)$  represents the dissociation rate of bound polaron pairs to free charge carriers in dependence of the field  $F$  and  $k_f$  is the recombination rate of polaron pairs to the ground state. In analogy to the charge carrier transport this frequently applied model, however, is only simplified. More complex considerations can be done via Monte-Carlo simulations which also consider energetic disorder or high local charge carrier mobility for example caused by delocalization of charge carriers along a polymer chain or due to nanocrystalline regions in one of the organic materials. After dissociation, the polarons are transported to the electrodes by the charge transport mechanism discussed in chapter 2.4. In that context it is important to note that an effective transport can only take place if continuous pathways for both types of charge carriers (positively and negatively charged polarons) towards the electrodes are available. Therefore, the formation of respective percolation paths in the nanomorphology of the blend system is necessary. Isolated islands where one material is completely surrounded by the other one will most probably not contribute to photocurrent generation since charge carriers generated in these regions are not able to leave for the electrode and will recombine with an oppositely charged polaron, thereby causing a loss of both charge carriers. Like in

the case of OLEDs a balanced charge carrier transport is necessary to maximize the solar cells' efficiency. If the discrepancy in the mobilities of electrons and holes is too high, space charge regions are formed which can considerably inhibit the charge transport. In a last step, the charges are extracted from the photoactive layer at the electrodes. An ideal extraction is again achieved by ohmic contacts between the organic material and the metal electrodes. In the non-ohmic case, the formation of an interface dipole as well as charge redistribution at the interface can lead to a piling up of charge carriers in front of the electrode leading as well to a space charge region which is further hindering the charge extraction and is thus reducing the devices' efficiency.

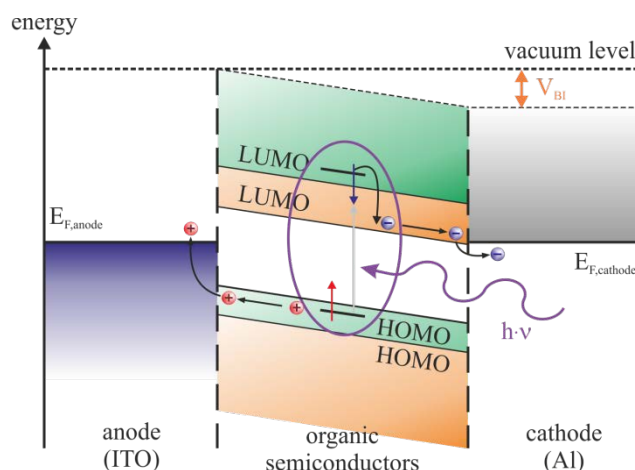


Figure 2-21: Working principle and energy levels of an OSC under short circuit conditions.

For the generation of the photocurrent, which corresponds to the generated charges that are able to reach the electrodes and can be extracted from the solar cell, an overall photocurrent efficiency  $\eta_I$  can be defined:

$$\eta_I = \eta_{abs} \cdot \eta_{diss} \cdot \eta_{extr} \cdot \quad (2.24)$$

In this formula  $\eta_{abs}$  stands for the fractions of photons absorbed from the incident light, thereby creating an exciton,  $\eta_{diss}$  is the amount of excitons that dissociate to a bound polaron pair at an interface and subsequently get separated to independent charge carriers and  $\eta_{extr}$  denotes the fraction of these charges that are able to reach the electrode and finally get extracted. The most important loss mechanism for the first term obviously comprises of photons that are not absorbed. Since most organic semiconducting materials, in particular conjugated polymers, show high absorption coefficients, the major loss stems from the fact that the absorption characteristics of these materials are a function of the wavelength which limits the absorption spectrum more or less to the visible range of the optical spectrum.<sup>[127,128]</sup> Furthermore, geometric parameters like the layer thickness as well as reflections at interfaces on the inside and outside of the device can show distinct impact on the absorption yield.<sup>[129]</sup> The fraction of dissociated excitons primarily is dependent on whether or not within their lifetime excitons are able to reach an interface where they can dissociate to a bound polaron pair and whether or not the bound state can be split up to free polarons. For the former case, when excitons are not able to reach the interface, they simply recombine to the ground state *via* one of the radiative or non-radiative decay channels. In the latter case, when a polaron pair was already generated, a failure in charge separation gives rise to the so called *geminate recombination*,<sup>[125,126]</sup> where two polarons stemming from a common excitonic state recombine to the ground state. Finally, the determining loss mechanism for  $\eta_{extr}$  comprises a *non-geminate* recombination of polarons. In this process charge

carriers with opposite electric charge recombine during the transport from the dissociation interface to their respective electrodes.

### 2.9.3 Characterization of OSCs

A solar cell's overall performance is determined by its efficiency to convert the power of the incident light into electrical power. This *power conversion efficiency* is consequently defined as

$$\eta = \frac{P_{max}}{P_{light}}, \quad (2.25)$$

which is the ratio between the maximum power generated by the solar cell ( $P_{max}$ ) and the power of the incident light ( $P_{light}$ ). To evaluate the PCE, the current density - voltage ( $J$ - $V$ ) characteristics of a device is investigated. Figure 2-22 shows a typical  $J$ - $V$ -characteristics achieved for a solar cell which enables the determination of the characteristic parameters of the cell, as there are the open circuit voltage ( $V_{OC}$ ), the short circuit current density ( $J_{SC}$ ), the current density and the voltage at the maximum power point ( $J_{mpp}$  and  $V_{mpp}$ , respectively) and the fill factor ( $FF$ ). The  $V_{OC}$  is the maximum photovoltage that can be measured for the solar cell under open circuit conditions and corresponds to the voltage that needs to be applied to the device in order to achieve a current density of zero under illumination. The  $J_{SC}$  is the maximum current that can be generated by the solar cell under illumination when the electrodes are short-circuited, i.e. when no external voltage is applied.  $J_{mpp}$  and  $V_{mpp}$  correspond to the values of  $V$  and  $J$  in the fourth quadrant (*power quadrant*) of the characteristics where  $P_{max}$  is generated. The  $FF$  finally specifies the quality of the  $J$ - $V$  characteristics and is defined by the relation

$$FF = \frac{J_{mpp}V_{mpp}}{J_{sc}V_{oc}}. \quad (2.26)$$

From this formula and Figure 2-22 it obvious that the more the  $J$ - $V$  characteristics approaches a rectangular shape the higher  $FF$  gets and the closer  $J_{mpp}$  and  $V_{mpp}$  get to  $J_{SC}$  and  $V_{OC}$ . Equation (2.25) consequently can be rewritten as

$$\eta = \frac{P_{max}}{P_{light}} = \frac{J_{mpp}V_{mpp}}{\Phi_{light}} = \frac{J_{sc}V_{oc}FF}{\Phi_{light}}. \quad (2.27)$$

Here  $\Phi_{light}$  denotes the power density of the incident light.

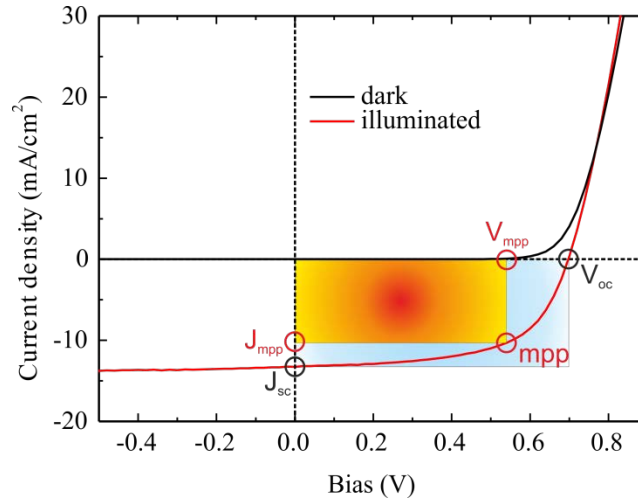


**Figure 2-22:** Typical current density – voltage characteristics of a solar cell in the dark (black) and under illumination (red). The characteristic parameters open circuit voltage  $V_{OC}$  and the short circuit current density  $J_{SC}$  as well as current density  $J_{mpp}$  and voltage  $V_{mpp}$  at the maximum power point are shown. The generated maximum power  $P_{max}$  is represented by the rectangle given by  $J_{mpp} \cdot V_{mpp}$ .

#### 2.9.4 Standard Test Conditions for Solar Cells

Considering the absorption characteristics of a solar cell it is instantly clear that the maximum power generated by the device is not only a function of the incident radiation power but in fact is dependent on the spectral distribution, i.e. on the intensity and wavelength, of the incident light. For this reason and in order to enable meaningful comparisons between all kinds of solar cells usually a specific set of standard test conditions is defined. These conditions are rated to a radiation density of  $1000 \text{ W/m}^2$ , to a temperature for the device of  $25^\circ\text{C}$  and to a spectral distribution of an AM1.5G sun spectrum. AM in this context means “air mass” and 1.5 is the “air mass coefficient” which refers to the length of the direct optical path the sunlight has to travel through the earth’s atmosphere at a specific solar zenith angle  $\theta$  relative to the length of the path exactly at zenith. For a specific path length ( $L$ ) the coefficient can be calculated by

$$AM(\theta) = \frac{L}{L_0} \approx \frac{1}{\cos \theta} \quad (2.28)$$

with  $L_0$  as the zenith path length at sea level and  $\theta$  the zenith angle. AM1.5 accordingly means that the sunlight has to overcome a distance in a dimension of 1.5 times the thickness of the atmosphere at zenith which corresponds to a solar zenith angle of  $48.2^\circ$  (c.f. Figure 2-23, left). The letter G in AM1.5G finally means “global irradiation”, which in contrast to AM1.5D, where D stands for direct, not only accounts for the irradiation coming directly from the sun but also sunlight reflected from the atmosphere towards the earth’s surface. Figure 2-23 (right) shows the solar spectrum at top of the atmosphere and under AM1.5G conditions. It can be observed that distinct absorption bands are formed, which are caused by the interaction of the incident light with molecules in the atmosphere.

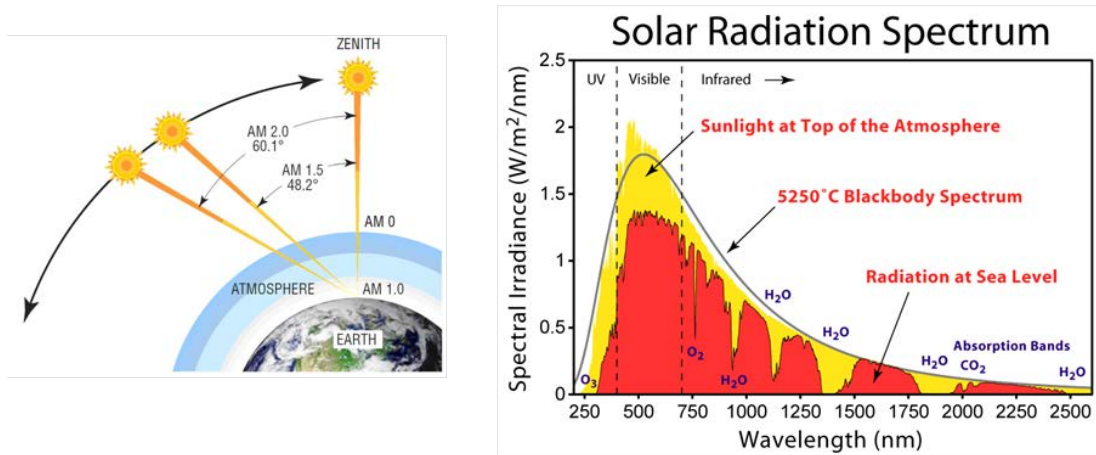


Figure 2-23: Various air mass conditions under different incident angles (left, modified from [130]) and solar radiation spectra (right, modified from [131]) at top of the atmosphere (yellow) and at sea level (red) under AM1.5G conditions. The solid line corresponds to the spectral radiation spectrum of a black body with a temperature of 5250°C.

### 3 Experimental Methodology

#### 3.1 Solution and Film Preparation

For spectroscopic investigations of organic materials in solution, the respective compounds were dissolved in toluene (TOL), xylene (XYL), tetrahydrofuran (THF), chlorobenzene (CB), cyclohexane (CH), methanol (MeOH) or acetonitrile (ACN), respectively, with a solid content of  $10^{-5}$  mg/ml - 2 mg/ml.

Organic thin films for spectroscopy were prepared on quartz glass substrates. Prior to the deposition of the organic materials the substrates were cleaned mechanically with ionized water, acetone and isopropanol followed by an ultrasonic treatment in toluene and isopropanol. Afterwards solutions with concentrations between 2 mg/ml - 10 mg/ml were spin cast onto the substrates under inert conditions with a spinning rate between 1000 rpm and 1500 rpm for 15 s to form the film followed by a drying step with 3000 rpm for 40 s.

#### 3.2 Absorption Measurements

In general, the optical absorption of light within a specific sample is determined by transmission measurements. The intensity  $I$  of the transmitted light thereby follows the Beer-Lambert law:

$$I = I_0 e^{-\alpha d} \quad (3.1)$$

where  $I_0$  is the intensity of the incident light,  $\alpha$  denotes the absorption coefficient of the sample and  $d$  is the sample thickness. Transmission measurements for solutions as well as for organic thin films were performed on a two beam PERKIN ELMER LAMBDA 900 Spectrophotometer, where the transmitted intensity is measured for the sample as well as for a substrate or solvent reference, respectively, enabling for an automatic substrate or solvent correction. The scanning speed was 82 nm/min and the transmission spectra were recorded from 250 nm to 800 nm. From the transmission data the *optical density* ( $OD$ ) and the *absorbance* ( $ABS$ ) can be calculated according to the equations:

$$OD = -\log \frac{I_{Sample}^T}{I_{Reference}^T} \propto \alpha d \quad (3.2)$$

$$ABS = -\ln \frac{I_{Sample}^T}{I_{Reference}^T} \quad (3.3)$$

where  $I_{Sample}^T$  and  $I_{Reference}^T$  are the recorded intensities of the transmitted light through the sample and through the reference,  $\alpha$  denotes the absorption coefficient and  $d$  represents the thickness of the sample. For solutions quartz glass cuvettes from HELMA with an optical path length of 10 mm were used and for organic thin films the respective material was deposited on quartz glass substrates from DELTA TECHNOLOGIES, LTD. All absorption measurements were performed under ambient conditions. An error of  $\pm 0.5$  nm can be estimated for the measured wavelengths.

### 3.3 Photoluminescence Measurements

Photoluminescence spectra were recorded with a SHIMADZU RF5301PC spectrofluorometer in air. In analogy to the absorption measurements HELLMA quartz glass cuvettes and quartz glass substrates from DELTA TECHNOLOGIES were used for PL measurements of solutions or thin films, respectively. In order to identify and avoid self-absorption or inner filter effects<sup>[84]</sup> PL spectra of dilution series in the range of  $10^{-6}$  mg/ml to 1 mg/ml as well as of films with a thickness below 20 nm were measured. All PL spectra were corrected with the corresponding response curve of the instrument. For the measured wavelengths and for the detected intensity an error of  $\pm 1$  nm and of  $\pm 1\%$  is estimated.

### 3.4 Photoluminescence Quantum Yield

As stated in equation (2.2) of chapter 2.3 the photoluminescence quantum yield (PLQY) is defined as the ratio of emitted photons to the amount of absorbed photons:

$$\eta_{PL} = \frac{N_e}{N_a} = \frac{\text{number of emitted photons}}{\text{number of absorbed photons}}. \quad (3.4)$$

Yet, since a direct measurement of the amounts of photons and thus for  $\eta_{PL}$  is not easy to realize, an indirect method was established and is highly accepted.<sup>[132–134]</sup> Thereby, to determine the absolute PLQY of a material the absorbance and emission characteristics of such a sample are related to a standard material with known PLQY according to

$$\eta_x = \eta_r \cdot \left( \frac{A(\lambda_r)}{A(\lambda_x)} \right) \cdot \left( \frac{I(\lambda_r)}{I(\lambda_x)} \right) \cdot \left( \frac{D_x}{D_r} \right) \cdot \left( \frac{n_x}{n_r} \right)^2 \quad (3.5)$$

where  $\eta_x$  and  $\eta_r$  are the photoluminescence quantum yields of the material under investigation and the reference standard,  $A(\lambda_x)$  and  $A(\lambda_r)$  denote the respective absorbance values at the wavelength  $\lambda$ ,  $I(\lambda_r)/I(\lambda_x)$  represents a correction factor accounting for different excitation intensities,  $D_x$  and  $D_r$  are the respective luminous intensities and  $n_x$  and  $n_r$  stand for the refractive indices of the investigated material and the reference, respectively.

For all PLQY determinations presented in this thesis, quinine sulfate is used as reference material. Dissolved in 0.5M  $H_2SO_4$  the quantum yield of this compound is 0.546.<sup>[135]</sup> To determine the PLQY of the investigated material, absorption and PL spectra of the compound as well as of the reference were measured in solution for different material concentrations. The PL spectra were multiplied by the respective wavelengths. To get the total luminous intensity in quanta per second the multiplied PL-spectra were integrated over the whole range of the emission. Since different concentrations were measured, the integrated emission over absorbance gives the gradient for this relationship and equation (3.5) can be written as

$$\eta_x = \eta_r \cdot \left( \frac{Grad_x}{Grad_r} \right) \cdot \left( \frac{n_x}{n_r} \right)^2. \quad (3.6)$$

A relative error in the range of 10% should be assumed for this method.<sup>[134]</sup>



### 3.5 Time Resolved Photoluminescence

The lifetime of singlet excited states is a characteristic feature of a photoexcited molecule. To determine the fluorescence lifetime, Prof. M.A. Loi and coworkers at the *Zernike Institute for Advanced Materials at the University of Groningen* (Netherlands) performed time resolved photoluminescence (TRPL) measurements. For optical measurements thin films were spin cast from a  $\sim 1$  mg/ml solution, while a concentration of  $\sim 1 \times 10^{-3}$  mg/ml was used for measurements in solution. The optical investigations were performed exciting the sample (solution or thin film) with a pulsed beam (150 fs pulse width, repetition rate 76 Mhz) of a mode locked Ti:sapphire laser ( $\lambda = 380$  nm). The repetition rate was varied by means of an optical pulse selector. A Si-CCD camera and a streak camera, respectively recorded PL spectra and dynamics. The streak camera was used in single sweep and in synchroscan mode. All measurements were carried out at room temperature. For these measurements, a maximum resolution of approximately 2 ps can be achieved. The emission decay times  $\tau$  are evaluated by fitting the data with the following single- or double exponential functions:

$$y = y_0 + Ae^{-\frac{t}{\tau}} \quad (3.7)$$

$$y = y_0 + Ae^{-\frac{t}{\tau_1}} + Be^{-\frac{t}{\tau_2}}. \quad (3.8)$$

In this functions  $A$  and  $B$  denote the values of the amplitudes at the time  $t = 0$ ,  $\tau, \tau_1, \tau_2$  are the respective decay constants and  $y_0$  represents a possible offset of the signal.

### 3.6 Photoinduced Absorption

As stated in chapter 2.3, singlet excited states decay in a nanoseconds regime. Triplet excitons in contrast show lifetimes in the range of nanoseconds to microseconds. In this time domain, photoinduced absorption (PIA) spectroscopy constitutes a measurement technique that is extremely well suitable to determine the characteristics of photogenerated states. PIA spectroscopy represents a pump-probe technique comprising an excitation beam (pump) for the generation of photoexcitations in a sample and a probe beam that allows for the detection of a change in the absorption due to the photoexcitation. In detail, the sample under investigation is illuminated by the probe beam comprising white light and the absorption characteristics is measured by dispersing the light through a monochromator and measuring the transmitted light by a photodetector for each wavelength yielding the transmission signal  $T$ . Upon illumination of the sample by the pump beam, which's wavelength is matched to the absorption band of the sample material in order generate an excited state population, the molecules in the sample get photoexcited resulting in a change of the transmission spectrum  $\Delta T$  of the probe light through the sample. Please note that the wavelength of the pump beam has to be monochromatic and of high intensity to create enough excited states that yield a measureable  $\Delta T$ . These prerequisites basically are fulfilled by the utilization of a laser as the pump beam. A synchronous detection of  $T$  and  $\Delta T$  in that context is realized by a mechanical modulation (chopping) of the pump beam. PIA measurements hence record the fractional change of the transmitted light through an excited sample and the regular transmission without excitation  $\Delta T/T$ . In general, the modulated PIA signal is orders of magnitude smaller than the signal of the regular absorption. Hence,

a lock-in amplifier is used to detect the probe beam amplitude and the phase modulation. For a thin film the PIA signal can be expressed as

$$-\frac{\Delta T}{T} \cong \Delta\alpha d = n\sigma d \quad (3.9)$$

where  $\Delta\alpha$  is the change in the linear absorption coefficient  $\alpha$ ,  $n$  denotes the density of excited states,  $\sigma$  represents the absorption cross-section of excitations and  $d$  is the film thickness. The density of states further can be expressed by the rate equation:

$$\frac{dn(t)}{dt} = G(t) - kn(t) - \gamma n^2(t) \quad (3.10)$$

where  $G(t)$  is the creation term expressing the generation rate,  $k$  is the monomolecular decay rate and  $\gamma$  represents the bimolecular decay rate. For low excitation densities it is possible to assume only monomolecular decay. In this case the change in transmission is proportional to the concentration of photoexcitations, which can be expressed as a function of the pump intensity  $I$ . Thus for  $-\Delta T$  the following proportionality can be written:<sup>[136]</sup>

$$-\Delta T \propto \frac{gI\tau}{\sqrt{1 + \omega^2\tau^2}} \quad (3.11)$$

with  $g$  as the excited states generation efficiency,  $\tau$  the monomolecular lifetime and where  $\omega$  denotes the angular frequency derived from the chopper frequency  $\nu$  by  $\omega = 2\pi\nu$ . The in-phase component  $x(\omega)$  and the out-of-phase component  $y(\omega)$  of the PIA signal can be expressed as

$$x(\omega) = \frac{G \cdot \tau}{1 + \omega^2\tau^2} \quad (3.12)$$

$$y(\omega) = \frac{\omega \cdot G \cdot \tau}{1 + \omega^2\tau^2} \quad (3.13)$$

and the monomolecular lifetime is

$$\tau = \frac{1}{k} . \quad (3.14)$$

The lifetime of the photoexcited state can be determined by varying the modulation frequency at a fixed wavelength. Upon frequency variation the out-of-phase component of the PIA signal shows a maximum at the frequency  $\nu_{max}$  which indicates the characteristic lifetime according to.<sup>[137]</sup>

$$k = \omega = 2\pi\nu_{max} . \quad (3.15)$$

For lifetimes in the range above approximately 10 ms the out-of-phase signal has its maximum at rather low frequencies which restricts the accessibility by the lock-in amplifier. Alternatively, an

estimation for the lifetime can be derived from the phase shift ( $\varphi$ ) of the PIA-signal compared to the reference:

$$\tau = \frac{\tan(\varphi)}{2\pi\nu}. \quad (3.16)$$

In order to assess if a monomolecular or bimolecular decay of the photoexcited states takes place the PIA signal is recorded as a function of the pump intensity  $I$ . In a double logarithmic plot of the PIA signal versus  $I$  a monomolecular decay exhibits a slope of one while a slope of 0.5 is obtained for a bimolecular decay. A value for the slope between 0.5 and 1 points out that both decay mechanisms take place.

The experimental PIA setup used for the measurements presented in this work is depicted in Figure 3-1. Thin films of conjugated polymers were deposited onto Infrasil substrates from solutions in the respective solvents. The samples then were mounted in an optically accessible cryostat under a dynamic vacuum of less than  $1.0 \times 10^{-6}$  mbar. The cryostat was cooled below 100 K with liquid nitrogen and the temperature in the vacuum chamber was monitored by a Pt-100 thermoresistor connected to a KEITHLEY 199 Ohmmeter. The pump beam was provided by the 351 nm and 364 nm UV double line of a COHERENT Innova 300 Argon-ion laser with a laser power of approximately 100 mW, which was mechanically chopped to modulate the photoexcitation. White light from a 50 W tungsten halogen lamp was used as probe beam for the transmission measurements. The probe beam intensity was recorded by a photodiode after passing through a monochromator. In order to prevent second order diffraction a 580 nm cut-off filter is inserted enabling measurements in the range of 250 nm to 1100 nm. The photodiode's signal was recorded by a KEITHLEY 192 voltmeter and an EG&G 5210 dual-phase lock-in amplifier. The chopper frequency was controlled by a chopper control unit which also provided the reference signal for the lock-in amplifier. All PIA spectra were corrected for PL and the optical throughput of the setup.

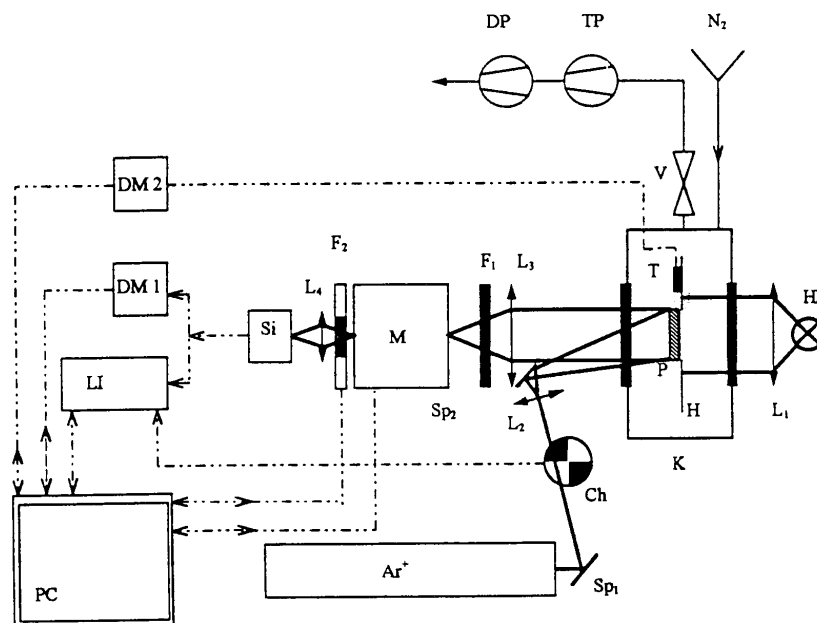


Figure 3-1: Experimental setup for PIA measurements: HL...halogen lamp, H... sample holder, K...cryostat, P...sample, T...thermoresistor, V...valve, TP...turbomolecular pump, DP...rotary pump, L...lenses, F...filters, M...monochromator, Si...photodiode, DM...digital multimeter, LI...lock-in amplifier, PC...computer, Ar...argon ion laser, Sp...mirrors, Ch...chopper. (from [138])

### 3.7 Photoelectron Spectroscopy

Photoelectron spectroscopy (PES) either by the utilization of ultraviolet light (ultraviolet photoelectron spectroscopy) or by X-ray radiation (X-ray photoelectron spectroscopy) is a well-established investigation technique used to probe energetic states at the surface of metals or semiconductors. It is based on the external photoelectric effect, which could be described by Einstein with the wave-particle duality of light already in 1905,<sup>[139]</sup> where an electron is emitted from a sample upon interaction with incident electromagnetic radiation. The theory of the photoelectric effect states that an electron can be emitted from the surface of a solid state body when a photon is absorbed exhibiting a higher energy than the ionization energy ( $IE$ ) of the solid at the surface. The maximum kinetic energy  $E_{kin}^{max}$  of that electron can be calculated according to

$$E_{kin}^{max} = h\nu - \phi \quad (3.17)$$

where  $h$  is the Planck-constant,  $\nu$  is the frequency of the incident photon and  $\phi$  is the workfunction of the sample at the surface. The photoemission of the electron in that context can be understood as a three-step process. First, the incident photon is absorbed in the solid by an electron and excites the electron from its initial state to an excited state. Next, the electron travels to the surface of the sample thereby losing kinetic energy due to inelastic collisions in the solid. In a final step, when the electron reaches the surface it is ejected into the surrounding vacuum.

In case of UPS the photon energies are in the range of 10 eV to 40 eV, while for XPS radiation energies between 200 eV and 2 keV are used. As a result UPS is well suitable for the investigation of weakly bound valence electrons of the investigated material or the investigation of the HOMO in case of an organic semiconductor, while for XPS the photon energies enable for the ionization of electrons from the atomic core levels thus allowing for an analysis of the sample's chemical environment. Due to the low mean free path length of electrons in the above mentioned energy range PES is a particularly surface sensitive investigation technique.

The photoemission process for a metallic sample, as it occurs in UPS as well as in XPS, is schematically depicted in Figure 3-2. Upon photon irradiation free electrons are generated with a certain kinetic energy depending on the photon energy ( $h\nu$ ), the binding energy of the excited electron  $E_b$  and the work function of the sample  $\phi_s$ . The photoemission spectrum then is formed by a superposition of two different components. The first component comprises primary electrons that did not lose energy due to inelastic collisions and the second component comprises secondary electrons. In the photoemission spectrum primary electrons show up as distinct features and they exhibit a kinetic energy ( $E_{kin}$ ) distribution of

$$E_{kin} = h\nu - E_b - \phi_s \quad (3.18)$$

Primary electrons picture the density of states of the sample material, which enables the determination of binding energies of the electronic states in the sample. Secondary electrons in contrast exhibit a continuous energy distribution down to zero kinetic energy and in general are used to determine the work function of the material under investigation. Consequently, the electrons with highest kinetic energy are primary electrons emitted directly from the Fermi edge of the metal where  $E_b$  is zero (c.f. equation (3.17)). Secondary electrons, which just escape the metal's surface after having lost all their kinetic energy ( $E_{kin} = 0$ ) due to scattering processes during their travelling through the sample, possess the lowest energy. Understandably, at this point of the energy scale a more or less sharp edge

is observed in the photoemission spectrum, i.e. electrons with negative kinetic energy cannot exist. This edge is termed secondary electron cutoff (SECO).

An analyzer measures the kinetic energies of the emitted electrons. Upon bringing the sample and the analyzer into contact, their Fermi levels are equilibrated and a contact potential develops between the sample and analyzer. With the work function of the analyzer ( $\phi_a$ ) and the contact potential ( $\phi_s - \phi_a$ ) equation (3.18) can be written as:

$$E_{kin} = h\nu - E_b - \phi_a . \quad (3.19)$$

Usually the work function of the analyzer is not known. However, by defining that the electrons right at the Fermi edge have a kinetic energy of  $h\nu$  and by shifting all kinetic energies accordingly an internal energy scale  $E_{kin}^{int}$  relative to the Fermi edge is introduced which provides the energy of the electrons right before they leave the sample.<sup>[140]</sup> Through this definition the work function of the sample can be determined immediately from the position of the SECO in this scale since the electrons at this point just have enough energy to leave the sample.

The binding energies for the emitted electrons accordingly can be determined by defining

$$E_b = h\nu - E_{kin}^{int} \quad (3.20)$$

which immediately sets  $E_b = 0$  for the electrons at the Fermi edge.

Please note that secondary electrons are also generated in the analyzer and their spectrum is overlapping the secondary spectrum of the sample. In order to clear this influence in the spectrum an additional accelerating potential is applied between the sample and the analyzer. Obviously, this potential only affects electrons coming from the sample and shifts them to higher kinetic energies. This simple manipulation consequently leads to a separation of the two different secondary electron contributions and the secondary spectrum of the sample can be investigated without the disturbing analyzer secondary electrons.

The determination of the work function of a material by PES is not limited to metallic sample but can also be applied for semiconductors. Yet, since in contrast to metals in semiconductors the IE and the Fermi level are found at different energies the PES investigation technique described above cannot be applied directly. The difficulty arises because the Fermi level of a non-degenerate semiconductor is located in the bandgap and therefore is not occupied by electrons and thus cannot be probed by PES. Thus, the semiconductor's PE-spectrum only provides a highest  $E_{kin}$  corresponding to the valence band maximum (VBM) – or HOMO onset in case of an organic semiconductor – and a SECO with  $E_{kin} = 0$ . Since the Fermi edge onset is missing as a reference point it is not possible to determine absolute values for the work function or binding energies. This problem, however, can be overcome by first measuring the work function of a metal and defining an internal energy scale as described above. This scale then can be used as a reference. When bringing the analyzer and the semiconductor into contact the Fermi levels of the analyzer and the semiconductor equilibrate and the samples PE spectrum is calibrated. This enables the determination of absolute energy values for the work function of the sample as well as of the VBM or HOMO-energy level, respectively.

As already indicated above UPS is predominantly used to determine VBM as well as HOMO levels and it is also commonly used for work function determination. Due to the higher photon energies, XPS in contrast is able to extract electrons from the samples' core levels atoms. Since the electrons in the electron shells exhibit discrete energy levels specific for every element, features in the XPS-spectra stemming from primary electrons provide detailed data on the composition of the sample. In addition,

since different bonds (e.g. single- and double bonds) lead to slightly different energetic levels of the electrons in one element it is even possible to distinguish differently bound species of the same element by XPS.

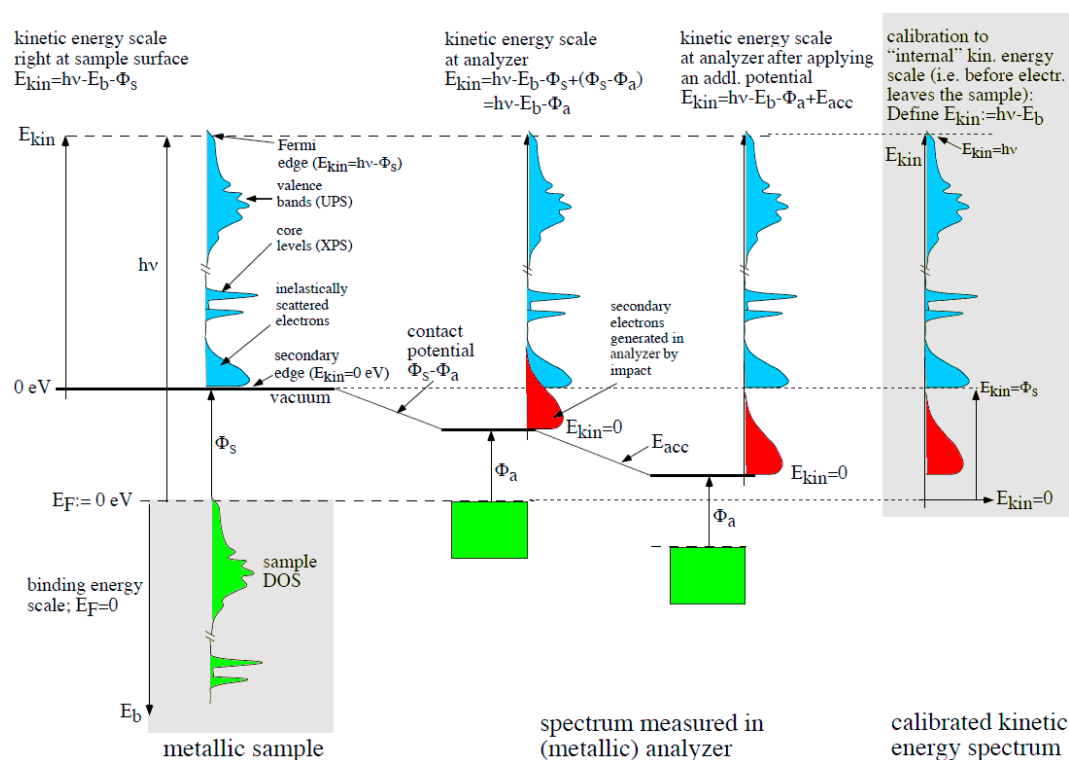


**Figure 3-2: Schematic of photoemission spectroscopy (PES) process on a metallic sample. The figure shows the correction according to the analyzer work function and the separation of the sample signal from secondary electrons generated in the analyzer. (modified from [140])**

PES measurements were performed at the endstation SurfCat (beamline PM4) of the synchrotron light source BESSY II (Berlin, Germany). For PES studies polymers were spin coated from the respective solutions on the conductive polymer poly(3,4-ethylenedioxythiophene)-polystyrenesulfonate (PEDOT:PSS; Clevious™ P VPAI 4083; Heraeus Precious Metals GmbH & Co. KG) on indium tin oxide. 1,3,5-tris(1-phenyl-1H-2-benzimidazol) (TPBi) was evaporated incrementally in situ from a resistively heated crucible; the deposited mass-thickness was monitored with a quartz-crystal microbalance. Spectra were collected with a hemispherical electron energy analyzer (Scienta SES 100) using an excitation photon energy of 30 eV to 35 eV for UPS and 600 eV to 650 eV for XPS. The energy resolution was 0.1 eV. SECO spectra to determine the sample work function were measured with the sample biased at -10 V to clear the analyzer work function. Standard procedures to ascertain the absence of sample charging were applied for every sample; these include variation of excitation photon flux and sample illumination with visible light. The error of reported binding energy is estimated to be smaller than  $\pm 0.05$  eV.

### 3.8 X-ray Diffraction

X-ray diffraction (XRD) is a widely used, powerful and non-destructive tool to characterize the crystallinity of a material. In this technique the sample under investigation is irradiated by a directed X-ray beam of a specific wavelength  $\lambda$ . The incident X-rays penetrate the surface of the sample and are diffracted due to elastic scattering from the material's atoms. Depending on the atomic structure

and the orientation of the crystalline planes of the sample, the diffracted X-rays are able to show constructive or destructive interference, just as visible light. Thus, diffracted beams will show destructive interference unless they are in phase. Constructive interference therefore will occur for conditions obeying Bragg's law:

$$n\lambda = 2d \sin \theta ; n = 0,1,2, \dots \quad (3.21)$$

where  $n$  is the order of the diffraction,  $\lambda$  is the wavelength of the incident X-ray radiation,  $d$  is the spacing between two parallel lattice planes contributing to the diffraction and  $\theta$  is the angle between the incident beam and the normal of the diffracting crystalline plane. By scanning a crystalline sample for different  $\theta$  a diffraction pattern is recorded, showing distinct diffraction peaks which in general are characteristic for the investigated material and thus enable the identification of the atomic composition and the crystal structure of the sample.

The size  $D$  of the crystallites can be calculated according to the Scherrer relation:<sup>[141,142]</sup>

$$D = \frac{\lambda}{FWHM \cdot \cos \theta} \quad (3.22)$$

with  $FWHM$  being the full width at half maximum of the corresponding diffraction peak under the assumption that the shape profile is Gaussian.

Specular X-ray diffraction was performed with a Siemens D501 Diffractometer using a  $\text{Cu}_{K\alpha}$  monochromated beam ( $\lambda = 1.54178 \text{ \AA}$ ). A Bragg-Brentano focusing geometry was used with divergence slits of  $1^\circ$  and a receiving slit of  $0.05^\circ$ . Monochromatisation was performed at the secondary side by a flat graphite single crystal.

Two-dimensional wide-angle X-ray scattering (2D-WAXS) experiments of orientated filaments were performed by means of a rotating anode (Rigaku 18 kW) X-ray beam with a pinhole collimation and a 2D Siemens detector with a beam diameter of 1.0 mm. A double graphite monochromator for the  $\text{Cu}_{K\alpha}$  radiation was used. The patterns were recorded with vertical orientation of the filament axis and with the beam perpendicular to the filament.

### 3.9 Atomic Force Microscopy

Atomic force microscopy (AFM) is used to acquire 3-dimensional images of sample surfaces with resolutions for surface height changes down to the sub-nanometer scale. The principle of AFM is based on mechanical short- and long-range forces acting between two neutral atoms when brought into proximity. For long distances, the interaction between the atoms is governed primarily by attractive van der Waals forces, while the interaction at short distances is governed by Pauli repulsion, which occurs due to overlapping electron orbitals. The *Lennard-Jones* potential describes the resulting potential between the atoms and is strongly dependent on the atomic distance.<sup>[143]</sup>

AFM exploits the characteristics of the governing forces by bringing a sharp tip that is mounted at the end of a cantilever into proximity of a specimen surface. The resulting force between the tip and the surface thereby leads to a deflection of the cantilever, which can be measured by a laser spot that is focused on the cantilever surface and reflected further into an array of photodiodes. Thus, via scanning an area in the x-y plane (x-y movement is usually performed by piezoelectric crystals) and monitoring the position of the laser spot reflection, genuine 3-dimensional images can be generated. A movement of the tip at a constant height (z-coordinate) in this context may induce the risk of a collision between

the tip and the surface. Hence, in general the tip height is adjusted by the feedback loop of a controller electronics, which controls another piezoelectric crystal that moves the tip in the z-direction depending on the signal recorded by the photodiodes, thereby maintaining a constant force and thus a constant distance between the scanning tip and the specimen surface.

Basically there exist three different modes an atomic force microscope can be operated in: contact mode, non-contact mode and tapping mode. As the name implies in contact mode the tip is in direct contact with the sample surface and changes in the morphology lead to a bending of the cantilever, which is measured by the photodetector. For each point of the sample surface, the feedback electronics adjusts the tip-sample distance in such a manner that the bending of the cantilever is held constant on the entire scanned area. In non-contact and tapping mode, the cantilever does not touch the sample but oscillates in a short distance above it at its resonance frequency. Since in the vicinity of the sample surface the oscillation is damped due to the forces described above, changes in the specimen surface morphology and thus of the mean sample-tip distance lead to a modification of the oscillations amplitude which again is recorded by the photodetector. In contrast to the non-contact mode, in tapping mode the oscillation's amplitude is higher which enables for example even the investigation of surfaces covered by a thin water film when measured under ambient conditions because the tapping tip is able to penetrate the film and slightly touching the surface at the end of its swing. In addition, tapping mode in contrast to contact mode reduces any possible damage to the sample due to the non-permanent contact.

Since all AFM investigations presented in this thesis are performed in tapping mode, it is briefly described in the following. For the measurement the cantilever is excited at its resonance frequency with a specific amplitude by a piezoelectric crystal mounted at the cantilever and moved line-by-line over a surface in the x-y plane. Simultaneously, the photodiode detector array measures the amplitude of the laser beam oscillation. When the tip approaches the surface, due to the Lennard-Jones potential the oscillation is damped. This damping of course is stronger the closer the tip comes to the surface. Upon changes in the topography (sample height) and thus the oscillation amplitude, the controller electronics applies a correction signal to the piezoelectric crystal in z-direction in order to maintain a constant sample-tip distance and amplitude (Figure 3-3). By performing this correction and recording the particular x-, y- and z-coordinates, a three dimensional image of the sample surface is generated.

All samples in this thesis were measured in tapping mode by a Veeco Dimension V atomic force microscope equipped with a Nanoscope V controller and a closed loop hybrid scan head under ambient conditions.

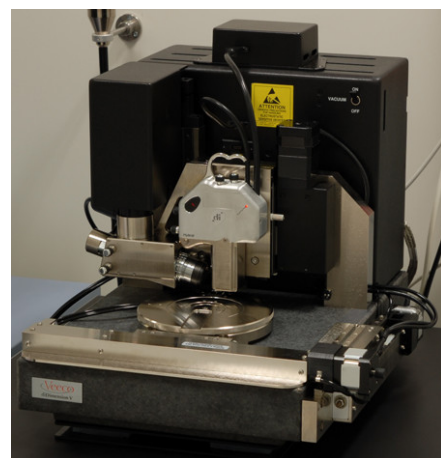
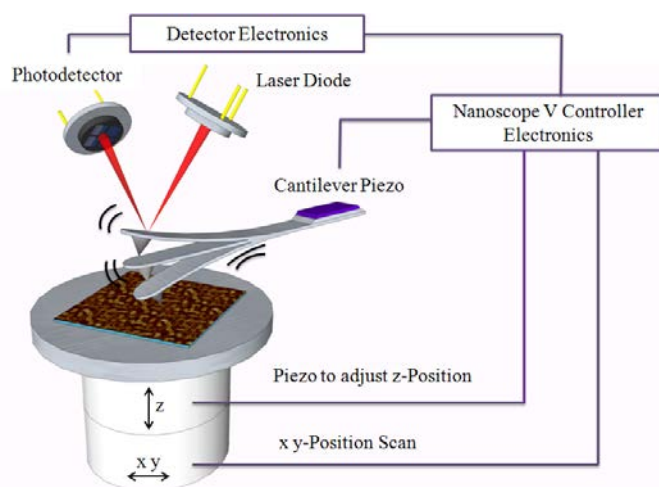


**Figure 3-3: Schematics of a feedback loop controlled scanning of the sample topography for AFM-investigations in tapping mode (left). Veeco Dimension V AFM at the NTC Weiz Forschungsgesellschaft mbH (right).**



## 3.10 OLED Preparation and Characterization

### 3.10.1 OLED Fabrication

For OLED/PLED sample preparation at first ITO-covered glass substrates (KINTEC Company) were structured by an etching process in concentrated hydrochloric acid (37 % HCl). Thereby the areas to remain were covered by Scotch Magic adhesive tape (3M). In order to improve and accelerate the etching, process zinc powder (Sigma-Aldrich) was deposited onto the uncovered areas of the substrate. After an etching process of 30 seconds the substrates were rinsed by deionized water and the adhesive tape was removed. All structured substrates were then cleaned mechanically using acetone and isopropanol. Afterwards the substrates were subdued to various supersonic treatments in toluene and isopropanol for 15 minutes each. The cleaning procedure was finished by a dry cleaning step in oxygen plasma for 10 minutes under a pressure of  $3 \times 10^{-1}$  mbar with a partial pressure of oxygen of  $1 \times 10^{-1}$  mbar.

A layer of PEDOT:PSS was spin-cast on the substrate in a laminar flow box under ambient conditions and dried under dynamic vacuum ( $p < 1 \times 10^{-5}$  mbar) at 120°C for 45 minutes. Still in vacuum the sample afterwards was cooled down to room temperature in approximately another 45 minutes. The thickness of this conducting polymer layer amounted to approximately 50 nm.

Active organic materials dissolved in the respective solvents were spin coated onto the PEDOT:PSS layer under argon atmosphere and dried at 60°C – 80°C for 1 h in vacuum ( $p < 1 \times 10^{-5}$  mbar).

Organic small molecules were thermally deposited from a resistively heated crucible at a deposition rate between 0.5 Å/s and 1 Å/s in a custom made evaporation chamber with an initial base pressure  $p < 1.0 \times 10^{-6}$  mbar.

As cathode materials layers of calcium (10 nm) or cesium fluoride (1-2 nm) and aluminum (100 nm) were thermally evaporated consecutively through a shadow mask forming a device-area of 9 mm<sup>2</sup> from tungsten boats with average deposition rates of 2 Å/s, 0.2 Å/s and 10 Å/s, respectively, under the same conditions as for organic small molecules. Layer thickness and evaporation rate were monitored and controlled by a quartz crystal microbalance monitor and controller (Sigma Instruments Inc.).

### 3.10.2 OLED Characterization

After mounting and sealing the sample in an optically accessible customized device-measuring cell under inert atmosphere electroluminescence spectra were acquired using an ANDOR Shamrock 163 spectrometer with an attached calibrated charge-coupled device (CCD) detector (ANDOR DU970N-UV). The current/luminance/voltage (I–L–V) characteristics were recorded in a customized computer controlled setup using a Keithley 2612A source measure unit for recording the I–V characteristics while simultaneously recording the luminance with a Keithley 6485 Picoammeter using a photodiode calibrated with a MINOLTA LS-100 luminancemeter. An error < 0.1% can be assumed for both, the sourced voltage and the measured current, and an error of 5% is estimated for the obtained luminance values.

## 3.11 OSC Preparation and Characterization

### 3.11.1 OSC Fabrication

For solar cell fabrication PEDOT:PSS layers were prepared on ITO substrates analogously as described for OLEDs (c.f. chapter 3.10.1). The active nanocomposite layers were deposited by spin-coating from chlorobenzene solutions containing copper xanthates, indium xanthates (copper and

indium O-2,2- dimethylpentan-3-yl dithiocarbonate) and the donor polymers under argon atmosphere. Subsequently the substrates were annealed in a Carbolite tube furnace at 200°C for 25 min in vacuum ( $p \sim 2$  mbar). Aluminum as the cathode material was thermally evaporated through a shadow mask forming a device-area of 16 mm<sup>2</sup> from a tungsten boat in an evaporation chamber with an initial base pressure smaller than  $1.0 \times 10^{-6}$  mbar.

### 3.11.2 OSC Characterization

Solar cells were mounted and sealed in an optically accessible customized device-measuring cell under inert atmosphere. Current–voltage (I–V) characteristics of the devices were recorded by a computer controlled Keithley 2400 SourceMeter. Solar simulation was achieved by using an ATLAS SolarTest 1200 Solar simulator equipped with an AM1.5G filter providing a spectrum similar to AM1.5G. The illumination intensity was determined using a KippZonen-CMP-11 pyranometer and it was set to 1000 W/m<sup>2</sup>. In order to exclude contributions to the current generation in the solar cell from areas of the active layer that are not embedded between the ITO anode and the aluminum cathode a shadow mask was aligned with the contact pads defining an active cell area of 16 mm<sup>2</sup>. An error < 0.1% can be stated for both, the sourced voltage and the measured current, and an error < 1% can be assumed for the illumination intensity.

### 3.11.3 Incident Photon to Current Efficiency

Another important method performed for the characterization of solar cells is the measurement of the incident photon to current efficiency (IPCE). As the name implies the IPCE measures the efficiency of the conversion of incident photons to charge carriers coming out of the solar cells. Thus, the IPCE is defined as the number of electrons per wavelength  $\lambda$  extracted from a solar cell divided by the number of incident photons at that particular wavelength. Since IPCE actually refers to electrons or a current, respectively, measured in an external circuit connected to it, the IPCE is also called external quantum efficiency (EQE) and as formula it reads as

$$IPCE(\lambda) = EQE(\lambda) = \frac{\text{number of extracte delectrons}}{\text{number of incident photons}} = SR(\lambda) \frac{hc}{q\lambda} \quad (3.23)$$

Here  $h$  is the Planck constant,  $c$  is the speed of light,  $q$  stands for the elementary charge and  $SR(\lambda)$  represents the spectral response of the solar cell which is defined as

$$SR(\lambda) = \frac{J_{sc}(\lambda)}{\Phi(\lambda)} \quad (3.24)$$

where  $J_{sc}(\lambda)$  represents the short-circuit current density at the wavelength  $\lambda$  and  $\Phi(\lambda)$  is the light intensity per unit area striking the cell at  $\lambda$ . The importance of the IPCE for the characterization and for a comparison of different solar cells gets instantly clear when considering that this parameter is independent from the spectrum of the incident light but gives an absolute measure for the efficiency of any given solar cell.

A Picture of the IPCE measurement setup used in this thesis is depicted in Figure 3-4. White light from a 150 W Xenon lamp (LOT Oriel) is mechanically chopped before it enters a monochromator (Oriel Cornerstone™ 130 1/8 m Monochromator). The light leaving the monochromator through a fiber optic is split by a beam splitter into two parts with a known and fixed division ratio. The different parts of the light are guided to the solar cell under investigation and to a Calibrated Silicon Detector

(Oriental Instruments) with known SR, respectively. The modulated signal measured at the contacts of the devices in general is small for single wavelengths and thus a lock-in amplifier (EG&G 7280 DSP) is used to record the signals. Since the  $SR(\lambda)$  of the photodiode and the division ratio of the two beams is known, from the signal of the diode the light intensity reaching the cell under investigation can be determined. With the current recorded for the investigated cell,  $SR(\lambda)$  and  $EQE(\lambda)$  can be calculated according to equations (3.24) and (3.23). A relative error of 10% can be estimated for the obtained values.

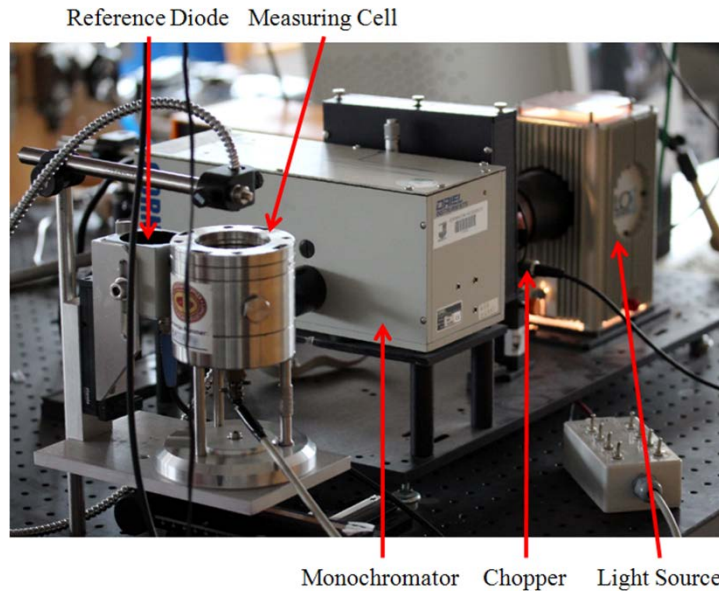


Figure 3-4: Picture of the IPCE measurement setup used in this thesis.

### 3.12 Statistical Relevance of the Device Results

For all OLEDs or PLEDs presented in the course of this thesis a series of 18 devices was investigated. Within these series, the device efficiencies exhibited a mean variation of less than 15%. For all shown OPV devices, a series of 18 NCSCs was characterized. Power conversion efficiencies exhibited a mean variation of less than 20% within these series.

## 4 Organic Light Emitting Devices

### 4.1 Introduction

The cornerstones for organic light emitting devices and polymer light emitting devices were already laid in 1987 by Tang et al.<sup>[18]</sup> describing the first realizations of a small molecule-based electroluminescent device as well as in 1990 by Burroughes et al.<sup>[19]</sup> realizing the first PLED based on a poly(phenylene vinylene) (PPV). In addition to small molecules and polymers acting as emitter in OLEDs, by the end of the last century, with dendrimers<sup>[144,145]</sup> a new class of materials has emerged, the opto-electronic properties of which can be tailored easily on the molecular scale by adequate composition and synthesis of the molecule. All of these works attracted huge attention within the academic community and triggered enormous efforts in industrial as well as in scientific research that led to presentations of ever new works in the field of organic electronics. The reported results are dealing with the realization of new materials suitable for OLED applications as well as their synthetic routes, respectively, for all three classes of emitting materials. Furthermore, various different types of device assemblies could be demonstrated presenting for example single-<sup>[146]</sup> and multilayer devices,<sup>[147]</sup> top emitting OLEDs<sup>[148]</sup> as well as transparent OLEDs.<sup>[149]</sup> Additionally, a lot of work has been dedicated to the investigation of different assembling techniques for OLEDs like thermal evaporation,<sup>[22]</sup> solution based processes (spin-coating,<sup>[150]</sup> as well ink-jet printing<sup>[151]</sup>) and processing steps like laminated or cold welding electrodes.<sup>[152,153]</sup> The devices resulting from these development lead to some fundamental advantages of OLEDs in comparison to liquid crystal display- (LCD) or LED-based technologies. In particular, OLEDs are self-luminous combined with high brightness levels and do not need any backlight illumination or polarizer, resulting in a low power consumption and high contrast ratio. In addition, state of the art OLEDs in general exhibit extremely low device thicknesses (several hundred nanometers without the substrate), allowing for an assembly of the devices on flexible substrates.<sup>[154]</sup> Their emission profile is Lambertian, which offers viewing angles of more than 160° without a change in emission brightness or color.<sup>[155]</sup> Moreover, OLEDs are easy to fabricate and PLEDs can even be solution processed allowing for cost effective and large-area mass production. Due to these advantages organic components bear a vast potential as active materials for flat-panel displays<sup>[20,21]</sup> and lighting applications<sup>[22,23,156]</sup> and first commercial OLED products have already been demonstrated on the market. Beginning with Pioneers car stereo front panel display in 1997 using a passive OLED-display more and more applications have entered the commercial market in the recent years and even TV sets like Sony's OLED-TV XEL-1<sup>[157]</sup> are already more than just visionary thoughts. In that context SAMSUNG, one of the most important global players on the mobile phone market, currently uses active matrix OLED displays (AMOLED) for all of its smartphones, including their flagship series SAMSUNG Galaxy.<sup>[158]</sup> Concerning lighting applications OSRAM with its OLED program ORBEOS<sup>[159]</sup> and Philips with its Lumiblade<sup>[160]</sup> already started to bring OLED products to the market.

Yet, while intense research has already led to commercial products, the lifetime and stability of OLEDs are still issues to be addressed in order to allow for an entire commercialization of various OLED products. In particular, while well-established active emitters can be found for the red and green spectral region<sup>[161]</sup> there is still a quest for stable, highly efficient and easy to synthesize molecules emitting light in the deep blue wavelength range. Moreover, device-assembling strategies allowing for an efficient exploitation of the luminescent properties of the materials as well a cost effective production of devices on the industrial scale are still topics that need further development. In

the next chapters novel blue light emitting compounds based on pyrene as the fundamental building block will be introduced for each class of materials – polymers (chapters 4.3-4.5), dendrimers (chapter 4.6) as well as small molecules (chapter 4.7). Their photophysical properties will be assessed and their suitability as light emitting components in OLEDs is shown. In addition, for a pyrene-based polymer a device assembly allowing for the realization of exceptionally bright and highly efficient PLEDs will be presented. Chapter 4.8 finally deals with macrocycles realized by a triangular combination of triphenylene rings exhibiting blue PL as well as EL, which constitute a new promising class of blue light emitting molecules.

## 4.2 Pyrene based Emitters

### 4.2.1 Introduction on Pyrene

Among possible compounds for blue light emitting chromophores, pyrene (Figure 4-1) is one of the most thoroughly investigated candidates. In particular, pyrene is known for its high fluorescence lifetime,<sup>[117,162]</sup> the sensitivity of its excitation spectra to microenvironmental changes,<sup>[163]</sup> but also for its liability to form light emitting excimers – as a result of  $\pi$ - $\pi$ -stacking (Figure 4-1) of the planar molecule – shifting the blue molecular emission into the green spectral region (Figure 4-2).<sup>[162,164,165]</sup> The formation of excimers made pyrene one of the most frequently applied dyes in fluorescence-labeled polymers<sup>[166]</sup> but it was also presented as laser dye<sup>[167]</sup>, building block for single- and multiwalled carbon nanotubes<sup>[168]</sup> and as highly effective hole transporter for OLEDs.<sup>[169]</sup> Nevertheless, the strong propensity for excimer formation constitutes the main limiting factor for the applicability of pyrene as blue emitter in OLEDs since it causes a significant red-shift of the fluorescence spectrum. Moreover, the extraordinary long lifetime of the excited state leads to enhanced luminescence quenching thus resulting in a low solid state fluorescence quantum yield. Nevertheless, the  $\pi$ - $\pi$ -stacking can be prevented in films by the introduction of spatially demanding substituents<sup>[170,171]</sup> or directly through avoiding the pyrene interaction via the implementation of a highly twisted structure in an appropriate molecular assembly.<sup>[172]</sup>

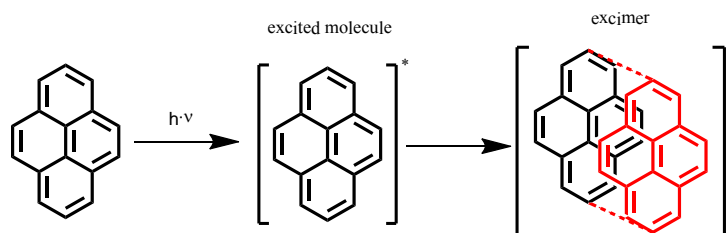


Figure 4-1: Molecular structure of pyrene and scheme for the excimer formation process.

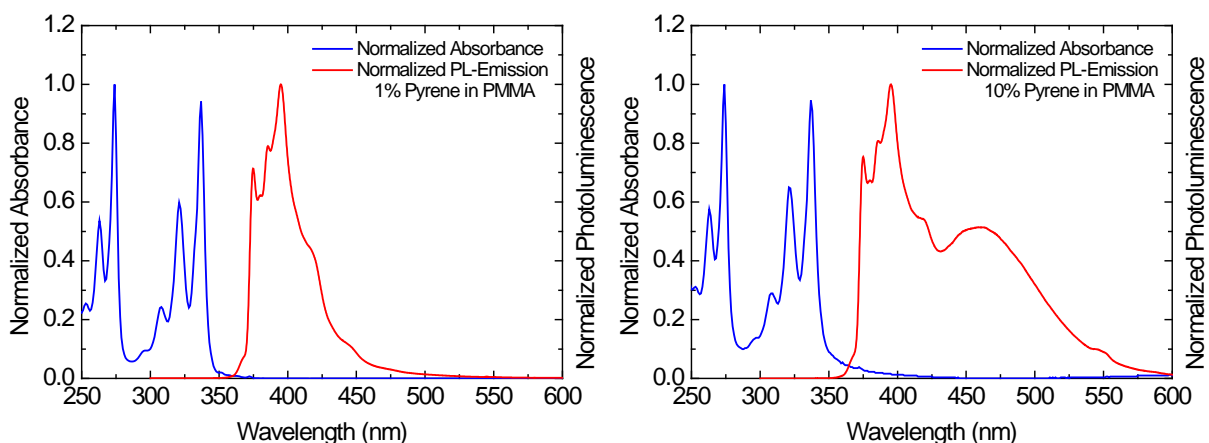


Figure 4-2: Absorption and PL spectra of 1wt.% (left) and 10 wt.% (right) pyrene molecules blended into polymethylmethacrylate (PMMA) films. In the PL spectra the development of a broad emission feature between 430 nm and 570 nm leading to a red shift of the overall emission at higher pyrene concentrations is clearly visible.

### 4.3 Designed Suppression of Aggregation in Polypyrene: Toward High-Performance Blue-Light-Emitting Diodes

*The content of this chapter is published in: Teresa M. Figueira-Duarte, Pablo G. Del Rosso, Roman Trattnig, Stefan Sax, Emil J.W. List and Klaus Müllen; Advanced Materials 2010, 22, 990-993.*

The author of the thesis co-authored to this publication. Exclusive contributions by the author: surface morphology measurements, device assembling and characterization. Collaborative contributions: photophysical characterizations, material degradation experiments. T.M.F.-D. and E.J.W.L. have written the publication. The author of the thesis contributed significantly to the physics related results. In the current chapter the publication text was expanded essentially by the thesis author.

#### 4.3.1 Introduction

Pyrene, a large conjugated aromatic system forming planar molecules is known for its tendency to aggregate via  $\pi$ - $\pi$  stacking. This behavior, however, strongly limited the use of pyrene as emitting material in OLED-applications, since the formation of aggregates in conjunction with an excimer formation leads to a distinct luminescence quenching which results in low solid state fluorescence quantum yields.

Yet, in recent years, there has been an increasing interest for the use of pyrenyl units in the synthesis of emissive and charge transport materials for OLEDs. Among the compounds reported so far oligothiophenes with pyrenyl side- or end-groups,<sup>[173]</sup> dipyrenylbenzene molecules,<sup>[174]</sup> pyrene-carbazole derivatives,<sup>[169,175]</sup> pyrenylamine-hexaphenylphenylenes,<sup>[176]</sup> pyrenyl-oligoquinolines,<sup>[177]</sup> and pyrene-fluorene derivatives<sup>[171,178-180]</sup> can be found. However, most of the pyrene derivatives which were introduced as efficient blue emitters for OLED applications present some degree of aggregation in solid state resulting in a considerable red-shift of the fluorescence emission in concentrated solution or thin film.<sup>[171,177]</sup>

The most effective effort in the prevention of aggregate formation for small molecules was achieved in tetra-substituted highly sterically hindered pyrenes, which show deep blue light emission in solution as well in the solid state with fluorescence quantum yields as high as 96% to 99%.<sup>[181]</sup> The best known material in this context is the 1,3,6,8-tetraphenylpyrene which has been used in OLEDs<sup>[181]</sup>, and OFETs<sup>[182]</sup> as well in OLEFETs,<sup>[183,184]</sup> but also other tetra-substituted systems including different phenyl derivatives<sup>[181]</sup> or pyridyl units<sup>[185]</sup> at the 1,3,6,8 positions have been reported. In 2008 Figueira-Duarte et al.<sup>[172]</sup> reported an effective suppression of aggregation for strongly twisted multichromophoric dendrimers that consisted exclusively of pyrene units attached to a center pyrene molecule at the 1,3,6,8-positions, which revealed significantly increased fluorescence quantum yields relative to unsubstituted pyrene. In addition to the already listed compounds, also 1,1'-bipyrenyl<sup>[186-189]</sup> and linear 1,6-disubstituted oligopyrenes<sup>[190-193]</sup> were investigated.

Relative to the majority of small molecules that are insoluble, conjugated organic polymers provide the advantage of being suitable for large area production of display and lighting devices at much lower manufacturing costs by the utilization of solution-based deposition techniques. Yet, only a limited number of investigations concerning the attachment of pyrene to the polymeric chain<sup>[194]</sup> or the incorporation of pyrene along the polymeric backbone<sup>[195-197]</sup> were reported as active materials for molecular electronics. Actually, the few publications that described the preparation of polypyrene<sup>[190,191,198]</sup> are based on electrochemical polymerization and the resulting polymers exhibited extremely low molecular weights. Furthermore, these polymers formed by 1-1' coupling of the pyrene rings yield insoluble and unprocessable films or a soluble material with low chain lengths of 2-13

repeat units. The low degree of polymerization is assumed to be a consequence of the low solubility of pyrene caused by the strong self-assembling tendency of pyrene segments.

In contrast, in this chapter a pyrene based polymer is presented and characterized the synthesis of which is based on a simple 3-step chemical route which yields a well soluble and processable polypyrene, the poly-7-*tert*-butyl-1,3-pyrenylene (PPyr, Figure 4-1). PPyr thereby constitutes the first reported polymer exhibiting a defect-free structure as well as a high degree of polymerization and is composed exclusively of pyrene units.

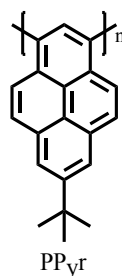


Figure 4-3: Chemical structure of PPyr ( $n = 115$ ).

#### 4.3.2 Synthesis of PPyr

PPyr was synthesized at the *Max-Planck Institute for Polymer Research* (MPI, Mainz) according to the simple chemical 3-step route depicted in Figure 4-4. Pyrene was mono-*tert*-butylated to afford 2-*tert*-butylpyrene,<sup>[199]</sup> which was then treated with bromine (2 equivalents) in  $\text{CH}_2\text{Cl}_2$  at  $-78^\circ\text{C}$ , to provide the 1,3-dibromo-7-*tert*-butylpyrene in 89% yield. The use of *tert*-butyl groups was strategic in order to selectively obtain the 1,3-dibromo-7-*tert*-butylpyrene derivative. The polymerization of the monomer was carried out in a Yamamoto coupling reaction with a Ni(0) catalyst.<sup>[200]</sup> After precipitation in a mixture of HCl and methanol (1:1) and subsequent removal of the low-molecular-weight species by Soxhlet extraction with acetone, gel permeation chromatography (GPC) analysis (THF, PPP standards) revealed  $M_n = 29800 \text{ g/mol}$ ,  $M_w = 51500 \text{ g/mol}$ , and  $\text{PD} = 1.7$ ; which corresponds to a molecular structure of approximately 115 repeat units. The resultant polymer exhibits high solubility in common organic solvents (e.g., THF, TOL and chlorinated solvents) enabling the investigation of the optical properties in solution.

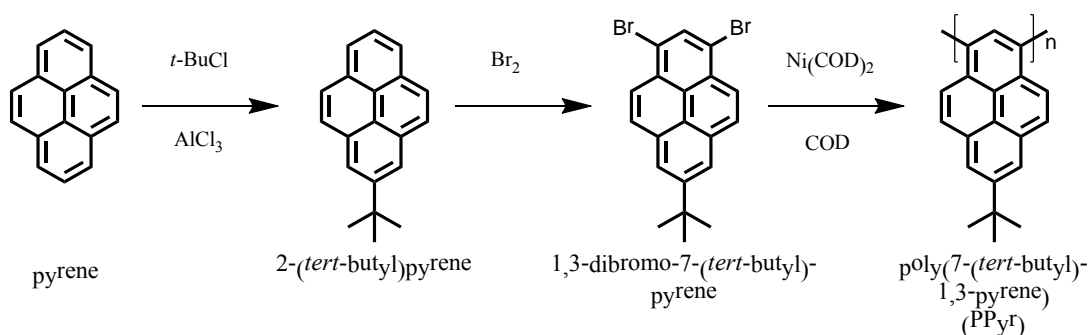
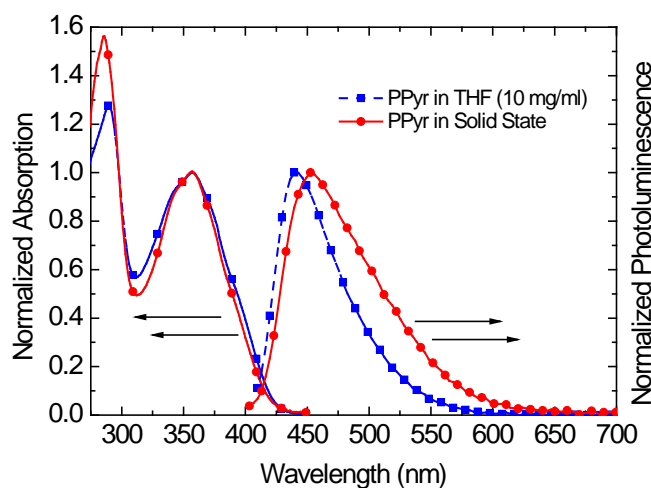


Figure 4-4: Three step synthesis of poly-7-*tert*-butyl-1,3-pyrenylene. COD represents cyclooctadiene and *t*-Bu is the *tert*-butyl group.



### 4.3.3 Photophysical Properties of PPyr

Figure 4-5 shows the UV-visible absorption and photoluminescence emission spectra of the PPyr in diluted THF solution (0.01 mg/ml) and in thin film. The absorption spectra of the solution as well as in the solid state both show an absorption maximum at 357 nm and a higher lying absorption band around 280 nm. The maximum at higher wavelengths corresponds to the  $\pi$ - $\pi^*$  transition of electrons in the polymer upon photoexcitation. In contrast to the almost identical absorption spectra, the PL emission of both, film and solution is characterized by one broad unstructured emission feature exhibiting a maximum at 441 nm in solution and an emission wavelength maximum with a small bathochromic shift to 454 nm for the solid state. In addition, a minor broadening of the emission spectrum in the solid state is observed which is attributed to an enhanced intermolecular interaction between the particular PPyr molecules in thin film. The absence of any vibrational features in absorption as well as in emission spectra is caused by the shape and nature of the torsional potential between the adjacent 1,3-coupled monomer units of the polymer. They exhibit a strong anharmonicity caused by pyrene molecule vibrations, a behavior similar to that observed for poly(*para*-phenylenes).<sup>[78]</sup>



**Figure 4-5:** UV-Visible absorption and photoluminescence emission spectra of PPyr in THF (dashed blue line with boxes) and in thin solid film (red line with circles).

An observation of very similar shapes and positions of absorption and emission spectra in film and dilute solution already can be considered as a good indicator for an absence of agglomerates and excimers in PPyr. However, in order to definitely rule out their occurrence a classical concentration dependence of the photoluminescence emission from the polymer content in solution over 5 orders of magnitude ranging from 0.1 mg/l to 1000 mg/l is performed. The respective emission spectra for solutions of PPyr in toluene are depicted in Figure 4-6. It clearly can be observed that for none of these solutions signs specific for aggregation or excimer formation like strong red shift or broadening of the emission spectrum is detected. For a concentration of 100 mg/l, however, a narrowing of the emission from the low wavelength side develops which is even more distinct for the emission at 1000 mg/l. This narrowing, which obviously is significant above a certain critical polymer concentration, occurs due to self-absorption of the polymer at emission wavelengths below 450 nm where an overlap of absorption and emission characteristics exists (Figure 4-5). Thus, the narrowing is just a filtering out of generated light at the lower wavelength edge of the emission spectrum. These results directly evidence against any excimer formation in PPyr. In addition, the formation of aggregates in polymer solutions should display pronounced concentration dependence as well. Since, as just explained, such dependence is not observed for the emission spectra, ground state aggregation can be ruled out for PPyr as well. This

conclusion is further corroborated by the fact that an excitation of PPy<sub>r</sub> in solution at wavelengths close to or below the bandgap (i.e. at wavelengths higher than 370 nm) does not result in the development of an additional emission band or even shift of the molecular emission, stemming from ground state aggregation.

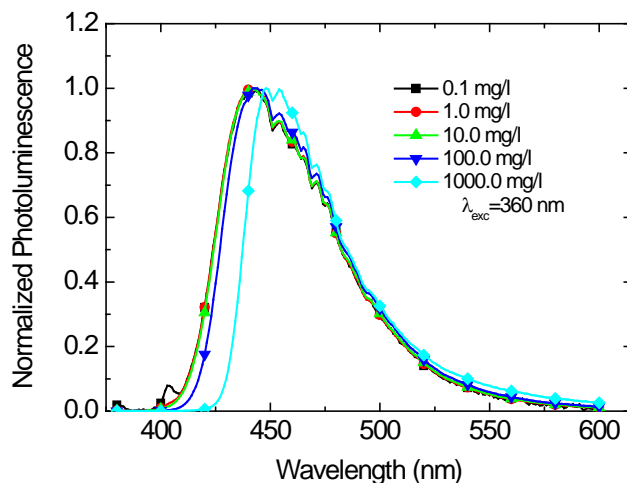


**Figure 4-6: Photoluminescence spectra of PPy<sub>r</sub> dissolved in toluene at different polymer concentrations in the range of 0.1 mg/l to 1000 mg/l. The two spectra with the highest concentrations show a reduced emission for wavelengths below 450 nm due to self-absorption.**

These results from the optical characterization of PPy<sub>r</sub> in toluene solution are further supported from the calculated molecular structure as it was modeled for 1,3-pentamer model compound at Austin Model 1 (AM1) level calculation using Spartan software package at the MPI shown in Figure 4-7. The modeling shows clearly that two adjacent pyrene units are twisted with respect to each other as a result of the sterical hindrance yielding a dihedral angle of approximately 70°. The twisted conformation of the 1,3-pentamer and likewise of the polymer leads to a significant inhibition of self-aggregation of pyrene units due to the  $\pi$ - $\pi$ -stacking. Consequently, possible self-quenching effects caused by the formation of aggregates or excimers are prevented which reflects in solid state properties comparable to those in solution. Moreover, a comparison of the absorption and emission properties of the polymer to those of a 1,3-trimer<sup>[172]</sup> exhibiting an absorption maximum at 350 nm and an emission maximum at 430 nm in solution compared to at 357 nm and 441 nm in the polymer, respectively, indicates that a longer effective conjugation in the polymer suppresses even stronger the tendency for excimer or aggregate formation. This behavior could be attributed to a large tensile stress promoted by the longer polymeric chain that should lead to a larger dihedral angle between neighboring pyrene units.

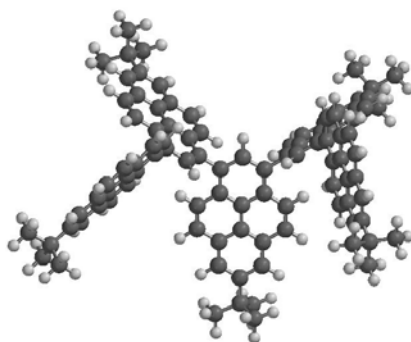


**Figure 4-7: Molecular model of a 1,3-pentamer of PPy<sub>r</sub> showing a highly twisted structure resulting from the sterical hindrance between adjacent pyrene units.**

As a summary of the photophysical properties it can be stated that the 1,3-coupling of pyrene units in combination with sterically hindering *tert*-butyl groups at the 7-position effectively suppresses an aggregation in pyrene due to the resulting highly twisted structure of the polymeric chain. In addition, as a result of the high dihedral angle between adjacent pyrene units in the polymer chain, PPyr shows high solubility in common organic solvents and a fluorescence quantum yield in TOL of  $\eta_f = 0.88$  could be measured (anthracene as reference with an excitation wavelength of 360 nm).

#### 4.3.4 Surface Morphology and Thermal Stability of PPyr Thin Films

The morphology of thin polymeric films and its stability upon thermal treatment display a crucial parameter for PLED fabrication and performance. Too high surface roughness as well as pinhole formation in a PLED under operation can lead to electric point effects or high local currents causing polymer degradation or even to the destruction of the device. To investigate the film formation of PPyr and its stability upon thermal treatment AFM investigations were conducted. Therefore an approximately 50 nm thick PPyr film was spin cast on a PEDOT:PSS covered ITO substrate and measured as spun and after heating the sample in vacuum at 150°C for 2 hours. Figure 4-8 displays AFM height images typical for the morphology of the film before and after thermal treatment. As can be observed both images show a similar morphology. It is characterized by a flat surface with shallow dimples homogeneously distributed over the whole scanning area. Obviously, no significant change in morphology is induced upon thermal treatment. An RMS-roughness  $R_q$  of 0.68 nm was measured for the as spun film and  $R_q = 0.77$  nm was obtained after thermal treatment of the PPyr layer. In addition, an average depth of approximately 5 nm was measured for the dimples (Figure 4-8, right).

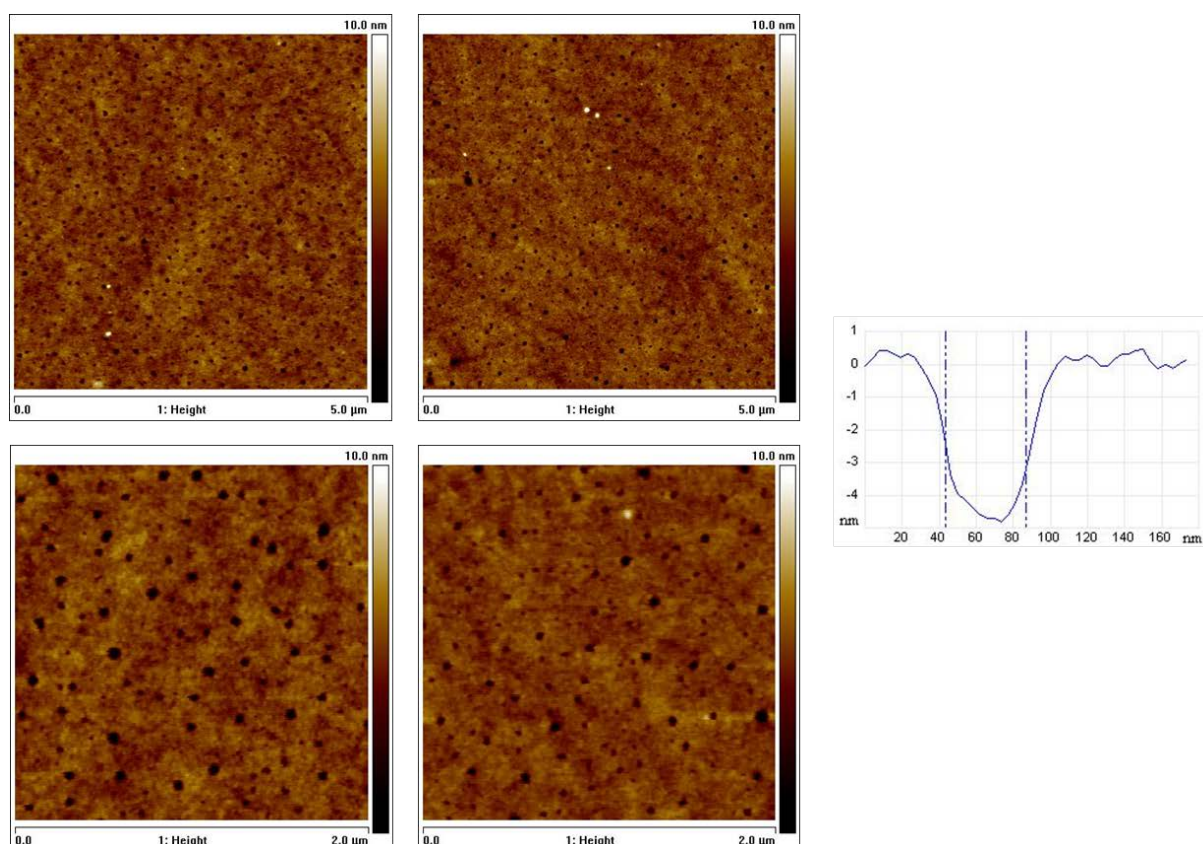
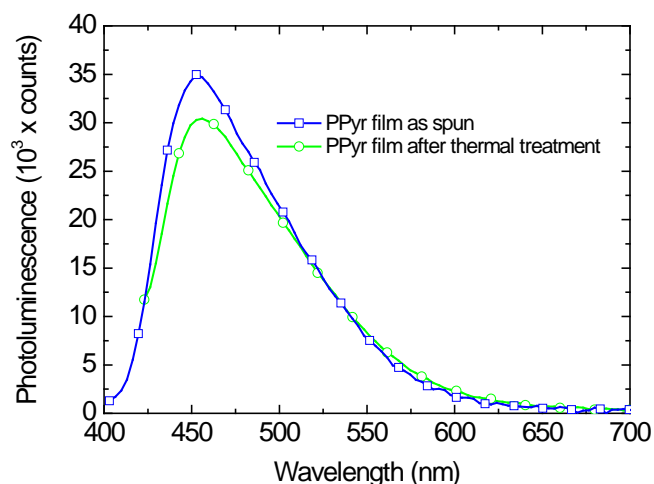


Figure 4-8: AFM height images (top: 5  $\mu\text{m}$  x 5  $\mu\text{m}$ , bottom: 2  $\mu\text{m}$  x 2  $\mu\text{m}$ ) of a PPyr film after deposition (left) and after thermal treatment at 150°C in vacuum (center). Both images show homogeneously distributed shallow dimples (~5 nm) in the film with a RMS-roughness of  $R_q=0.68$  nm right after deposition and  $R_q=0.77$  nm after thermal treatment, respectively. Right: height profile of a dimple cross section.

Thus, AFM investigations evidence an exceedingly thermally stable morphology for PPy thin films, which prevents the formation of aggregates even at high temperature. Moreover, since the dimples detected in the surface of PPy films are only shallow a detrimental effect on the performance of PLEDs using PPy as active material is not expected.

Besides morphological stability also the chemical stability with respect to thermal treatment constitutes an important prerequisite for light emitting polymers used in OLEDs. The formation of chemical defects like for example oxidation often reflects in a change of the photophysical properties, i.e. of the fluorescence emission spectrum. Thus, the PL emission of a PPy film on a quartz substrate as deposited and after an annealing step at 150°C for 24 h under Argon atmosphere was recorded. Figure 4-9 shows the absolute PL emission spectra obtained before and after annealing. Remarkably, only a slight variation of the emission maximum of 4 nm, from 452 nm right after deposition to 456 nm after annealing the film, is detected. Furthermore, the solid state fluorescence quantum yield is reduced only by a low degree of 9% after the thermal treatment of the film. Similar results were obtained for annealing experiments under ambient conditions. These results in conjunction with those obtained by AFM of thermally annealed films display that PPy not only possesses thermal stability with respect to morphology but also that the formation of chemical defects for example upon oxidation at elevated temperature is sufficiently prevented.



**Figure 4-9:** Absolute photoluminescence spectra obtained for a PPy film before and after annealing under argon atmosphere at 150°C for 24 hours.

### 4.3.5 PPy – Device Characterization

After these photophysical and morphological investigations, PLEDs were fabricated in a standard sandwich geometry: ITO/PEDOT:PSS/PPy/CsF/Al. Current density-voltage-luminance (J-V-L) characteristics of the respective PLEDs are depicted in Figure 4-10. As can be observed, the PLEDs show a bright blue electroluminescence emission with a maximum luminance value of 300 cd/m<sup>2</sup> at a bias voltage of 8 V. A detectable onset of electroluminescence emission could be measured at approximately 4.2 V and the maximum luminous efficiency was 0.04 cd/A. The inset of Figure 4-10 shows the EL-emission spectrum at a current density of 1.0 kA/m<sup>2</sup> and a bias voltage of 5.2 V. The spectrum shows a maximum at 459 nm and a profile very similar to the photoluminescence emission in the solid state. The corresponding color coordinates of the emission are located in a favorable blue region with  $x = 0.16$  and  $y = 0.21$  according to the Commission Internationale de l'Éclairage standard of 1931 (CIE 1931).

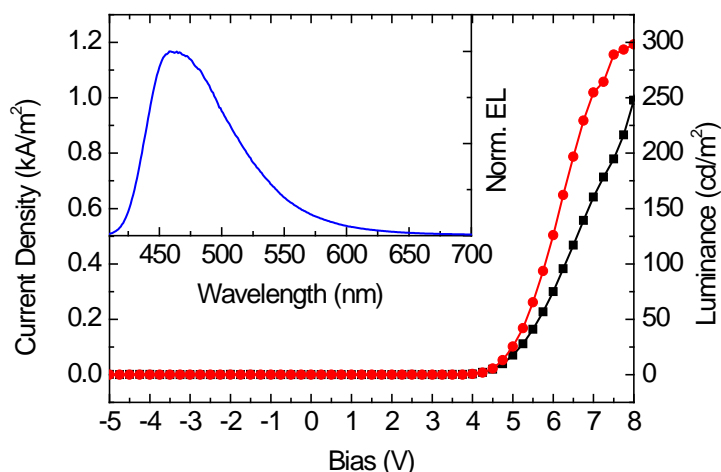


**Figure 4-10:** Current density (black line with squares) and luminance (red lines with circles) as a function of the bias voltage in an ITO/PEDT:PSS/PPyr/CsF/Al device. The inset shows the electroluminescence emission spectrum at a current of  $1.0 \text{ kA/m}^2$  and a bias of 5.2 V for the same device.

As depicted in Figure 4-11 the devices showed remarkable spectral stability even for high current densities above  $4 \text{ kA/m}^2$  as well as during continuous operation with only very minor changes in the spectrum as a consequence of a thermal annealing under device operation.

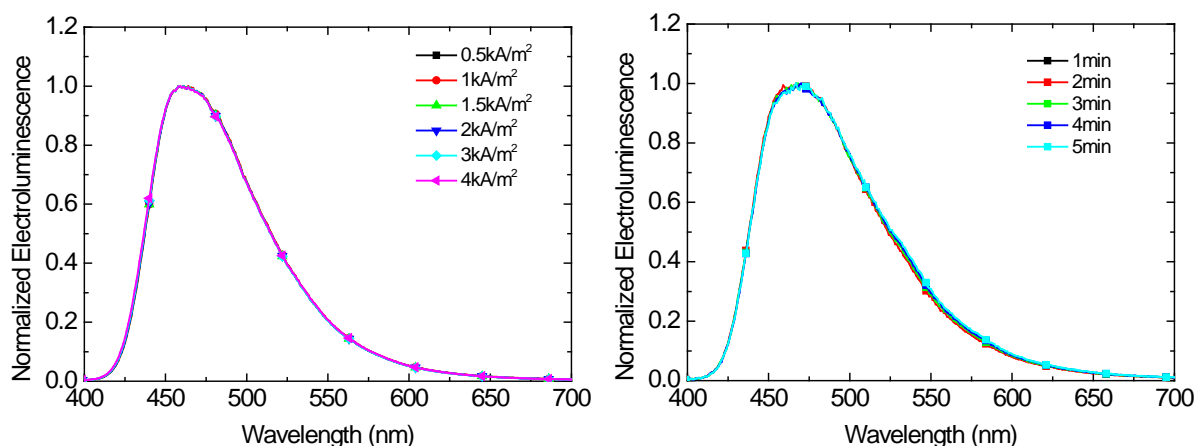


**Figure 4-11:** Current density (left) and time dependent (right, recorded at a current density of  $4 \text{ kA/m}^2$ ) EL-spectra of ITO/PEDOT:PSS/PPyr/CsF/Al devices.

It is important to note that the device related parameters like the low luminous efficiency constitute preliminary results obtained by a non-optimized device assembly. Nevertheless, the performance of the devices presented in this chapter is comparable to those fabricated without evaporated transport layers from similar poly(para-phenylene)-type based materials with respect to the overall device efficiency and brightness.<sup>[201–204]</sup> However, regarding the overall device stability PPyr shows clear superiority based on its molecular design. In addition, the simple three-step chemical synthetic route allows for the fabrication of high purity and defect free polymers. Due to the molecular structure of PPyr oxidative degradation processes, such as “aliphatic CH (photo)oxidation” which was observed for non-conjugated polymer segments,<sup>[205]</sup> and oxidation of the main chain segments, such as observed for the 9-position in polyfluorene<sup>[156,206]</sup> are absent in the presented polymer.

### 4.3.6 Conclusion

In conclusion, a novel deep blue light emitting polymer, PPyr, and its photophysical, morphological and optoelectronic characterization was presented in this chapter. It was shown that, because of the 1-3 linking PPyr presents the benefit of very stable deep-blue emission in thin film and solution. Furthermore, it could be demonstrated that PPyr exhibits an extraordinary spectral and morphological stability with respect to thermal treatment. These properties are caused by a high dihedral angle between adjacent pyrene units, which enables to fully prevent  $\pi$ - $\pi$ -stacking. Consequently, the formation of aggregates and excimers, which provoke an altered emission and considerably lowered fluorescence quantum yields, is completely suppressed. The mentioned characteristics in combination with a simple three-step synthetic route and a high fluorescence quantum yield make PPyr a particularly promising material for polymer light emitting diodes. This conclusion also is corroborated by preliminary device results for PLEDs using PPyr as emitting layer. As it was demonstrated, the devices exhibit a deep blue electroluminescence emission, which is stable even for high current densities in the device and under continuous operation. However, the low luminous efficiencies presented for the first PLEDs demand for further improvements to the device concept in order to be able to compete with other blue light emitting high performance polymers for PLED applications.

## 4.4 Deep Blue Polymer Light Emitting Diodes Based on Easy to Synthesize, Non-aggregating Polypyrenes

*The content of this chapter is published in: Roman Trattnig, Teresa M. Figueira-Duarte, Dominik Lorbach, Wolfgang Wiedemair, Stefan Sax, Stefanie Winkler, Antje Vollmer, Norbert Koch, Marianna Manca, Maria-Antonietta Loi, Martin Baumgarten, Emil J.W. List and Klaus Müllen; Optics Express, 2011, 19 Suppl.6, A1281-93.*

The author of the thesis is the main author of this publication. Exclusive contributions by the author: Planning und supervision of the overall work, photophysical characterization, photoinduced absorption experiments, surface morphology measurements, device assembling and device characterization. Collaborative contributions: material degradation investigations and discussion of the results. The author of the thesis has written the publication and expanded its text essentially in the current chapter.

### 4.4.1 Introduction

In chapter 4.3 it was shown that in a pyrene-based polymer comprising 1,3-coupled pyrene-molecules bearing a *tert*-butyl group at the 7-position,  $\pi$ - $\pi$ -stacking can be fully prevented through the spatially demanding character of the *tert*-butyl substituent. Furthermore, this polymer features a high solid state fluorescence quantum yield and exhibits a stable emission in the blue spectral region. In addition to these advantageous physical properties the polymer is highly soluble in common organic solvents and its simple 3-step synthetic route allows for a large scale synthesis of highly pure and defect-free polymers.

Yet, in order to exploit the full potential of polymers for large scale fabrication of PLEDs *via* solution based processes like roll-to-roll slot die coating or inkjet printing, the device efficiencies of PLEDs using PPyr as emitting material need to be increased significantly. Even when the results of preliminary devices in the preceding chapter are comparable to those of similar poly(para-phenylene)-type based materials with respect to the overall device efficiency and brightness,<sup>[201–204]</sup> the achieved performance is modest compared to the top results reported for blue light emitting polymers based for example on polyfluorene<sup>[207]</sup> or anthracene<sup>[208]</sup> achieving luminous efficiencies above 1 cd/m<sup>2</sup>. Taking a considerably increased luminous efficiency as a prerequisite for polymer light emitting devices, however, demands for a more detailed understanding of the photophysical properties of pyrene than it was presented so far. While the formation of agglomerates and excimers, can be ruled out for PPyr, it is demonstrated by several examples in literature<sup>[197,209,210]</sup> that the polarity of the solvent used for dissolution and deposition of the pyrene-based polymer is likely to have an influence on the emission characteristics as well. The change in the emission properties thereby is caused by an altered conformation of the pyrene moieties in different molecular environments. In addition, the pyrene molecule is known for the exceptionally long lifetime of its excited states, which are able to give rise to an enhanced luminescence quenching yielding low fluorescence quantum yields in the solid state. In that context, triplet excitons and their lifetime additionally need to be considered, since TEs are able to reduce luminescence efficiently by singlet-triplet annihilation.<sup>[211]</sup> Finally, the device assembly itself needs to be adapted. From literature it is known that in order to realize highly efficient devices balanced charge carrier injection and transport are necessary.

Thus, following the previous chapter (chapter 4.3) on the synthesis and basic properties of PPyr, in the current part of this thesis the photo-physical, electronic and device relevant properties, including results on optimized devices using a triphenylamine(TPA)/pyrene copolymer, are presented in higher detail. In particular, absorption and photoluminescence measurements are used to investigate the observed influence of solvent polarity on the emission in solutions and in thin films. Singlet exciton

and triplet exciton lifetimes are studied by means of time resolved photoluminescence spectroscopy and photoinduced absorption, respectively, in order to evaluate possible TE quenching effects in devices.<sup>[211]</sup> Photoemission spectroscopy is performed to determine the energy levels of PPyr that are relevant for the fabrication of device assemblies leading to higher luminance values, device efficiency and deep blue electroluminescence.

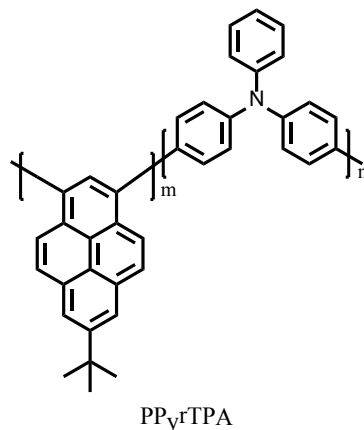


Figure 4-12: Molecular structure of triphenylamine/pyrene copolymer PPyrTPA (m:n ratio is 97:3).

#### 4.4.2 Synthesis of PPyrTPA

Poly(pyrene-*co*-TPA) (PPyrTPA) was synthesized at the MPI according to the route depicted in Figure 4-13 by a Yamamoto coupling with Ni(0) from 1,3-dibromo-7-*tert*-butylpyrene and commercially available 4-bromo-*N*-(4-bromophenyl)-*N*-phenylaniline (dibromotriphenylamine). The 1,3-dibromo-7-*tert*-butylpyrene was prepared in three steps as described for PPyr. The dibromotriphenylamine was purified by three-time crystallization from *n*-hexane. The polymerization reaction was carried out with three percent of triphenylamine derivative, thus the sequence of the monomers is statistically distributed over the polymer strand. Copolymer PPyrTPA was precipitated in a mixture of hydrochloric acid and methanol (1:1). After Soxhlet extraction the yield was 45% with a weight-average molecular weight of  $M_w = 27400$  g/mol ( $M_n = 10300$  g/mol) as determined by GPC (THF, PPP standards) and a polydispersity of PD = 2.6

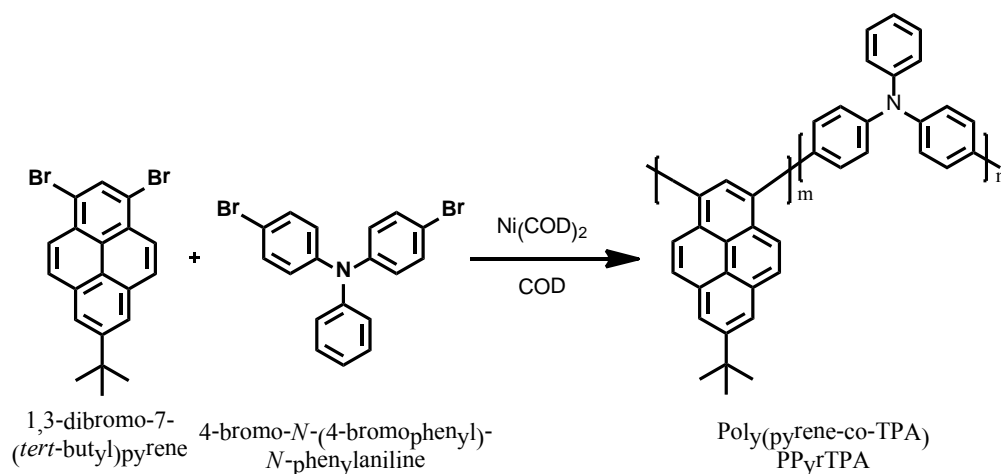
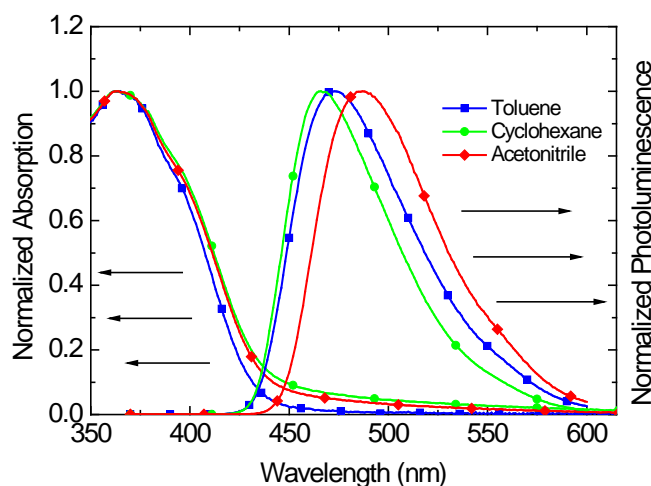


Figure 4-13: Synthesis of PPyrTPA. COD represents cyclooctadiene (m:n ratio is 97:3).



#### 4.4.3 Dependence of Absorption and Emission Characteristics on Solvent Polarity

As documented by many examples in literature, unsubstituted pyrene,<sup>[209]</sup> and macromolecules containing pyrene moieties<sup>[197,210]</sup> typically display a strong solvatochromic effect as a consequence of the influence of solvent polarity on the molecular conformation. To investigate this influence on the photoluminescence and absorption of PPy a series of solvents with increasing polarity (CH, TOL and ACN) has been tested. The corresponding absorption and PL emission spectra were recorded and are shown normalized in Figure 4-14. The PL emission in general is characterized by a broad structureless spectrum peaking at 466 nm for CH, 472 nm for TOL and 487 nm for ACN. Thus, an enhancement of the solvent polarity leads to a distinct bathochromic shift of the PL peak maximum. In the absorption spectra, on the contrary, no shift of the maxima can be observed. All solutions exhibit an absorption peak maximum for the  $\pi$ - $\pi^*$  transition of PPy around 360 nm, yet the onset of the absorption spectra of the ACN and CH solutions show a minor broadening. Since the respective solutions exhibited a slight turbidity, this broadening is attributed to scattering of light by not fully dissolved polymer particles. From a comparison to pyrene dimers having a 1,1-coupling the bathochromic shift can be assigned to the formation of a charge transfer state in solvents with higher polarity, forcing the highly twisted molecules into a more planar structure yielding the observed change of the photoluminescence.<sup>[189,210,212,213]</sup>



**Figure 4-14: UV-Visible absorption (360 nm) and photoluminescence emission spectra (466–487 nm) of PPy dissolved in toluene, cyclohexane and acetonitrile.**

In addition to absorption and emission spectra of dilute solutions, also thin films cast from each of the named solvents were investigated. It can be seen in Figure 4-15 that, remarkably, the shift observed in the photoluminescence of different solutions can also be partly found in a series of thin films spin coated from the mentioned solvents. The photoluminescence spectra of films cast from CH and TOL exhibit a maximum at 475 nm, while the film cast from ACN possesses a maximum at 482 nm. From this observation it is concluded that the conformation of the molecules as found in solution may be also present in the solid state. Here in particular this is of high significance for the fabrication of organic light emitting devices from this polymer since a red shift of the maximum in the as discussed range results in a shift from the preferable deep blue spectral region to the unpreferable blue-green region.

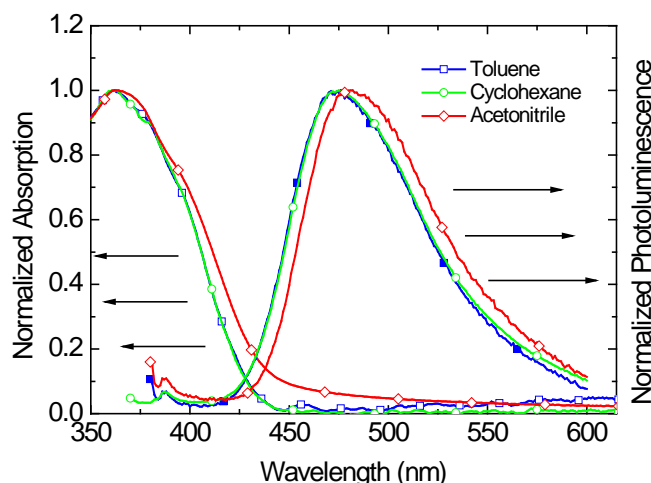


Figure 4-15: UV-Visible absorption (360 nm) and photoluminescence emission spectra (475–482 nm) of PPy thin films spin cast from in toluene, cyclohexane and acetonitrile solutions.

#### 4.4.4 Photophysical Properties of PPyTPA

For light emitting devices not only the emission spectrum is of high importance but also a balanced charge carrier transport to realize efficient devices.<sup>[214]</sup> To achieve an improved charge carrier transport for holes in the polymer, 3% triphenylamine-groups, known for their good hole transport properties,<sup>[215]</sup> were statistically co-polymerized into PPy resulting in the copolymer PPyTPA (Figure 4-12).

Absorption and photoluminescence spectra of PPyTPA in TOL-solution and in thin film are presented in Figure 4-16. The absorption maximum can be found again in the range of 360 nm in toluene and in the solid state. The fluorescence maximum is located at 450 nm for the dissolved polymer and the solid states emission maximum is detected around 460 nm for PPyTPA. As already noticed for PPy, PPyTPA shows no sign of an excimer band emission at lower energies.

The fluorescence maxima of 475 nm for PPy and 460 nm for PPyTPA reveal that both polymers exhibit blue fluorescence in the solid state and thus fulfill well the requirement for blue emitting materials. In addition, analyses of the fluorescence quantum yield of both pyrene based polymers in toluene solutions resulted in photoluminescence quantum yields of  $\eta_f = 0.88$  for PPy and  $\eta_f = 0.77$  for PPyTPA (quinine sulfate as reference with an excitation wavelength of 360 nm).

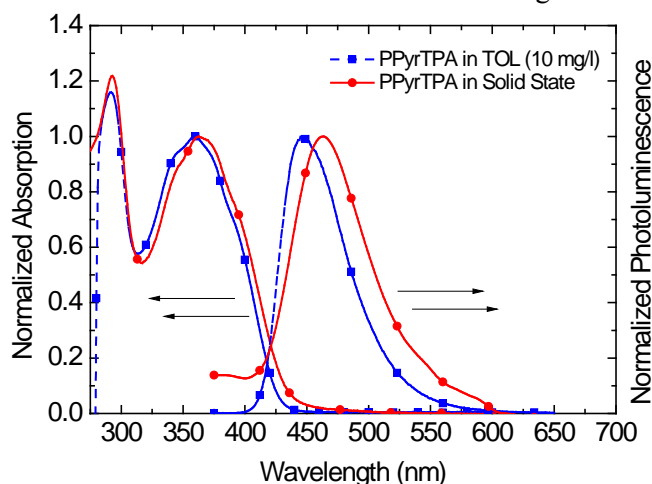
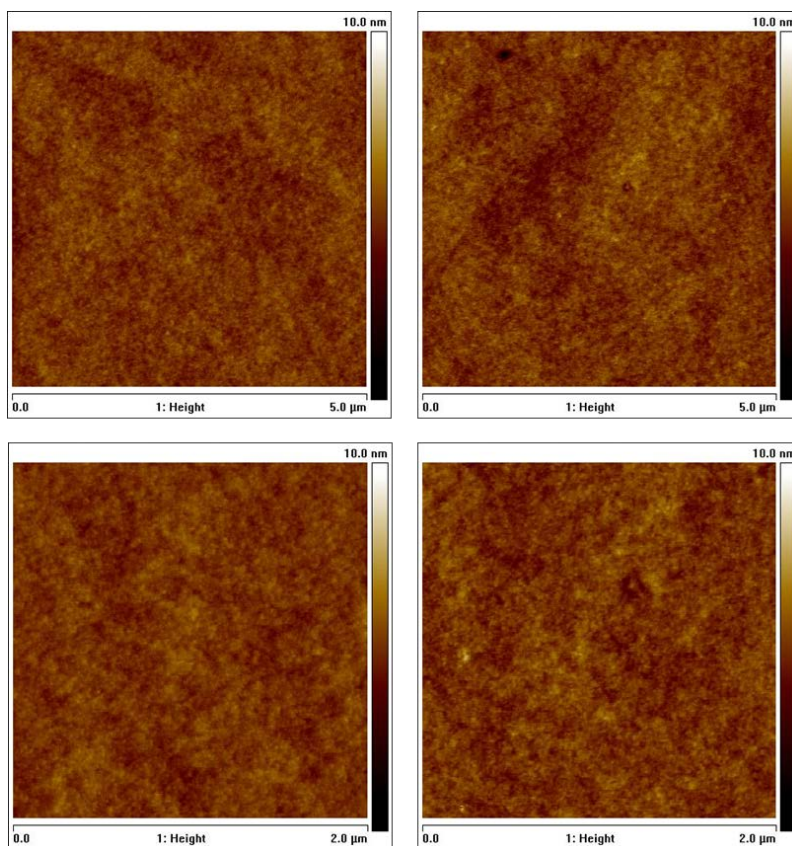


Figure 4-16: UV-Visible absorption and photoluminescence emission spectra of PPyTPA in TOL (dashed blue line with boxes) and in thin solid film (red line with circles).

#### 4.4.5 Surface Morphology and Thermal Stability of PPyrTPA Thin Films

In analogy to the analyses for PPyr, PPyrTPA thin films – spin coated on PEDOT:PSS covered ITO substrates – were measured directly after spin-coating as well as after annealing for 2 hours under vacuum in order to examine probable changes in surface morphology due to the thermal treatment. It can be observed in Figure 4-17 that this second pyrene-based polymer again displays a remarkable morphological stability. Both images show an extremely flat surface of the polymer film with  $R_q = 0.42$  nm for the as-spun film and  $R_q = 0.50$  nm for the annealed polymer and no significant change is detected upon thermal treatment. In contrast to PPyr, however, PPyrTPA films do not form the previously observed dimples, but a completely homogenous surface area.



**Figure 4-17:** AFM height images (top:  $5\ \mu\text{m} \times 5\ \mu\text{m}$ , bottom:  $2\ \mu\text{m} \times 2\ \mu\text{m}$ ) of PPyrTPA films after deposition (left) and after thermal treatment at  $150^\circ\text{C}$  in vacuum (right). The morphology images show a homogenous flat film surface with a RMS-roughness of  $R_q=0.42$  nm before and  $R_q=0.50$  nm after thermal treatment, respectively.

The influence of a thermal treatment on the emission characteristics of PPyrTPA was assessed just as for PPyr. Therefore, a 50 nm PPyrTPA film on quartz substrate was examined directly after spin-coating from a TOL solution and after annealing at  $150^\circ\text{C}$  for 24 hours in argon atmosphere. The respective absolute photoluminescence emission spectra are depicted in Figure 4-18. Obviously, only a small difference of 6 nm can be found for the emission maximum after spin-coating (464 nm) compared to the maximum after annealing (458 nm). The solid state fluorescence quantum yield thereby is reduced by 10% upon thermal treatment. As in the case of PPyr, PPyrTPA films annealed under ambient conditions yield a similar outcome. These results evidence that the incorporation of TPA-groups, statistically distributed over the polymer backbone, does not bear a detrimental effect on the polymers performance, neither regarding its film morphology nor its optical behavior. Moreover, also for PPyrTPA it can be summarized that this polymer shows the desirable properties of an

extremely flat surface morphology combined with a deep-blue fluorescence emission, which are both stable under thermal treatment.

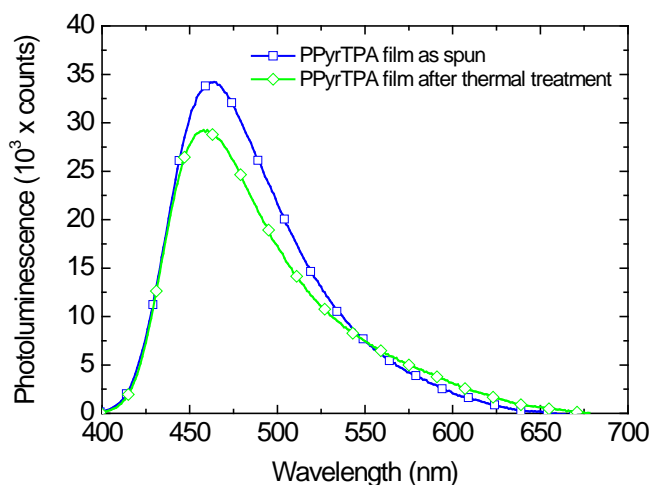


**Figure 4-18:** Absolute photoluminescence spectra obtained for a PPyrTPA film before and after annealing under argon atmosphere at 150°C for 24 hours.

#### 4.4.6 Exciton Lifetime in PPyr

Unsubstituted pyrene molecules are known for their exceptionally long fluorescence lifetimes,<sup>[117,162]</sup> which especially in OLEDs can lead to a high fluorescence quenching rate and consequently to low device efficiencies. In order to elucidate the effect of polymerization of pyrene as compared to a single molecule on the excited states decay dynamics (SE and TE lifetime) TRPL spectra of solutions and thin films of PPyr as depicted in Figure 4-19 and PIA spectra in the solid state as shown in Figure 4-20 have been recorded and evaluated. The results are summarized in Table 1 and are compared to literature values obtained for the pyrene molecule as well as for other blue emitting conjugated polymers to assess possible non-radiative quenching effects of TE in devices.

By TRPL measurements a lifetime  $\tau_f$  of 1.9 ns is obtained for PPyr in toluene solution. This result presents a completely different decay dynamics of pyrene SEs within the polymer as compared to the single pyrene molecule where a SE-lifetime of 458 ns was measured.<sup>[164]</sup> Note that an intermolecular excimer emission as the origin of the fluorescence emission for PPyr can be ruled out since no spectral evidence for a low energy emission band is found at the low concentrations of the compound in the solution under investigation ( $\sim 1 \times 10^{-3}$  mg/ml). This leads to the conclusion that polymerizing pyrene in a 1,3-configuration shortens the detected fluorescence lifetime by ca. 200 times, however, still conserving the high PLQY of 88% in solution. It is important to note further that very similar results are found when pyrene is incorporated into pyrene-dendrimers.<sup>[216]</sup>

In thin film PPyr exhibits double exponential fluorescence decay with lifetimes  $\tau_f$  of 27 ps and 146 ps with a relative weight of 65% and 35%, respectively. These results display that the SE lifetimes of PPyr are drastically shorter (ca. 2700 times) than those of pyrene molecules in thin films. In addition, as already presented in chapter 4.3.3, the PL results in solutions with different polymer content and of thin films show no evidence for excimer formation.

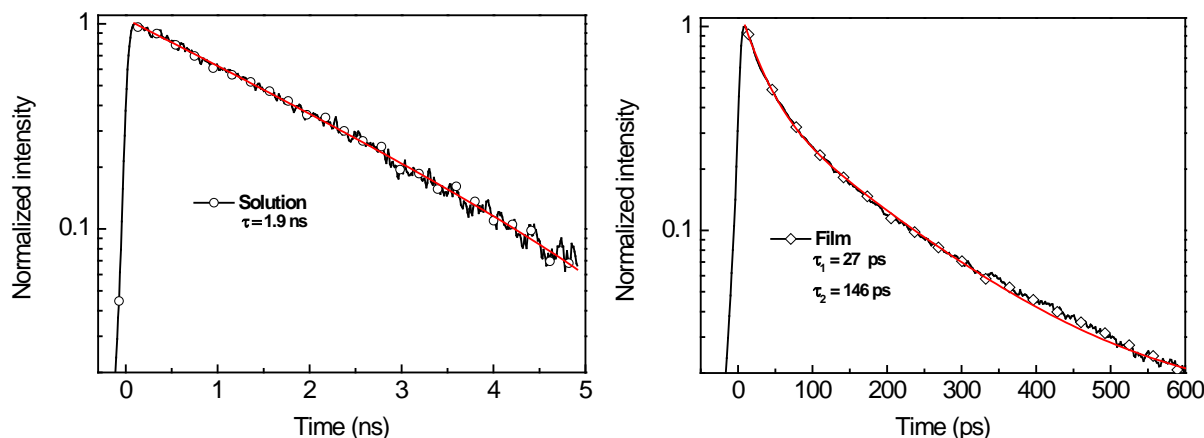


**Figure 4-19: TRPL decay of PPy dissolved in toluene (left) and of in thin film (right;  $\lambda_{\text{exc}}=380$  nm). Solid red lines: mono-exponential (solution) and double-exponential (thin film) fits for fluorescence lifetime evaluation.**

The graph in Figure 4-20 shows the PIA spectrum as well as the regular absorption of a PPy film. The PIA exhibits one broad feature with a maximum at 744 nm. From a comparison of this feature in shape and position to other phenylene type polymers<sup>[217]</sup> this transition is assigned to a triplet-triplet transition T1.

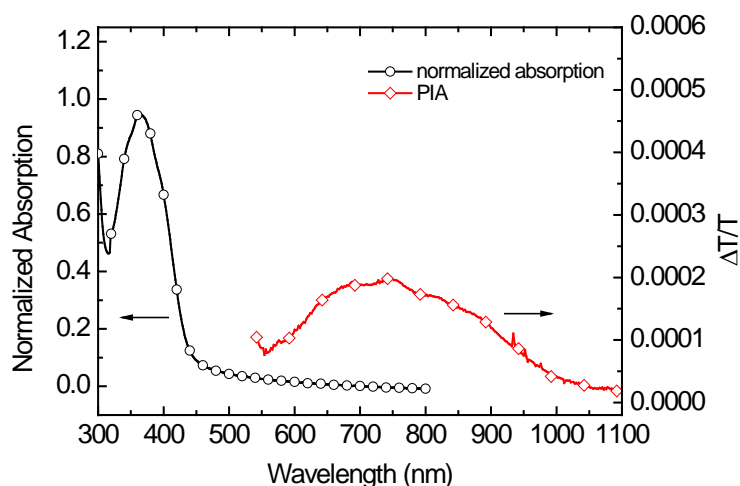


**Figure 4-20: Normalized absorption spectrum of polypyrrole and photoinduced absorption spectrum of PPy at 100K. (100mW laser power,  $\lambda_{\text{exc}}=364$  nm).**

To determine the lifetime of the T1 transition and hence the TE state dynamic, a first approximation can be made according to equation (3.16). With a phase angle of  $38.6^\circ$  at 744 nm and a chopping frequency of 13.3 Hz the calculation yields a TE lifetime of 9.5 ms (c.f. Figure 4-21, left). To attain a more precise value the dependence of the in phase, out-of-phase and quadrature signals of the lock-in amplifier on the modulation frequency have been measured and the results are depicted in Figure 4-21 (right). Based on the fact that one can directly extract the lifetime of the state  $k_{\text{TE}}$  from the global maximum of the out-of-phase component corresponding to equation (3.15),<sup>[137,218]</sup> an average TE lifetime of 8.3 ms ( $\nu_{\text{max}} = 17.82$  Hz) is obtained.

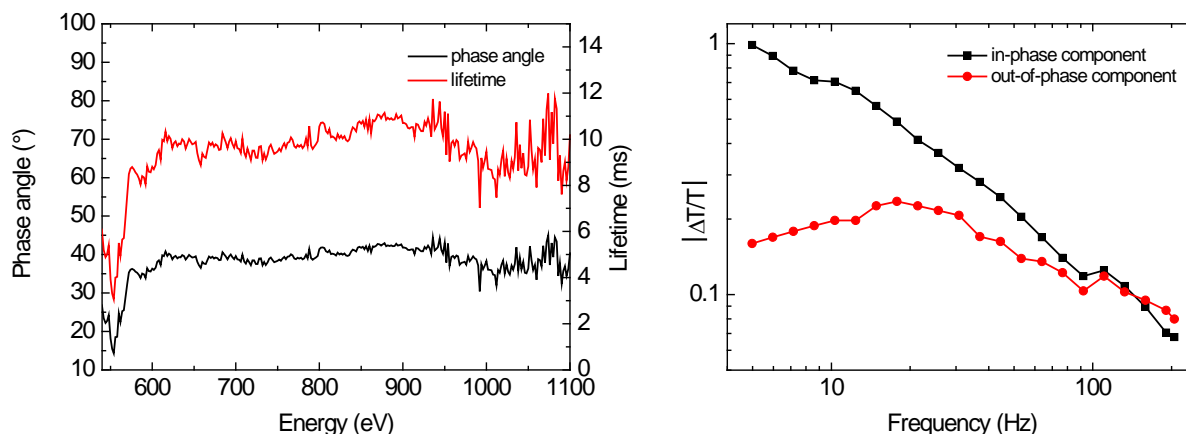


**Figure 4-21: Phase angles (left) and absolute value of In-phase- and Out-of-phase component (right) to determine the lifetime of triplet excitons at 744 nm (100mW laser power,  $\lambda_{exc}=364$  nm).**

Figure 4-22 shows a double logarithmic plot of excitation intensity dependent measurements of the PIA signal. For higher excitation energies the slope of the linear regression of the PIA signal has a value of  $k=0.47$  which clearly indicates that the excitons display a bimolecular recombination (theoretical slope  $k=0.5$ ). In contrast, for lower intensities the slope of 1.03 as expected yields a monomolecular decay (theoretical slope  $k=1$ ).

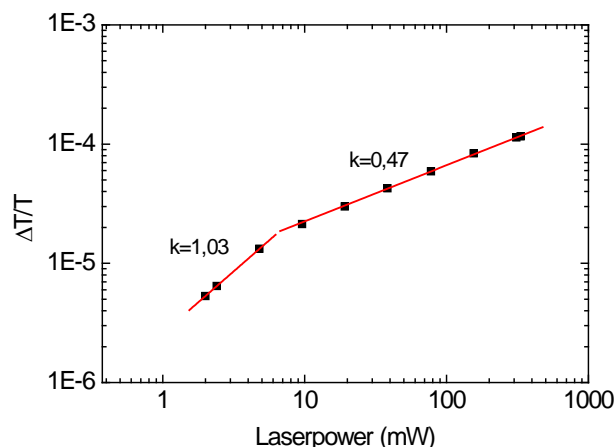


**Figure 4-22: Excitation intensity dependent PIA measurement of a PPy film detected at 744 nm. The linear regression slopes indicate the regions of monomolecular ( $k=1.03$ ) and bimolecular ( $k=0.47$ ) decay.**

A comparison of the TE lifetimes of isolated pyrene molecules and PPy in thin films (Table 1) shows a 50 times shorter TE lifetime in the polymer. Consequently, it can be expected that conceivable quenching processes of SE by SE-TE annihilation due to long lived TEs (resulting in a large steady state population of TEs) resulting in a major reduction of the fluorescence quantum yield are of second order in PPy thin films.

An expansion of the comparison in Table 1 with established values for the well-studied blue emitting poly(para-phenylene)(PPP)-type polymer polyfluorene (PF) shows in fact that the excited states decay dynamics of PPy resembles much more that of PF than that of the single pyrene molecule. This in particular can be concluded by comparing the SE-TE-lifetime ratio of PPy and PF in the solid state. Within the error of the experiment these values are located in the same order of magnitude and consequently processes like SE-TE annihilation are expected to be similar in PPy as compared to PF.

**Table 1: Singlet exciton and triplet exciton lifetimes of pyrene-molecule, pyrene-polymer PPyr and polyfluorene in solution and in solid state.**

	Pyrene Molecule		PPyr			PF	
	solution	Film	solution	film		solution	film
<b>SE-lifetime</b>	458 ns <sup>[164]</sup>	400 ns <sup>[117]</sup>	1.9 ns	146 ps	27 ps	370 ps <sup>[219]</sup>	170 ps <sup>[219]</sup>
<b>SE-LT rel. weight</b>	100%	100%	100%	35%	65%	100%	100%
<b>TE-lifetime</b>	9.4 ms <sup>[220]</sup>	0.45 s <sup>[117]</sup>	-	8.9 ms		108 $\mu$ s <sup>[221]</sup>	2 ms <sup>[222]</sup>
<b>SE-TE-LT Ratio</b>	1:2 $\times$ 10 <sup>4</sup>	1:1 $\times$ 10 <sup>6</sup>	-	1:6 $\times$ 10 <sup>7</sup>	1:3 $\times$ 10 <sup>8</sup>	1:3 $\times$ 10 <sup>5</sup>	1:1 $\times$ 10 <sup>7</sup>

At that point, however, it should be mentioned that compared to PF PPyr is considered to be chemically more stable than the PPP-type polymer. While both compounds exhibit low TE lifetimes which lower the probability of oxidization of the organic molecules by ground state oxygen, PPyr lacks the instable 9-position of PF which is known for its irreversible formation of on-chain oxidative keto-defects upon photooxidation.<sup>[206,223]</sup>

#### 4.4.7 UPS-studies on PPyr and PPyrTPA

In OLEDs an unfavorable energy band alignment of the emitting material with respect to the adjacent layers can significantly lower the device efficiency because of possible charge carrier blocking and subsequent imbalanced charge carrier injection.<sup>[224]</sup> Consequently, it is of particular importance for optimizing the proper OLED configuration to gain knowledge about the corresponding energy levels of the highest occupied molecular orbital (HOMO) and the lowest molecular orbital (LUMO) of the light emitting material. To evaluate the energy levels of PPyr UPS measurements were conducted and are presented in the following.

Valence UPS spectra of PPyr and PPyrTPA are depicted in Figure 4-23. The low binding energy (BE) regions of the spectra show three prominent features for both materials. In case of PPyr they are centered at 1.4 eV, 2.2 eV, and 3.2 eV below the Fermi-level of the conductive polymer substrate while for PPyrTPA they are found at 1.8 eV, 2.6 eV and 3.6 eV. The lowest BE feature is derived from the highest occupied molecular orbital of the pyrene monomers. The BE onset of this emission features are at 0.8 eV and 1.0 eV, respectively, and in conjunction with the secondary electron cutoff the ionization energies are 5.6 eV for PPyr and PPyrTPA. Noteworthy, the HOMO-derived emissions are rather narrow in UPS, which points towards little wavefunction delocalization beyond the pyrene monomer. Typically in polymers with pronounced electronic interaction between individual monomers HOMO-derived bands of several eV width develop, which show up in UPS as flat features.<sup>[225]</sup> Consequently, the PPyr and PPyrTPA frontier electronic structures resemble more that typically found for molecular materials rather than for polymers.

As already stated repeatedly an efficient charge carrier injection into the emitting layer is decisive for the realization of efficient light emitting devices. In order to observe the suitability of the electron transporting material TPBi (Figure 4-24) for PPyr-based OLEDs UPS measurements were performed on substrates where the small molecule compound was evaporated incrementally onto the polymer layer. The deposition of TPBi results in a suppression of the PPyr features and in the emergence of two strong peaks (Figure 4-23). The BE of the peaks monotonically increases by ca. 0.2 eV/nm up to 5 nm coverage and remains constant for higher thicknesses. The low BE onset of the HOMO-derived TPBi

feature is at 1.8 eV below EF, the ionization energy is 6.2 eV (at 5 nm coverage). In contrast, the SECO shifted by 0.4 eV to lower BE, implying an electrostatic potential shift across the PPyr/TPBi interface by -0.4 eV. The reason for this shift is most likely due to TPBi adopting a different conformation right at the interface as compared to the bulk, resulting in a collective effect of intramolecular dipoles.<sup>[226]</sup> Pinning of EF at the TPBi interface induced gap states or impurity levels is improbable because of the substantial energy separation between the TPBi frontier levels and EF.

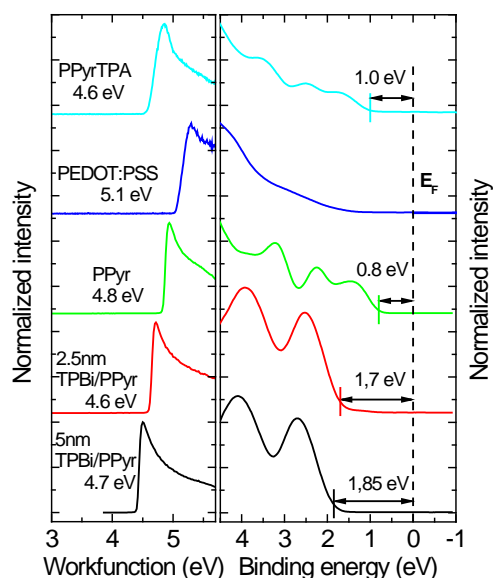


Figure 4-23: SECO (left) and valence region UPS spectra (right) of PEDOT:PSS, PPyr, PPyrTPA and of PPyr covered by 2.5 nm and 5 nm thick layer of TPBi.

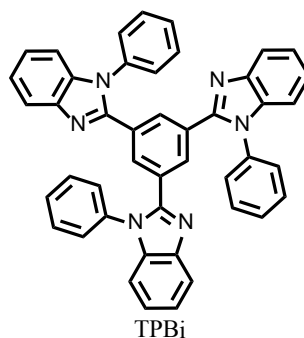


Figure 4-24: Chemical structure of TPBi

The energy levels across the PEDOT:PSS/PPyr/TPBi interfaces are summarized in Figure 4-25. As can be observed the positions of corresponding energy levels of TPBi seem to be well suited for an OLED application with PPyr. This can be concluded firstly because the electron affinity of the electron transporting TPBi is located at lower energy compared to the polymer thus forming no energy barrier at the PPyr/TPBi interface for electrons injected from the cathode. Secondly, the high ionization potential of TPBi generates a blocking energy barrier for positive charges at the interface to the emitting layer hence constraining their extraction. These properties should be leading to high charge carrier densities in the active polymer layer which are necessary for high recombination densities.<sup>[214]</sup>



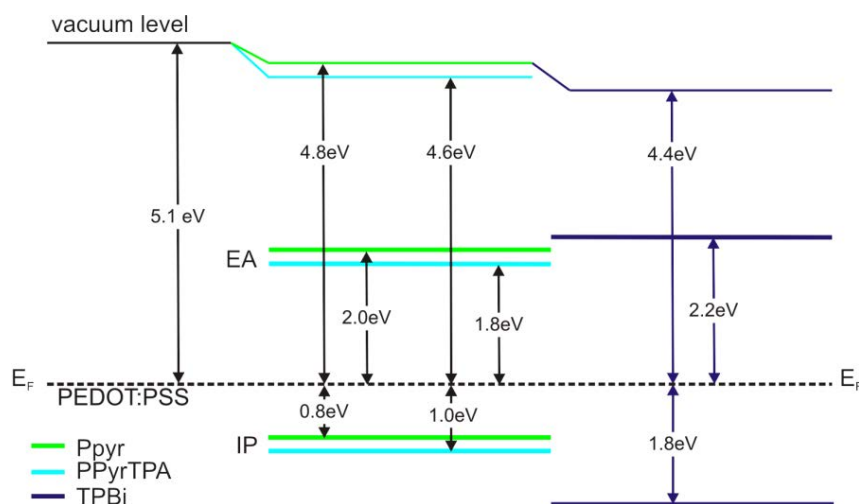


Figure 4-25: Energy level diagram for PEDOT:PSS/PPyr/TPBi and PEDOT:PSS/PPyrTPA. EA and IP denote the electron affinity and the ionization potential, respectively.

#### 4.4.8 Modified PPyr-based Devices

To finally investigate the electroluminescent properties of PPyr and their spectral stability over time in a modified assembly PLEDs were fabricated using the following standard sandwich geometry: ITO/PEDOT:PSS/PPyr/TPBi/Ca/Al. TPBi was used at the cathodes side since it is known for its electron transporting and hole blocking abilities.<sup>[227,228]</sup> Additionally, possible interface defect-states at the emitting layer/Ca-interface should be prevented by the small molecules.<sup>[229]</sup>

Figure 4-26 shows the current density-voltage-luminance characteristics of a device with PPyr as emitting layer. The PLED exhibited a deep blue electroluminescence emission achieving a maximum luminance of 1043 cd/m<sup>2</sup> at a bias of 6.2 V, which is a threefold improvement compared to the first publication on that material.<sup>[66]</sup> The device showed a fairly low onset of the electroluminescence at 3.2 V and a maximum efficiency of 0.12 cd/A was reached. This rather limited device efficiency is assigned to an unbalanced charge transport in the active polymer. The electroluminescence spectrum depicted in the inset of Figure 4-26 shows a structureless molecular emission peak between 430 nm and 550 nm with its maximum at 460 nm. This corresponds to CIE1931 coordinates of  $x = 0.158$  and  $y = 0.176$ , thus resulting in a deep blue emission. Both, shape and maximum of the EL-emission are very similar to the PL-spectrum in thin film (c.f., chapter 4.3), showing no signs of often observed excimer emission. This once again provides definite evidence for the effective suppression of molecular aggregation due to the *tert*-butyl groups attached to the 7-position.

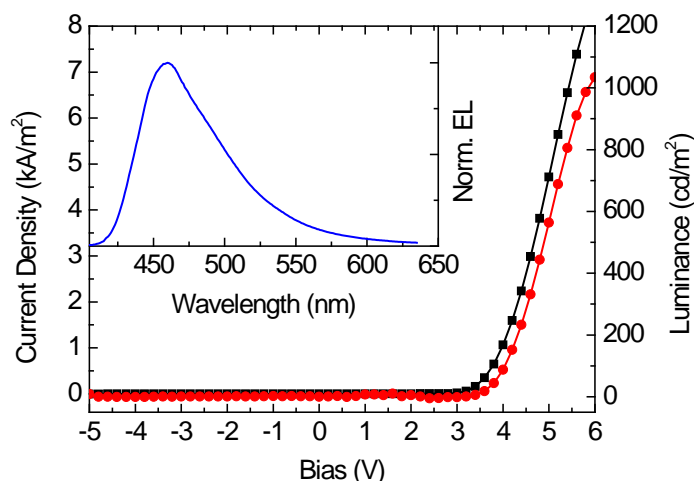


Figure 4-26: Current density (line with squares) / luminance (line with circles) as a function of the bias voltage in an ITO/PEDOT:PSS/PPyr/TPBi/Ca/Al device. The inset shows the electroluminescence emission spectrum obtained at a current density of  $1.0 \text{ kA/m}^2$ .

Current density dependent electroluminescence spectra of the devices, as depicted in Figure 4-27, display that also PPyr-based PLEDs fabricated with the TPBi-modified assembly showed extraordinary spectral stability up to current densities higher than  $5 \text{ kA/m}^2$ . Furthermore, Figure 4-27 presents the development of the EL-emission during continuous operation with a current density of  $1.0 \text{ kA/m}^2$ . As can be observed the material did not show a significant spectral change during the time of five minutes.

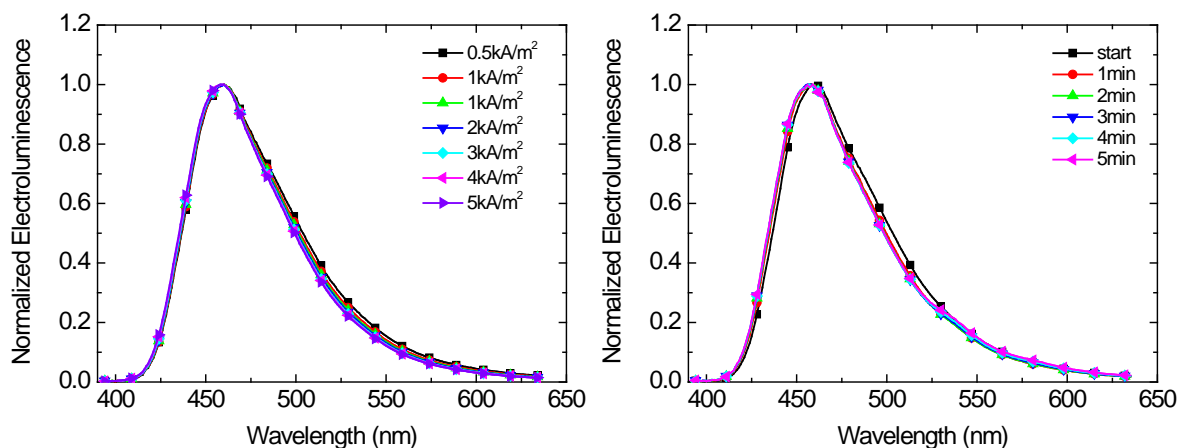
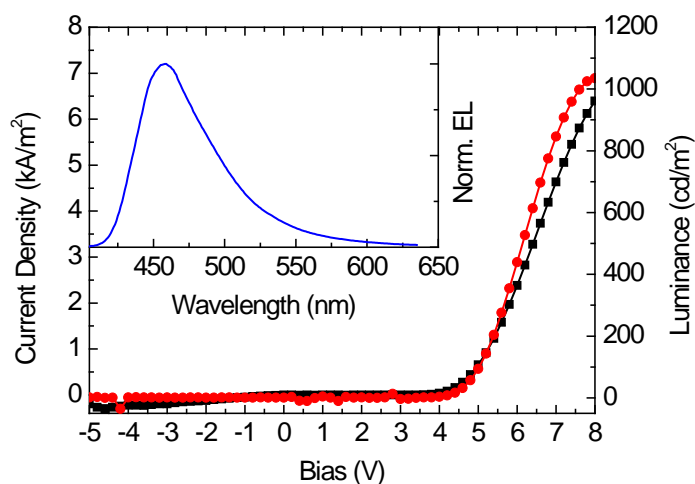


Figure 4-27: Current density (left) and time dependent (right) EL-spectra of ITO/PEDOT:PSS/PPyr/TPBi/Ca/Al devices. The time dependent emission spectra have been obtained at a current density of  $1.0 \text{ kA/m}^2$  and a bias of ca. 4.1 V.

PLEDs with PPyrTPA as emitting layer were fabricated in the same assembly as for PPyr: ITO/PEDOT:PSS/PPyrTPA/TPBi/Ca/Al. Due to the implementation of the TPA-groups the hole transport mobilities were expected to be improved. Therefore, the overall device efficiencies should be considerably enhanced compared to PLEDs containing pure PPyr. Figure 4-28 depicts the J-V-L characteristics of a PPyrTPA device. Again, a deep blue electroluminescence emission was observed with a maximum brightness of  $1035 \text{ cd/m}^2$  at a bias of 6.2 Volts. An onset bias of 3.8 V was detected and the maximum efficiency yield  $0.19 \text{ cd/A}$  at 6.4 V. A comparison to the peak efficiency of the PPyr device clearly demonstrates that only a small amount of TPA-groups was sufficient to enhance the device efficiency considerably. Figure 4-29 shows current density dependent EL-spectra as well as EL-spectra of a device at turn-on and during operation at a current density of  $1.0 \text{ kA/m}^2$ . These spectra

reveal the same exceptional spectral stability of PPyTPA as it was already found for PPy. In particular, for devices with PPyTPA as emitting material a molecular emission peak in the range between 420 nm and 540 nm was detected with its maximum at 450 nm, corresponding to CIE1931 coordinates of  $x = 0.155$  and  $y = 0.141$ . Thus, the EL-emission is located clearly in the deep blue region of the visible spectrum and does not show any significant change for high current densities ( $> 5 \text{ kA/m}^2$ ) or during operation.



**Figure 4-28:** Current density (line with squares) / luminance (line with circles) as a function of the bias voltage in an ITO/PEDOT:PSS/PPyTPA/TPBi/Ca/Al device. The inset shows the electroluminescence emission spectrum obtained at a current density of  $1.0 \text{ kA/m}^2$ .

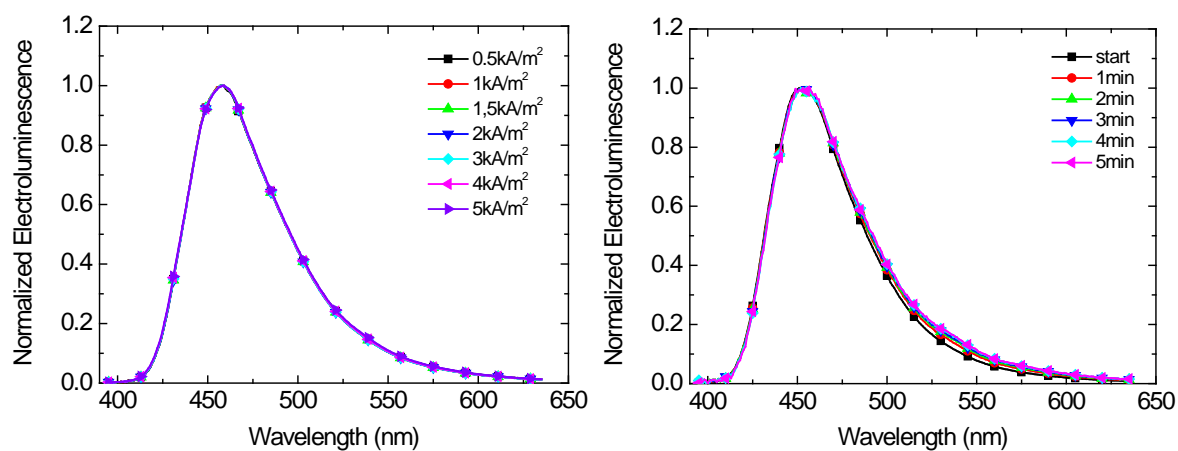


**Figure 4-29:** Current density (left) and time dependent (right) EL-spectra of ITO/PEDOT:PSS/PPyTPA/TPBi/Ca/Al devices. The time dependent emission spectra were recorded at a current density of  $1.0 \text{ kA/m}^2$  and a bias of ca. 5.3 V.

#### 4.4.9 Conclusion

In conclusion, this chapter demonstrated detailed photo-physical investigations on a new easy to synthesize non-aggregating class of pyrene-based polymers. PPy and PPyTPA exhibit deep blue fluorescent light emission and results from PL-measurements show that neither in solution nor in thin film a sign of polymer aggregation and resulting excimer emission can be found. Furthermore, it could be shown for PPyTPA that the desired properties of PPy, like spectral and morphological stability in thin films even after annealing at high temperatures, were not altered by the implementation of triphenylamine groups to the polymer backbone and high photoluminescence quantum yields of 88%

and 77% could be measured for PPy<sub>r</sub> and for PPy<sub>r</sub>TPA, respectively. The influence of the solvents polarity on the photoluminescence spectrum is demonstrated to play a significant role in order to prevent possible charge transfer states within the materials causing an undesirable red-shift of the emission. TRPL- and PIA-measurements revealed that SE and TE lifetimes are significantly reduced compared to the single pyrene molecule and in thin film the lifetimes are in the same order of magnitude as in well-known PPP-type polymers like polyfluorene. UPS measurements show only little inter-monomer wavefunction delocalization for both polymers. Consequently, the high dihedral angle between two adjacent monomer units obviously not only hinders the interaction of different polymer chains, preventing excimer emission, but also limits the electronic interaction between different monomers on the same chain. Moreover, polymer light emitting devices with considerably enhanced maximum luminance and luminous efficiency values as compared to the previous section (chapter 4.3) were realized using an improved assembly with TPBi as electron transporting material. The PLEDs exhibited a bright deep blue and stable electroluminescence emission and the possibility to further improve the device's efficiency by copolymerizing triphenylamine groups at a monomer ratio of 3% into the polymer backbone was demonstrated. Thus, it can be summarized that both polymers, PPy<sub>r</sub> as well as PPy<sub>r</sub>TPA, display well the requested requirements for blue light emitting polymers for OLED applications. Yet, even when a five-fold improvement regarding the overall device efficiency could be realized the performance of the presented devices still is located about one order of magnitude below the desired efficiency of 1 cd/A. While an imbalanced charge transport should not occur after the implementation of TPA groups to the polymer backbone, a look at the energy level diagram across the PEDOT:PSS/PPy<sub>r</sub>/TPBi-interfaces in Figure 4-40 reveals that an unbalanced charge injection due to high injection limiting energy barriers is still an issue for the presented devices.

## 4.5 Bright Blue Solution Processed Triple-Layer Polymer Light Emitting Devices realized by Thermal Layer Stabilization and Orthogonal Solvents

*The content of this chapter is accepted for publication: Roman Trattnig, Leonid Pevzner, Monika Jäger, Raphael Schlesinger, Marco Vittorio Nardi, Giovanni Ligorio, Christos Christodoulou, Norbert Koch, Martin Baumgarten, Klaus Müllen, and Emil J.W. List, Advanced Functional Materials 2013.*

The author of the thesis is the main author of this publication. Exclusive contributions by the author: planning und supervision of the overall work, photophysical characterization, surface morphology measurements, device assembling and device characterization. Collaborative contributions: photoemission spectroscopy measurements and discussion of the results. The author of the thesis has written the publication and expanded its text essentially in the current chapter.

### 4.5.1 Introduction

Apart from constant research on new or improved emitting materials, in academic and industrial research, particular focus is laid on the realization and development of solution based fabrication processes like ink-jet printing or roll-to-roll processing. These techniques generally provide the benefit of allowing for cost effective and high throughput fabrication of large area devices even on flexible substrates.<sup>[41]</sup>

The challenges in that context for both technologies – displays and lighting – can be found in the realization of highly efficient, highly luminescent and moreover during operation spectrally stable materials and devices achieving lifetimes of several hundred thousands of hours. While these requirements are already met for devices emitting in the red and green spectral region, blue light emitting materials and devices, especially concerning their lifetime and efficiency, still lag behind.<sup>[230,231]</sup> Among possible candidates for the realization of blue emitting devices fluorene-<sup>[232–234]</sup> or pyrene-based<sup>[66,235]</sup> compounds belong to the most thoroughly investigated and analyzed materials. Yet, while fluorenes can be synthesized with the requested purity the devices often lack of discoloration due to material degradation during operation.<sup>[236–238]</sup> In contrast, specifically tailored and easy to synthesize pyrene-based polymers, as could be presented in the previous chapters, not only show a deep blue emission but also provide the advantages of a high luminescence quantum yield combined with extraordinary chemical stability during operation.<sup>[66,235]</sup>

Yet, to achieve the necessary requirements of high brightness values in the device, alongside with high efficiency and stable operation, OLEDs require balanced charge carrier injection and charge carrier transport.<sup>[214]</sup> This issue up to date is mainly addressed by a so-called multilayer device structure. These structures comprise a layered assembly of two or more organic semiconducting materials exhibiting different bandgaps and charge carrier transport properties. The main objectives for such multilayer structures are firstly to provide an efficient injection and transport of positive (holes) and negative (electrons) charge carriers coming from the electrodes into the emitting layer and secondly to block to flow of charges out of the EML without a formation of excitons. In detail, this means that, besides an EML, additional hole transporting or hole injecting layers (HIL) are established at the anodes' side of the EML while electron transporting layers or electron injecting layers (EIL) are used at the cathodes' side. This kind of assembly finally results in a confinement of charge carriers within the emitting material thus enhancing the exciton density in the EML and consequently leading to higher luminance values and higher overall device efficiency.<sup>[214]</sup>

For OLEDs based on small molecules, defined multilayer structures can easily be realized layer by layer using high-vacuum vapor deposition techniques. However, because of the cost intensive equipment, the high material waste in the production process and the slow processing speed there is a huge barrier to bring devices produced that manner to industrial mass production and the size of the fabricated devices stays rather limited. Additionally, many small molecular materials show a potential drawback of changes in morphology caused by recrystallization or molecular migration at elevated temperature during operation or even at room temperature.<sup>[239,240]</sup> A different and cost-effective approach allowing for large area production is to apply organic materials (polymers and small molecules) by solution-based processes like inkjet-printing or slot-die roll-to-roll processing. While the issues concerning changes in morphology still exist for small molecules, polymers comprise a viable alternative. Polymers can exhibit good film formation properties upon solution processing, high morphological stability and a higher resistance to molecular diffusion than small molecules.<sup>[241]</sup> However, the implementation of multilayer device structures by subsequent solution processing of different layers displays the crucial point of this technique. Exceptional care has to be taken on the selection of solvents and materials to ensure that upon deposition of the sequent material the preceding layer does not redissolve. This is especially valid when two sequentially applied materials are in principle soluble in the same solvent. Different approaches addressing this issue were already presented and are based on cross linking reactions,<sup>[242-244]</sup> use of orthogonal solvents,<sup>[207,245]</sup> a layer-stabilizing “hard-bake” process<sup>[246]</sup> or on liquid buffer layers in between when applying the subsequent polymer layer.<sup>[247]</sup>

In this chapter the realization of a fully solution processed triple-layer PLED assembly is presented that combines a hard bake process – to insolubilize the bottom hole transporting layer - and the deposition of polymers from orthogonal solvents for both the emissive layer and the electron transport layer. For the single layer as well as for all multilayer devices the pyrene-triphenylamine copolymer PPyrTPA (Figure 4-12) is used as emitting material. For a bilayer device with enhanced hole injection properties poly(9,9-dioctyl-fluorene-co-N-(4-butylphenyl)-diphenylamine) (TFB, Luminescence Technology Corp.) acts as hole injecting/hole transporting material at the anode’s side of the emissive layer. TFB is known as a high mobility hole transport polymer<sup>[248]</sup> forming smooth and insoluble layers with a thickness of only a few nanometers, when heated at temperatures between 180-200°C and spin-rinsed afterwards.<sup>[246]</sup> In a last step the TFB/PPyrTPA assembly is completed by an electron injecting and hole blocking layer at the cathode’s side of the EML, forming a triple layer device. The ETL comprises a properly tuned polyfluorene polymer (PEGPF, Figure 4-30). PEGPF bears poly(ethylene glycol) (PEG) side chains, which ensure the solubility of the material in polar solvents like methanol thus preventing an intermixing with PPyrTPA during the deposition process of the ETL. Furthermore, PEGPF provides the advantages of PEG as electron injection material<sup>[249]</sup> and surfactant<sup>[250]</sup> with the conducting properties of the conjugated polyfluorene, which compensates for the insulating properties of PEG when the layer thickness is controlled properly.<sup>[251]</sup> The implementation of two different solution based multilayer approaches – based on orthogonal solvents and thermal stabilization of a polymeric layer – for several sequential spin-coating and annealing steps without harming the preceding layer is proven by atomic force microscopy investigations. Ultraviolet photoemission spectroscopy measurements evidence that the combination of materials and their assembly in PLEDs, as presented in this work, exhibit a favorable energy level alignment i.e., efficient electron blocking at the HTL/EML-interface and hole blocking at the EML/ETL-interface. This allows for efficient charge carrier confinement within the EML resulting in an enhancement of the maximum luminance and electroluminescence efficiency for multilayer PLEDs in comparison to single layer devices. Furthermore, the magnitude of the improvement is in the same range as for previously reported works on PLEDs with an assembly based on polar soluble polyfluorene,<sup>[207]</sup> thermally crosslinked<sup>[252-254]</sup> or thermally stabilized polymer interlayers.<sup>[246,247]</sup>

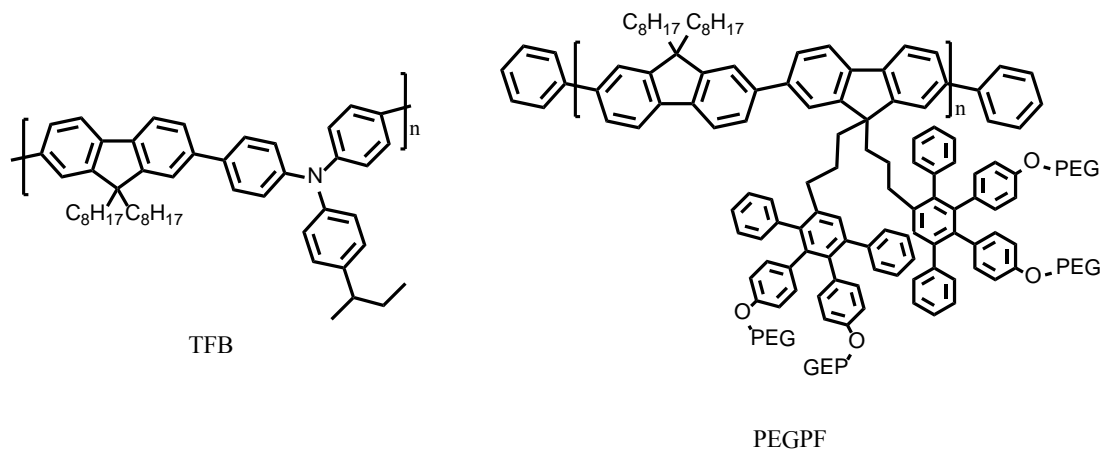


Figure 4-30: Chemical structures of charge carrier transport materials TFB (left) and PEGPF (right).

#### 4.5.2 Synthesis of PEGPF

Polar soluble polyfluorenes for orthogonal processing have been previously reported by Sax et al.<sup>[207]</sup> For this current work the synthesis for a new polar PF has been developed in which the PEGylation is carried out in the last step, thereby allowing to overcome the limitations to the applicability of this process and especially to the reproducibility of the molecular weight. Since the Suzuki polycondensation is a step-growth polymerization technique, the use of equimolar amounts of both monomers is crucial to obtain high conversion and thus high molecular weight polymers. However, the PEGylated monomer used for the synthesis of the previously reported polar soluble PF was polydisperse due to the intrinsic polydispersity of the PEG chains. Additionally, the monomers are waxy, hygroscopic substances and thus hard to handle. These issues limited the accuracy of the initial weight and often led to low molecular weight polymers. By using the synthetic route presented in the current work, it was possible to lower the reaction time of the Suzuki polycondensation considerably to less than 1 day in comparison to the very slowly proceeding process (reaction time  $\sim$  6 days) reported earlier.<sup>[207]</sup>

In this new approach, a polar soluble PF has been developed at the MPI where the PEG chains were introduced in a polymer-analogous reaction (c.f., Figure 4-31). **Monomer A** was synthesized in a microwave assisted Diels-Alder cycloaddition from an alkynyl functionalized 2,7-dibromofluorene (**Alkynyl-FIn**) and the doubly methoxy functionalized tetraphenylcyclopentadienone **CP(OMe)<sub>2</sub>**. The **comonomer B** was necessary to lower the steric hindrance during the polymerization and to prevent aggregation on a later stage. The alternating copolymer **MeO-PF** was obtained by Suzuki polycondensation and subsequent endcapping. The molecular weight was reproducible ( $M_n > 15,000$  g/mol). In the next step, the methoxy groups were cleaved using boron tribromide (BBR<sub>3</sub>) solution yielding a THF soluble hydroxyl functionalized polyfluorene **OH-PF** which can be used for further functionalization (e.g. grafting). **OH-PF** was PEGylated using PEG750-Br (endcapped with methoxy and bromine). The degree of functionalization was proven by <sup>1</sup>H-NMR to be nearly quantitative (not shown). The number average molecular weight exceeded 48,000 g/mol, depending on the size of the core PF. PEGPF proved to be soluble in methanol and ethanol in addition to the typical solvents used for PF. Unlike most amphiphilic PF, PEGPF does not aggregate in solution in concentrations as high as 1 mg/ml over at least a month. A low tendency to aggregate is a crucial property for thin film device applications.

Hence, based on its good solubility in methanol and ethanol and due to its film formation properties, PEGPF presents an attractive material for solution processed multilayer PLEDs. In particular, without

re-dissolving it facilitates the deposition of an additional layer by spin-coating on top of a preceding material like PPyTTPA which is soluble primarily in non-polar solvents.

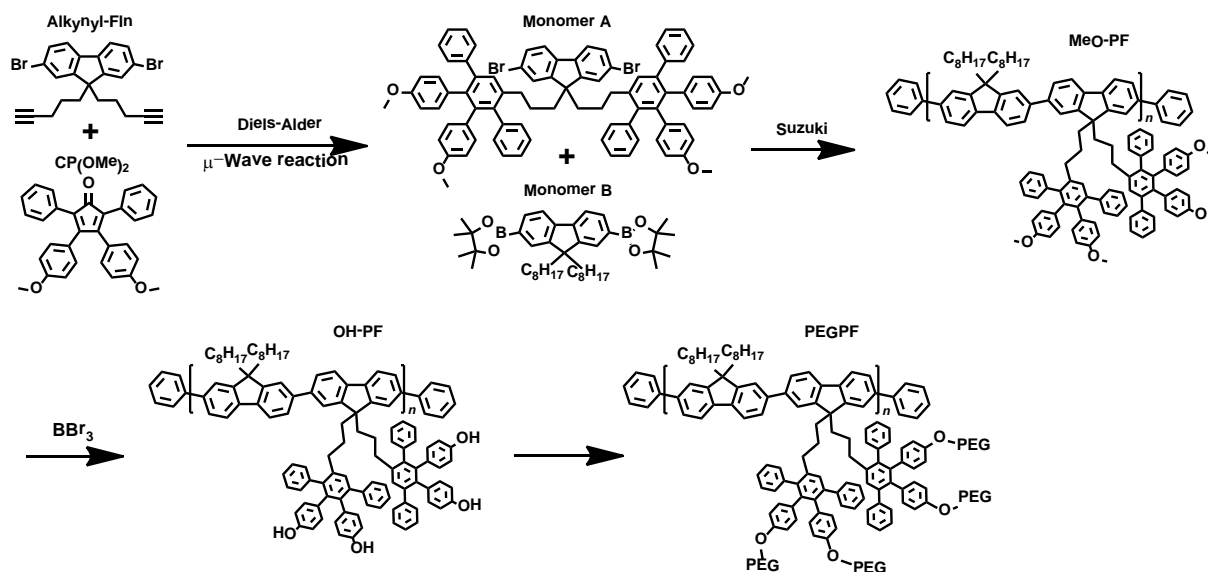


Figure 4-31: Synthesis scheme for the polar soluble PEGPF.

#### 4.5.3 Optical and Morphological Characteristics of PEGPF

Absorption and photoluminescence spectra of PEGPF in MeOH solution and in thin film are depicted in Figure 4-32. It can be observed that the material exhibits a main absorption feature in the range between 325 nm to 425 nm with peak maxima around 400 nm for solution as well as in the solid state corresponding to a  $\pi$ - $\pi^*$  transition in the material. A structured molecular emission feature that is typical for polyfluorene<sup>[156]</sup> ranging from 400 nm to approximately 520 nm characterizes the PL in both states. The peak maximum for the thin film can be found at 425 nm and in MeOH solution only a small solvatochromic shift occurs resulting in a PL maximum of 423 nm, which means a moderate Stokes shift of ca. 25 nm. Vibrational progressions of the emission spectra can be found at 448 nm and around 480 nm. A PLQY of 78% could be determined for PEGPF in MeOH.

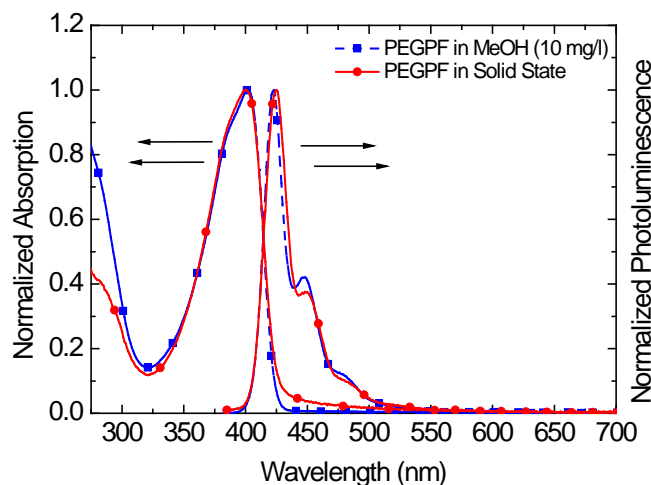


Figure 4-32: UV-Visible absorption and photoluminescence emission spectra of PEGPF in MeOH (dashed blue line with boxes) and in thin solid film (red line with circles).



To assess in general the suitability of PEGPF used as a functional layer in a PLED assembly the film formation property, i.e., the surface morphology was investigated by AFM. Figure 4-33 displays height images of a PEGPF film on PEDOT:PSS substrates. As can be observed the polymer films form a homogenous and flat surface without any pinholes or protruding spikes yielding a very low roughness of only  $R_q = 0.60$  nm. Thus, PEGPF in general meets the prerequisites for an application in multi-layered PLEDs. Its applicability in the particular assembly, however, needs to be investigated separately.

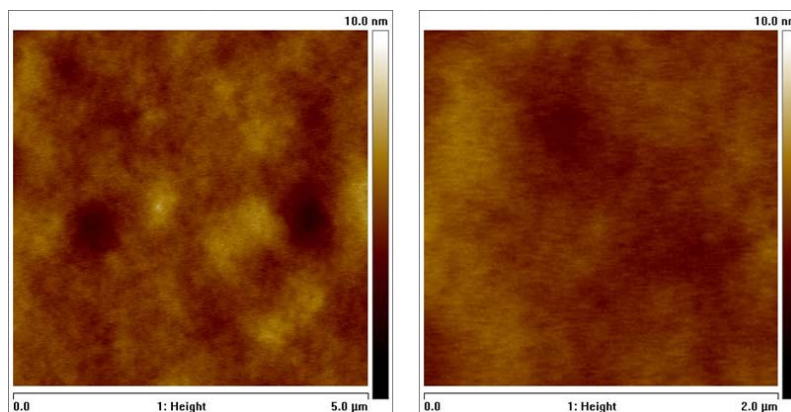


Figure 4-33: AFM height images (left:  $5\ \mu\text{m} \times 5\ \mu\text{m}$ , right:  $2\ \mu\text{m} \times 2\ \mu\text{m}$ ) of a PEGPF thin film. The morphology images show a homogenous flat film surface with a RMS-roughness of  $R_q=0.60$  nm.

#### 4.5.4 Optical and Morphological Characteristics of TFB

TFB is a well-established polymer comprising a backbone formed by a fluorene unit copolymerized with a triphenylamine group. TFB was presented already in 1999 by Redecker et al.<sup>[248]</sup> as a high mobility hole transport polymer combining the charge transport properties of arylamine glasses with the processability of a polymer. Kim et al. further reported that TFB forms smooth and insoluble layers with a thickness of only a few nanometers, when heated at temperatures between 180-200°C and spin-rinsed afterwards.<sup>[246]</sup> These properties make TFB an extraordinary useful candidate for hole-injecting layers in solution-processed heterojunction PLEDs.<sup>[147,255,256]</sup>

The absorption and photoluminescence characteristics of TFB are depicted in Figure 4-34. As can be seen the absorption is characterized by a broad peak in the UV-region of the spectrum with peak maxima at 386 nm in TOL solution and in thin film coated from this solution. The PL spectra consist of an only slightly structured emission feature with maxima at 432 nm in solution and 436 nm in thin film. A small shoulder can be detected around 460 nm for both emission spectra. In comparison to typical polyfluorenes, as for example PEGPF, TFB shows a stronger Stokes shift of ca. 36 nm, which is a result from the copolymerization with triphenylamine group and the thereby decreased planarity of the conjugated segments in the polymer. Even higher shifts can be found for fluorene-triphenylamine copolymers with two or more of the hole transporting groups.<sup>[257]</sup>

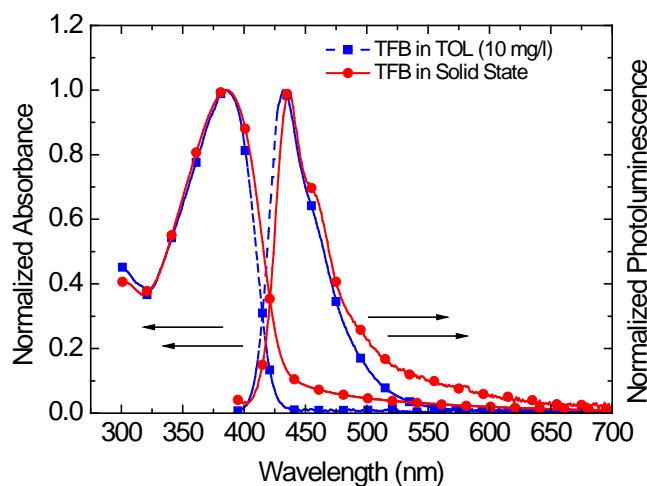


Figure 4-34: UV-Visible absorption and photoluminescence emission spectra of TFB in TOL (dashed blue line with boxes) and in thin solid film (red line with circles).

Figure 4-35 shows AFM height images of representative surface areas of TFB thin films on PEDOT:PSS. It can be observed that TFB obviously develops homogeneously flat films. No contaminations, pinholes or spikes, respectively, can be detected in the scanning area and a roughness of  $R_q = 0.40$  was measured for the TFB film.

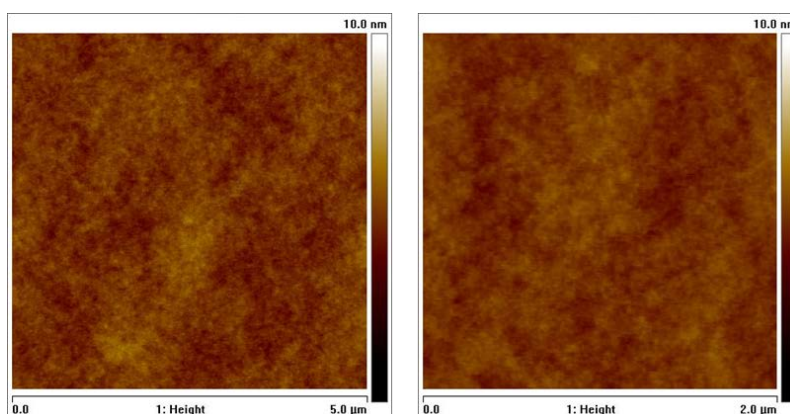
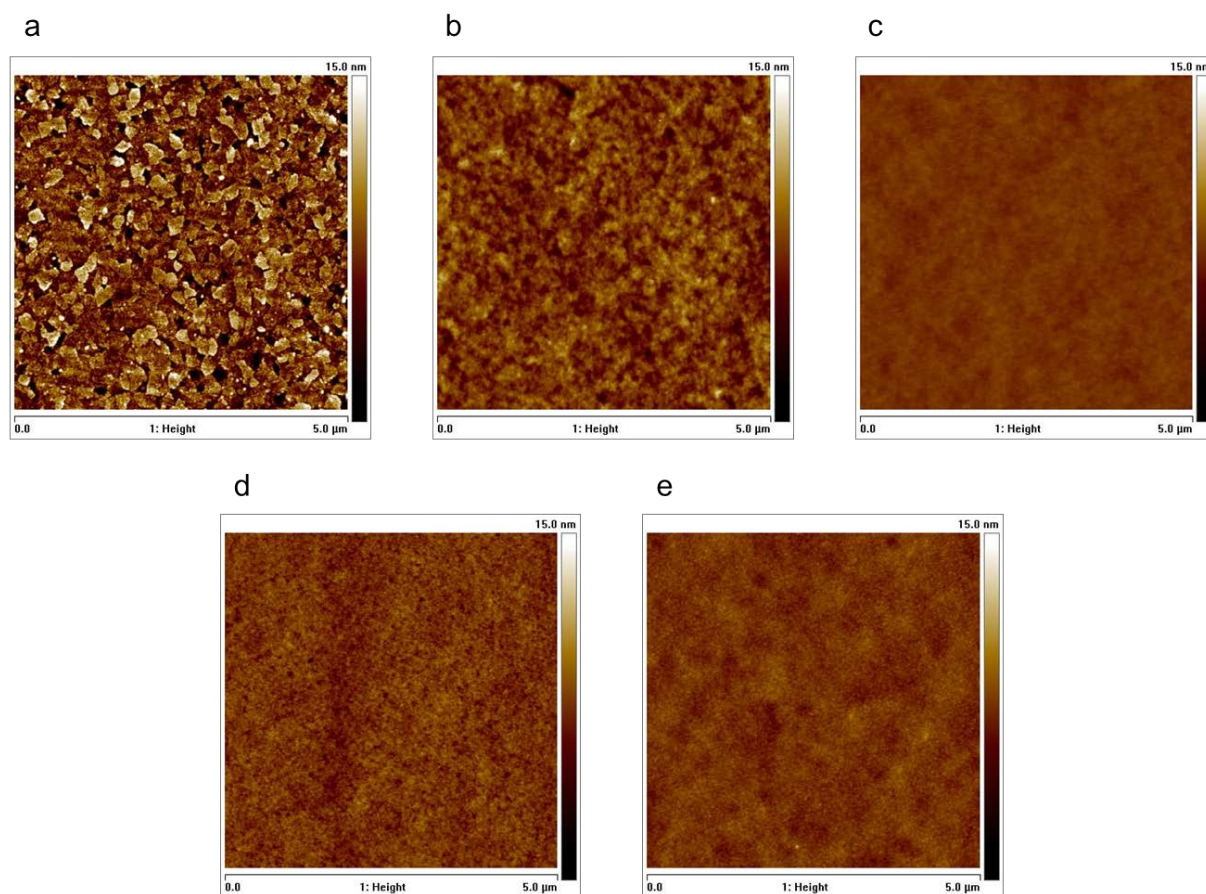


Figure 4-35: AFM height images (left:  $5\ \mu\text{m} \times 5\ \mu\text{m}$ , right:  $2\ \mu\text{m} \times 2\ \mu\text{m}$ ) of a TFB thin film on PEDOT:PSS. The morphology images show a homogeneous flat film surface with a RMS-roughness of  $R_q = 0.40$  nm.

#### 4.5.5 Morphological Stability of Solution Processed Polymeric Multilayers

As mentioned in the introduction of this chapter, the realization of multilayer assemblies by thermal treatment or by the utilization of orthogonal solvents has already been presented in previous work.<sup>[245,246]</sup> Nonetheless, especially for the latter approach the feasibility of the particular processes with respect to film formation and layer stability upon sequential deposition needs to be assessed assiduously. This is particularly valid when orthogonal solvents are used. While this approach enables the sequential deposition of materials without extensively dissolving an existing layer, adverse effects like reduced wettability can easily occur caused by the difference in the polarity of the layer and the coating solution.<sup>[258]</sup> Thus, the usability of TFB, PPyTPA and PEGPF in a multilayer assembly in terms of their film formation properties (film thickness and surface morphology) was investigated by AFM. As a first layer PEDOT:PSS, acting as a smoothing layer, was deposited on ITO-covered glass-substrates. As is shown in Figure 4-36a, ITO exhibits a rather rough and spiky surface with a RMS-

roughness of 2.6 nm which is strongly smoothed by PEDOT:PSS (Figure 4-36b) to 1.2 nm. In particular, no more distinct and sharp spikes could be detected. The second layer, comprising TFB, was spin cast onto PEDOT:PSS from a xylene solution and annealed at high temperature (200°C) afterwards. After cooling down, the sample was spin-rinsed with pure toluene to remove any soluble portion of TFB leading to a final thickness of the remaining TFB layer of 5 nm with a roughness of 0.3 nm (Figure 4-36c). Noteworthy, no signs of any changes or of polymer dissolution like holes or an increased roughness could be detected by AFM after further additionally conducted spin rinsing steps. This confirms the insolubility and stability of the thermally treated TFB layer. As a next step, a 50 nm PPy<sub>r</sub>TPA layer was deposited from a toluene solution. To provide good wettability, prior to the deposition of the next layer, PPy<sub>r</sub>TPA substrates were spin rinsed with pure methanol. AFM demonstrates that PPy<sub>r</sub>TPA exhibited excellent morphological stability and stayed completely intact upon this solvent treatment and a  $R_q$  of 0.8 nm was measured (Figure 4-36d). The topmost organic material PEGPF was deposited from methanol solution forming a smooth layer without wettability issues. The thickness of PEGPF was 10 nm and exhibited a  $R_q$  of 0.5 nm (Figure 4-36e). In summary, layer morphologies and stabilities, as confirmed by AFM, reveal that the described combination of a layer stabilizing hard-bake process and an orthogonal solvent approach is well suitable for the targeted solution processed multilayer assembly of TFB, PPy<sub>r</sub>TPA and PEGPF.



**Figure 4-36:** AFM surface topography images (5 x 5 μm) measured in tapping mode of (a) ITO, (b) PEDOT:PSS, (c) TFB, (d) PPy<sub>r</sub>/TPA and (e) PEGPF. The RMS-surface roughness amounted to 2.6, 1.2, 0.3, 0.8 and 0.5 nm.

#### 4.5.6 Energy-Level Alignment across the Multilayer Assembly

Efficient charge carrier injection into as well as their confinement within the EML, are decisive for the realization of efficient PLEDs. These properties strongly depend on the frontier energy level offsets at the interfaces. Hence, in order to provide a first estimate for the interface energetics UPS measurements of TFB, PPyrTPA and PEGPF single layers, respectively, on PEDOT:PSS were performed. Valence region UPS and SECO spectra for the particular materials are depicted in Figure 4-37. The photoemission onset of the respective valence bands were determined to be 0.8 eV below the Fermi level for TFB, 1.0 eV for PPyrTPA and 1.2 eV for PEGPF. The corresponding  $\phi$  values were 4.5 eV, 4.6 eV and 4.6 eV, respectively, and thus the ionization energies could be evaluated to 5.3 eV for TFB, 5.6 eV for PPyrTPA and 5.8 eV for PEGPF.

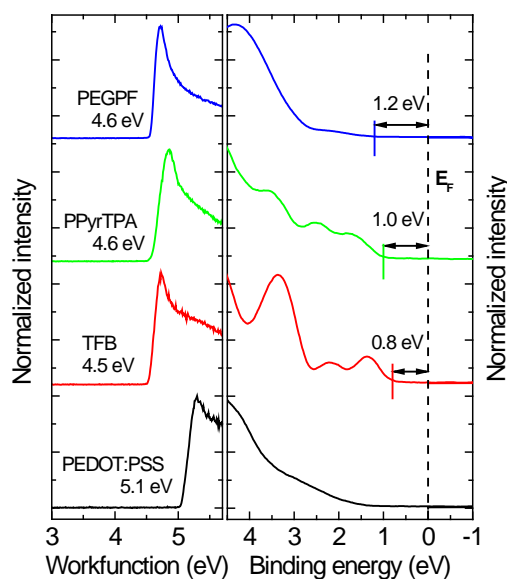


**Figure 4-37:** SECO- (left) and Valence region UPS- spectra (right) of PEDOT:PSS and of TFB, PPyrTPA and PEGPF on PEDOT:PSS.

A diagram for the energy levels across the PEDOT:PSS/polymer interfaces is depicted schematically in Figure 4-38. It shows the valence band maximum (VBM) and conduction band minimum (CBM) levels as well as  $\phi$  values for the particular materials. Values for the electron affinity can be approximated by  $EA = IE - E_g$ , where  $E_g$  denotes the energy of the optical bandgap derived from the onsets of the particular absorption spectra. It can be observed from Figure 4-37 and Figure 4-38 that strong shifts of the vacuum level  $\Delta_{vac}$  develop between the semiconducting polymer layers and PEDOT:PSS. The most distinct shift occurs between PEDOT:PSS and TFB where  $\Delta_{vac}$  is -0.6 eV. According to Hwang et al. interface dipoles as well as band bending account for this shift.<sup>[259]</sup> Likewise shifts of  $\Delta_{vac} = -0.5$  eV were observed between PEDOT:PSS and PPyrTPA as well as between PEDOT:PSS and PEGPF, which also are assigned to interface dipoles. Taking PPyrTPA as an example, the in general merely moderate performance of the single layer PLEDs with respect to luminous efficiency and maximum brightness clearly can be explained. On the one hand there exist significant charge injecting barriers for holes at the PEDOT:PSS/PPyrTPA interface as well as for electrons at the PPyrTPA/Ca interface. While the latter is in the range of 0.1 eV ( $\phi_{Ca} = 2.9$  eV), the blocking barrier at the anodes side amounts to 0.5 eV, which both clearly hinder the injection of charge carriers. Moreover, the discrepancy in the dimension of the barriers clearly leads to imbalanced charge carrier injection and thus to limited exciton formation probability in the EML due to disproportionate charge carrier densities in the device. In addition, from Figure 4-38 it can be deduced

that for single layer devices no blocking barriers exist at the respective interfaces that are able to limit the charge extraction from the EML. As a consequence, excess charge carriers are able to “spill” out of the EML without forming an exciton, i.e., without contributing to the light generation process. The combination of these aforementioned conditions finally leads to low luminance values and low luminous efficiency.

Yet, the location of the VBM and CBM for the single polymer layers on PEDOT:PSS as depicted in Figure 4-38 suggests that a favorable energy alignment can be achieved through a layer by layer assembly of TFB, PPyrTPA and PEGPF. In particular, the VBM of 5.3 eV for TFB in comparison to 5.6 eV for PPyrTPA is expected to lead to a significant reduction of the injection-limiting hole-blocking barrier at the anode’s side of PPyrTPA. In contrast, on the cathode’s side an energy barrier of 0.2 eV should be formed by PEGPF with an IE of 5.8 eV, which is expected to block the holes from flowing out of the PPyrTPA layer. Similar conditions are estimated from Figure 4-38 regarding electron injection from a Ca cathode. Since Ca exhibits a work function of approximately 2.9 eV an ohmic contact should be formed by PEGPF with an EA of 2.9 eV. Furthermore, a barrier of 0.1 eV between PEGPF and PPyrTPA is expected that needs to be overcome in order to inject electrons into PPyrTPA (EA = 2.8 eV). In contrast to that, a strong barrier inhibiting electron extraction should be present at the PPyrTPA/TFB interface due to the low EA of 2.3 eV for the latter polymer.

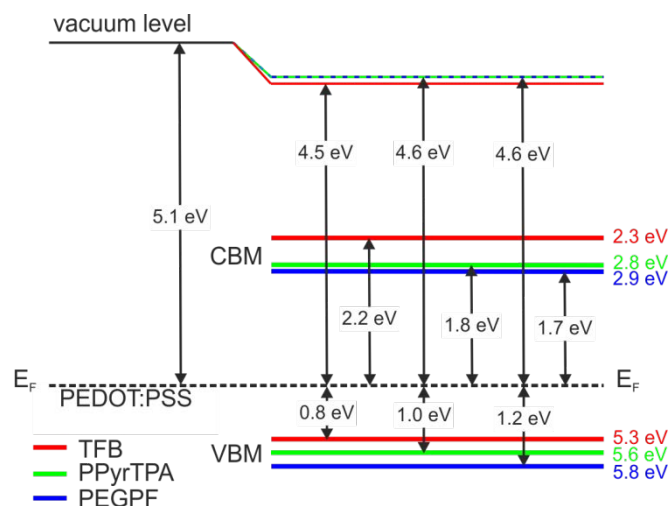


**Figure 4-38: Interface energetics for PEDOT:PSS/TFB, PEDOT:PSS/PPyrTPA and PEDOT:PSS/PEGPF interfaces.**

Yet, while this first approximation suggests a favorable energy level alignment for a triple layer assembly from the presented materials, UPS measurements were conducted layer by layer in order to assess the actual interface energetics of the PEDOT:PSS/TFB/PPyrTPA/PEGPF assembly fabricated analogously as described in chapter 4.5.5. Valence region UPS and secondary electron cutoff spectra to measure the work function and interface dipoles are depicted in Figure 4-39. In this assembly the photoemission onset of the respective valence bands were evaluated to be 0.8 eV below  $E_F$  for TFB, 1.0 eV for PPyrTPA and 1.5 eV for PEGPF. The corresponding  $\phi$  values could be determined to 4.5 eV, 4.7 eV and 4.4 eV, respectively. Consequently, the ionization energies were 5.3 eV for TFB, 5.7 eV for PPyrTPA and 5.9 eV for PEGPF. The valence region spectra of TFB on PEDOT:PSS are clearly different to those achieved for the conducting polymer. While PEDOT:PSS exhibits one broad feature tailing towards lower binding energies, TFB shows three minor peaks between 0.8 eV and 4 eV. The respective UPS spectra of PPyrTPA on TFB show no sign of TFB features and are in good accordance with the data presented in chapter 4.4.7. The deposition of PEGPF finally suppresses all PPyrTPA features and one broad peak exhibiting a distinct tail towards lower binding energies is observed.

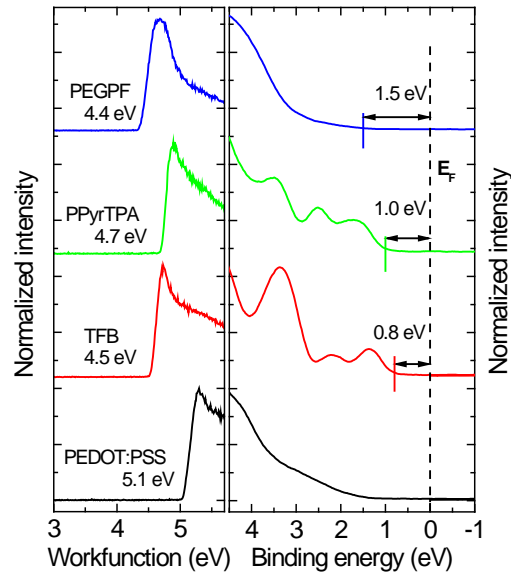


**Figure 4-39:** SECO- (left) and valence region UPS- spectra (right) of PEDOT:PSS, TFB, PPy/TPA and of PEGPF in a layer by layer assembly.

A scheme of the energy level alignment across the PEDOT:PSS/TFB/PPyrTPA/PEGPF interfaces is depicted in Figure 4-40, displaying again VBM and CBM levels as well as  $\phi$ , IE and estimated EA values. As can be seen in Figure 4-39 and Figure 4-40 shifts of the vacuum level occur between the different layers. Again a shift of  $\Delta_{\text{vac}} = -0.6$  eV develops between PEDOT:PSS and TFB caused by already mentioned interface dipoles. In addition,  $\Delta_{\text{vac}} = 0.2$  eV between TFB and PPyTPA, and  $\Delta_{\text{vac}} = -0.3$  eV at the PPyTPA/PEGPF-interface were observed, which are most likely due to a preferential orientation of intra-molecular dipoles at the interfaces.<sup>[260]</sup> From Figure 4-40 it can be deduced that the selected assembly provides the necessary prerequisites for charge carrier confinement in the emissive layer. Between TFB and PPyTPA as well as between PPyTPA and PEGPF the estimated CBM levels have an offset of 0.4 eV, which are the offsets relevant for electron injection from PEGPF into the EML and extraction from the EML into TFB. The offset for injecting holes from TFB into PPyTPA (0.2 eV) however is smaller than the one for extracting them to PEGPF (0.4 eV). As a consequence of these barriers charge carrier extraction (electrons and holes) from the emitting layer is expected to be significantly constrained compared to PPyTPA-single layer devices.

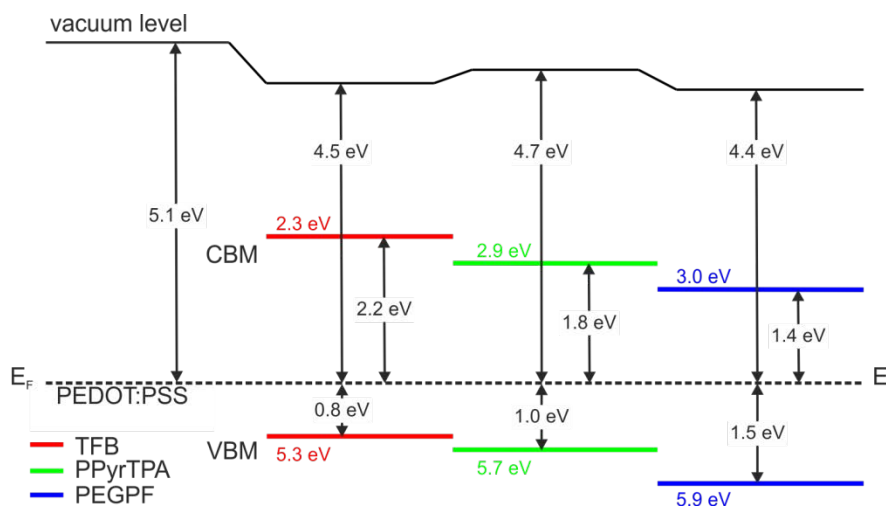


**Figure 4-40:** Energy level diagram for a PEDOT:PSS/TFB/PPyrTPA/PEGPF multilayer PLED stack.

XPS spectra of the layers, as depicted in Figure 4-41, further corroborate the AFM-results. Complete coverage can be concluded from the fact that elemental core levels specific to the underlying layers were strongly attenuated or vanished completely upon overlayer deposition.

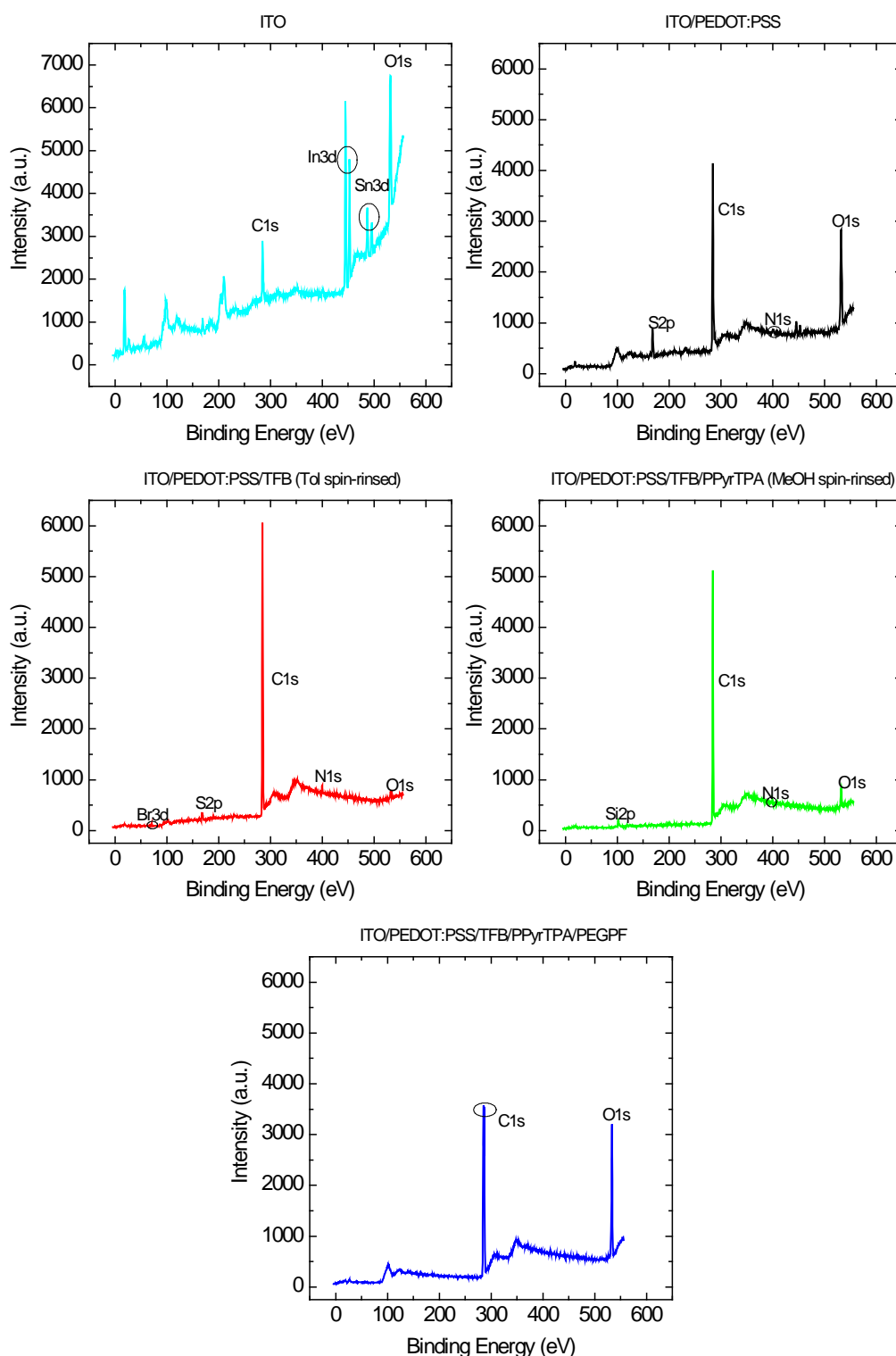


**Figure 4-41: Layer by layer XPS spectra of the particular materials in the ITO/PEDOT:PSS/TFB/PPyTPA/PEGPF multilayer assembly. The core levels specific for the respective materials are highlighted.**

In particular, the double peak signals of the indium (In3d) and tin (Sn3d) core levels vanish completely upon PEDOT:PSS deposition on ITO. Instead, strong signals stemming from sulfur (S2p) and carbon

(C1s) can be detected. As expected the oxygen (O1s) core level emission is strong for both materials. After the deposition of TFB the sulfur and oxygen related signals are strongly attenuated. In exchange, nitrogen (N1s) and bromine (Br3d) peaks show up in the spectrum. While the N1s peak originates from the nitrogen atom in the triphenylamine group of the polymer the bromine peak could be identified as remainder from the TFB synthesis. The Br3d double peak vanished upon PPyTPA deposition. The nitrogen related peak gets attenuated as well, which is understandable due to the much lower amount of TPA groups present in the pyrene-based polymer. Furthermore, the development of a silicon feature (Si2p) and an enhancement of the O1s peak can be observed in the spectrum. These peaks are assumed to be caused by contaminations from silicone grease used for the glassware during the synthesis of PPyTPA. The XPS-spectrum of PEGPF finally shows just peaks from carbon and oxygen. In contrast to the other materials, the carbon peak actually constitutes a distinct double peak. This double feature is assigned to a chemical shift due to different binding energies between the carbon-carbon and carbon-oxygen bonds in the polymer (Figure 4-42).<sup>[261]</sup>

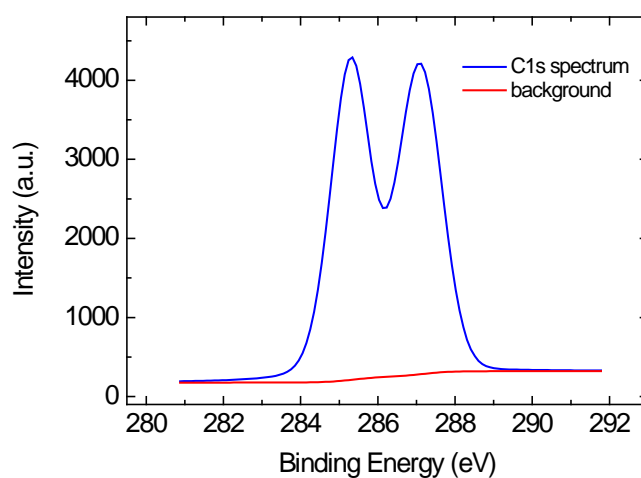


**Figure 4-42:** Development of a C1s double peak at 285.3 eV and 287.1 eV in the XPS-spectrum of PEGPF due to the different binding energies of carbon-carbon and carbon-oxygen bonds in the polymer.

#### 4.5.7 Electroluminescent Properties and Device Performance of Single- and Multilayer PLEDs

For the evaluation of the electroluminescent properties and efficiencies of TFB, PEGPF and PPyTPA in single layer PLEDs, devices were fabricated in the standard sandwich structure ITO/PEDOT:PSS/polymer/Ca/Al. The thickness of the emitting layer was 50 nm for all devices and was optimized for PPyTPA with respect to its luminous efficiency. All relevant device parameters [EL-emission onset, maximum luminance and luminous efficiency (LE)] are listed in Table 2. Figure 4-43 presents the current density-voltage-luminescence characteristics and EL-emission spectra (insets of Figure 4-43) for the single layer devices. The maximum luminance can be determined to 157 cd/m<sup>2</sup> in the case of TFB, 1870 cd/m<sup>2</sup> for PEGPF and 2924 cd/m<sup>2</sup> for PPyTPA. The PLEDs showed a LE between 0.02 cd/A and 0.27 cd/A and exhibited deep blue emission, as typical for these materials. In detail, the EL spectra of TFB and PEGPF (insets of Figure 4-43, top) both show a slightly structured molecular emission between 410 nm and 575 nm with their peak maxima at 432 nm and at 420 nm, respectively. PPyTPA exhibits a structureless molecular emission peak between 430 nm and 550 nm with a maximum at 462 nm (inset of Figure 4-43 bottom). These spectra correspond to CIE1931 coordinates of  $x = 0.17$ ,  $y = 0.10$  for TFB,  $x = 0.16$ ,  $y = 0.15$  for PEGPF and  $x = 0.16$ ,  $y = 0.20$  for



PPyrTPA. The EL-spectra are identical, in terms of shape and position, to the photoluminescence spectra of the particular materials in solid state (c.f. chapters 4.4.4, 4.5.3 and 4.5.4). In addition, no difference in the PEGPF emission characteristics was detected, e.g., caused by the polar PEG-sidechains, compared to polyfluorene with non-polar side-chains.<sup>[156]</sup>

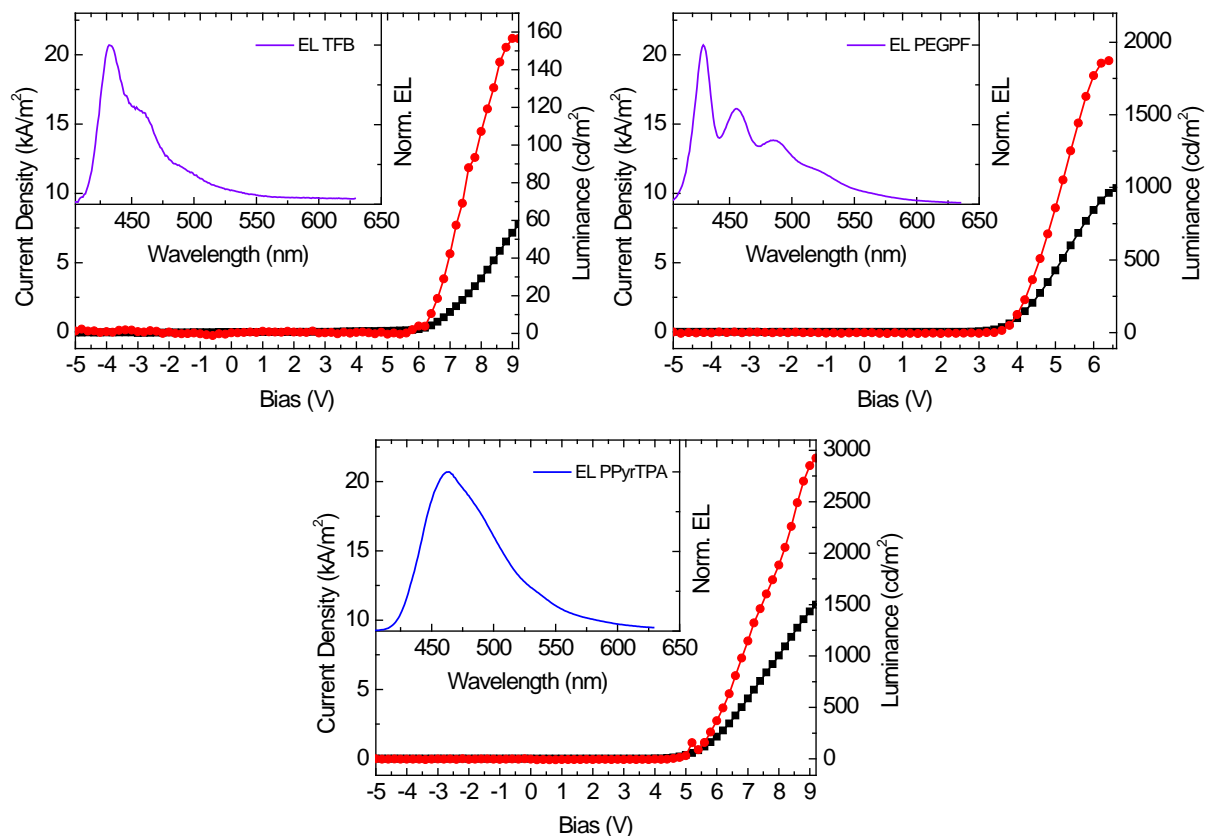


**Figure 4-43:** Current density (line with squares) / luminance (line with circles) as a function of the bias voltage in an ITO/PEDOT:PSS/TFB/Ca/Al device (top left), an ITO/PEDOT:PSS/PEGPF/Ca/Al device (top right) and an ITO/PEDOT:PSS/PPyrTPA/Ca/Al device (bottom). The insets show the electroluminescence emission spectra of the same devices at a current density of  $1.0 \text{ kA/m}^2$  and at a bias around 6.8 V, 4 V and 5.7 V, respectively.

Figure 4-44 shows current density dependent EL spectra of the ITO/PEDOT:PSS/polymer/Ca/Al devices. The figures display once more the exceptional spectral stability of the pyrene based material under operation. In contrast to the fluorene-type polymer TFB and PEGPF, which both show an increase of the vibrational features or at higher wavelengths in their EL emission at higher current densities, the emission characteristics of PPyrTPA stays perfectly the same up to current densities in the range of  $5 \text{ kA/m}^2$ .

Yet, the performance of all single layer devices was moderate. An unfavorable energy level alignment, forming injection inhibiting barriers for charge carriers of up to 0.7 eV at the PEDOT:PSS/EML-interface (c.f. Figure 4-38) and/or at the EML/Ca-interface, is identified as the cause for the low efficiencies. These findings display explicitly that, in order to realize bright and highly efficient PLEDs, the device assembly has to be adapted in a proper way with respect to the energy levels of the materials.

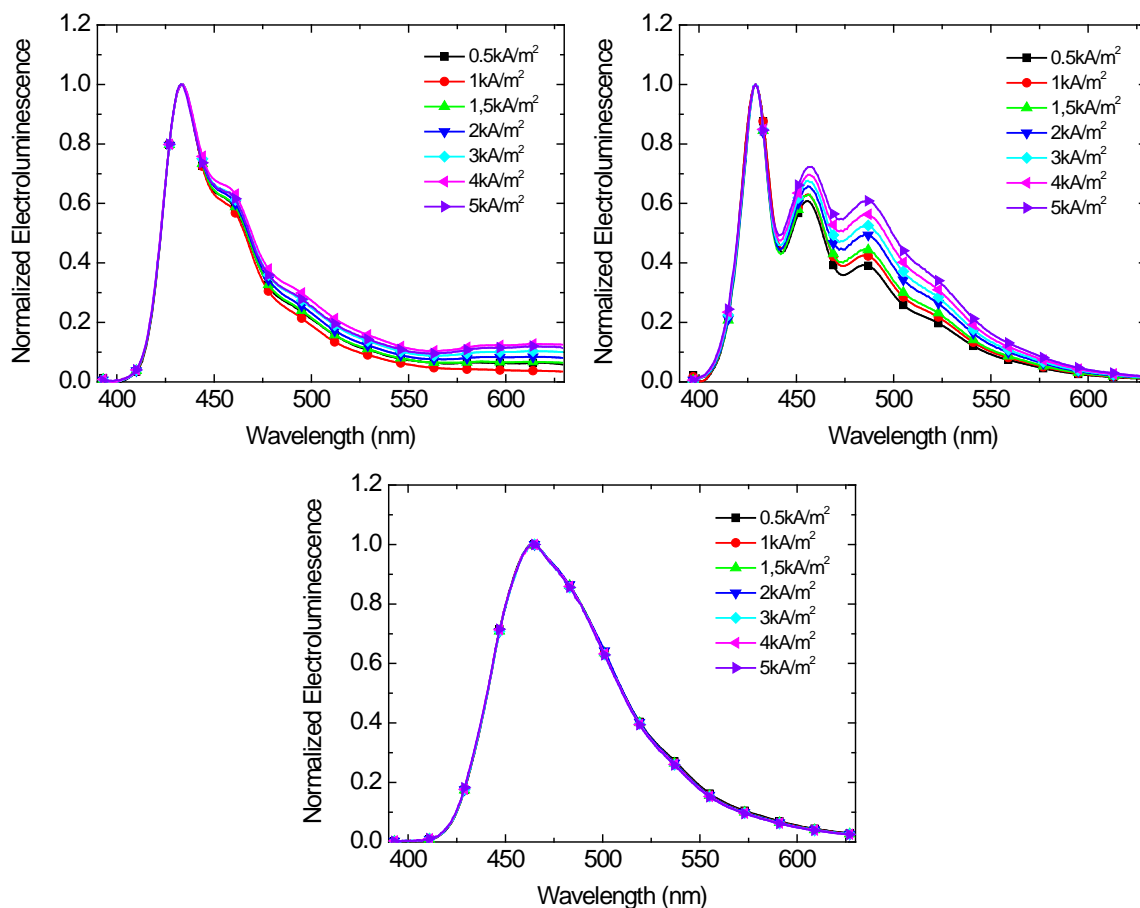


**Figure 4-44:** Current density dependent EL-spectra of an ITO/PEDOT:PSS/TFB/Ca/Al device (top left), an ITO/PEDOT:PSS/PEGPF/Ca/Al device (top right) and an ITO/PEDOT:PSS/PPyrTPA/Ca/Al device (bottom).

Figure 4-45 compares J-V-L-characteristics of a single layer, two bilayer and a triple-layer device using PPyTPA as emitting material. Bilayer devices were fabricated in the following sandwich structures: ITO/PEDOT:PSS/PPyrTPA/PEGPF/Ca/Al and ITO/PEDOT:PSS/TFB/PPyrTPA/Ca/Al. The triple layer device comprised an ITO/PEDOT:PSS/TFB/PPyrTPA/PEGPF/Ca/Al assembly (Figure 4-47). All pyrene-based devices exhibited a deep-blue electroluminescence emission achieving maximum luminance values of  $2924 \text{ cd/m}^2$  for the single layer device,  $4269 \text{ cd/m}^2$  and  $7817 \text{ cd/m}^2$  for the for the bilayer devices utilizing PEGPF or TFB as transport layers, respectively. For the triple-layer PLED a maximum luminance of  $16540 \text{ cd/m}^2$  could be measured. Compared to the PPyTPA-single layer device these results mean a more than 1.4-fold, 2.5-fold and more than 5.6-fold enhancement, respectively, of the maximum luminance for the bilayer devices and for the triple-layer PLED. The enhancement of the devices' overall performance also reflected itself in the reduction of the onset voltage from 4.4 V in the single layer PLED to 3.9 V for the triple-layer assembly. In addition, through the utilization of PEGPF as ETL in a bilayer device the maximum LE increased from  $0.27 \text{ cd/A}$  to  $0.34 \text{ cd/A}$ . Likewise, by the application of TFB as HTL into the assembly the maximum LE could be raised from  $0.27 \text{ cd/A}$  to  $0.43 \text{ cd/A}$ . The insertion of both transporting materials in the triple-layer device led to a maximum luminous efficiency of  $1.42 \text{ cd/A}$ .

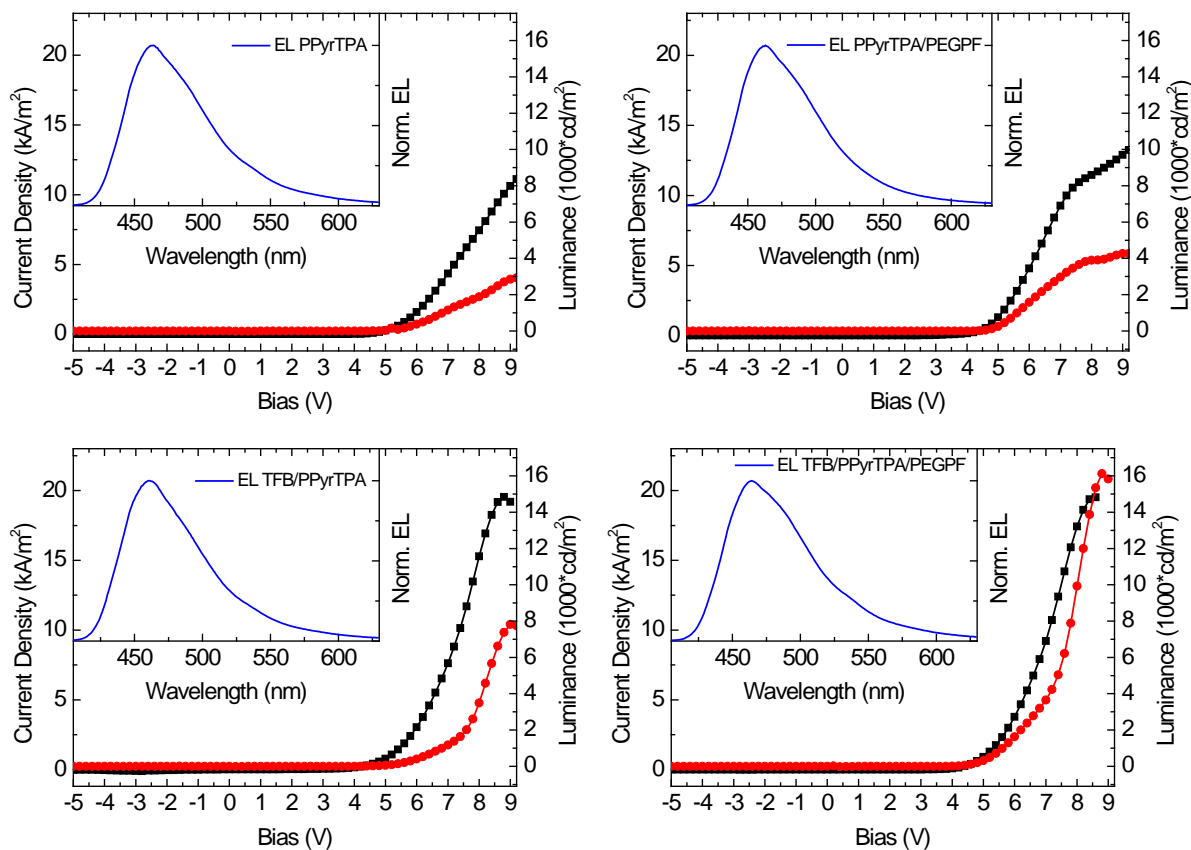


**Figure 4-45:** Current density (line with squares) / luminance (line with circles) as a function of the bias voltage in an ITO/PEDOT:PSS/PPyrTPA/Ca/Al device (top left), an ITO/PEDOT:PSS/PPyrTPA/PEGPF/Ca/Al device (top right), an ITO/PEDOT:PSS/TFB/PPyrTPA/Ca/Al device (bottom left) and an ITO/PEDOT:PSS/TFB/PPyrTPA/PEGPF/Ca/Al device (bottom right). The insets show the electroluminescence emission spectra of the same devices at a current density of 1.0 kA/m<sup>2</sup> and at a bias of 5.7 V, 4.9 V, 5.2 V and 5.1 V, respectively.

EL-spectra of the multilayer (bilayer- and triple-layer) PLEDs at a current density of 1.0 kA/m<sup>2</sup> and depending on the current density are presented in the insets of Figure 4-45 and in Figure 4-46, respectively. All these spectra show a deep-blue emission in the same range as PPyrTPA single layer devices [CIE1931:  $x = 0.153$ ,  $y = 0.188$  (PPyrTPA/PEGPF);  $x = 0.157$ ,  $y = 0.174$  (TFB/PPyrTPA);  $x = 0.163$ ,  $y = 0.216$  (TFB/PPyrTPA/PEGPF)]. More importantly, a comparison of these emission characteristics to the EL-spectra of the TFB and PEGPF single layer PLEDs (insets of Figure 4-43 and Figure 4-44) shows that no EL contribution of the transporting materials can be detected which evidences that the EL-emission stems exclusively from PPyrTPA. These results (summarized in Table 2) demonstrate the improvement of PPyrTPA-based PLEDs by the application of the triple-layer assembly. The following causes are responsible for the enhancement of the PLEDs performance. For the PPyrTPA/PEGPF PLED UPS results revealed that the incorporation of PEGPF leads to the generation of a barrier for holes at the cathode side of PPyrTPA. Due to the VBM offset between PPyrTPA and PEGPF the extraction of holes from the EML is hindered significantly. In case of the TFB/PPyrTPA bilayer device firstly the insertion of TFB leads to a stepwise reduction of the hole injection barrier between the Fermi-level of PEDOT:PSS and the VBM of PPyrTPA enabling an improved hole injection. Secondly, as shown by the UPS measurements, a pronounced energy barrier is formed between the PPyrTPA and TFB CBM levels, blocking electrons at that interface and inhibiting their extraction from the EML. The triple-layer PLED combines the conditions of both bilayer assemblies. The formation of mentioned energy barriers consequently leads to an enhanced charge carrier density within the EML, which induces an increased exciton formation probability

within the EML resulting in higher luminance and luminous efficiency values for both bilayer PLEDs and even more for the triple-layer device. Please note that, as reported by Kim et al.,<sup>[262]</sup> oxidative doping of the emissive layer at the PEDOT:PSS/EML-interface is able to significantly reduce the luminescence efficiency of a device. Hence it is very likely that the spatial separation of PEDOT:PSS and PPyTPA by TFB plays a decisive role for the enhancement of the LE in the respective bilayer and the triple-layer devices.

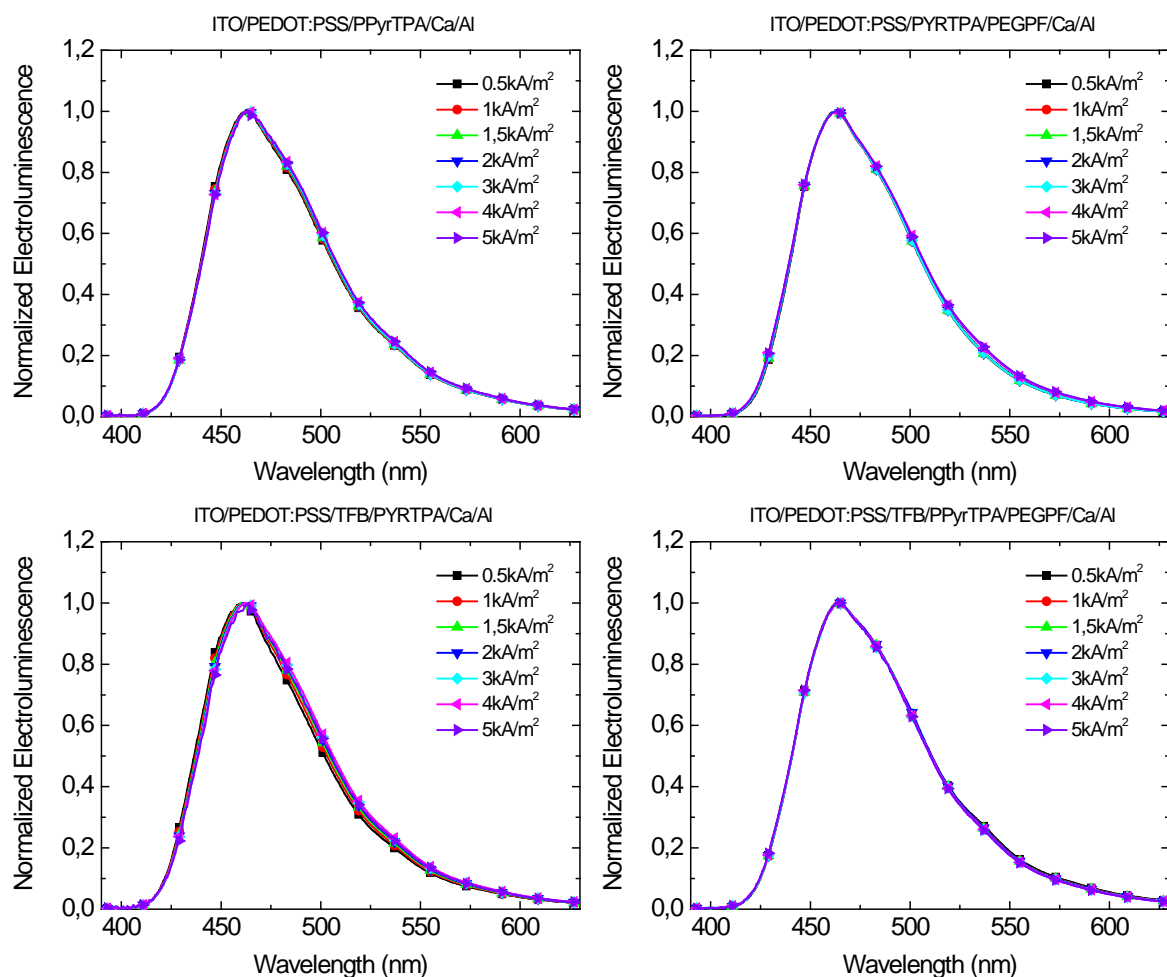


**Figure 4-46:** Current density dependent EL spectra of an ITO/PEDOT:PSS/PPyrTPA/Ca/Al device (top left), an ITO/PEDOT:PSS/PPyrTPA/PEGPF/Ca/Al device (top right), an ITO/PEDOT:PSS/TFB/PPyrTPA/Ca/Al device (bottom left) and an ITO/PEDOT:PSS/TFB/PPyrTPA/PEGPF/Ca/Al device (bottom right).

Compared to already reported results the utilization of TFB – stabilized by thermal treatment – as an HTL in PLEDs resulted in similar relative enhancement to the device performance as presented in previous work.<sup>[247]</sup> With respect to the luminous efficiency, its enhancement or the maximum luminance values, respectively, the performance of the triple layer device presented herein even superseded previous works using polar soluble polyfluorenes as ETL or atracene based polymers as blue emitters.<sup>[207][208]</sup> Yet, when comparing the presented LEs to the work published by Tseng et al.<sup>[263]</sup>, where a liquid buffer method was used, or even more important to the single layer devices presented by Huang et al.<sup>[264]</sup>, one has to state that the luminous efficiencies of the devices presented in this current work stayed moderate. Nevertheless, to the best of the authors knowledge the results presented in this chapter, are among the best for conceptual studies on blue emitting solution processed PLEDs with more than two polymer layers and realized without the utilization of any cross linking agents or buffer liquids.

For future work, however, at least an efficiency beyond 5 cd/A for blue emitting devices has to be the goal to aim for in order to exploit the advantages of solution based processing techniques. Therefore, improved hole and electron transport materials will be tested in a multilayer assembly in order to reach that goal with PPyrTPA as emitting material, whereby especially the performance limiting charge injection barriers between charge transport layers and the EML have to be reduced. Moreover, low work function metals like Li or Cs, their fluorides or carbonates, respectively, could be used as cathode materials, providing an ohmic contact and thus further enhance the device overall efficiency.

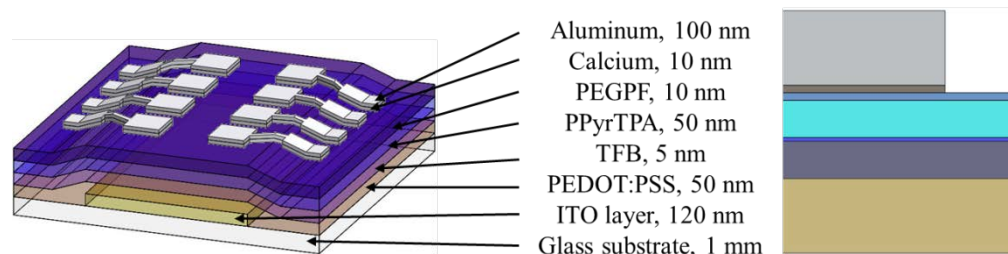


**Figure 4-47:** Scheme of the layer by layer assembly of the PLED-stack (left) and schematic cross section of the multilayer assembly without glass substrate (right). The relative thicknesses of the individual layers of the cross section are depicted true to scale.

**Table 2:** Electroluminescent characteristics of investigated single- and multilayer devices

organic layer geometry	onset voltage <sup>a</sup>	$\eta$ <sup>b</sup>	max. luminance	EL peak <sup>c</sup>	CIE 1931 coordinates <sup>c</sup>
	[V]	[cd/A]	[cd/m <sup>2</sup> ]	[nm]	x, y
TFB	5.7	0.02	157	432	0.173, 0.102
PEGPF	3.6	0.2	1872	429	0.164, 0.145
PPyrTPA	4.4	0.27	2924	462	0.159, 0.197
PPyrTPA/PEGPF	4.0	0.34	4269	463	0.153, 0.188
TFB/PPyrTPA	4.0	0.43	7817	460	0.157, 0.174
TFB/PPyrTPA/PEGPF	3.9	1.42	16540	465	0.163, 0.216

<sup>a</sup> voltage at a luminance of 1 cd/m<sup>2</sup>; <sup>b</sup> value of maximum efficiency; <sup>c</sup> at a current density of 1.0 kA/m<sup>2</sup>

#### 4.5.8 Conclusion

This chapter presented the realization of a fully solution processed triple-layer polymer light emitting diode. A successive deposition of the individual organic layers without a redissolving of an already present layer was realized by two strategies. Firstly, for the hole injection polymer a layer stabilization was achieved by thermal treatment making the material insoluble for non-polar solvents, thus enabling the deposition of the next, i.e. the emissive layer from a non-polar solution. Secondly, for the application of a third layer an orthogonal solvent approach was applied. For that purpose, a new polyfluorene polymer was designed, bearing polyethylene glycol side chains. The specific molecular design of this polymer ensures the polymer's solubility in polar solvents and facilitates electron injection into the device. Detailed investigations of the layers' surface morphology and electronic structure at the interfaces evidenced the feasibility as well as a favorable energy level alignment of the presented assembly. In detail, layer by layer AFM and XPS investigations of an assembly comprising the structure ITO/PEDOT:PSS/TFB/PPyrTPA/PEGPF revealed that the presented approach allows for a non-erosive sequential deposition of different polymers on top of each other. UPS measurements demonstrated that the chosen combination of materials exhibits a favorable energy-level alignment forming pronounced energy barriers for electrons and holes at the EML/HTL- and EML/ETL-interface, respectively. Thereby charge carrier confinement is generated within the emitting layer of a

triple-layer PLED. These findings resulted in solution-processed triple-layer PLEDs with deep blue electroluminescence emission from the pyrene-based emitting material and significantly enhanced efficiencies as a consequence of improved exciton formation probability in the EML. In particular, a maximum luminance of 16540 cd/m<sup>2</sup> and a maximum device efficiency of 1.42 cd/A was achieved, which constitutes a five-fold increase compared to single layer devices. In future effort will be made to test different hole- or electron transport polymers, in order to reduce charge injection limiting energy barriers between the EML and the transport layers and thus to further enhance the devices' luminous efficiency.

## 4.6 Blue Dendrimer Light-Emitting Diodes Based on Core, Shell and Surface-Optimized Dendrimers

*The content of this chapter is published in: Tianshi Qin, Wolfgang Wiedemair, Sebastian Nau, Roman Trattnig, Stefan Sax, Stefanie Winkler, Antje Vollmer, Norbert Koch, Martin Baumgarten, Emil J.W. List and Klaus Müllen; Journal of the American Chemical Society, 2011, 133, 1301-1303.*

The author of the thesis co-authored to this publication. Exclusive contributions by the author: surface morphology measurements, device assembling and device characterization. Collaborative contributions: Photophysical investigations, photoemission spectroscopy measurements, discussion of the overall results. T.Q. and E.J.W.L. have written the publication. The author of the thesis contributed significantly to the physics related results (photophysics, surface morphology and devices) thus in the current chapter the publication text was expanded essentially by the author.

### 4.6.1 Introduction

Reliable structure-to-property relations and exceptional stability have proven to be the key requirements for commercialization of organic semiconductor based applications.<sup>[265]</sup> In the ever ongoing material development effort conjugated dendrimers, alongside small molecules and conjugated polymers, constitute an increasingly important and promising class of macromolecules in optoelectronic applications.<sup>[266]</sup> In particular, employed as emissive layers in OLEDs, dendrimers exhibit remarkable properties with respect to operational stability, efficiency and adjustability. Recent progress in organic synthesis<sup>[267]</sup> facilitated the rational molecular design and 3-dimensional synthesis of dendrimers bearing different functional building blocks in the core, shell and on the surface.

Different from both, typical small molecules or linear conjugated polymers, the stepwise generation-by-generation growth of dendrimers thereby allows for the controlled synthesis of highly defined three-dimensional shape-persistent dendritic structures comprising designated molecular units with selected functions in defined positions, including their relative positions to each other.<sup>[144,268]</sup> Based on this approach of building a defined core-shell-surface dendrimer from individual molecular building blocks it is possible to optimize and fine tune the relevant dendrimer properties.<sup>[269]</sup> Thereby it is possible to realize design concepts particularly optimized for “dendrimer light emitting diodes” (DLEDs), such as PLQY, exact emission color, overall stability, solubility, and the ability of charge capture and injection in the periphery of the molecule. In particular, the use of such an approach in a dendrimer offers the following clear advantages: First, the utilization of appropriate donor – acceptor molecular units, exhibiting resonance energy transfer systems on the molecular level, has proven to be a very successful means in order to optimize the quantum yield of emissive molecules. Thus, the shape-persistence of a dendrimer provides perfect site-definition of individual chromophore units as required for implementing a resonance energy transfer donor-acceptor system to boost the quantum yield and control the emission color at the same time.<sup>[270]</sup> Secondly, at the same time the spherical nature of the molecule provides a steric shield for the central energy acceptor unit from which the emission will occur. Thereby, efficiently emitting chromophores, such as pyrene, can be utilized, which otherwise are hardly accessible since their molecular emission in the solid state is typically quenched or strongly red shifted due to intermolecular interaction and excimer formation, respectively.<sup>[271]</sup> Moreover, suitable redox-active moieties on the surface enhance selective charge capturing and optimized carrier injection from the electrode.<sup>[272]</sup> Finally, the strongly twisted benzene rings of the dendrimer scaffold provide high solubility without necessity of further side chain substitution.

Recently reported investigations on second generation blue light-emitting polytriphenylene dendrimers yield promising results with respect to brightness and electroluminescent efficiency.<sup>[273]</sup> Qin et al. thereby were able to present dendritic molecules synthesized *via* non-catalytic Diels-Alder cycloaddition, which illustrated its potential advantages in purification and fabrication of DLEDs. Based on the chemistry developed as well as from the attained spectroscopic results this basic study showed that the triphenylene (TP) unit can act as a building block for the shell of the dendrimer where light generation takes place.<sup>[273]</sup> However, due to the limited photoluminescence quantum yields of the triphenylene building units with 9% for the planar triphenylene<sup>[273,274]</sup> and only 4.8% for a phenyl substituted twisted non-planar TP,<sup>[273]</sup> additional molecular building blocks in a molecularly designed way are essential to improve this material concept. In order to overcome this limitation and to improve the overall efficiency of such polytriphenylene dendrimer based blue light-emitting materials, it is obligatory to incorporate other high PLQY blue light emitting chromophores into different positions of the dendrimer. In addition, the surface of the dendrimer needs to be functionalized in such a way that charge carrier trapping is optimized and charge transport to the molecular units in the shell is facilitated. With respect to PLQY the pyrene molecule is the most promising chromophore due to its high intrinsic PLQY of 65% and deep blue molecular emission.<sup>[275]</sup> However, its tendency towards strong intermolecular stacking always results in the already presented excimer emission (chapter 4.2.1), exciton quenching and poor processability.<sup>[276]</sup> These weaknesses could be relieved by encapsulating isolated pyrene molecules as the core with shape-persistent polyphenylene dendrons.<sup>[277]</sup> The present chapter of this current thesis presents a novel core-shell-surface multifunctional structure for dendrimers using a blue fluorescent pyrene core with triphenylene dendrons and triphenylamine surface groups. It is shown that efficient excitation energy transfer from the triphenylene shell to the pyrene core substantially enhances the quantum yield in solution and the solid state compared to dendrimers without a core emitter. In addition, TPA groups on the dendrimer surface facilitate the hole capturing and injection ability in device applications. Moreover, the presented dendritic architecture provides high solubility without necessity of further side chain substitution and yields thermally stable amorphous thin films with high glass transition temperatures. Thereby the omitting of alkyl chains as solubilizing side groups prevents the occurrence of degradation processes associated with such side chains.<sup>[268]</sup>

#### 4.6.2 Dendrimer Synthesis

A scheme of the dendrimer synthesis, which was conducted at the MPI, is depicted in Figure 4-48. According to a divergent synthesis strategy, starting from the easily available 1,3,6,8-tetraethynylpyrene,<sup>[278]</sup> two generations of polytriphenylene dendrimers [PYG1 (not shown) and PYG2] based on a fourfold substituted pyrene core have been prepared in high yields. In a next step, two second-generation dendrimers were synthesized with different functionalities: PYGCAP (Figure 4-48) with polyphenyl groups providing a shielding function to the dendrimer shell and core and PYGTPA (Figure 4-48), facilitating triphenylamine groups onto the surface of the dendrimer. The synthesis of the 1,3,6,8-tetraethynylpyrene core **1** followed an earlier published procedure.<sup>[278]</sup> The first-generation pyrene cored polytriphenylene dendrimer PYG1 was achieved from the Diels-Alder cycloaddition between 1,3,6,8-tetraethynylpyrene core **1** with excess of phencyclone **4** in refluxing *o*-xylene in 91% yield. The reaction of **1** with the AB<sub>2</sub> building unit 1,3-diphenyl-6,9-bis((triisopropylsilyl)-ethynyl)-cyclopentaphenanthrene **5** gave the first-generation dendrimer **6** in 91% yield, decorated with 8 triisopropylsilyl (TiPS) protected ethynyl groups. Quantitative desilylation of the TiPS protecting groups with TBAF resulted in the first-generation dendrimer **7** in 88% yield with activated ethynyl groups for further dendrimer growth. The following Diels-Alder cycloaddition of dendrimer **7** with



different termination units **4**, **8**, and **9** provided the second-generation dendrimer PYG2 in 84%, PYGTPA in 82% and PYGCAP in 81% yield, which are all highly soluble in common organic solvents (ca. 20 mg/ml in dichloromethane, THF and toluene).

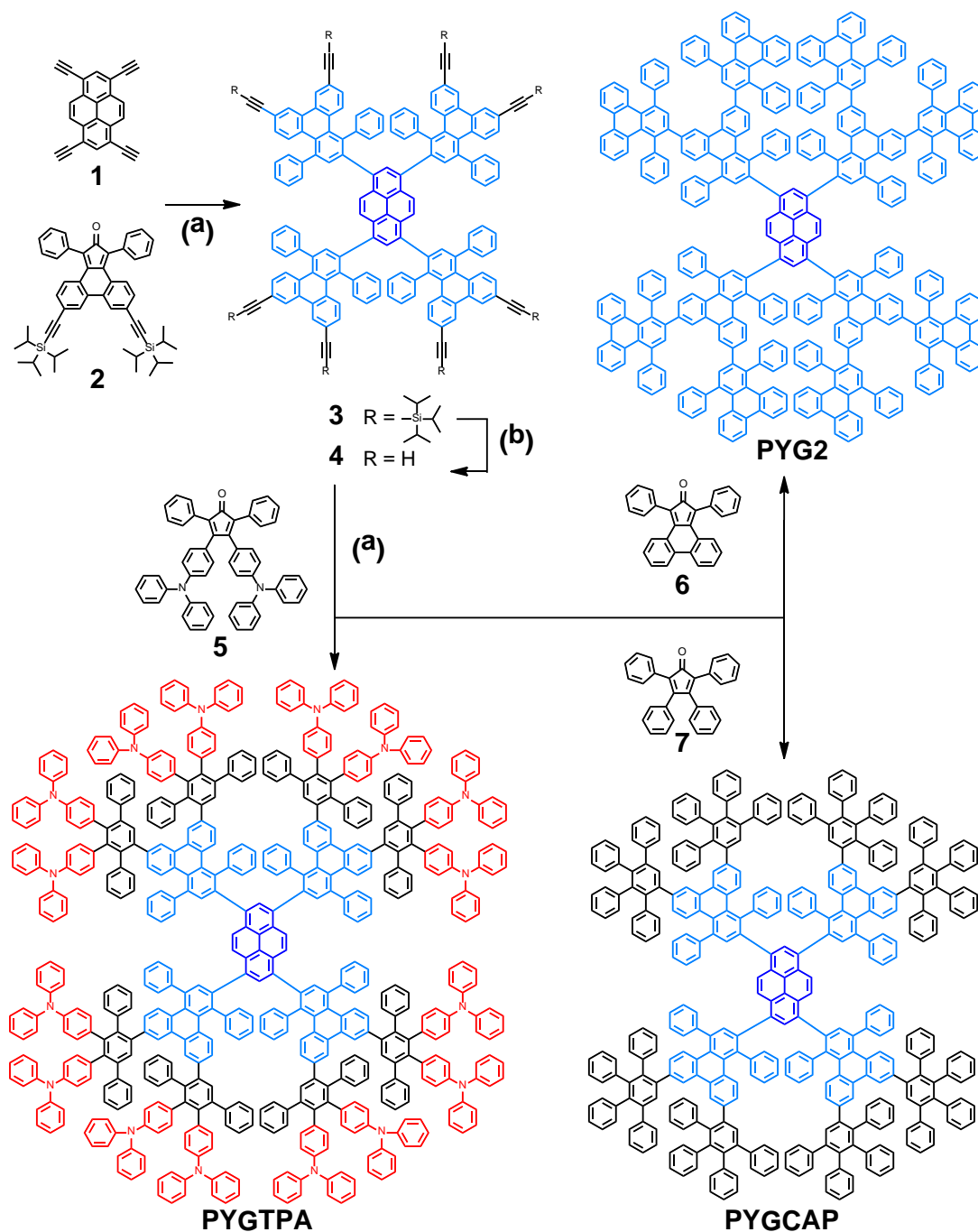


Figure 4-48: Synthesis strategy towards dendrimers PYG2, PYGCAP and PYGTPA

### 4.6.3 Photophysics of Pyrene-cored Dendrimers

The emission and absorption properties of PYG2, PYGCAP, PYGTPA as well as for the previously reported TPG2<sup>[273]</sup> are depicted in Figure 4-49 for dendrimers dissolved in toluene and for 30 nm films spin-coated from these solutions. It can be observed that in solution as well as in thin film TPG2

shows only one dominant absorption feature around 300 nm, while PYG2, PYGCAP and PYGTPA exhibit this absorption band at 300 nm and in addition an absorption shoulder between 375 nm and 430 nm. The observed absorption bands in the UV region at 300 nm can be attributed predominantly to the polytriphenylene dendrons<sup>[279,280]</sup> as well as polyphenylene dendrons.<sup>[201]</sup> The additional shoulder above 400 nm, which is not present in the TPG2 type dendrimer, is assigned to the  $\pi$ - $\pi^*$  transition of the tetra-substituted pyrene core.<sup>[281,282]</sup> Note that this absorption band shows a red-shift of up to 55 nm compared to that of the isolated pyrene molecule (337 nm, c.f. chapter 4.2.1), which is caused by the direct linking of the pyrene core to the triphenylene dendrons.

The photoluminescence spectra of all dendrimers in solution show one unstructured emission band with a maximum at 408 nm, 456 nm, 450 nm and 450 nm for TPG2, PYG2, PYGCAP and PYGTPA, respectively. All relevant photophysical data also is summarized in Table 3. In solid state all photoluminescence spectra are shifted bathochromically to 428 nm, 469 nm, 463 nm and 463 nm. With an observed red-shift of 20 nm this effect thus is more pronounced for TPG2 than for all the other dendrimers, where it is only about 13 nm. The comparison of all spectra demonstrates that all pyrene containing dendrimers PYG2, PYGCAP and PYGTPA (PYGx) exhibit very similar emission properties in contrast to TPG2 without the pyrene core. The attained results clearly indicate that the observed emission stems exclusively from the shielded pyrene core as a consequence of the excitation energy transfer from the shell to the core.<sup>[273]</sup> The minor variation between the PYG2 PL spectrum and the PYGCAP or PYGTPA emission spectra may be attributed to the reduced conjugation as a consequence of using polyphenylene units in the second generation instead of polytriphenylenes in the latter.

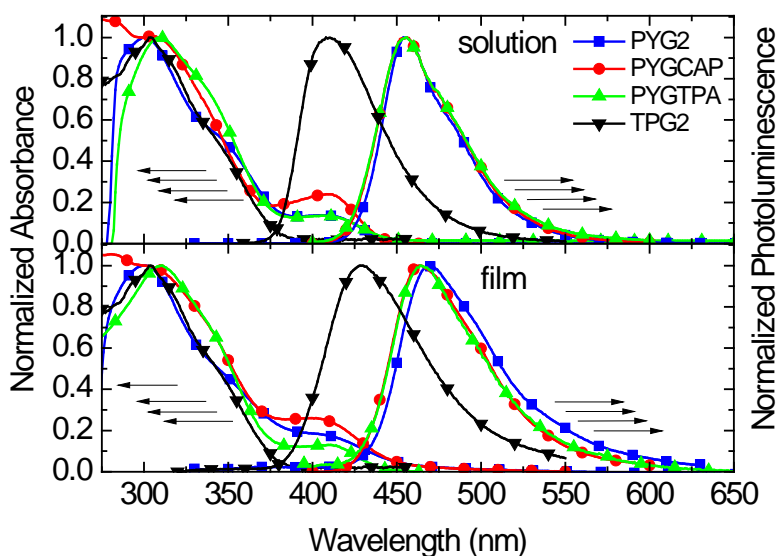


**Figure 4-49:** Normalized absorption and photoluminescence spectra of PYG2, PYGCAP, PYGTPA and TPG2 in toluene solution (top) and in thin film (bottom).

The shape and similarity of the PL spectra of all pyrene-cored dendrimers in solution as well as in solid state already suggest that in analogy to the pyrene-polymers presented in the previous chapters, pyrene agglomeration and excimer formation is not an issue. Yet, in order to investigate their occurrence, again the dependence of the photoluminescence emission on the polymer content in solution over 5 orders of magnitude ranging from 0.1 mg/l to 1000 mg/l was evaluated. The respective emission spectra for solutions of PYG2, PYGCAP and PYGTPA in toluene are depicted in Figure 4-50. It clearly can be observed that for none of these solutions any sign specific for aggregation or excimer formation occurs. These results evidence doubtlessly that no formation of agglomerates or of any excimer states are present in the pyrene dendrimers.

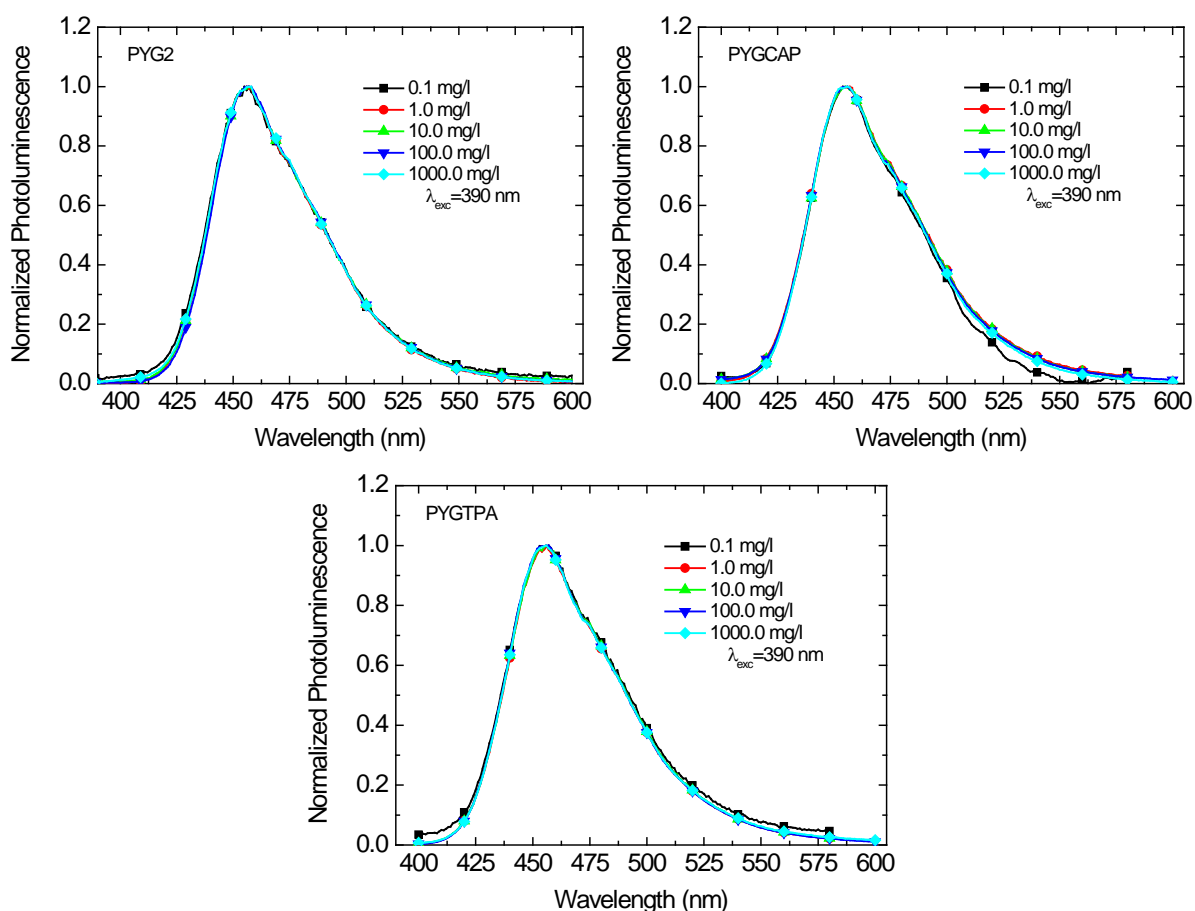


**Figure 4-50:** Photoluminescence spectra of PYG2 (top left), PYGCAP (top right) and PYGTPA (bottom) dissolved in toluene at different polymer concentrations in the range of 0.1 mg/l to 1000 mg/l. All spectra perfectly demonstrate the stability of the dendrimers emission properties and evidence doubtlessly the absence of any agglomerate or excimer states.

A scheme describing schematically the stepwise implementation of different functionalities in the core the shell and on the surface of the dendrimer and their impact on the photophysics of the molecules is depicted in Figure 4-51. Figure 4-51a starts at TPG2, which comprises a second-generation dendrimer with a carbon core and triphenylene units in the shells for the generation of blue light. The introduction of a pyrene unit as the core results in the dendrimer PYG2 (Figure 4-51b). Due to an energy transfer between the triphenylene units towards the core molecule the implementation of pyrene as presented leads to a significant enhancement of the quantum yield which. Following the scheme from b to c, shielding poly-phenylene units are introduced in the outer shell instead of the triphenylene, yielding PYGCAP. For this molecule the introduction of the poly-phenylenes entails a reduction of the conjugation which results in the described blue shift of the PL emission in comparison to PYG2. In addition, PYGCAP exhibits a less pronounced solid state effect, i.e., the solvatochromic shift of the PL emission maximum is considerably lower in PYGCAP than in PYG2. The final step in Figure 4-51, from c to d, is given by adding triphenylamine groups to the surface of the shielding poly-phenyl units. Triphenylamine units are well known for their hole-transporting properties and at the surface of the dendrimer these entities enhance the trapping of holes. These holes are transferred subsequently to the triphenylene shells, where excitons are formed which further are transferred to the pyrene core, where they are able to recombine radiatively.

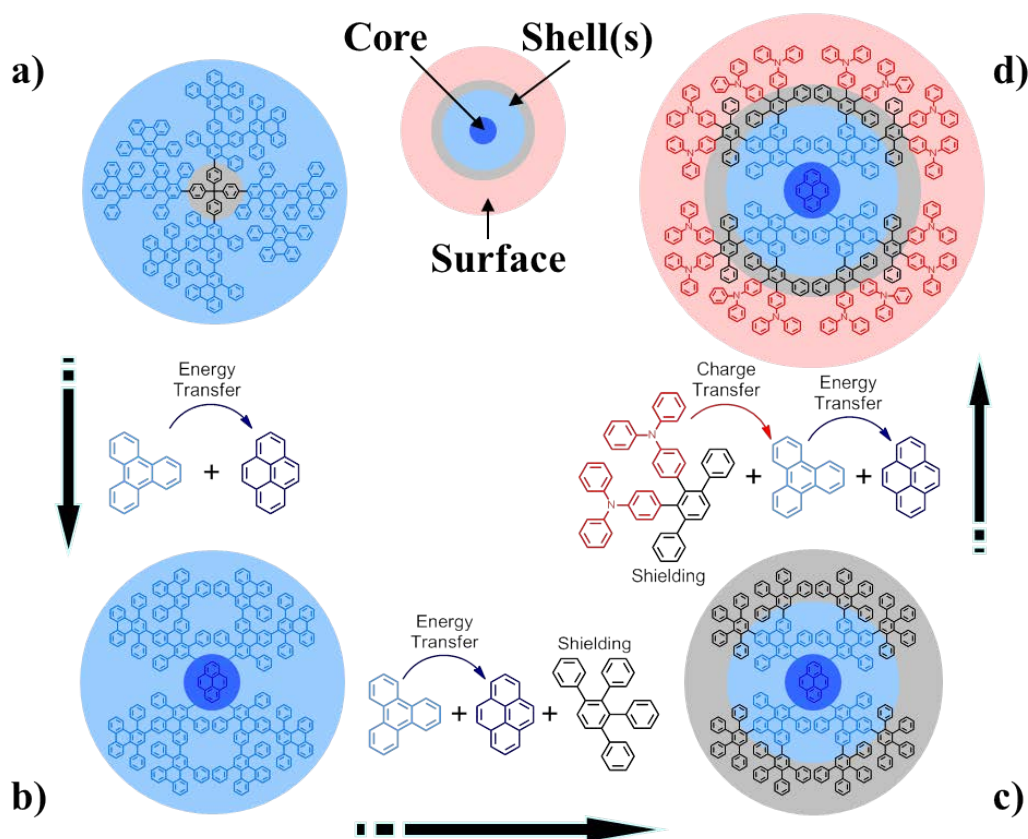


**Figure 4-51: Schematic explanation of charge transfer and energy transfer processes within the dendrimer molecules.**

The occurrence of an efficient Förster-type energy transfer process<sup>[91]</sup> (c.f. chapter 2.5.1) becomes evident when comparing the absorption of the PYGx pyrene core, acting as acceptor, to the emission of triphenylene units acting as donors. In fact, the pyrene core absorption peaks in PYGx dendrimers around 400 - 430 nm coincide with the emissions of triphenylene units in TPG2, which shows emission maxima at 408 nm and 428 nm in solution and in the solid state, respectively (Figure 4-49). Considering this spectral overlap of the two emitting compounds, an intramolecular energy transfer is likely to take place in such a configuration. This is moreover indicated by the fact that upon excitations of the triphenylene units in PYG2 between 240 and 340 nm, where pyrene absorption is at a minimum, no corresponding triphenylene emission (400 - 430 nm) was observed in the corresponding solid state PL spectrum, but the same emission maximum from the pyrene core at 464 nm (Figure 4-52). The Förster radius  $R_0$  for PYG2 was calculated according to equation (2.14) from the obtained spectra to be  $R_0 = 2.2$  nm. From this result it becomes evident that in all PYGx dendrimers one finds the donor and acceptor molecules to be significantly closer in distance than  $R_0$ . Given that the transfer rate  $k_{ET}$  scales with  $R_0^6$  a calculated Förster radius of  $R_0 = 2.2$  nm can very well account for the observation that all the detected luminescence in the PYGx dendrimers stems from the pyrene cores. The efficient dipolar coupling due to excitation energy transfer – resulting from the rational molecular design of the core/shell triphenylene-pyrene system – becomes in particular obvious by the drastically enhanced PLQY of all PYGx systems in comparison to TPG2. A comparison reveals that PYGx show an absolute PLQY of up to 88% compared to 27% of previously reported TPG2 in solution.<sup>[273]</sup> As a consequence of the shape persistent molecular design of PYGx dendrimers the relative PLQY in thin films was even improved threefold for PYG2 and fourfold for PYGCAP and PYGTPA relative to TPG2 (c.f. Table 3).

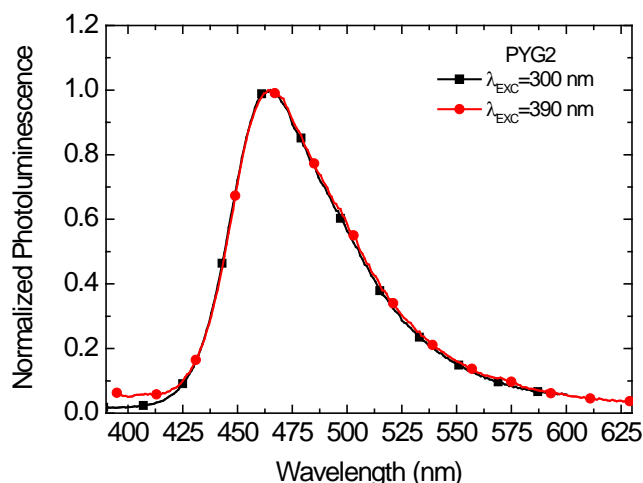
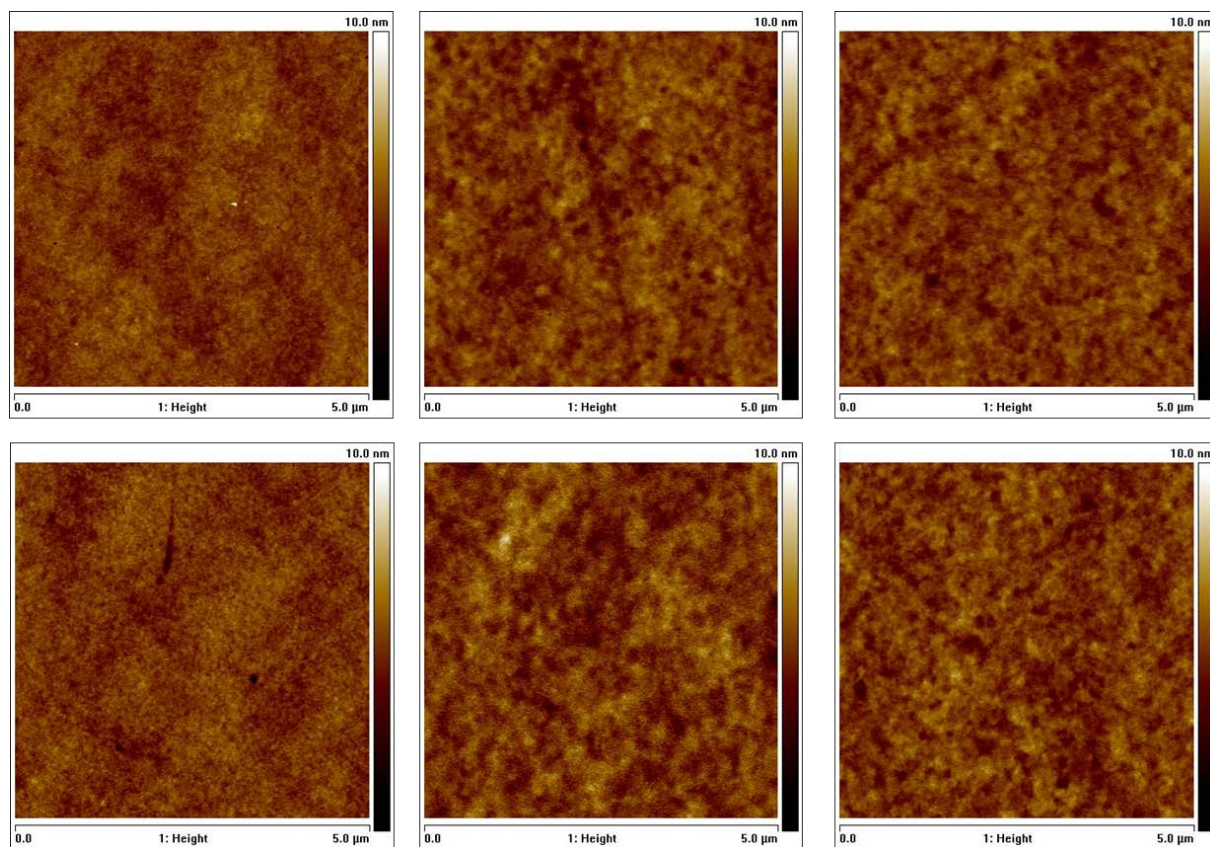


Figure 4-52: Photoluminescence emission spectrum of PYG2 excited at a wavelength of  $\lambda_1 = 300$  nm and of  $\lambda_2 = 390$  nm.

#### 4.6.4 Surface Morphology and Thermal Stability of PYGx Thin Films

The influence of a thermal treatment on the morphology of PYGx films was conducted in analogy to the investigation presented for PPy and PPyTPA (chapters 4.3.4 and 4.4.5). AFM was performed of PYG2, PYGCAP and PYGTPA films directly after spin-coating on PEDOT:PSS covered ITO substrates. The same films were measured again after they were annealed at 150°C in vacuum for 2 hours. AFM surface topography images with a scan size of 5  $\mu\text{m} \times 5 \mu\text{m}$  are depicted in Figure 4-53. As it is shown all films show very similar surface structures before and after the thermal treatment. Interestingly, an apparently finer structured surface morphology is developed for PYG2 in comparison to PYGCAP and PYGTPA. Nevertheless, all materials showed extremely flat film morphologies with a RMS roughness before and after thermal treatment of 0.52 nm for the PYG2 film, 0.64 nm and 0.72 nm for PYGCAP and 0.57 nm and 0.63 nm for the PYGTPA film, respectively.

As in the case of pyrene polymer the stability of the PL emission with regard to thermal treatment was investigated. Absolute photoluminescence emission spectra of PYGx dendrimer films on quartz substrates recorded after spin-coating from TOL solution and after thermal treatment at 100°C for 24 hours under inert conditions are depicted in Figure 4-54. The results once more display the exceptional spectral stability of the materials under investigation. In particular, none of the dendrimers showed a shift of the emission maximum. The maxima could be found at 467 nm, 464 nm and at 462 nm for PYG2, PYGCAP and PYGTPA, respectively. More importantly, all dendrimer films showed outstanding stability upon annealing regarding their solid state fluorescence quantum yield. The respective reduction of the quantum yield could be determined to be as small as 7% for PYG2, 5% for PYGCAP and 7% for PYGTPA, respectively. Thus, as a summary so far it can be stated that the presented pyrene-cored dendrimers show photoluminescence characteristics in the deep blue spectral region combined with high photoluminescence quantum yield and exceptional spectral as well as structural stability with respect to thermal treatment. All these properties suggest that these dendrimers represent suitable materials for blue light-emitting DLEDs.



**Figure 4-53:** AFM surface topography images ( $5\ \mu\text{m} \times 5\ \mu\text{m}$ ) measured in tapping mode of PYG2 (left), PYGCAP (center) and PYGTPA films (right) on PEDOT:PSS investigated directly after spin-coating (top) and after thermal annealing at  $150^\circ\text{C}$  (bottom). The RMS-surface roughness, before and after annealing, was 0.52 nm for PYG2, 0.64 nm and 0.72 nm for PYGCAP and 0.57 nm and 0.63 nm for the PYGTPA film.

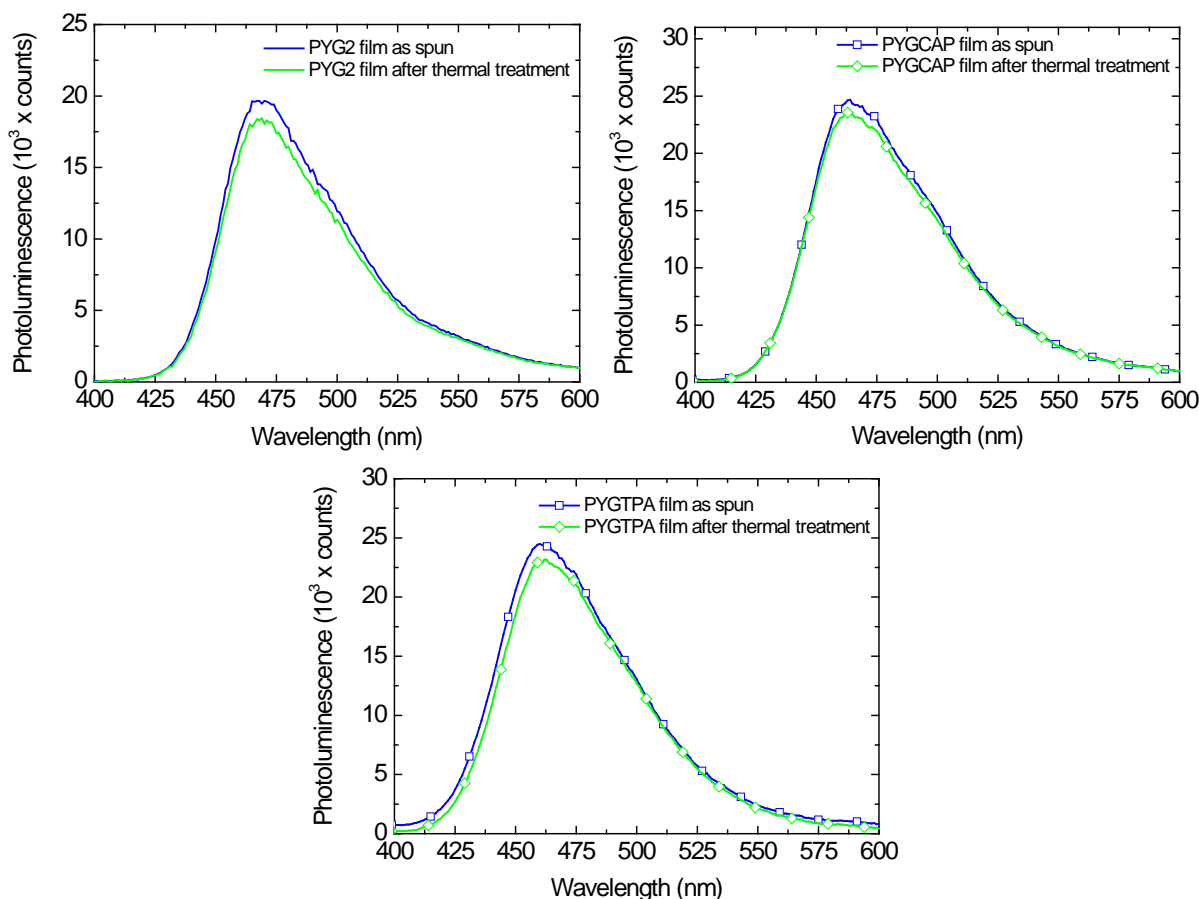
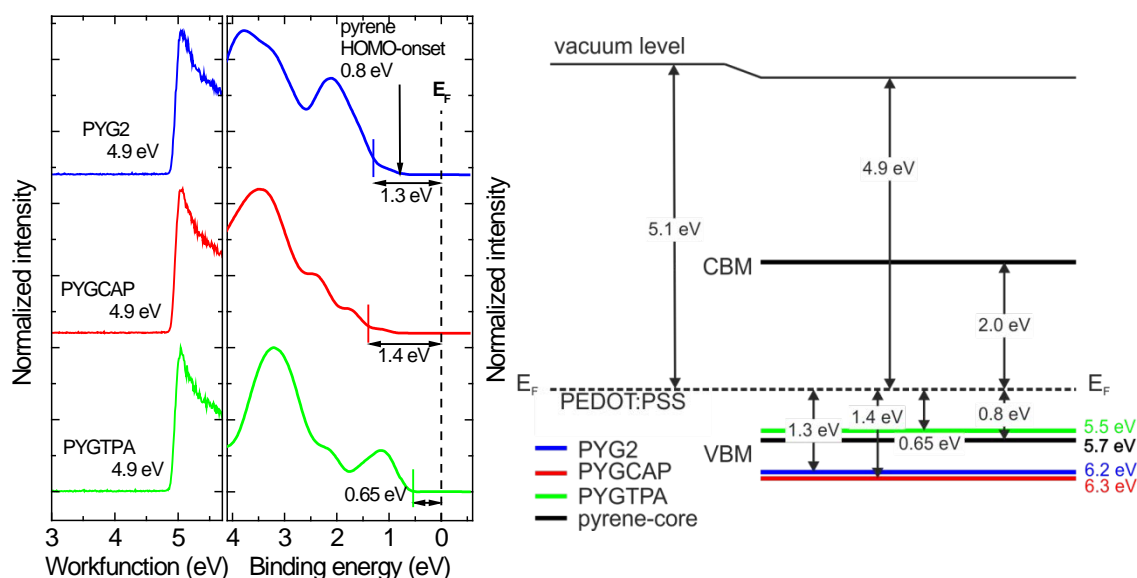


Figure 4-54: Absolute PL spectra of PYG2 (top left), PYGCAP (top right) and PYGTPA films on quartz substrates recorded directly after spin-coating and after thermal annealing at 100°C under inert conditions for 24 hours.

#### 4.6.5 UPS-Studies on Pyrene-cored Dendrimers

To determine the absolute location of the energy levels of the PYG<sub>x</sub> dendrimers and the relative energy alignment of the core-shell and surface groups ultraviolet photoelectron spectroscopy was performed. The corresponding valence region UPS and SECO spectra are depicted in Figure 4-55. From these spectra the photoemission onset of the valence bands of the PYG<sub>x</sub> dendrimers could be determined to be 1.3 eV below the Fermi level for PYG<sub>2</sub>, 1.4 eV for PYGCAP and 0.65 eV for PYGTPA. In addition, a small feature with an onset of approximately 0.8 eV could be detected. A comparison to the valence band structure of PPy strongly suggests that this feature originates from the pyrene core of the dendrimers. The corresponding  $\phi$  value was ca. 4.9 eV for all dendrimers and consequently the ionization energies were 6.2 eV, 6.3 eV and 5.5 eV for PYG<sub>2</sub>, PYGCAP and PYGTPA. In combination with a bandgap of 2.9 eV for the pyrene core and 3.4 eV for triphenylenes, derived from the absorption onsets of the respective spectra, the following conclusions can be drawn from the UPS results. Firstly, the energy levels of the pyrene core with its HOMO at 5.7 eV and the LUMO at 2.8 eV are located within the bandgap of the triphenylene (HOMO = 6.2 eV; LUMO = 2.8 eV) as required for energy transfer. Secondly, adding the TPA groups to the surface of PYGTPA drastically reduces the injection barrier from the PEDOT:PSS electrode ( $\phi = 5.1$  eV) by ca. 0.65 eV compared to PYG<sub>2</sub> and PYGCAP; thus PYGTPA represents indeed an optimized molecular core-shell-surface design for device applications.



**Figure 4-55: SECO (left) and valence region UPS spectra (center) of PYG2, PYGCAP and PYGTPA on PEDOT:PSS. The arrow indicates the low binding energy onset from the pyrene core. Right: Schematic energy level diagram derived from UPS data.**

#### 4.6.6 Electroluminescent Properties and Device Performance of Single Layer DLEDs

To assess the performance of the pyrene-cored dendrimers in a DLED, based on the results from UPS, devices were fabricated comprising the following standard sandwich configuration: ITO/PEDOT:PSS/PYG<sub>x</sub>/TPBi/CsF/Al. Cesium fluoride was used since it is known to greatly improve electron injection from the cathode side due to a very low located electron affinity.<sup>[283]</sup> J-V-L characteristics for the respective dendrimer devices are shown in Figure 4-56 and the key results for the devices are summarized in Table 3. An electroluminescence onset for the devices was measured at a voltage of 4.4 V for PYG2, 3.4 V for PYGCAP and 3.2 V for PYGTPA and the maximum brightness was 1132 cd/m<sup>2</sup>, 728 cd/m<sup>2</sup> and 1443 cd/m<sup>2</sup>, respectively. An overall efficiency of 0.57 cd/A was achieved for PYG2 compared to efficiencies of 0.4 cd/A for PYGCAP and 0.27 cd/A for PYGTPA.

The inset Figure 4-56 shows electroluminescence spectra of the devices recorded at a current density of 1.0 kA/m<sup>2</sup>. As can be observed, all devices exhibited blue light emission with their electroluminescence peak maxima at 469 nm, 464 nm and 458 nm for PYG2, PYGCAP and PYGTPA. All spectra show clear similarity to the materials' PL emission in the solid state (c.f. Figure 4-49) and the respective CIE1931 coordinates were calculated to be  $x = 0.167$ ,  $y = 0.256$ ,  $x = 0.167$ ,  $y = 0.208$  and  $x = 0.148$ ,  $y = 0.152$ , situating the overall emission color in the deep blue region of the spectrum. Figure 4-57 displays that the observed spectral stability of thin dendrimer films (c.f. Figure 4-54) also reflects itself in the spectral stability of the devices' EL emission. The devices in the presented configuration showed good stability as demonstrated by a comparison of the electroluminescent spectra recorded for current densities of up to 5.0 kA/m<sup>2</sup>. As depicted in the graphs, PYG2 and PYGCAP exhibit only a slight broadening of the emission feature at higher current densities, which results from a thermal stress under device operation. The best performance concerning stability obviously is achieved by PYGTPA. Even for highest current densities, no broadening of the emission feature or any other effect can be detected in the spectra.



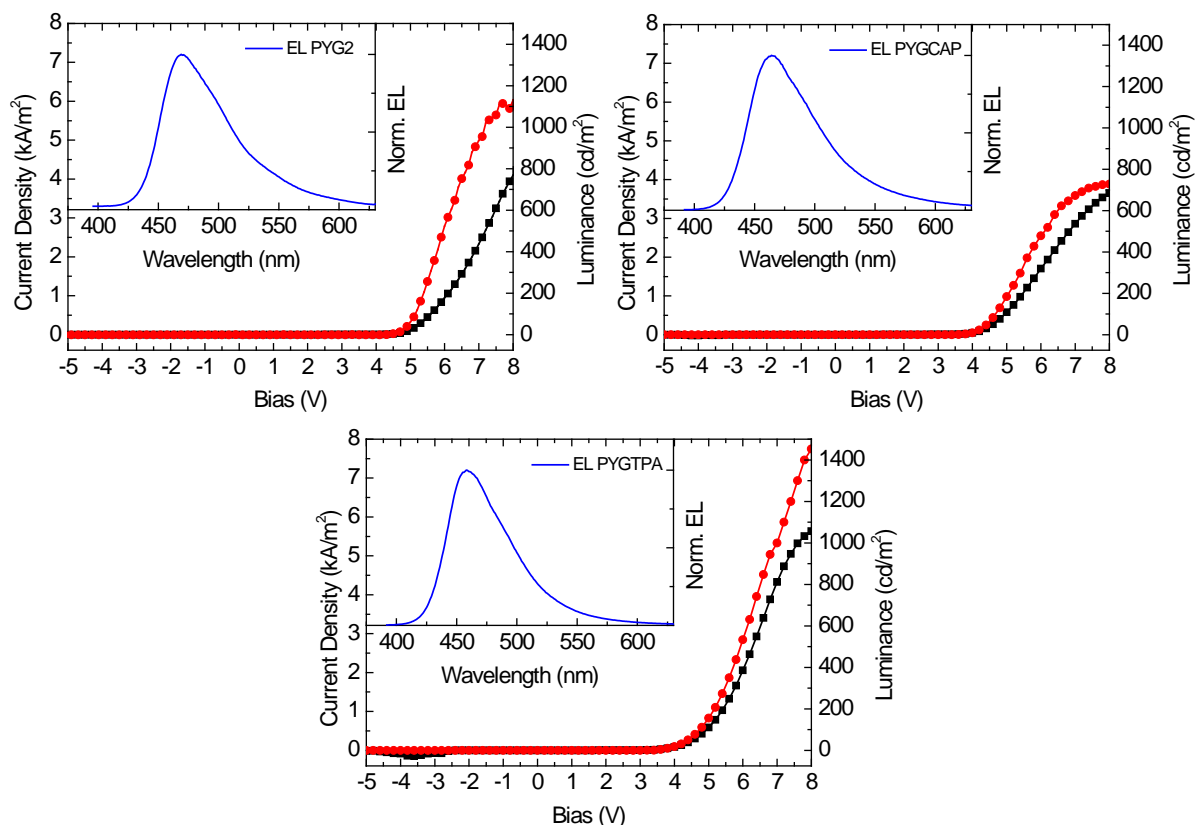


**Figure 4-56:** Current density (line with squares) / luminance (line with circles) as a function of the bias voltage in an ITO/PEDOT:PSS/PYG2/TPBi/CsF/Al device (top left), an ITO/PEDOT:PSS/PYGCAP/TPBi/CsF/Al device (top right) and an ITO/PEDOT:PSS/PYGTPA/TPBi/CsF/Al device (bottom). The insets show the electroluminescence emission spectra of the same devices at a current density of 1.0 kA/m<sup>2</sup> and at a bias of 6.0 V, 5.5 V and 5.4 V, respectively.

With these device related results the presented dendrimers possess the best brightness and stability values reported so far for solution processed saturated blue emitting dendrimer based devices.<sup>[284]</sup> As compared to fluorescent poly(para-phenylene) based blue emitting materials our results are comparable with respect to device brightness and stability to single layer devices.<sup>[207,285]</sup> The excellent material performance can be attributed to both the presented dendrimer design as well as the chosen synthetic concept allowing for perfect site-definition of the dendrimer.

Yet, as in the case of pyrene-based polymers, the luminous efficiencies of the presented devices are rather moderate. Even when a LE of 0.57 cd/A could be achieved for PYG2, the efficiencies of PYGCAP (0.4 cd/A) and PYGTPA (0.27 cd/A) are considerably lower. Again charge carrier injection inhibiting barriers, primarily at the PEDOT:PSS/dendrimer interface, are identified as the cause for this weak performance. The energy level diagram, depicted in Figure 4-55, clearly evidences this statement. It can be seen that hole injection limiting energy barriers from 0.65 eV up to 1.4 eV develop between PEDOT:PSS and PYGx. Furthermore, also for this single layer DLEDs obviously no charge carrier confinement is achieved. Thus, charge carriers which are injected into the EML are able to escape this layer without the formation of an exciton and consequently without having the possibility to contribute to the light generation process.

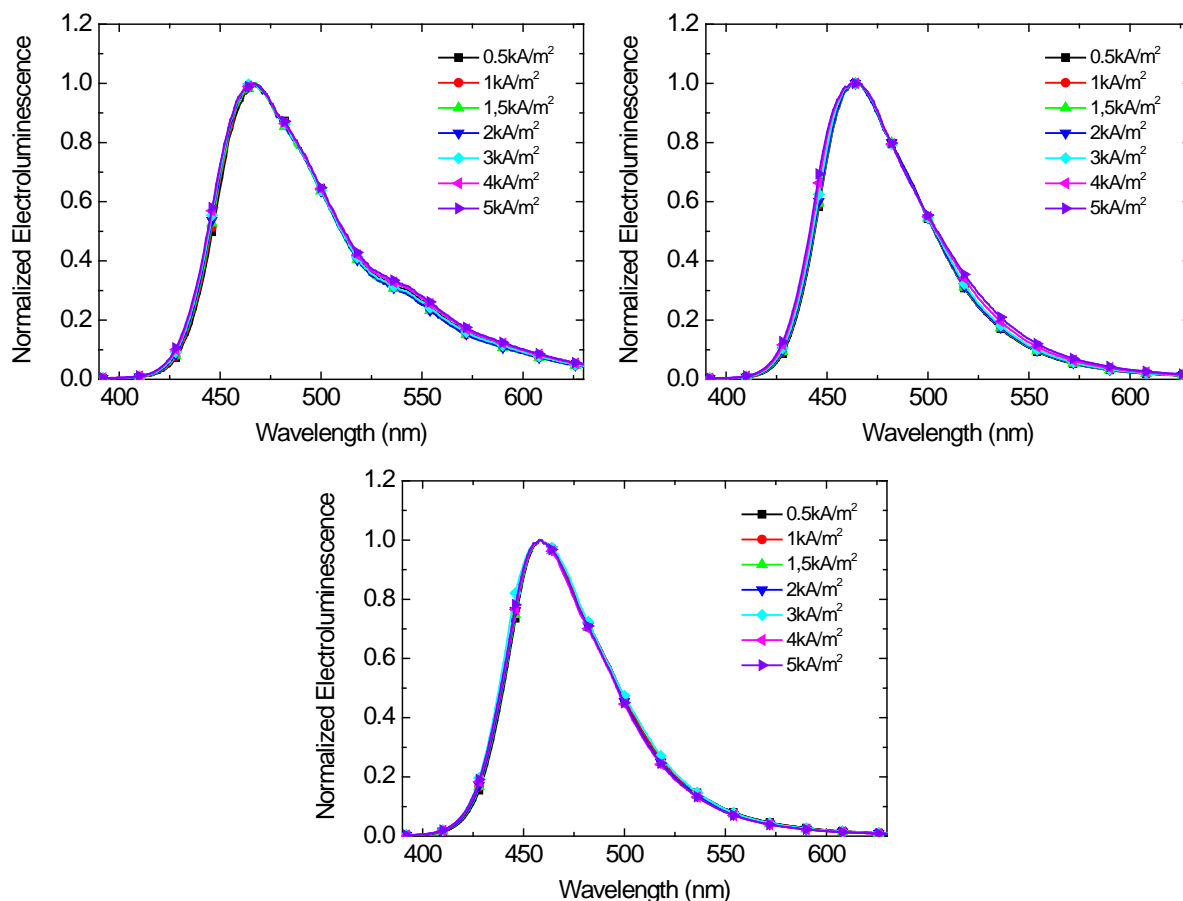
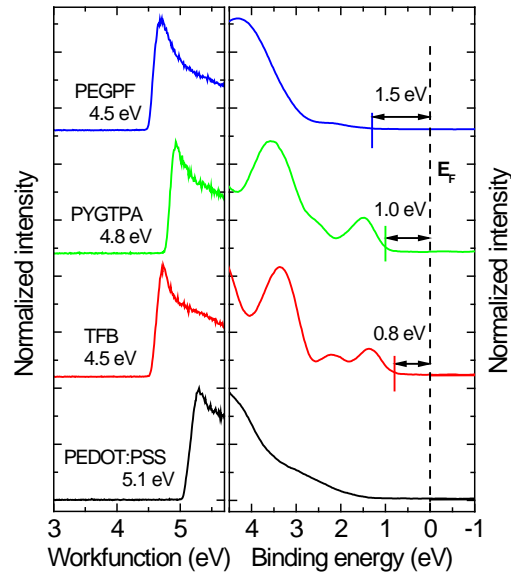


Figure 4-57: Current density dependent EL spectra of an ITO/PEDOT:PSS/PYG2/TPBi/CsF/Al device (top left), an ITO/PEDOT:PSS/PYGCAP/TPBi/CsF/Al device (top right) and an ITO/PEDOT:PSS/PYGTPA/TPBi/CsF/Al device (bottom).

#### 4.6.7 PYGTPA Multilayer DLEDs

To evaluate in principle the applicability of the presented multilayer approach for pyrene-polymer based PLEDs (c.f. chapter 4.5) in DLEDs with the pyrene-cored dendrimers as emitting material, multilayer devices were assembled using PYGTPA as the light emitting component. The selection of PYGTPA out of all dendrimers presented in this thesis despite showing the lowest efficiency in single layer devices is based on its exceptional spectral stability in conjunction with its high luminance values. In analogy to the assembly presented in chapter 4.5, TFB and PEGPF were used as hole transporting and electron transporting materials, respectively. All substrates and devices were as well assembled in the same way as described in chapter 4.5.

Layer by layer UPS measurements were performed in order to assess the interface energetics of the PEDOT:PSS/TFB/PYGTPA/PEGPF assembly. The respective valence region UPS and SECO spectra to measure the work function and interface dipoles are depicted in Figure 4-58. The photoemission onset of the valence bands was determined to be again 0.8 eV below  $E_F$  for TFB, 1.0 eV for PYGTPA and 1.3 eV for PEGPF. The corresponding  $\phi$  values could be evaluated to 4.5 eV, 4.8 eV and 4.5 eV, respectively. Thus, the resulting ionization energies were 5.3 eV for TFB, 5.8 eV for PYGTPA and 5.8 eV for PEGPF. The UPS spectrum of PYGTPA on TFB, just as in the case of PPyTPA, shows no sign of TFB features and regarding its shape it is in good agreement to the spectrum achieved for PYGTPA on PEDOT:PSS presented in Figure 4-55. The deposition of PEGPF as the topmost organic material results in a complete attenuation of all PYGTPA features and one broad peak with a local maximum at a binding energy of 4.3 eV tailing towards lower binding energy values is observed.



**Figure 4-58:** SECO- (left) and Valence region UPS- spectra (right) of PEDOT:PSS and of TFB, PYGTPA and PEGPF on PEDOT:PSS.

A schematic picture of the interface energetics across the PEDOT:PSS/TFB/PYGTPA/PEGPF interfaces is shown in Figure 4-59. The figure again displays VBM and CBM levels as well as  $\phi$ , IE and estimated EA values. It can be observed from Figure 4-58 and Figure 4-59 that vacuum level shifts occur between the adjacent layers. Besides the already known shift of  $\Delta_{\text{VAC}} = -0.6$  eV between PEDOT:PSS and TFB, a shift of  $\Delta_{\text{VAC}} = 0.3$  eV between TFB and PYGTPA, and a vacuum level shift of  $\Delta_{\text{VAC}} = -0.3$  eV at the PYGTPA/PEGPF-interface develop, which are attributed again to a preferential orientation of intra-molecular dipoles at the interfaces.<sup>[260]</sup> The offsets relevant for electron injection from PEGPF into the EML and extraction from the EML into TFB are 0.2 eV between the estimated CBM levels of PEGPF and PYGTPA and 0.4 eV between PYGTPA and TFB. The offset of the VBM levels for injecting holes from TFB into PYGTPA (0.2 eV) however is smaller than the one for extracting them to PEGPF (0.3 eV). Thus, the alignment in Figure 4-59 again suggests the existence of the prerequisites for a charge carrier confinement in the emissive layer of the presented multilayer assembly. As a consequence of these barriers charge carrier extraction (electrons and holes) from the emitting layer is expected to be significantly constrained compared to PYGTPA-single layer devices.

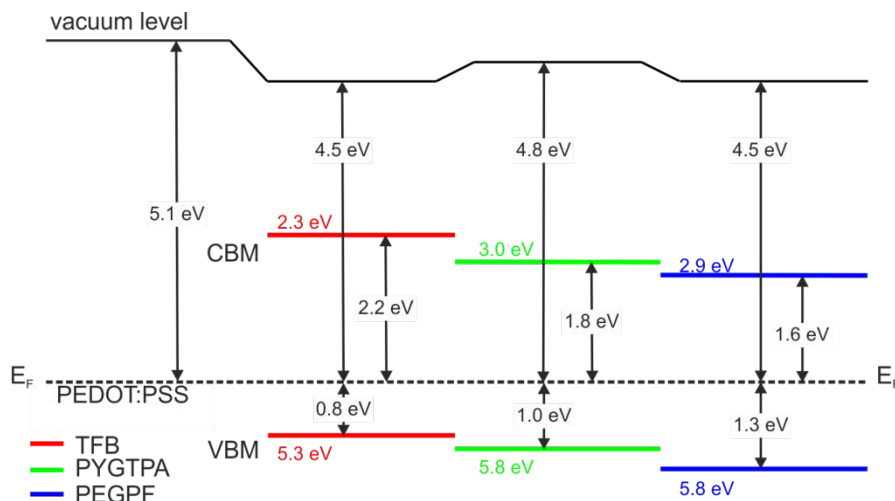


**Figure 4-59:** Interface energetics for a PEDOT:PSS/TFB/PYGTPA/PEGPF multilayer DLED assembly.

J-V-L characteristics and the device related key results of a triple-layer device consisting of the assembly ITO/PEDOT:PSS/PYGTPA/PEGPF/Ca/Al are depicted in Figure 4-60 and summarized in Table 3, respectively. The PYGTPA based devices exhibited a deep-blue electroluminescence emission and a maximum luminance value of 9242  $\text{cd}/\text{m}^2$  could be measured. In comparison to the PYGTPA-single layer device this result means a more than 6.4-fold enhancement for the triple-layer DLED. At the same time the luminous efficiency increased from 0.27  $\text{cd}/\text{A}$  to 0.85  $\text{cd}/\text{A}$  and the EL onset was detected at 4.4 V.

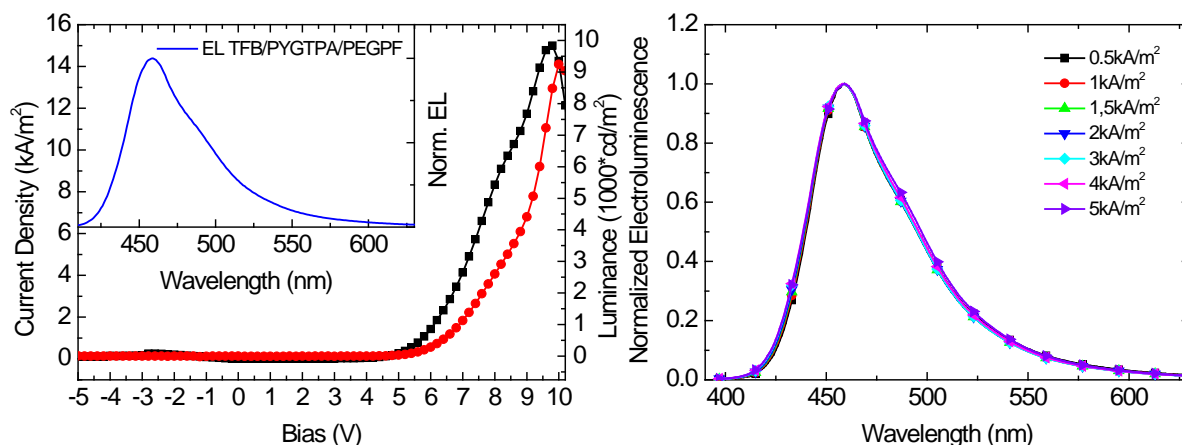


**Figure 4-60:** Current density (line with squares) / luminance (line with circles) as a function of the bias voltage in an ITO/PEDOT:PSS/TFB/PYGTPA/Ca/Al device (left) and current density dependent EL spectra of the same device. The inset shows the electroluminescence emission spectrum of the same device at a current density of 1.0  $\text{kA}/\text{m}^2$  and at a bias of 5.8 V.

An EL-spectrum of the multilayer DLEDs at a current density of 1.0  $\text{kA}/\text{m}^2$  is presented in the inset on the left side of Figure 4-60. The spectrum shows a deep-blue emission in the same range as for PYGTPA single layer devices with CIE1931 coordinates of  $x = 0.153$ ,  $y = 0.155$ . EL emission spectra at various current densities are shown on the right hand side of Figure 4-60. It can be observed that the PYGTPA based DLEDs exhibit the same exceptional spectral stability as already presented for the single layer devices. In addition, when compared to the EL-spectra of TFB and PEGPF single layer PLEDs (insets of Figure 4-43 and Figure 4-44), again no EL contribution of the transporting materials can be observed in any of the multilayer DLEDs emission spectra. This fact evidences that also in the presented triple-layer DLEDs the EL-emission stems exclusively from PYGTPA. A summary of all these results demonstrates the applicability of the multilayer assembly, as presented in chapter 4.5, for multilayer DLEDs as well. As confirmed by UPS the insertion of PEGPF leads to the generation of a barrier for holes at the cathode side of PYGTPA due to the VBM offset between PYGTPA and PEGPF which hinders significantly the extraction of holes from the EML. The insertion of TFB leads to the already explained stepwise reduction of the hole injection barrier between the Fermi-level of PEDOT:PSS and the VBM of PYGTPA resulting in an improved hole injection. Finally, a pronounced energy barrier of 0.4 eV is formed between the PYGTPA and TFB CBM levels, constraining their extraction from the EML. These conditions consequently lead again to an enhanced charge carrier density within the EML and result in increased maximum luminance and LE values for the triple-layer device in comparison to its single layer counterpart.

In that context, however, it is important to note that these presented multilayer DLEDs only constitute first preliminary results for dendrimer-based multilayer devices. In contrast to the pyrene PLEDs presented in chapter 4.5, the EML of the DLEDs was not optimized with respect to maximum luminance values. As a consequence further efforts will be undertaken in order to maximize the luminance as well as the LE efficiency values.

**Table 3: Photophysical properties of dendrimers and device performances of DLEDs. The last line presents the results for a multilayer DLED comprising the assembly: ITO/PEDOT:PSS/TFB/PYGTPA/PEGPF/Ca/Al.**

Compound	$\lambda_{em}$	$\Phi_{PL}$	$\lambda_{em}^{max}$	$\Phi_{PL}$	onset voltage <sup>a</sup>	$\eta^b$	max. luminance	CIE 1931 coordinates
	[nm]	[%] <sup>d</sup>	[nm]	[rel.%] <sup>e</sup>	[V]	[cd/A]	[cd/m <sup>2</sup> ]	x, y
	solution		film				device	
TPG2 <sup>c</sup>	410	27	431	100	6.0	0.4	300	0.19, 0.18
PYG2	456	74	469	324	4.4	0.57	1132	0.19, 0.27
PYGCAP	450	88	463	410	3.4	0.4	728	0.15, 0.18
PYGTPA	450	73	463	442	3.2	0.27	1443	0.15, 0.17
<b>MULTI LAYER</b>	–	–	–	–	4.3	0.85	9242	0.15, 0.16

<sup>a</sup> voltage at a luminance of 1 cd/m<sup>2</sup>; <sup>b</sup> value of maximum efficiency; <sup>c</sup> taken from ref. [273]; <sup>d</sup> relative to quinine sulfate dehydrate; <sup>e</sup> relative to TPG2 as 100%.

#### 4.6.8 Conclusion

In conclusion, pyrene cored polytriphenylene dendrimers with a core-shell-surface design that yields dendritic molecules with high photoluminescence quantum yield and optimized charge injection properties were presented in this chapter. Because of the shape persistent molecular design, the materials maintain all these properties in the solid state. The utilization of a synthetic route based on non-catalytic Diels-Alder cycloaddition in that context not only allows for a defined generation-by-generation growth of the dendrimers yielding highly defined monodisperse molecular weight materials, which are free of unknown structural defects, but also completely rules out metal catalyst contamination and polymeric defects. The investigation of the emission and absorption properties of the PYG<sub>x</sub> dendrimer reveals an efficient energy transfer system between the polytriphenylene dendrons and the pyrene core leading to an increase of the PL quantum yield from 27% to 88% in solution when compared to the tetraphenylmethane-cored dendrimer TPG2. Dendrimer films showed a more than threefold increase. Moreover, it is shown that the implementation of polyphenylene shielding units in the shell of the dendrimers leads to a blue-shift of the dendrimers fluorescence emission and to a reduced solid state effect. An attachment of triphenylamine groups to the surface of the molecule finally results in an enhanced charge carrier trapping at the dendrimer surface. An exceptional spectral and morphological stability could be proven for all pyrene-cored dendrimers upon various thermal annealing procedures. Simple single layer DLEDs could show the spectral stability as well as the general suitability of the PYG<sub>x</sub> dendrimers. Furthermore, multilayer device results revealed a luminous efficiency of 0.85 cd/A with a peak luminance reaching as high as 9242 cd/m<sup>2</sup>, and proved that pyrene cored polytriphenylene dendrimers are promising candidates for blue DLEDs, which are able to compete with the best reported fluorescence-based blue-emitting dendrimers.

## 4.7 Photophysics and Electroluminescent Properties of Bis(Carbazolyl) Derivatives of Pyrene and Tetrahydropyrene in Small Molecule Organic Light Emitting Devices

*The content of this chapter is published in: Bilal R. Kaafarani, Ala'a O. El-Ballouli, Roman Trattnig, Alexandr Fonari, Stefan Sax, Brigitte Wex, Chad Risko, Rony S. Khnayzer, Stephen Barlow, Digambara Patra, Tatiana V. Timofeeva, Emil J. W. List, Jean-Luc Brédas and Seth R. Marder, Journal of Materials Chemistry C, 2013, 1, 1638-1650.*

The author of the thesis co-authored this publication. Exclusive contributions: Surface morphology measurements, device assembling and device characterization. Collaborative contributions: photophysical investigations and discussion of the attained results. B.R.K. has written the publication. The author of the thesis contributed significantly to the physics related results (photophysics and devices). In the current chapter the author expanded the publication text essentially.

### 4.7.1 Introduction

Efficient charge injection from electrodes into the adjacent organic layers, balanced charge-transport, confinement of hole / electron recombination and the resultant excitons in the desired emissive layer, and high quantum efficiencies of luminescence are all important factors in achieving efficient devices. In addition, ideally they should exhibit low driving voltages and high current and power efficiencies.<sup>[227]</sup> Efficient blue-emitting devices are challenging to fabricate because the large bandgap required for the emitter means that efficient hole and/or electron injection might be hard to achieve at moderate driving voltages while care has to be taken to avoid the possibility of energy transfer of excitons from the emissive layer to neighboring materials. Besides the already presented blue light-emitting devices based on polymers or dendrimers, such OLEDs can also be obtained by utilizing fluorescent small molecules.

In that context, polyaromatic molecules, such as diphenylanthracene,<sup>[286]</sup> have been studied as potential fluorescent blue emitters. Pyrene, as already stated, has a remarkably long fluorescence lifetime,<sup>[166]</sup> yet also exhibits high PLQY. In addition, it has a strong tendency to form excimers,<sup>[166,287]</sup> while pyrene excitation spectra are sensitive to microenvironment changes. Despite the pyrene molecule exhibits high charge-carrier mobility and a lower ionization potential than many other efficient blue emitters, e.g. polyfluorenes, facilitating hole injection, pyrene itself is generally unsuitable for a use in OLED applications because of its tendency to crystallize.<sup>[179]</sup> Yet, as it was reported in literature<sup>[213]</sup> and also presented in the previous chapters a number of functionalized pyrenes have been developed as blue emitters.

Another interesting class of molecules for organic semiconducting applications constitutes carbazole derivatives. These carbazole-based materials have been widely exploited as donor materials in a variety of organic electronic devices. In general, these compounds exhibit good hole-transport properties, however, hybrids with various acceptor moieties such as oxadiazoles,<sup>[288-290]</sup> and even 4,4'-di(carbazol-9-yl)biphenyl (CBP)<sup>[291]</sup> show ambipolar transport characteristics. In OLEDs, carbazole-based materials have been used as hole-transport materials,<sup>[292-294]</sup> as emitters,<sup>[289,292,294]</sup> and as hosts for other fluorescent<sup>[295]</sup> or phosphorescent emitters.<sup>[286,290,296]</sup>

Considering the fluorescent properties of pyrene and the transport properties of carbazoles, a combination of these two compounds in a single molecule may offer an interesting combination of physical properties and possibly a route to new electroluminescent materials. Actually, several examples of this combination realized by a variety of architectures have already been reported. However, these materials in general exhibited an extensive conjugation length and consequently

emitted in the green spectral region.<sup>[169,297,298]</sup> In the current chapter this thesis reports on the characterization, and electroluminescent properties of blue-emitting molecules in which two carbazole or 3,6-di-*tert*-butylcarbazole moieties are attached through the nitrogen atom to the 2,7 positions of pyrene (CPY and *tb*-CPY, Figure 4-61), which, in contrast to previously reported carbazole-pyrene materials, show blue fluorescence. The photophysical properties of these materials are compared to those of analogous compounds in which the pyrene is replaced by tetrahydropyrene (CTPY and *tb*-CTPY, Figure 4-61).

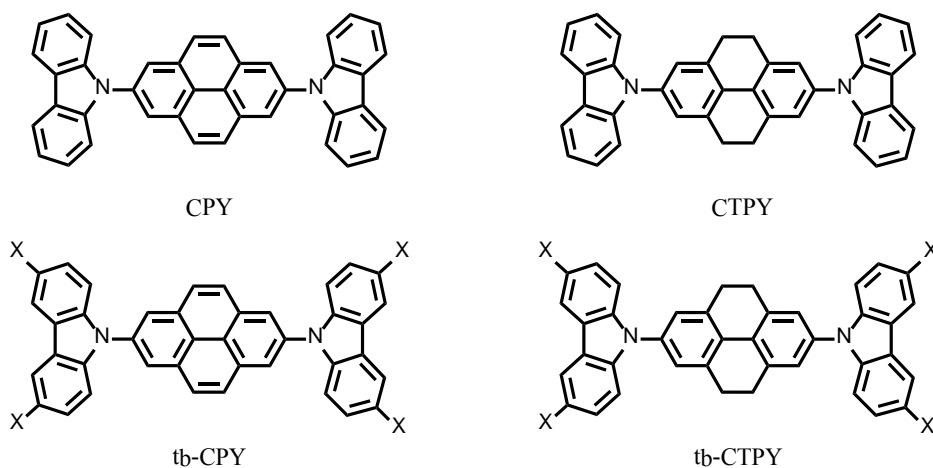


**Figure 4-61:** Chemical structures of carbazole-pyrene small molecules CPY (top left), *tb*-CPY (top right) CTPY (bottom left) and *tb*-CTPY (bottom right).

#### 4.7.2 Synthesis of Carbazole-Pyrene Small Molecules

All carbazole-pyrene compounds were synthesized at the *American University of Beirut* from *Ullmann* or *Buchwald-Hartwig* coupling of the appropriate carbazole to the dibromo derivatives of the bridging groups, as depicted in Figure 4-62. The bridging groups required for the synthesis were prepared from pyrene **1** according to literature procedures. Pyrene was first activated using Raney-nickel and then hydrogenated at 2.76 bar for 3 days in the presence of Pd/C to yield 4,5,9,10-tetrahydropyrene **2**. 2,7-Dibromo-4,5,9,10-tetrahydropyrene **3** was obtained through the bromination of **2** using bromine in acetic acid.<sup>[299]</sup> Oxidation of **3** using bromine and CS<sub>2</sub> at room temperature yielded 2,7-dibromopyrene, **4**.<sup>[300]</sup> 3,6-Di-*tert*-butyl-9*H*-carbazole **5b** was synthesized from 9*H*-carbazole **5a** using a previously described ZnCl<sub>2</sub>-mediated *Friedel-Crafts* alkylation with 2-chloro-2-methylpropane in nitromethane (Figure 4-62).<sup>[301]</sup>

The *Ullmann* approach requires stoichiometric quantities of copper reagent, typically high temperatures (>200 °C), long reaction times and often results in only moderate yields. An alternative route is given by the *Buchwald-Hartwig* palladium-catalyzed C–N coupling reaction.<sup>[302,303]</sup> All carbazole-pyrene compounds were achieved in moderate to good yield from reaction of the appropriate dibromopyrene and carbazole derivatives (Figure 4-62), using the tris(dibenzylideneacetone)dipalladium(0) / tri-*tert*-butylphosphine catalyst system, as described for *N*-arylation of carbazole in reference [304]. Microwave irradiation was used to accelerate the reaction (with a maximum temperature of 125 °C, run time of 2 min, hold time of 60 min, pressure of 120 psi, and power of 180 W).

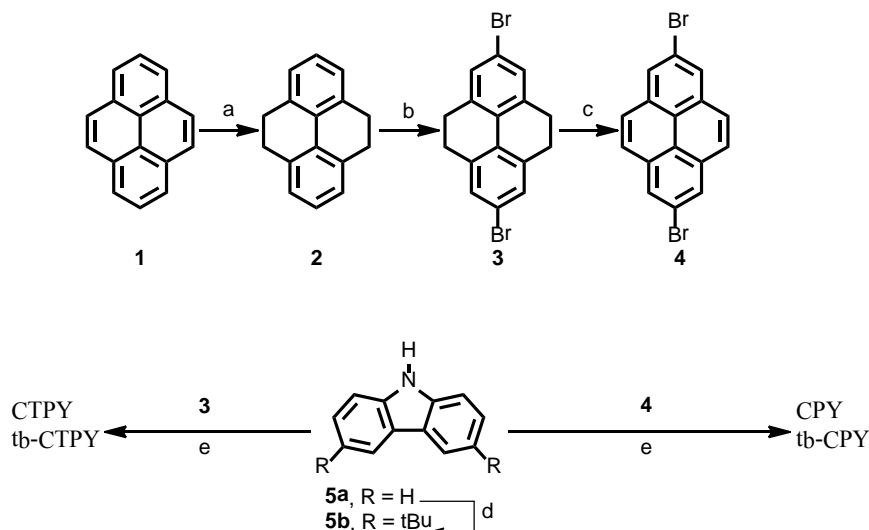


**Figure 4-62:** Scheme of the synthesis of the Bis(Carbazolyl)-Pyrene Derivatives CPY, tb-CPY, CTPY and tb-CTPY. (a) Raney-nickel, Pd/C, H<sub>2</sub> (2.76 bar); (b) AcOH, Br<sub>2</sub>, NaOH; (c) CS<sub>2</sub>, Br<sub>2</sub>; (d) *t*-BuCl, nitromethane, ZnCl<sub>2</sub>; (e) Pd<sub>2</sub>(dba)<sub>3</sub>, P<sup>t</sup>Bu<sub>3</sub>, NaO<sup>t</sup>Bu, toluene (8.27 bar), 1 h (microwave).

### 4.7.3 Photophysical Properties of Carbazole-Pyrene Molecules

Figure 4-63 shows the absorption and fluorescence spectra, respectively, of the tetrahydropyrene- and pyrene-carbazole derivatives in the solid state. It can be observed that the absorption spectra show a distinct similarity among equally bridged molecules but are clearly different to compounds with a different bridging. In particular, tetrahydropyrene-bridged molecules showed a broad absorption feature in the range of 350 nm combined with a sharp absorption at 300 nm. The pyrene-bridged molecules in contrast show more or less one broad but distinctively structured absorption feature between 280 nm and 370 nm. For the former class of compounds the absorption features are assigned to carbazole-localized transitions at 300 nm and to  $\pi$ - $\pi^*$  transitions for the broad peak, respectively,<sup>[305,306]</sup> although carbazole itself also shows a broad feature between 310 nm and 340 nm in addition to a strong absorption at ca. 290 nm. For the pyrene-bridged compounds the absorption features cannot be assigned unambiguously, however a comparison to the absorption features of pyrene (Figure 4-2) indicates that the peaks in the spectrum can be assigned to transitions at the bridging moiety. The PL emission features of the compounds display a completely different picture. While the PL emission of tb-CTPY with a maximum at 371 nm shows only a small Stokes-shift in the range of 20 nm, strong shifts can be observed for the other materials. Due to their emission maxima being located at 407 nm, 428 nm and 433 nm, respectively, CTPY, CPY and tb-CPY show shifts of ca. 55 nm, 80 nm and 90 nm. The development of a red-shift in the fluorescence maxima upon 3,6-*tert*-butyl substitution of the carbazole moieties compared to their unsubstituted analogues is consistent with a previous comparison for phenyl-bridged carbazole derivatives.<sup>[286]</sup> The absorption and emission maxima of each compound are summarized in Table 4.

The comparison of all PL spectra shows two general trends: First, the pyrene-bridged components show distinctively red-shifted emission characteristics compared to their tetrahydropyrene counterparts. This behavior can clearly be explained by the lower conjugation of the latter, since in contrast to pyrene in tetrahydropyrene the conjugation is only present at the center and does not extend over the whole molecule. Secondly it is obvious that the *tert*-butyl substituted materials show narrower emission features. Considering the impact of these side-groups for pyrene-based polymers in chapter 4.3 an enhanced steric hindrance can clearly be assigned as a cause for this effect.



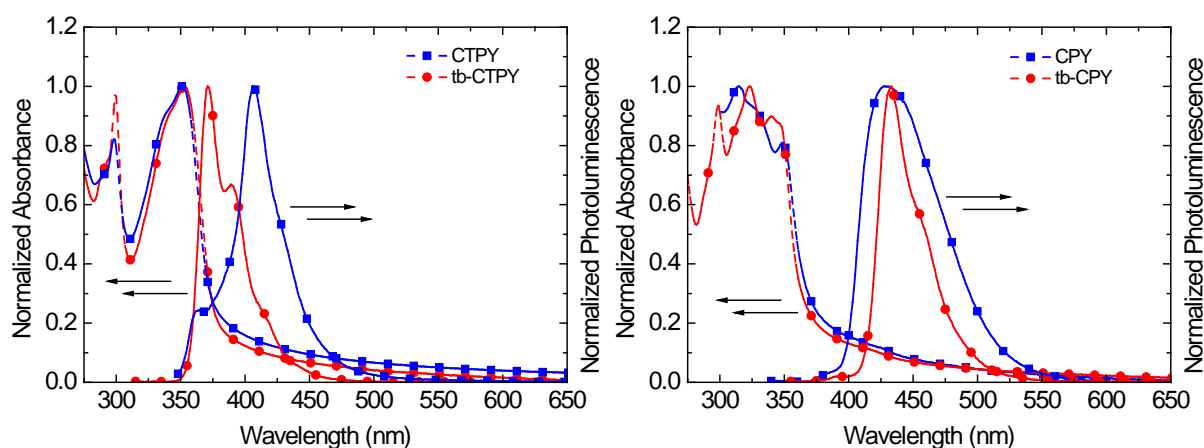


Figure 4-63: Left: Absorption (dashed lines) and normalized emission (solid lines) spectra of compounds CTPY (blue boxes) and tb-CTPY (red circles) in solid state. Right: Absorption (dashed lines) and normalized emission (solid lines) spectra of compounds CPY (blue boxes) and tb-CPY (red circles) in solid state.

Table 4: Absorption and emission maxima for CTPY, tb-CTPY, CPY and tb-CPY in solid state.

Compound	Bridge	Substituent	$\lambda_{\text{abs}}^{\text{max}}$ [nm]	$\lambda_{\text{em}}^{\text{max}}$ [nm]
CTPY	tetrahydropyrene	carbazole	351	407
tb-CTPY	tetrahydropyrene	3,6-di- <i>tert</i> -butylcarbazole	353	371
CPY	pyrene	carbazole	350	428
tb-CPY	pyrene	3,6-di- <i>tert</i> -butylcarbazole	340	433

Fluorescence quantum yields and fluorescence lifetimes of all materials were determined in THF (Table 5). The respective PLQYs were  $\eta_f = 0.36$ ,  $\eta_f = 0.43$ ,  $\eta_f = 0.43$  and  $\eta_f = 0.40$  for CTPY, tb-CTPY, CPY and tb-CPY. With respect to fluorescence lifetimes it can be noticed that considerably lower lifetimes were obtained for the tetrahydropyrene compounds. All corresponding measured values ( $\tau_1$  for single-exponential fit or  $\tau_{\text{avg}}$  for biexponential fit), were less than 10 ns, while the pyrene-based compounds revealed higher lifetimes with values up to  $\sim 19$  ns. Nonetheless, these lifetimes fall considerably short of those found for pyrene itself (ca. 460 ns).<sup>[164]</sup> The observed biexponential decays may be attributed to various origins of the radiative transitions such as intramolecular twisting in the excited state or charge transfer states.<sup>[307]</sup>

Table 5: Fluorescence lifetimes, average fluorescence lifetimes, of CTPY, tb-CTPY, CPY and tb-CPY in THF.

Compound	Solvent	$\tau_1$ [ns] [%]	$\tau_2$ [ns] [%]	$\tau_{\text{avg}}$ [ns]	$\eta_f$
CTPY	THF	1.71	--	--	0.36
tb-CTPY	THF	1.87 (42%)	9.26 (58%)	5.57	0.43
CPY	THF	2.67 ( $\sim 1\%$ )	18.9 (99%)	10.8	0.43
tb-CPY	THF	17.9	--	--	0.40

#### 4.7.4 Thin Film Surface Morphology

A difference in morphology of small molecular materials, deposited either by solution-based processing or by thermal evaporation in vacuum showed to have a major influence on device performance and lifetimes. In this regard, primarily possible crystallization or phase aggregations need to be considered. While a high packing density in nanocrystalline structures or agglomerates may lead

to enhanced charge carrier mobility in the organic material, they also are known to account for non-negligible fluorescence quenching processes.<sup>[308,309]</sup> For AFM investigations CTPY, and CPY were deposited by thermal deposition in vacuum on PEDOT:PSS covered ITO substrates, since these two compounds are soluble in common organic solvents only to a low extent. tb-CTPY and tb-CPY were spin coated on equal substrates from THF solution and annealed at 80°C in high vacuum for 2 hours. Corresponding AFM height images are depicted in Figure 4-64. The morphologies of the evaporated layers are about the same. They show a surface with a vague development of some agglomerates that can be recognized from bright and dark spots in the images. The solution processed layers in comparison show a much better uniformity. No signs of agglomeration or crystallization can be observed for tb-CPY or tb-CTPY thin films. The surface roughness could be determined to be  $R_q = 1.29$  nm for CPY, 1.14 nm for CTPY, 0.38 nm for tb-CPY and 0.52 nm for tb-CTPY. In addition to these results, Figure 4-64 shows AFM height images of CPY and CTPY films, which were evaporated uniformly on quartz-glass substrates with a thickness of 50 nm and stored under ambient conditions for about 6 months. While their surface morphology directly after deposition was comparable to that of just described films on PEDOT:PSS they showed a totally different surface after storage. As can be observed in Figure 4-64 for both materials thread-like or branched structures have been developed. As a result, the surface roughness increased severely and an  $R_q$  of 17 nm for CPY and 9 nm for CTPY was measured. Phase images (not shown) of the same scanning area revealed that the dark areas in between the thread-like structures comprised of pure quartz glass. The exact cause for this morphological change has not yet been investigated but molecular migration and strong recrystallization processes are a first tentative assumption.<sup>[239,240]</sup>

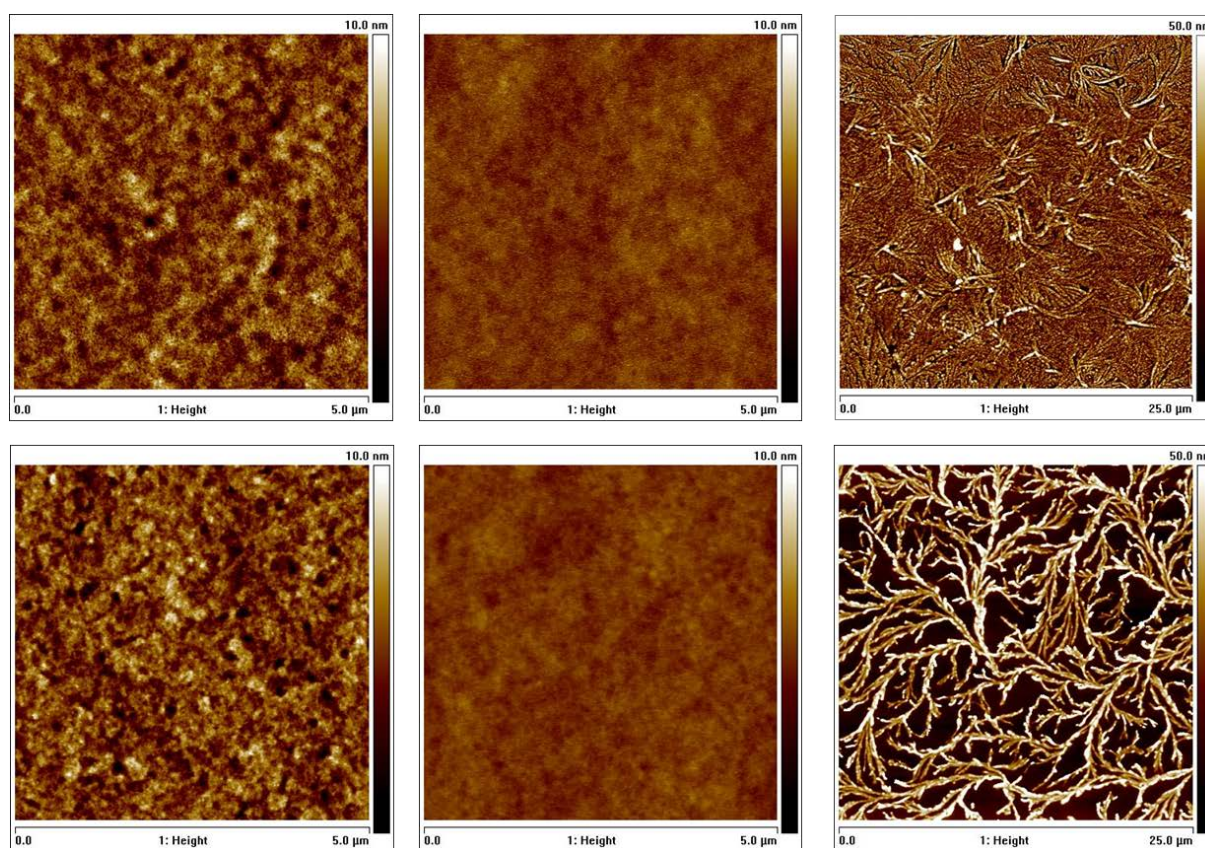


**Figure 4-64:** AFM height images of CTPY (top left), tb-CTPY (top center), CPY (bottom left), tb-CPY (bottom center) thin films on PEDOT:PSS. The corresponding roughness was 1.14 nm, 0.52 nm, 1.29 nm and 0.38 nm, respectively. The right column shows the surface morphology of a CTPY and a CPY film after storage for 6 months under ambient conditions.

### 4.7.5 Electroluminescent Properties of Pyrene-Carbazole Derivatives

To investigate the electroluminescent properties of CTPY, tb-CTPY, CPY and tb-CPY OLEDs were assembled in a standard sandwich geometry: ITO/PEDOT:PSS/[carbazole derivative]/TPBi/Ca/Al. CTPY and CPY were deposited by evaporation, while tb-CTPY and tb-CPY were spin-cast from THF solutions. TPBi was deposited again by thermal evaporation to facilitate electron injection into the active layer.<sup>[227,228]</sup> All devices give deep blue EL, with maxima in the range 422-435 nm, suggesting that emission occurs primarily from the carbazole-material layer since TPBi films show a fluorescence maximum at 383 nm.<sup>[310]</sup>

Figure 4-65 depicts the current density-voltage-luminance (J-V-L) characteristics of devices using CTPY and tb-CTPY, respectively, as light emitting layers. The OLEDs showed deep blue EL-emissions achieving maximum luminance values of 138 cd/m<sup>2</sup> at 9 V for CTPY and 361 cd/m<sup>2</sup> at 10.8 V for tb-CTPY. The onset voltages of 5.3 V for CTPY and 5.5 V for tb-CTPY were rather high and indicate either imbalanced charge injection or charge transport within the devices. Consequently, the maximum device efficiencies of 0.02 cd/A and 0.07 cd/A remained low.

As the inset of Figure 4-65 shows the electroluminescence spectra of the two tetrahydropyrene compounds at a current density of 1.0 kA/m<sup>2</sup> differ significantly. Devices using CTPY as light emitting layer show a structured molecular emission between 350 nm and 550 nm with a peak maximum at 422 nm and a weak shoulder around 375 nm. These spectra correspond to CIE1931 coordinates of  $x = 0.159$  and  $y = 0.046$ , thus being located in the deep blue region of the visible spectrum. For devices where tb-CTPY was the emitting material a narrower electroluminescence emission peak between 360 nm and 550 nm was detected. The emission maximum can be found at 425 nm. In addition to this part the EL-emission of tb-CTPY shows a small and slightly structured emission in the red spectral region around 620 nm. Similar EL features in polyvinylcarbazole (PVK) films have been attributed to electrophosphorescent emission.<sup>[311]</sup> The overall spectrum corresponds to CIE1931  $x = 0.193$  and  $y = 0.078$  which means a slight shift to the red compared to the EL-emission of CTPY but is still located in the far blue region of the visible spectrum.

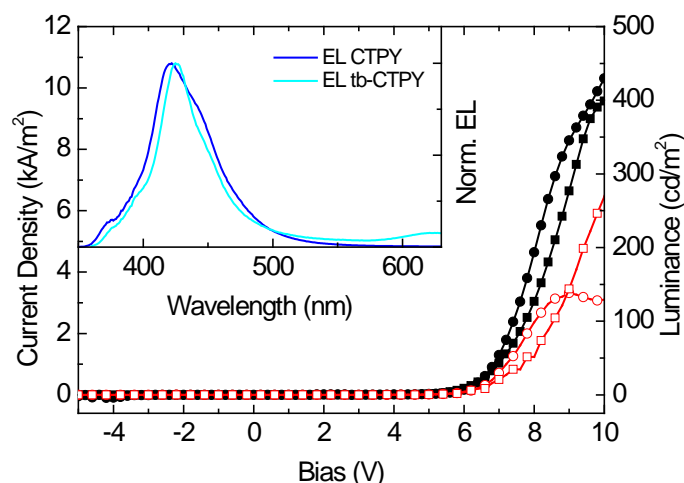


**Figure 4-65:** Current density (CTPY: line with filled circles; tb-CTPY: line with filled squares) / luminance (CTPY: line with open circles; tb-CTPY: line with open squares) as a function of the bias voltage of ITO/PEDOT:PSS/CTPY, tb-CTPY/TPBi/Ca/Al devices. The inset shows electroluminescence emission spectra of the same devices at a current density of 1.0 kA/m<sup>2</sup>.

Figure 4-66 shows the J-V-L characteristics of analogous devices in which CPY and tb-CPY are used as emitters. Maximum luminance values of 1076 cd/m<sup>2</sup> were obtained for the CPY device at 7.0 V and 316 cd/m<sup>2</sup> at 7.6 V for tb-CPY, respectively. The onset voltages of 4.0 V (CPY) and 4.2 V (tb-CPY) are somewhat smaller than when tetrahydropyrene-bridged molecules CTPY and tb-CTPY were used

as the active layer. However, the overall device efficiencies of 0.16 cd/A for CPY and 0.04 cd/A for tb-CPY still remain low and can again be attributed to an unbalanced charge-carrier transport in the active materials. The EL-spectra in the inset of Figure 4-66 show a broad and slightly structured EL emission peak for compound CPY in the range 410-570 nm with its maximum at 435 nm and a distinct shoulder around 455 nm. The spectrum corresponds to CIE1931 coordinates  $x = 0.151$  and  $y = 0.092$  (deep blue). A comparison to literature about PVK<sup>[312]</sup> and pyrene based compounds<sup>[66,235,313]</sup> suggests that the shape of the EL-spectrum is based on fluorescent emission from both, the carbazole as well as the pyrene-part of the compound CPY. For compound tb-CPY a narrow and structureless molecular emission peak between 410 nm and 525 nm, peaking at 435 nm can be observed, resulting in  $x = 0.156$  and  $y = 0.044$  (CIE1931), at the far blue end of the visible spectrum. None of the reported devices exhibited any sign of excimer emission.

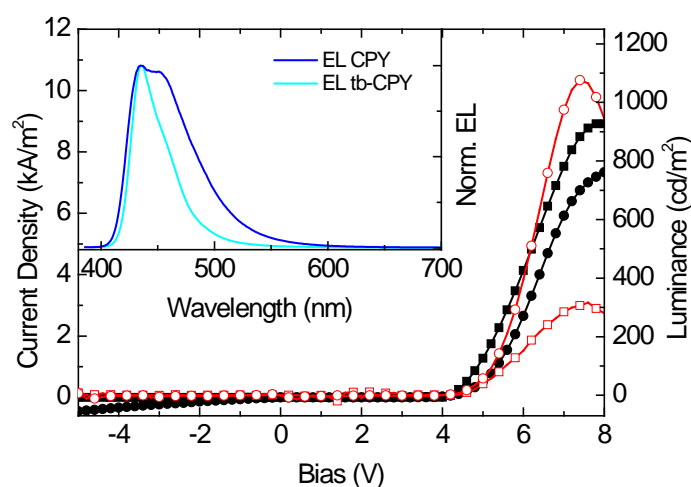


**Figure 4-66:** Current density (CPY: line with filled circles; tb-CPY: line with filled squares) / luminance (CPY: line with open circles; tb-CPY: line with open squares) as a function of the bias voltage of ITO/PEDOT:PSS/ CPY, tb-CPY /TPBi/Ca/Al devices. The inset shows electroluminescence emission spectra of the same devices at a current density of 1.0 kA/m<sup>2</sup>.

The device results demonstrate that the tetrahydropyrene and pyrene-bridged compounds are in principle suitable emitting materials for deep-blue OLEDs. While brightness levels and efficiencies are low, compared to state-of-the-art multilayer electrophosphorescent devices employing iridium-based emitters,<sup>[314,315]</sup> some of the presented devices compare reasonably well to blue electrofluorescent devices with comparably simple device architectures, such as devices reported based on dendronized or polymerized pyrene derivatives (c.f. chapters 4.3-4.6).

#### 4.7.6 Conclusion

In conclusion a new class of carbazolepyrene derivatives where carbazole moieties were attached at the 2,7-position of a pyrene molecule were presented. In addition, the dependence of the photo-physical characteristics on exchange of the pyrene bridge by tetrahydropyrene and on an attachment of *tert*-butyl groups to the 3,6-position of the carbazole entity were assessed. It was demonstrated that the PL emission of tetrahydropyrene compounds is considerably blue-shifted in comparison to their pyrene counterparts, due to a lower conjugation. Moreover, the attachment of *tert*-butyl groups leads to a narrower emission of the respective materials, which can be explained by a lesser molecule-molecule interaction due to steric hindrance. AFM investigations showed that, even when evaporated small molecules showed a higher surface roughness, all materials are in principle suitable as light emitting layer for OLEDs. Finally, both tetrahydropyrene and pyrene derivatives have been used

successfully as blue fluorescent emitters in simple OLED architectures. Moreover, these molecules may also have applications as hole-transporting materials and perhaps as hosts for green phosphors in OLEDs.

## 4.8 Molecular Triangles: Blue Emission of Cyclic Triphenylene Trimers

The content of this chapter is published in: Matthias G. Schwab, Tianshi Qin, Wojciech Pisula, Alexey Mavrinskiy, Xinliang Feng, Martin Baumgarten, Hun Kim, Frédéric Laquai, Sebastian Schuh, Roman Trattnig, Emil J. W. List and Klaus Müllen, *Chemistry – An Asian Journal*, **2011**, *6*, 3001-3010.

The author of the thesis co-authored to this publication. Exclusive contributions: device assembling and device characterization. Collaborative contributions: photophysical investigations and discussion of the attained results. M.G.S. has written the publication. The author of the thesis contributed significantly to the physics related results (photophysics and devices) and accordingly expanded the publication text in this chapter.

### 4.8.1 Introduction

Besides, pyrene and fluorene, which were already introduced as suitable chromophores for organic light emitting devices, triphenylene was shown to play an important role in pyrene-cored dendrimers in chapter 4.6. In these dendrimers, TP was used as a functional unit that significantly contributes to an enhancement of the photoluminescence quantum yield of the respective molecules due to an efficient excitation energy transfer to the pyrene core. In contrast, in this current section the emission of TPs themselves as building blocks for cyclic macromolecules is investigated.

Triphenylene is a polycyclic aromatic hydrocarbon (PAH) that has been widely studied in chemistry and material science. The triangular molecule is built from four annelated benzene units and owes its particular chemical stability to the fully benzenoid character of the aromatic system.<sup>[316,317]</sup> TP chemistry is well developed and various strategies for the build-up of substituted derivatives are available.<sup>[318,319]</sup>

A considerable interest in monomeric TP derivatives arised, when their liquid-crystalline nature was first reported by Billard et al. in 1978,<sup>[320]</sup> triggering extensive research efforts on 2,3,6,7,10,11-hexasubstituted TP mesogens in particular.<sup>[321–326]</sup> Liquid-crystallinity is driven by the strong  $\pi$ -stacking tendency of the planar TP core and *van der Waals* interactions of lateral side chains. Additionally, polymers<sup>[327–329]</sup> and dendrimers<sup>[273,313,330]</sup> based on TP are known to exhibit a distinct self-assembling behavior. The second major field of application deals with the optoelectronic properties of the molecule. TP is a famous blue-emitter and has recently been investigated in organic optoelectronic devices.<sup>[273,328,329,331–333]</sup> Interestingly, only few macrocycles containing TP have been reported and little is known about the self-assembling of these cyclic systems in solution, on surfaces and in the bulk state so far.<sup>[334–337]</sup> Moreover, only moderate PLQYs are reported for monomeric TPs<sup>[274]</sup> and thus it is not clear if and to what extent a direct linkage of three TP units in a cyclic arrangement is able to boost the light generation efficiency. It is presumed that putting TPs in a cyclic arrangement will enhance the transition dipole moment of the otherwise symmetry forbidden  $S_0 \rightarrow S_1$  transition.<sup>[280]</sup> This presumption is based on similar approaches, where the symmetry in the TP was broken by means of mono-functionalization using cyano-substituents leading to a three-fold increase in the luminescence yield<sup>[338]</sup> or by symmetric methyl substitution forcing the molecule to adopt a twisted conformation instead of a symmetric planar one.<sup>[339]</sup>

The current section of the thesis reports on a set of three novel cyclo-7,10-tris-tri-phenylenyl macrocycles (CTP1, CTP2, CTP3, Figure 4-68) that are based on a cyclic linkage of three functional TPs, resulting in the formation of triangular-shaped molecules. The fully planar derivative CTP1 thereby revealed pronounced self-assembling behavior, which was analyzed by 2D wide-angle X-ray scattering to study the liquid crystallinity of this new discotic mesogen in the bulk state. Moreover, the

nonplanar, laterally substituted derivatives CTP2 and CTP3 were successfully tested as blue emitting components in organic light-emitting diodes. For these molecules, intermolecular packing was suppressed efficiently by a substitution with sterically demanding phenyl groups, thus preventing undesired quenching effects.

#### 4.8.2 Synthesis of Macrocycles

The synthesis was performed at the MPI under a two-fold motivation. Firstly, a strong propensity to self-assembling can be anticipated due to the flat dodecyloxy-substituted core of macrocycle CTP1. Columnar mesophases adopted by discotic molecules are of great interest because of the possible application of such highly organized structures in organic electronics.<sup>[322,324,340,341]</sup> Secondly, in contrast to the desired strong intermolecular packing of CTP1, the two derivatives CTP2 and CTP3 were designed to be used as fluorophores in OLEDs. In these devices, as shown, the aggregation in the solid state generally needs to be prevented in order to avoid self-quenching effects arising from intermolecular packing as well as bathochromic shifts in the emission spectrum due to excimer formation.<sup>[342,343]</sup> The versatility of the presented design concept has been demonstrated already for polymeric<sup>[328]</sup> and dendritic<sup>[273]</sup> materials containing TP units of identical topology (c.f. chapter 4.6). Consequently, shorter alkyl chains and additional twisted benzene units characterize macrocycles CTP2 and CTP3. Furthermore, six regularly distributed propyl chains are attached to the TP-core for CTP2 whereas a statistic hexyl substitution pattern is applied to CTP3 in order to further suppress the aggregation of this molecule.

In the first step two functionalized TP precursors **4** and **8a/8b** were prepared according to the two synthetic routes depicted in Figure 4-67. The functionalized TP **4** was built from 1,2-dibromo-4,5-bis(dodecyloxy)benzene **1**<sup>[344]</sup> by adopting a reported procedure for analogous alkyl-derivatives.<sup>[345]</sup> A double *Suzuki-Miyaura* coupling of **1** with phenyl boronic acid yielded the functionalized *ortho*-terphenyl **2**. The key step of this route consisted in the build-up of the TP backbone *via* oxidative photocyclization of **2** yielding 2,3-bis(dodecyloxy)triphenylene **3** in 73 % which can be considered a model compound for the macrocycle itself. The final bromination towards 7,10-dibromo-2,3-bis(dodecyloxy)triphenylene **4** was achieved by treatment of **3** with bromine in the presence of catalytic amounts of iron and iodine.

For the synthesis of the second precursor **8a/8b** another strategy had to be applied because of the different molecular topology compared to **4** (Figure 4-67). The synthetic route started with a bromination of phenanthrene-9,10-dione **5** according to a literature-established route.<sup>[346]</sup> A subsequent *Knoevenagel* condensation of 3,6-dibromophenanthrene-9,10-dione **6** with diphenylacetone gave the functionalized phencyclone derivative **7**. In a final *Diels-Alder* cycloaddition of **7** with oct-4-yne or oct-1-yne the functionalized TPs **8a** (symmetric) and **8b** (asymmetric) were obtained in high yields, respectively.

The cyclotrimerization reaction towards the cyclo-7,10-tris-triphenylene macrocycles CTP1, CTP2 and CTP3 was achieved following standard *Yamamoto* conditions.<sup>[347,348]</sup>

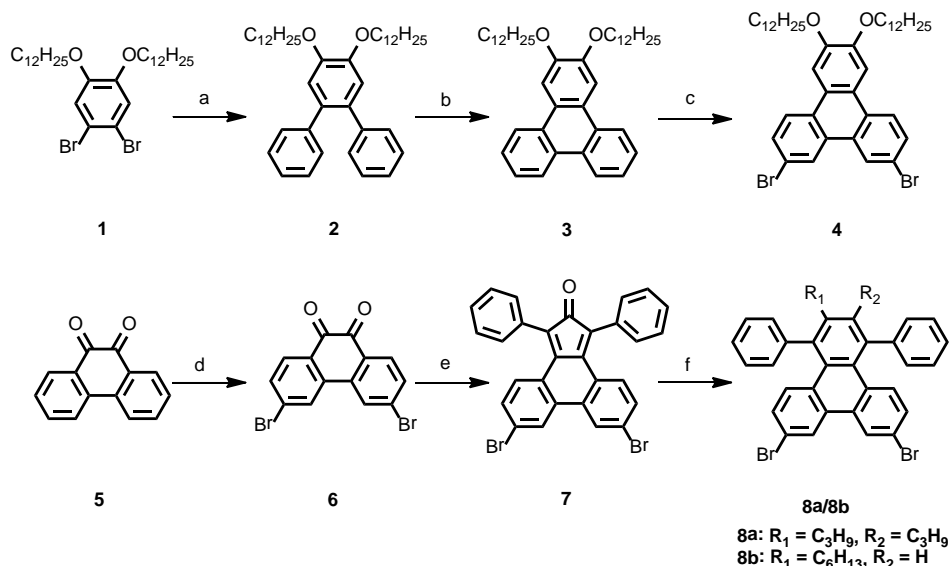


**Figure 4-67:** Synthetic route to the macrocycle precursors **4** and **8a/8b**. (a) phenylboronic acid,  $Pd(PPh_3)_4$ ,  $K_2CO_3$ , dioxane ( $100^\circ C$ ); (b)  $hv$ ,  $I_2$ , propylene oxide, toluene (RT); (c)  $Br_2$ ,  $Fe/I_2$ , ( $-5^\circ C$ ); (d)  $hv$ ,  $Br_2$ , nitrobenzene ( $100^\circ C$ ); (e) 1,3-diphenylpropan-2-one,  $KOH/MeOH$  ( $80^\circ C$ ); (f) **8a:** oct-4-yne, diphenyl ether ( $220^\circ C$ ), **8b:** octy-1-ene, *ortho*-xylene, ( $170^\circ C$ ).

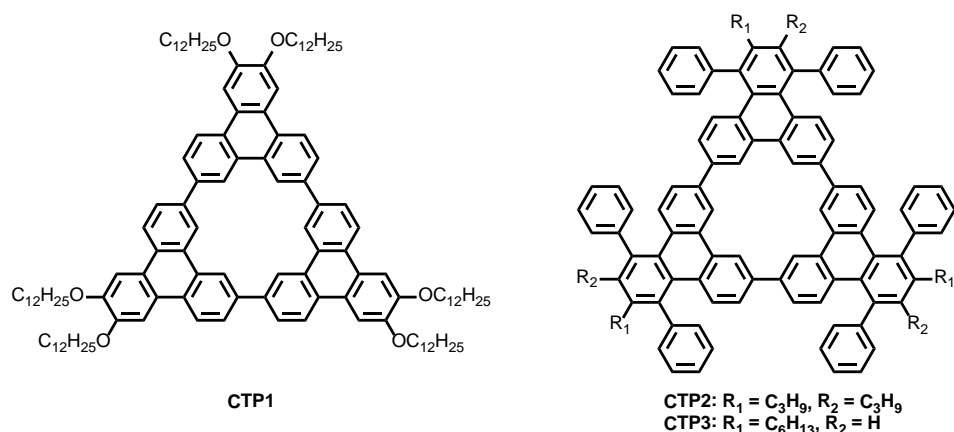


**Figure 4-68:** Chemical structures of macrocycles **CTP1** (left) and **CTP2, CTP3** (right)

Quantum chemical calculations (B3LYP, 6-311G\*)<sup>i</sup> carried out on macrocycle **CTP1** indicated a propeller-like structure of  $C_3$  symmetry. As seen in the side view representation in Figure 4-69, this manifests in a dihedral angle of  $24.0^\circ$  between two neighboring TP units. A cavity diameter of  $5.9 \text{ \AA}$  was derived. Similar geometric parameters ( $22.2^\circ$ ,  $5.9 \text{ \AA}$ ) were found for the core of **CTP2** and **CTP3** (Figure 4-69). Yet, the aforementioned twisted arrangement of the lateral benzene rings is clearly visible and in addition leads to a bent, non-planar conformation of the three TP units itself.

<sup>i</sup> Quantum chemical calculations were performed at the MPI by DFT approach with B3LYP hybrid functionals.



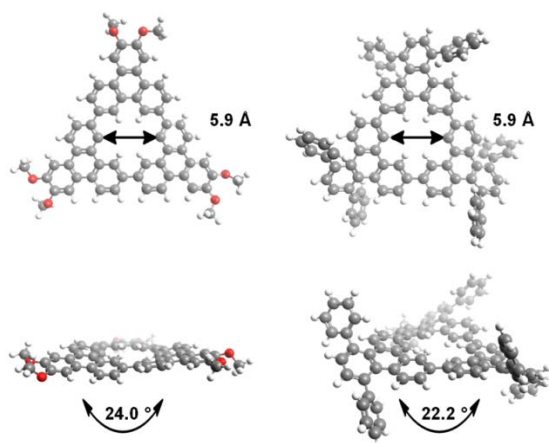


Figure 4-69: Conformation and geometric parameters of macrocycles CTP1 (left) and of the core of CTP2/CTP3 as derived from quantum chemical analysis (side chains omitted).

### 4.8.3 Liquid Crystallinity of CTP1

Monomeric, alkyl-substituted TPs have been widely studied in the field of discotic liquid crystals due to the formation of mesophases that are characterized by a high ordering degree.<sup>[321,322,324–326]</sup> This structural perfection is caused by the highly symmetric, disc-like aromatic core of TPs favoring liquid-crystallinity when attaching peripheral alkyl chains. Macrocycle CTP1 exhibits several important features of TP-based liquid crystals like the common triangular architecture and the positioning of six alkoxy substituents in the periphery of the molecule. Thus, 2D-WAXS experiments determined the bulk phase properties of CTP1 and were correlated to results from thermal analysis by differential scanning calorimetry (DSC) (Figure 4-70).

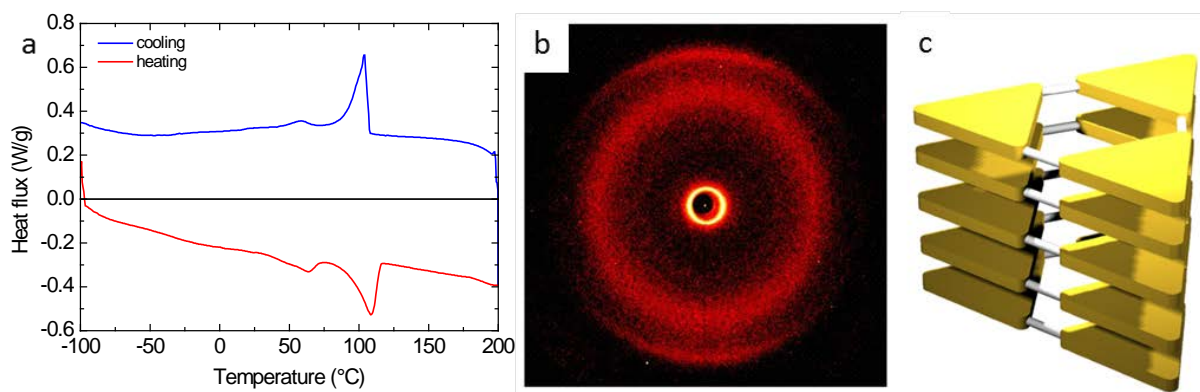


Figure 4-70: DSC trace of CTP1 (a) upon heating (red) and cooling (cyan); 2D-WAXS patterns of an extruded fiber of CTP1 (b) at 130 °C; schematic illustration of the proposed molecular packing of CTP1 in columnar structures (c, side chains are omitted for clarity).

The DSC trace upon heating showed two fully reversible phase transitions at  $T_{H1} = 64.3^\circ\text{C}$  and at  $T_{H2} = 109.1^\circ\text{C}$ . Both were found to reappear during cooling as exothermic transitions at  $T_{C1} = 55.5^\circ\text{C}$  and  $T_{C2} = 103.6^\circ\text{C}$ , respectively (Figure 4-70a). 2D-WAXS measurements carried out on a mechanically extruded fiber of CTP1<sup>[349]</sup> indicated that above the phase transition temperature of  $109.1^\circ\text{C}$  a liquid crystalline hexagonal columnar organization ( $Col_h$ ) is adopted.<sup>[322]</sup> The corresponding pattern (Figure 4-70b) revealed that the molecules pack in columnar structures assembled in a hexagonal unit cell. Characteristic for the liquid-crystalline phase, an amorphous halo appeared which can be attributed to the disordered dodecyloxy chains. Cooling down the sample to  $30^\circ\text{C}$ , this halo remained unaffected,

while the columnar arrangement changed to a rectangular unit cell. In comparison, in a monomeric TP containing an identical number of dodecyloxy chains<sup>[326]</sup> the transition to the hexagonal columnar mesophase  $Col_h$  occurred at a much lower temperature of 55°C and the clearing point was reached at 63°C. This indicates a significantly stronger aggregation of CTP1, which is corroborated by the fact that heating of the compound to temperatures of 400 - 450°C did not lead to the isotropization of the sample and was ultimately limited by the thermal decomposition of the macrocycle. A schematic illustration of the packing is shown in Figure 4-70c.

#### 4.8.4 Photophysics of CTP1, CTP2 and CTP3

To investigate the photophysical properties of CTP1, CTP2 and CTP3, which exhibit a strong difference in their degree of planarity and symmetry (c.f. Figure 4-69), the basic optical properties and aggregation behavior have been characterized in solution and thin films with respect to their absorption properties, PL emission and PLQY (Figure 4-71). All relevant data is summarized in Table 6. With respect to the absorption spectrum of PAHs, according to Clar,<sup>[316]</sup> the occurring absorption bands can be classified as  $\alpha$ -,  $\beta$ -, and  $p$ -bands, respectively.<sup>[317]</sup> As in the case of parent TP,<sup>[350]</sup> these characteristic bands can be observed in the absorption spectrum of all macrocycles and appear at similar wavelength due to the common aromatic structure of the cyclic backbone (Figure 4-71). For the macrocycles in this chapter, the bands were detected at  $\lambda_\beta = 302$  nm,  $\lambda_p = 346$  nm and  $\lambda_\alpha = 386$  nm in the case of CTP1, at 311 nm, 346 nm and 377 nm for CTP2 and at 314 nm, 347 nm and 374 nm for CTP3, respectively. The high degree of vibronic fine structure that is found for CTP1 is also mirrored in the corresponding PL emission spectrum in solution as depicted in Figure 4-71. All three materials exhibit a PL emission in the deep blue range of the visible spectrum, which is close to the ideal value for blue emitting OLEDs.<sup>[273,313,329,331–333,351]</sup> The emission maxima are found at 421 nm, 422 nm and 430 nm for CTP1, CTP2 and CTP3, respectively. The observed bathochromic shift of the three PL spectra in comparison to monomeric TP with an emissions maximum located at 376 nm<sup>[350]</sup> as well as compared to the emission maximum of 1,2,4-triphenyltriphenylene (TTP) at 401 nm<sup>[273]</sup> can be clearly attributed to the cyclic conjugated arrangement.

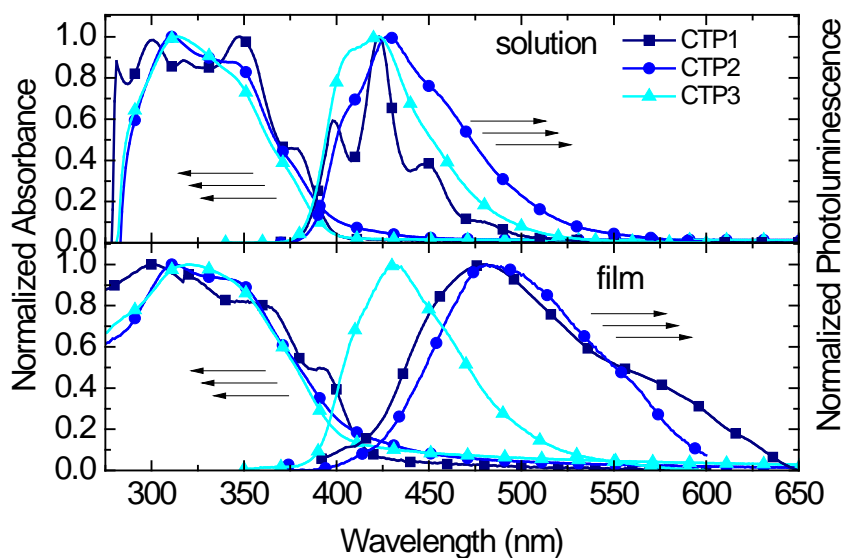


Figure 4-71: Normalized absorption and PL emission spectra of macrocycles CTP1, CTP2 and CTP3 in toluene (top) in thin film (bottom).

Thin film PL spectra (Figure 4-71) indicated significant differences in the characteristics of the three macrocycles. As clearly observed for CTP1 and CTP2 a dramatic bathochromic shift develops for the PL emission maxima from ca. 420 nm to 480 nm in thin film compared to toluene solutions. A severe broadening of the emission spectrum and a loss of the vibronic structure accompany the shift of the PL maximum. In contrast, for CTP3 with its three statistically arranged hexyl side chains only a very moderate red shift of 5 nm is detected for the emission maximum and no loss of the vibronic features is observed. A PLQY of 64% and 68% in toluene solution was determined for CTP1 and CTP2, respectively, while for CTP3 a PLQY of 38% was determined. In thin, film for CTP1 and CTP2, a significant decrease in PLQY is observed while for CTP3 no significant quenching of the PLQY in the solid state is measured (Table 6). CTP3 exhibits a PLQY, which is ca. 40 % of that of poly(fluorene), which exhibits a state of the art PLQY and documented good OLED performance. The drastically reduced PLQYs and the broadening of the PL emission in the solid state clearly suggest an aggregation of the CTP1 and CTP2 in the bulk state and excimer formation due to intermolecular packing.<sup>[333,343]</sup> Comparing the PLQY values of the cyclic triphenylenes in solution to those of parent TP<sup>[274]</sup> with 6.0% or to TPTP with only 3.8%,<sup>[273]</sup> an up to ten-fold improvement in the PLQY for the macrocyclic arrangement can be observed. This result clearly confirms the aforementioned presumption for this work aiming at the increase of the transition dipole moment of the otherwise symmetry forbidden  $S_0 \rightarrow S_1$  transition through a cyclic conjugated arrangement.<sup>[280]</sup> Thus, the PLQY of the TP unit is strongly enhanced while the emission maximum displays only a minor shift from the near UV to the deep blue region of the spectrum. Similar to other systems the oscillator strength of the emissive transition is enhanced by the macrocycle approach as the overall symmetry of the TP unit is effectively broken (Figure 4-69).<sup>[338]</sup> Additionally, the applied molecular design induces a contorted instead of a fully planar confirmation of the TPs (Figure 4-69), which further influences the transition dipole of the molecule.<sup>[339]</sup>

**Table 6: Summary of relevant optical properties macrocycles CTP1, CTP2 and CTP3.**

Compound	$\lambda_{em}^{max}$	$\Phi_{PL}$	$\lambda_{em}^{max}$	$\Phi_{PL}$
	[nm]	[%] <sup>a</sup>	[nm]	[%] <sup>b</sup>
	solution		film	
TP <sup>[274]</sup>	365	9%	-	-
TPTP <sup>[273]</sup>	401	4%	402	-
CTP1	421	68%	479	<1%
CTP2	422	64%	480	13%
CTP3	430	38%	425	43%

<sup>a</sup> taking quinine sulfate dehydrate as standard reference. <sup>b</sup> relative to polyfluorene.

#### 4.8.5 Electroluminescent Characteristics of CTP1, CTP2 and CTP3

Due to the extremely low PLQY of CTP1 in the solid state only the electroluminescent properties of CTP2 and CTP3 as active blue emitters were investigated in a standard solution processed OLED device configuration ITO/PEDOT:PSS/CTP2, CTP3/TPBi/Ca/Al. The corresponding results are shown in Figure 4-72 and Figure 4-73, respectively. From Figure 4-72 it is observed that the electroluminescence onset for the devices was detected at 4.3 V for CTP2 and 3.9 V for CTP3. The maximum luminance is found to be 578 cd/m<sup>2</sup> at 7.6 V (CTP2) and 200 cd/m<sup>2</sup> at 6.5 V (CTP3). CTP2 shows an unstructured molecular emission feature between 410 nm and 625 nm peaking at 479 nm that leads to a greenish emission with CIE1931 coordinates  $x = 0.191$ ,  $y = 0.303$ . CTP3 in contrast exhibits a slightly structured, narrow deep blue emission between 380 nm and 550 nm with a peak maximum at 428 nm which corresponds to CIE1931 coordinates of  $x = 0.158$ ,  $y = 0.062$  in the far blue region of the visible spectrum. The overall device efficiencies were typically below 0.15 cd/A for both

macrocycles. All fabricated devices from both compounds showed good stability over time (c.f. insets of Figure 4-72), yet a slight broadening of the emission can be seen for the EL spectrum of CTP3 after being operated at a constant current for 5 minutes due to thermal annealing under device operation.

A more pronounced difference concerning the stability of the emission characteristics of CTP2 and CTP3 was observed when the EL spectra were acquired at different current densities (Figure 4-73). While CTP2 manifests perfect spectral stability, a stable emission without any aggregation effects and related changes in the emission spectrum was observed for CTP3 only when keeping the current density in the device below  $2.0 \text{ kA/m}^2$ . Above this value, a red shift of the emission is detected which is attributed to a thermally induced reorganization/recrystallization of the active layer because of *Joule* heating during device operation.

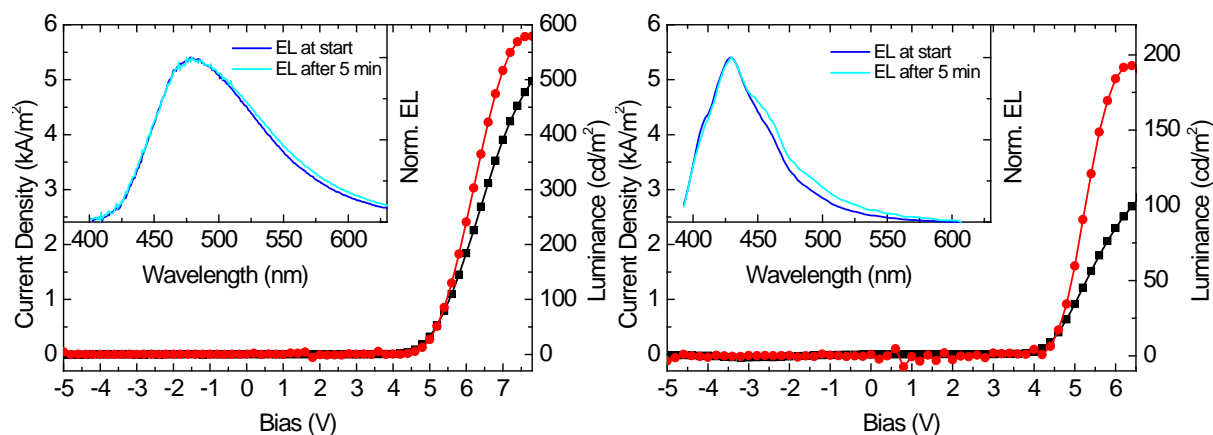


**Figure 4-72:** Current density (line with squares) and luminance (line with circles) as a function of the bias voltage in an ITO/PEDOT:PSS/CTP2/TPBi/Ca/Al device (left) and an ITO/PEDOT:PSS/CTP3/TPBi/Ca/Al device (right). The inset shows electroluminescence emission spectra of the same devices at a current density of  $1.0 \text{ kA/m}^2$ .

Benchmarking the attained device performance against results obtained for devices based on polymers<sup>[327–329]</sup> and dendrimers<sup>[273,330,352]</sup> using TP building blocks clearly shows that the cyclic TP trimers exhibit good improvement regarding the PLQY, an essential parameter of high performance OLEDs. Yet, a further improvement of the materials is needed with respect to their thermal stability to avoid reorganization/recrystallization before further device optimization work can take place to improve the overall device efficiency and luminance so that TP macrocycles can be considered for solution processed small molecule OLED applications.

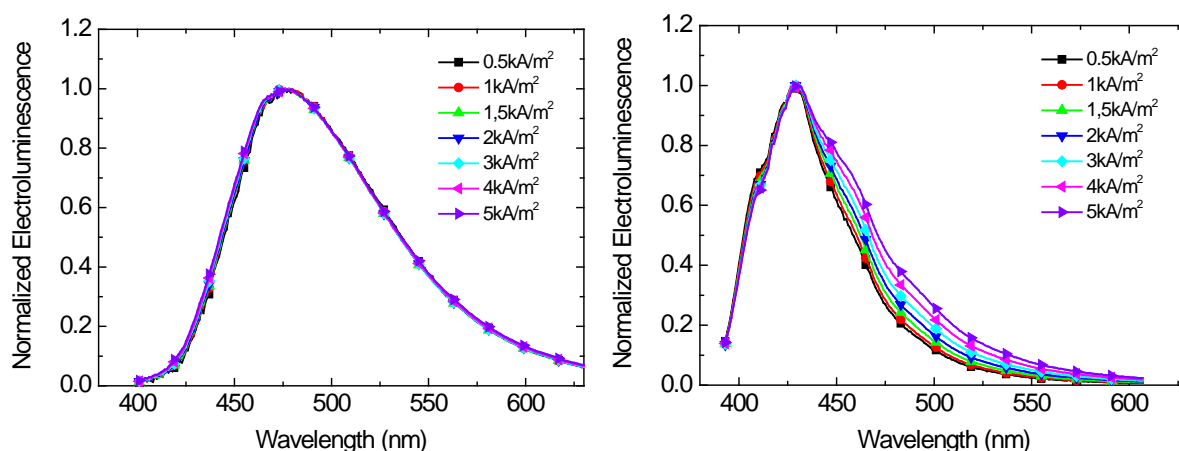


**Figure 4-73:** Current density dependent EL-spectra of an ITO/PEDOT:PSS/CTP2/TPBi/Ca/Al device (left) and an ITO/PEDOT:PSS/CTP3/TPBi/Ca/Al device (right).

#### 4.8.6 Conclusion

In summary, three novel cyclo-7,10-tris-triphenylene macrocycles in which the TP units are directly linked to each other were presented. It was shown that by introducing long alkoxy side chains to the core of the macrocycle a strong self-assembling behavior can be induced for CTP1 that is in analogy to the properties of monomeric alkyl-substituted TPs. 2D-WAXS was used to study the liquid-crystallinity of the discotic molecule and correlated to its thermal properties. The results demonstrated liquid crystalline character and stable molecular packing up to high temperatures. A comparative study of the optical properties of the three cyclic trimers revealed significant differences, which could be correlated to the nature of the peripheral groups and their substitution pattern. On the one hand, all three compounds showed deep blue emission in solution and an up to ten-fold increase in the PLQYs with respect to parent TP that results from the conjugation along the cyclic structure. On the other hand, only for CTP3 the intrinsic intermolecular packing tendency could be sufficiently disrupted in order to sustain the favorable PL properties in the solid state. CTP2 and CTP3 were tested successfully as light emitting material in the emissive layer of an OLED and showed promising performance regarding, both emission properties and device stability. For future molecules, however, a suppression of the observed thermal reassembly and consequential change in emission color at high driving currents needs to be addressed.

## 4.9 Conclusions – Organic Light Emitting Devices

The focus of the presented chapter is set on the investigation of photophysical properties of blue light-emitting materials – polymers, dendrons, small molecules as well as macromolecules – and their suitability as emitting component in blue emitting OLEDs. The assessment of the respective material properties was performed by means of absorption and photoluminescence studies, photo induced absorption spectroscopy, atomic force microscopy, photoelectron spectroscopy as well by optoelectrical characterization in OLEDs assembled with the particular compounds.

At first (chapter 4.3) a novel blue light emitting pyrene based polymer, PPyr, is introduced, which exhibits stable blue emission in solution as well as in the solid state. Thereby it is shown that the extraordinary spectral stability of this polymer is based on its specific molecular conformation. In particular, the results of this chapter evidence that due to a 1-3 linking of the pyrenylene monomer units and the attachment of a sterically demanding *tert*-butyl group to the 7-position of the molecule a high dihedral angle between adjacent monomer units is provoked. As a result, the well-known  $\pi$ -stacking of pyrene molecules is fully prevented and no altering of the emission characteristics caused by the formation of aggregates or excimers occurs, even when the material is annealed at elevated temperatures.

In chapter 4.4 a more detailed photo-physical investigation on PPyr as well as on PPyrTPA – a PPyr derivative with 3% of triphenylamine groups statistically distributed over the polymer strand – is presented. The individual studies reveal that the desired properties of PPyr, like spectral and morphological stability, are preserved for PPyrTPA. Furthermore, it is shown that the solvent polarity is able to considerably influence the position of the fluorescence emission spectrum and needs to be considered in order to prevent possible charge transfer states in the material that cause a red-shift of the overall emission color. Important parts of chapter 4.4 constitute time resolved photoluminescence and PIA spectroscopy studies on PPyr. While the pyrene molecule exhibits exceptionally long lifetimes for triplet as well as for singlet excited states they are considerably reduced in PPyr. In fact it is demonstrated that the respective lifetimes in PPyr thin films are in the same order of magnitude than for comparable PPP-type polymers. UPS measurements on PPyr and PPyrTPA finally unveil that the high dihedral angle between adjacent monomer units in the presented pyrene based polymers not only prevents excimer formation, but also limits the electronic interaction between the different monomer units on the same chain. This conditions lead to highly fluorescent blue emitting polymers PPyr and PPyrTPA, which exhibit photoluminescence quantum yields in solution of 77% and 88%.

In the course of chapters 4.3 and 4.4 the electro-optical properties of PPyr and PPyrTPA are assessed as well. While the former chapter presents first results for non-optimized single layer PLEDs utilizing the novel material as emitter, chapter 4.4 presents a first device optimization by the insertion an electron transport layer to the device assembly. As a result, considerably enhanced maximum luminance and efficiency values are achieved for PPyr and are even excelled by PPyrTPA PLEDs. Yet, the overall device efficiencies as well as UPS measurements evidenced that in order to realize highly efficient devices, the device assembly needs for significant modifications. This issue is actually addressed in chapter 4.5, wherein the realization of a fully solution processed triple-layer device assembly is demonstrated. The successive deposition and layer formation of different materials from solutions without redissolving of already existing layers thereby is based on the approaches of thermal layer stabilization as well as orthogonal solvents. The feasibility of these tactics is illustrated by detailed AFM studies. Moreover, UPS investigations evidence a favorable energy level alignment in the presented assembly which culminates in the presentation of bright and efficient blue light emitting PLEDs which exhibit a maximum luminance of 16540 cd/m<sup>2</sup> and an efficiency of 1.42 cd/A.

The fact that the successful utilization of pyrene as light emitting chromophore in OLEDs is not exclusively limited to specifically designed polymers is demonstrated in chapters 4.6 and 4.7. In

particular, chapter 4.6 presents the insertion of pyrene as core molecule in polytriphenylene dendrimers. The highly sophisticated molecular core-shell design of these molecules thereby enables an efficient Förster resonant energy transfer from the triphenylene shell to the pyrene core which results in high photoluminescence quantum yields of up to 88%. Moreover, an exceptional spectral and morphological stability upon various thermal annealing procedures is found for the dendritic molecules. Enhanced charge injection and charge transport properties in the pyrene-cored dendrimers are achieved finally by the attachment of triphenylamine groups to their surface and form the basis for the realization of dendrimer light emitting devices. An assessment of the basic electro-optical properties reveals deep blue emission for all dendrimers under investigation. At last the realization of multilayer DLEDs is shown, based on the same strategy as presented for PPyrTPA PLEDs, yielding blue emitting DLEDs with a maximum luminance of 9242 cd/m<sup>2</sup> and an efficiency of 0.85 cd/A.

A novel class of pyrene-carbazole derivatives is presented in chapter 4.7. The chapter discusses in detail the dependence of the photo-physical and electro-optical characteristics of the respective compounds on the substitution of a pyrene bridge by tetrahydropyrene and on the attachment of tert-butyl moieties as solubilizing side groups. Preliminary OLEDs show that all components exhibit blue EL emission and might be utilized either as hole transport materials or as host materials for phosphorescent compounds in OLED applications.

With triphenylenes a totally different chromophore is utilized as the source for blue light emission in chapter 4.8. Therein a comparative study of macromolecules comprising a cyclic assembly of three triphenylenes reveals that the optical properties are strongly depending on peripheral groups attached to the macrocycles and their respective substitution pattern. In particular, an attachment of long alkoxy groups results in the formation of a strong self-assembling behavior, which strongly quenches fluorescence for one compound. Molecules bearing short alkyl groups, statistically attached to the triphenylene core in contrast show clear blue emission. OLEDs fabricated with the blue emitting molecule showed promising results with respect to emission properties and device stability, yet for future applications an adaption of the molecular structure needs to be applied in order to prevent reassembling of the molecules during operation, which results in a change of the emission color.

## 5 Organic Photovoltaics

### 5.1 Introduction

In times when a raising amount of extraordinary climatic events is witnessed, an intelligible increased interest in the search for their causes arises. One identified originator, at least by parts, is global warming due to the greenhouse effect and in this regard, the high volume of carbon dioxide emission. Thus, the call and need for affordable and efficient sources of sustainable energy is particularly loud. One of the most important roles in this context aside wind, biomass and hydropower can be attributed to photovoltaic technologies. This is evidenced not at least by the increasing amount of global annual photovoltaic installations over the last decade. (Figure 5-1)

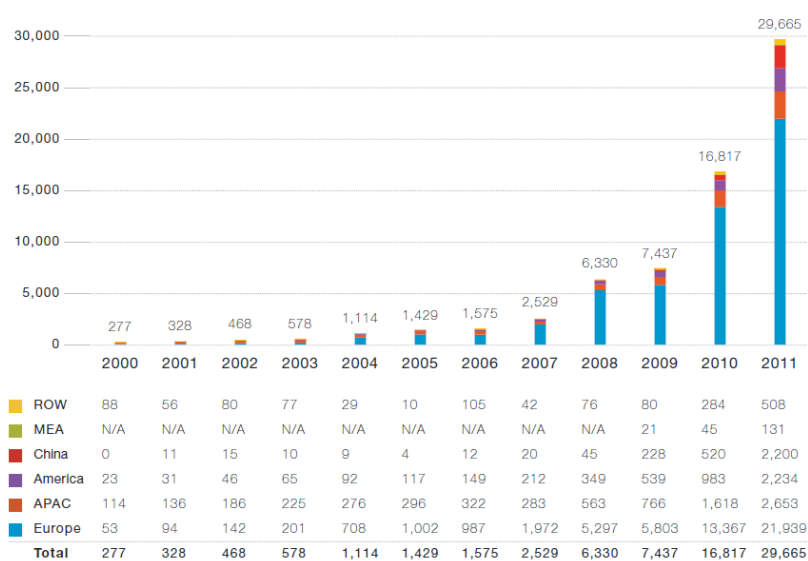


**Figure 5-1: Development of the global annual photovoltaic installations in MW. ROW... Rest of the World, MEA... Middle East and Africa, APAC...Asia Pacific. (modified from [353])**

Despite this impressive development, PV is by far not yet competitive to fossil fuel. Up to now the production of PV cells and modules, and in this respect due to its market leadership especially silicon-based technologies are far too expensive.

Organic solar cells might constitute a promising candidate to lead a way out of this dilemma. A lot of effort has been undertaken in this field of research since the first report on a heterojunction solar cell by Tang et al.,<sup>[26]</sup> who was able to demonstrate the importance of a heterojunction – i.e. an interface between two different semiconducting materials – regarding efficient charge carrier generation. Major improvements to the devices' PCE were achieved by blending one semiconducting material into another<sup>[354]</sup> creating so called bulk heterojunction devices and with the realization of polymer:fullerene BHJ solar cells<sup>[28]</sup> the final breakthrough for organic solar cells was achieved in the scientific community.

The main potential for success of organic solar cells – especially of polymer-based devices – results from some fundamental advantages compared to their inorganic counterparts. The probably most important one can be found in the high absorption coefficient of typical conjugated polymers, which enables strong light absorption already for thin layers in the range of 100 nm, whereas typical Si based solar cells need a thickness of about 100  $\mu\text{m}$  in order to absorb about 90% of the incoming light.<sup>[355]</sup> Another important benefit of polymer solar cells is, as in the case of OLEDs, that they can be



assembled by solution-based processing techniques and do not need for high temperature steps during production. These properties thus, in principle, allow for large area, low cost and high throughput device fabrication via gravure-printing<sup>[356]</sup> or roll-to-roll processing.<sup>[357]</sup>

Yet, despite the vast amount of scientific effort and their fundamental advantages compared to inorganic solar cells, OSCs still do not play a significant role on the market. This fact primarily results from the still rather low efficiencies of these organic devices. Even if BHJ solar cells containing small molecular semiconducting materials have already reached power conversion efficiencies of up to 12%,<sup>[38]</sup> these efficiency values are still considerably lower than for silicon based devices (Figure 5-2).<sup>[358]</sup>

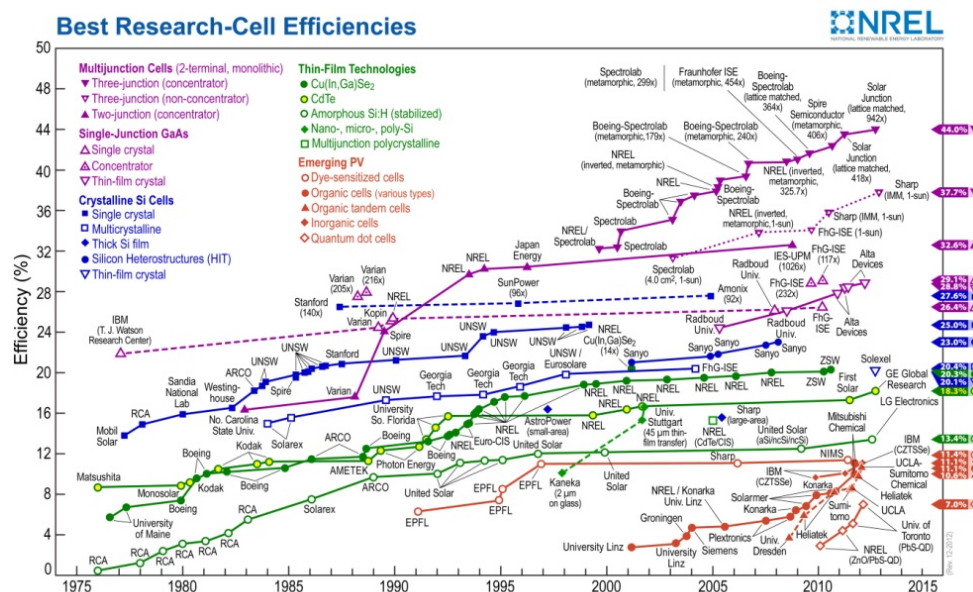


**Figure 5-2: Development of best research cell efficiencies for inorganic as well as organic solar cells. (from [358])**

In contrast to organic solar cells, single crystal silicon solar cells with a PCE of 27.6% already significantly approach their theoretically upper limit of 32% predicted by Shockley and Queisser.<sup>[359]</sup> The Shockley-Queisser limit thereby is estimated based on two considerations: Firstly, only incident photons having energies above the bandgap of the semiconducting material are absorbed in the device and contribute to the charge generation process. Secondly, all excess energy of the photons exceeding the band-gap is lost for charge generation, but dissipates as phonons in the material.<sup>[360]</sup> An application of this concept to organic solar cells yields in principle a limit that can even be found above the Shockley-Queisser limit for inorganic solar cells. However, for organic materials the calculation of the theoretical limit has to be adapted since the conjugated compounds, despite their high absorption coefficients, usually only show narrow absorption bands, which automatically reduce the maximum efficiency limit.<sup>[361]</sup> Nevertheless, an exemplary calculation of the Shockley-Queisser limit for organic solar cells exhibiting an absorption width of 300 nm and an external quantum efficiency of 100% is shown in Figure 5-3 and yields a maximum PCE around 20%, which is a twofold of the currently highest reported PCE for OSCs.

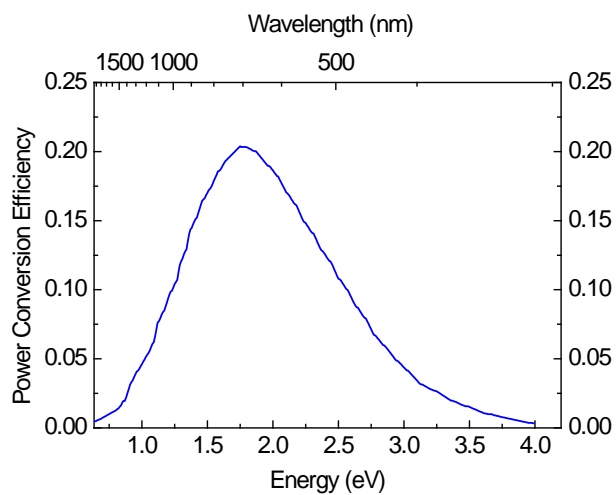


**Figure 5-3: Theoretical efficiency limit for organic solar cells exhibiting an absorption width of 300 nm and an EQE of 100%. (modified from [361])**

## 5.2 Nanocomposite Solar Cells – In-situ Formation of Inorganic Nanoparticles and their Potential in MDMO-PPV:CIS Hybrid Cells

### 5.2.1 Introduction to Nanocomposite Solar Cells

According to the aforementioned considerations regarding the theoretical upper limit for (organic) solar cell efficiency, one route to enhance the current efficiencies opens by a broadening of the absorption width of the photoactive material, i.e. the material where excitons are created by photons.

Precisely this strategy is employed in nanocomposite solar cells, which are also called hybrid solar cells and have attracted a considerable amount of attention during the recent years.<sup>[362–364]</sup> In these solar cells, which typically comprise a BHJ structure, the photoactive layer consists of both, an organic conjugated polymer and an inorganic semiconductor. In this assembly, the polymer usually serves as electron donating compound – the donor – and the inorganic, in general nanocrystalline material is the electron accepting component – the acceptor.

In that context a large number of possible inorganic materials have already been reported for NCSCs. Applications containing metal oxides like titanium dioxide (TiO<sub>2</sub>)<sup>[365–367]</sup> and zinc oxide (ZnO)<sup>[368–370]</sup> were as well presented as metal sulphides like cadmium sulphide (CdS)<sup>[371–373]</sup>, copper indium disulphide (CuInS<sub>2</sub>)<sup>[374,375]</sup> lead sulphide (PbS)<sup>[376]</sup> or metal selenides like cadmium selenide (CdSe)<sup>[377–379]</sup> copper indium diselenide (CuInSe<sub>2</sub>)<sup>[32,380]</sup> and lead selenide (PbSe).<sup>[381]</sup> The main reason for the attraction of NCSCs and their in principle main advantage compared to OSCs thereby is based on their possibility to harvest light across the whole spectrum of visible light, which should lead to an enhanced PCE.<sup>[382]</sup> In particular, inorganic nanoparticles offer the potential to harvest light down to the near-infrared region, while conjugated polymers feature extraordinary high absorption yields in the visible part of the spectrum.<sup>[383]</sup> A further advantage of inorganic nanoparticles, in comparison to fullerene derivatives used in polymer solar cells, is that they offer higher absorption coefficients and thus are able to harvest light more efficiently. Beyond that, the absorbance characteristics of inorganic nanoparticles can be fine-tuned due to the quantum size effect<sup>[384]</sup> and the inorganic compound hence can be tailored specifically in size and shape (dots, rods, branched structures)<sup>[385–389]</sup> to complement the absorption and charge transport properties of the polymer.<sup>[390,391]</sup> At last, the nanoparticles offer the potential to generate more than one electron per absorbed photon.<sup>[382,392]</sup> Based on all these properties inorganic nanoparticles not only provide a tool for the realization of optoelectronic layers with enhanced light harvesting properties but, in combination with an improved charge transport, power conversion efficiencies of NCSCs should be able to exceed those of polymer:fullerene solar cells.

At the same time the fundamental fabrication methods that constitute the characteristic advantages of polymer solar cells compared to inorganic devices, such as slot-die or gravure-coating are preserved and further allow low-cost roll-to-roll production technologies on light weight and flexible substrates.

This section of the current thesis reports on a complete route towards the realization of highly efficient polymer–copper indium sulphide (CIS) NCSCs. The synthesis of novel precursor materials, the photophysical characterization of the respective CIS nanocrystals as well as their interplay with a poly(phenylene-vinylene) derivative in thin films as well as in NCSCs is presented. The fabricated solar cells offer various technically important features. First, the active layers are prepared in a direct, in situ, single step without utilization of capping ligands for nanoparticle stabilization. Second, the nanocomposite layers show extended absorption characteristics due to a contribution of the polymer as well as of the nanoparticles. Lastly, a significant contribution of the inorganic component to photocurrent generation can be deduced from external quantum efficiency investigations on the as presented fabricated NCSCs.

## 5.2.2 Experimental

Transmission electron microscopy (TEM) investigations were conducted at the *Institute for Electron Microscopy and Fine Structure Research (FELMI)* at the Graz University of Technology. Therefore solar cell devices were sectioned and thinned using focused ion beam (FIB) lift out specimen preparation technique.<sup>[393]</sup> TEM investigations were conducted on a Tecnai F20 microscope (FEI Company, 200 kV, Schottky emitter), a Gatan GIF Quantum energy filter system, an UltraScanCCD camera and a Gatan model 806 HAADF STEM Detector.

## 5.2.3 Nanoparticle Formation Approaches

Polymer:nanoparticle nanocomposite films generally are realized by two different strategies. Either the nanoparticles are grown lithographically or by molecular beam techniques and subsequently blended into a polymer solution or they are synthesized *via* a chemical approach, where the particles are grown in various (polymer-)matrices or by methods of colloidal chemistry.<sup>[394]</sup> The limiting factor for the former approach is given by the high tendency of the nanoparticles to aggregate due to their high surface energy. Thus, it is in general difficult to dissolve and disperse the inorganic semiconductors in polymer solutions. Caused by this aggregation propensity the synthetic approach is by far more common. In this strategy the solubility of the nanoparticles is achieved by capping ligands like oleylamine,<sup>[384,395]</sup> triphenylphosphite<sup>[33]</sup> or trioctylphosphite.<sup>[389,396]</sup> However, the attached capping ligand sphere often proves to be disadvantageous or even isolating with respect to charge separation at the polymer/nanoparticle interface and for charge transport in the inorganic semiconductor, respectively.<sup>[397]</sup> Consequently, additional procedures are necessary in order to remove the excess capping agent<sup>[398,399]</sup> or at least to substitute bulky ligands by smaller ones.<sup>[390]</sup> Applying these strategies, polymer:CdSe solar cells have already been reported and achieved PCEs above 3%.<sup>[388,391,400–402]</sup>

In contrast to the aforementioned strategies, an in-situ formation of nanostructures in a conjugated polymer matrix bears the advantages of avoiding a separate nanoparticle synthesis and that no detrimental capping ligands are needed. Such an in-situ nanoparticle formation in a polymer solution has already been demonstrated for ZnO- and binary metal sulphide-polymer solar cells.<sup>[403–406]</sup> Nanoparticle formation in the solid state was realized for CdS, ZnS<sup>[372]</sup> and CuInS<sub>2</sub>.<sup>[375]</sup>

The approach presented in this thesis is based on a nanoparticle formation technique reported by Leventis et al.,<sup>[383]</sup> where metal xanthates (metal salts with the chemical formula ROCS<sub>2</sub>M, where R is an alkyl group and M the metal) decompose to pure binary metal sulphides and volatile decomposition products. This technique is expanded to the preparation of polymer:CIS–nanocomposite solar cells. CIS thereby exhibits a bandgap of only 1.5 eV which extends the overall absorption characteristics to higher wavelengths compared to CdSe (1.74 eV) or CdS (2.4 eV).<sup>[33,375,407]</sup>

## 5.2.4 Synthesis of Precursor Xanthates:

*The synthesis described in this chapter is published in: Thomas Rath, Michael Edler, Wernfried Haas, Achim Fischereder, Stefan Moscher, Alexander Schenk, Roman Trattnig, Meltem Sezem, Gernot Mauthner, Andreas Pein, Dorith Meischler, Robert Saf, Neha Bansal, Saif A. Haque, Ferdinand Hofer, Emil J.W. List, and Gregor Trimmel, Advanced Energy Materials, 2011, 1, 1046-1050;*

Ethyl xanthates containing copper and indium are readily available.<sup>[408,409]</sup> Yet, the copper salt only exhibits limited solubility in most organic solvents and thus is hardly applicable to solution based

deposition techniques, which demand good solubility properties in order to realize homogeneous coatings. However, through a substitution of the ethyl-group by a 2,2-dimethylpentan-3-yl-group a different copper xanthate can be achieved that is readily soluble in common organic solvents like chloroform, toluene, or chlorobenzene. The synthesis of the xanthates was conducted at the *Institute for Chemistry and Technology of Materials* at the *Graz, University of Technology* (ICTM, TU Graz) and the corresponding reaction scheme, starting from potassium xanthate as precursor, is depicted in Figure 5-4. For the reaction copper (II) chloride dihydrate was dissolved in deionized water. A solution of potassium xanthate **1** in deionized water was added dropwise while being stirred fiercely and a sticky brown residue was formed immediately. After stirring and decanting off the water, the residue was dried in vacuum, dissolved subsequently in chloroform, and added to methanol to obtain the copper xanthate **2** as a yellow powder. Indium (III) xanthate **3** was synthesized analogously by the utilization of indium (III) chloride instead of the copper chloride dehydrate and was achieved as a white powder (Figure 5-4).

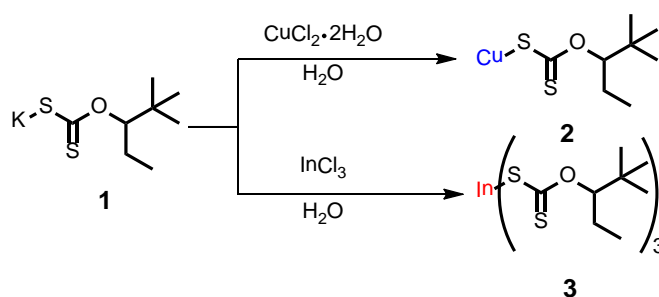


**Figure 5-4:** Reaction scheme for the synthesis of copper- and indium xanthates from potassium xanthates.

The thermal decomposition characteristics (not shown) of the xanthates in vacuum were studied by means of high-resolution mass spectrometry (HRMS) at the ICTM. Volatile products were monitored continuously, while the samples were heated from room temperature to 350 °C directly in the mass spectrometer. Copper xanthate started to decompose at approximately 155°C and COS, dimethylpentene as well as some CS<sub>2</sub> were identified as evaporating products. In the case of indium xanthate, thermal decomposition as well as an evaporation of the indium xanthate occurred and both processes started at approx. 130 °C. Moreover, compared to copper xanthate significant higher relative amounts of CS<sub>2</sub> and alkyloxy-fragments were detected as evaporating products. The observation of volatile indium xanthate itself is an important result with respect to the formation of CIS nanoparticles during device fabrication since, in order to attain stoichiometric CuInS<sub>2</sub> particles, the corresponding fractions of the precursor materials need to be adjusted accordingly.

### 5.2.5 Photophysical Properties of MDMO-PPV

As the first material serving as a polymer matrix poly[2-methoxy-5-(3',7'-dimethyloctyloxy)-1,4-phenylenevinylene] (MDMO-PPV) was used. MDMO-PPV is a well known red-emitting polymer<sup>[410,411]</sup> which is widely utilized as donor material in organic heterojunction as well as BHJ devices. Solar cell efficiencies of more than 3% were already presented for organic BHJ solar cells containing this polymer.<sup>[412]</sup>

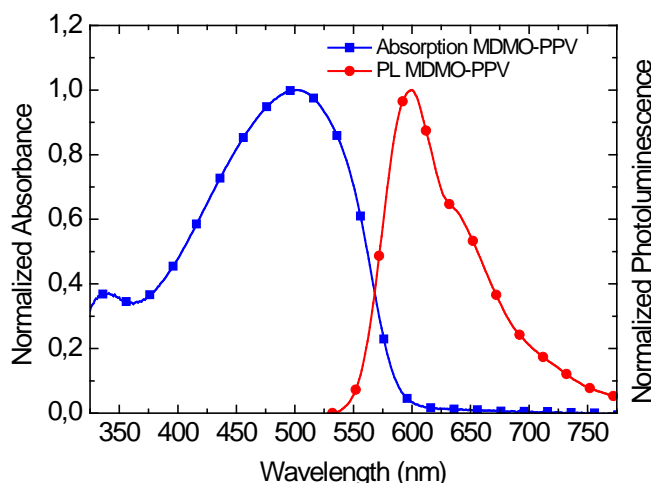


**Figure 5-5: Absorption (blue line) and PL emission (red line) characteristics of MDMO-PPV in the solid state.**

Figure 5-5 shows absorption and photoluminescence emission spectra of pristine MDMO-PPV in thin film. The absorption edge and absorption maximum of the polymer are located at a wavelength of 502 nm and 590 nm, respectively. In the PL spectrum a slightly structured emission feature can be observed in the range between 550 nm and 775 nm peaking at 600 nm. A bandgap of 2.1 eV can be derived from the absorption onset and combined with a HOMO level of 5.3 eV this yields a LUMO energy of 3.2 eV.

### 5.2.6 MDMO-PPV:CIS Morphology Investigations

For the fabrication of MDMO-PPV:CIS thin films at first copper- and indium xanthate precursors were blended into a MDMO-PPV solution using chlorobenzene as a solvent. The obtained solution was spin-coated onto quartz glass substrates and subsequently converted into the nanocomposite thin films by a mild annealing step at 200°C in vacuum (Figure 5-6).

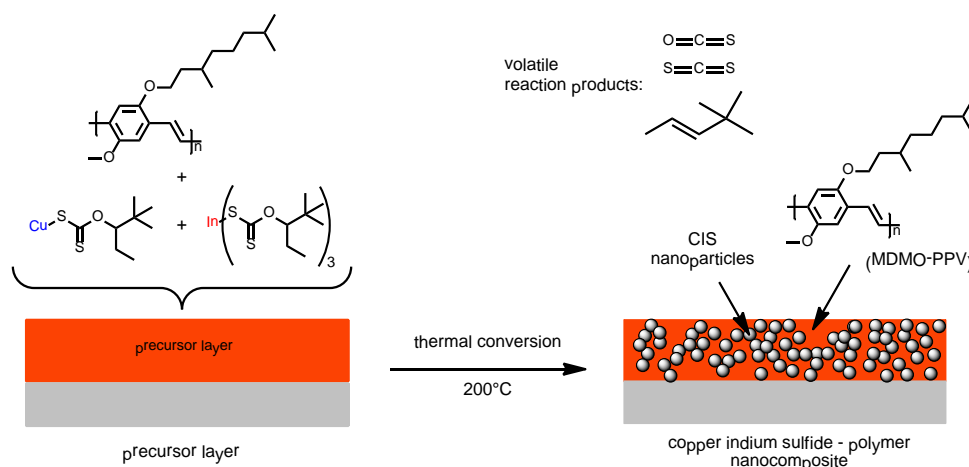


**Figure 5-6. Schematic representation of the polymer:CIS nanocomposite formation. (modified from [374])**

To analyze the surface topography of MDMO-PPV:CIS nanocomposite films and to evaluate the influence of the CIS content on the surface roughness, films fabricated in the described manner were investigated by AFM. Figure 5-7a and b show AFM surface topography images of a pristine MDMO-PPV and a pristine CIS thin film. These layers are very smooth and the determined RMS roughness is 1.6 nm for MDMO-PPV and 1.3 nm for CIS. The flat surface morphology, however clearly changes its characteristic upon blending the two components. As can be observed from Figure 5-7c at a weight

ratio of MDMO-PPV:CIS=1:1 the surface roughness is still low with a value of 4.0 nm. The elevated roughness compared to the pristine films is caused by the formation of agglomerates, which show as bright features in the figure. In contrast to the pristine films and to the layer with an even weight content for both components, the morphology for films with a distinct CIS majority exhibits a totally different appearance. In these cases, the surface displays a significantly corrugated structure with partially branched channels between pronounced hills and valleys. For a MDMO-PPV:CIS-ratio in the nanocomposite film of 1:3 already a  $R_q$  of 11 nm can be determined (Figure 5-7d), which only slightly increases to 12 nm at a ratio of 1:5 (Figure 5-7e). This characteristic is attributed to the generation of the CIS nanocrystals in the active layer, which naturally is more pronounced for higher CIS concentrations. From a comparison of these values to that of standard organic BHJ photovoltaic layers, e.g. poly(3-hexylthiophene):phenyl- $C_{61}$ -butyric acid methyl ester (P3HT:PCBM), it can be observed that such material systems show significantly lower surface roughness (0.5 nm - 3 nm).<sup>[413–416]</sup> Thus, a detrimental effect of the elevated surface roughness might occur since large grain features in the MDMO-PPV:CIS nanocomposite film can lead to a reduced exciton dissociation. This is caused by the fact that the typical exciton diffusion length is expected to be in the range of up to 10 nm.<sup>[417–419]</sup> Thus, excitons generated in a material agglomeration at higher distances are not able to reach the interface and consequently recombine radiatively or non-radiatively without contributing to the charge generation process. In addition, the charge collection efficiency at the electrodes can be lowered as well. Since a clustering of MDMO-PPV or CIS at a large grain size can cause the formation of inefficient conduction paths to the contact electrodes, charge carrier mobility is decreased and results in smaller photocurrent available.

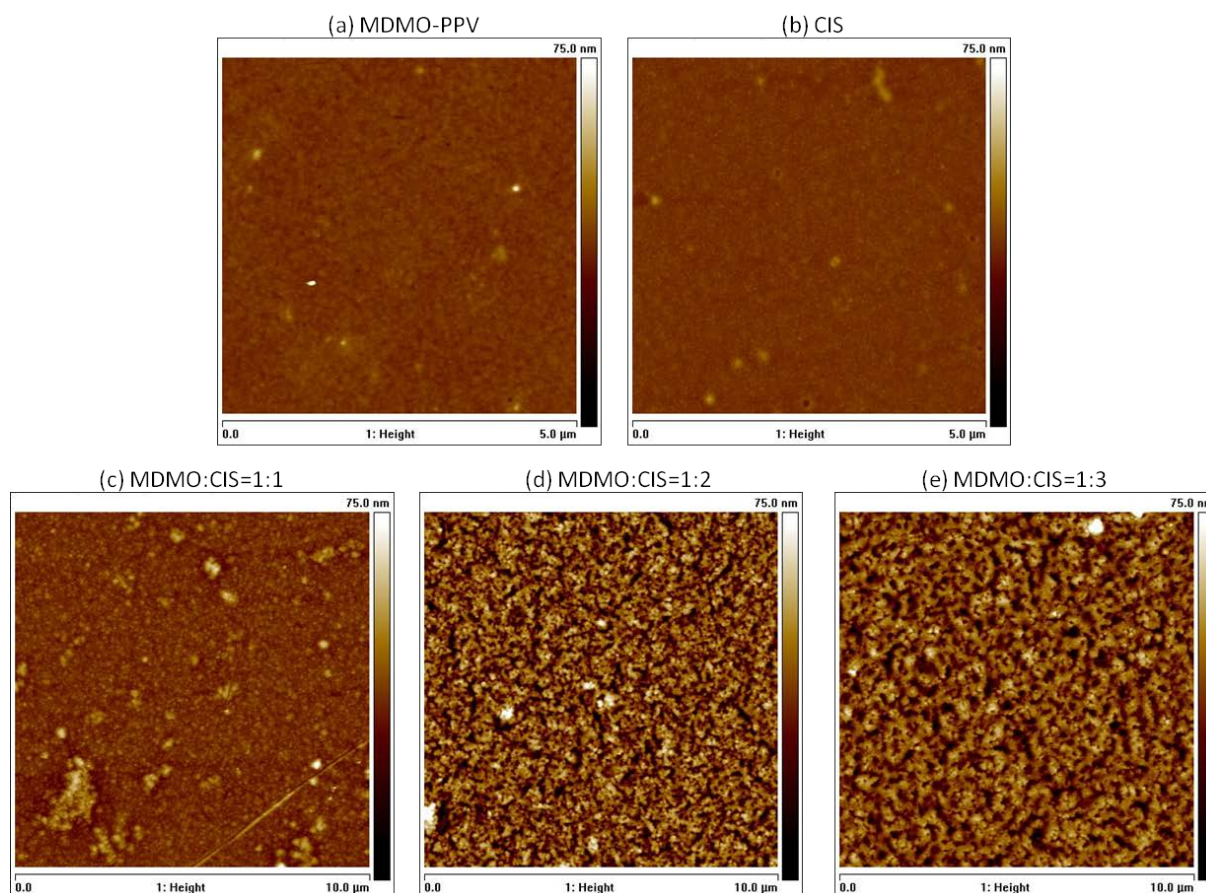


**Figure 5-7:** AFM height images ( $10\mu\text{m} \times 10\mu\text{m}$ ) of pristine MDMO-PPV and pristine CIS, and three nanocomposite layers with MDMO-PPV:CIS ratios of (c) MDMO-PPV:C=1:1, (d) M:C=1:3, and (e) M:C=1:5.

Since AFM measurements are limited to the investigation of the surface morphology of a sample, the nanocomposite bulk morphology was studied by TEM. Therefore cross sections of samples with the configuration ITO/MDMO-PPV:CIS/Al were sectioned and thinned using focused ion beam (FIB) lift-out specimen preparation technique.<sup>[393]</sup> A corresponding TEM image of the assembly is depicted in Figure 5-8. The picture shows a sequence of thin layers in which the nanocomposite layer is enclosed on top by a Al layer of approximately 100 nm with some rectangular features – stemming from Al grains – and at the bottom by ITO with a size of ~160 nm. The nanocomposite layer displays two characteristic features. The first one constitutes bright spots or island that are attributed to the polymer phase. The second one are dark areas and can be assigned to the inorganic CIS rich phase. Thus Figure 5-8 evidences that by means of a thermal annealing of a polymer:xanthate precursor layer a proper interpenetrating network between the electron donor material and the electron acceptor material is formed. Since both materials obviously are distributed homogeneously in the layer, on the one hand a satisfying exciton dissociation can be expected in NCSCs due to a large interfacial area between the polymer and CIS and on the other hand it can be concluded that this morphology provides suitable pathways to enable the generated charges to reach their respective electrode.

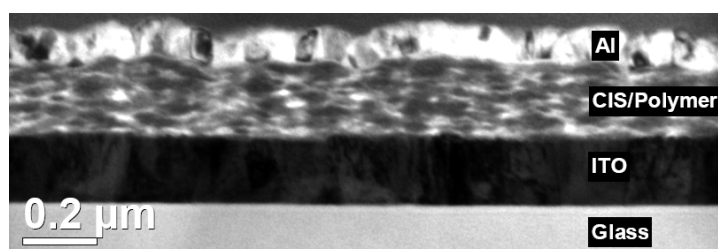


**Figure 5-8:** TEM image of a MDMO-PPV:CIS nanocomposite film embedded between an ITO-covered glass substrate and an aluminum film.

### 5.2.7 Photophysical Properties of MDMO-PPV:CIS Nanocomposite Films

Before actually turning towards device fabrication the photophysical properties of the polymer:CIS nanocomposite films need to be investigated. These investigations are meant to provide valuable information about the interplay of both materials in the film. As a first step, therefore, the absorption characteristics are assessed which allow for an estimate to what extent the two different materials contribute to the light harvesting process in the nanocomposite film.

Figure 5-9 (left) shows a comparison of the absorption characteristics of MDMO-PPV and pristine CIS in thin films. In contrast to the polymer, the CIS-absorption increases continuously with decreasing wavelength of the incident light. An absorption edge can be determined at 800 nm which corresponds to a bandgap of 1.5 eV and is in accordance to values presented in literature.<sup>[33]</sup>

Figure 5-9 (right) depicts the absorption characteristics of MDMO-PPV:CIS nanocomposite films with increasing CIS weight content. It is evident that the absorption spectra of the composite films constitute a superposition of both materials, the polymer and the inorganic nanoparticles. In particular, a distinct contribution of the inorganic phase to the absorption can be observed in the high wavelength region of the spectrum between 600 and 800 nm, where MDMO-PPV exhibits no absorption. Additionally, below a wavelength of approximately 420 nm an absorption enhancement develops with increasing CIS content. Thus, the overall absorption is clearly enhanced for MDMO-PPV:CIS films compared to the pure polymer. This enhancement thereby is not limited to an increased absorption at wavelengths where the incident light is already absorbed by MDMO-PPV, but is clearly extended to wavelengths between 600 nm to 800 nm, which are located above the absorption edge of the polymer.



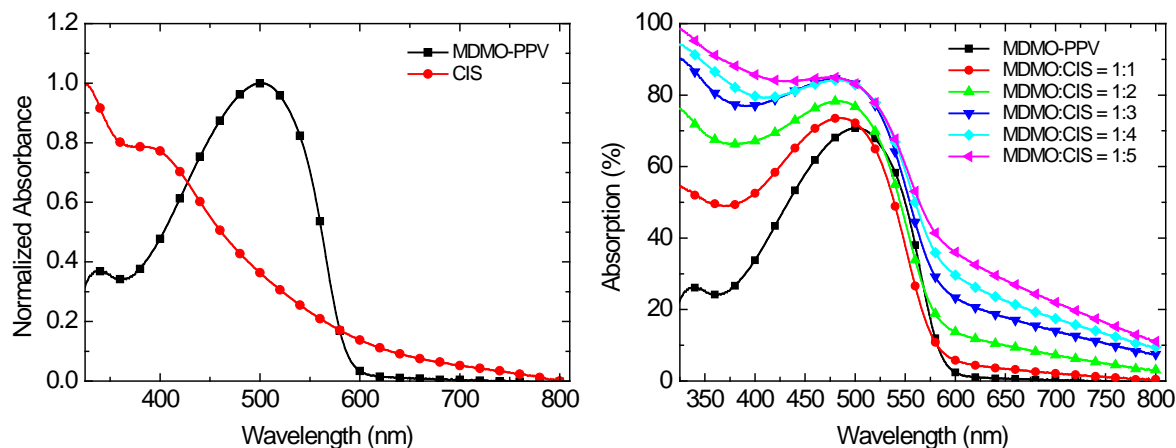


**Figure 5-9 left: Absorption characteristics of MDMO-PPV (black) and of pristine CIS (red) in thin films. right: Absorption spectra of MDMO-PPV:CIS nanocomposite layers containing different polymer:CIS weight ratio.**

Since, in general, for solar cells it is of highest importance that excitons created upon absorption of incident photons, dissociate efficiently to polarons at the donor–acceptor heterojunction in order to contribute to the photocurrent, the second step in the photophysical investigations aims to provide an assessment for the efficiency of charge transfer at the polymer:CIS interface. This estimate can be given by classical photoluminescence quenching measurements. For these investigations, the fluorescent polymer is blended with an increasing amount of a potential quenching material and the PL intensity of the blend system is measured. The extent of the PL quenching thereby allows for an estimation of the charge transfer efficiency at the heterojunction interface since a strong interaction among the participating materials results in significant fluorescence quenching.

Figure 5-10 (left) depicts the PL spectra of a pristine MDMO-PPV film as well as of MDMO-PPV:CIS films containing different CIS weight ratio excited at a wavelength of 500 nm (absorption maximum of MDMO-PPV). The plot on the right side of Figure 5-10 shows the integrated PL intensity relative to pristine MDMO-PPV as a function of the CIS weight content. It can be observed that the pristine MDMO-PPV film shows the known emission spectrum with its maximum emission at 590 nm. Blending the polymer with CIS, however, results in a significant quenching of the overall PL emission. At a CIS content of only 20% (weight ratio of polymer:CIS = 1:0.25), the PL emission from MDMO-PPV is reduced drastically to only 12% of the initial emission intensity and decreases further to values below 5% for a CIS content of 66% and higher. These characteristics clearly evidence an efficient photoluminescence quenching by the CIS nanoparticles which indicates efficient exciton dissociation at the MDMO-PPV:CIS interface. In addition, in that context it should be noted that the presented in-situ grown polymer:CIS nanocomposite films exhibit higher PL quenching efficiencies than those typically reported for nanocomposite layers containing ligand-capped nanoparticles.<sup>[407,420]</sup> However, though all results acquired so far – suitable interpenetrating network of both phases, significantly broadened absorption width compared to classical organic solar cells, strong PL quenching – indicate that the presented MDMO-PPV:CIS nanocomposite layers might serve well as active layers in photovoltaic applications their effective suitability can only be verified by a characterization in an actual photovoltaic device.

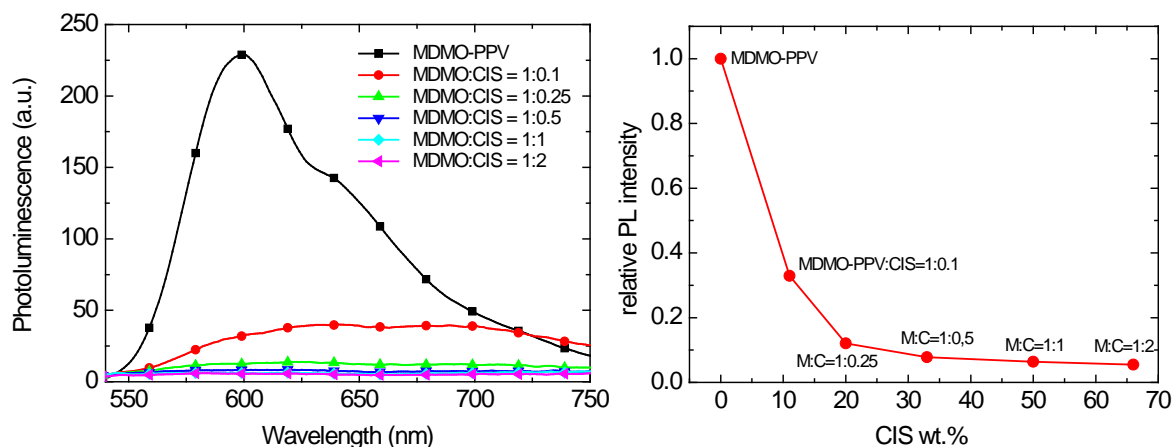


Figure 5-10 Left: Thin film PL spectra of pure MDMO-PPV and MDMO-PPV:CIS films with different CIS weight content (left). Right: Dependence of the PL intensity of MDMO-PPV:CIS nanocomposite layers on the CIS weight ratio.

### 5.2.8 MDMO-PPV:CIS Nanocomposite Solar Cells

Nanocomposite solar cells were fabricated in a standard sandwich geometry: ITO/PEDOT:PSS/MDMO-PPV:CIS/Al. The precursor layer was spin-coated from a chlorobenzene solution with a polymer:CIS ratio of 1:4. A copper:indium xanthate ratio of 1:1.7 was found to be favorable for the realization of polymer:CIS nanocomposite solar cells.<sup>[375]</sup> The J-V characteristics of a typical MDMO-PPV:CIS device in dark and under AM1.5G illumination at 100 mW/cm<sup>2</sup> is shown in Figure 5-11. The device exhibited an  $I_{SC}$  of 8.9 mA/cm<sup>2</sup>, an open circuit voltage  $V_{OC}$  of 0.6 V and a FF of 42%, which results in an overall PCE of 1.75%. Compared to efficiencies already reported in literature for polymer:nanocrystall solar cells this value is located in the upper range.<sup>[373,383,388]</sup> However, the device performance is low in comparison to the efficiency values presented for OSCs.<sup>[421,422]</sup> The weak performance of the MDMO-PPV:CIS NCSCs reflects itself in all three device related parameters, the  $J_{SC}$ ,  $V_{OC}$  and FF. Low results for the first and the last parameter can be explained by the observed rather coarse nanomorphology of the films, as shown by TEM and AFM investigations. Even though the layers exhibit a significant interpenetrating network for both phases, the structure itself obviously displays the formation of clusters with sizes located considerably above the exciton diffusion length. These conditions lead on the one hand towards a lowering the amount of dissociated excitons, since they might not be able to reach the interface, and on the other hand geminate recombination of already separated charge carriers can occur, when they cannot be transported away from the interface efficiently. Both effects result in a lowering for  $I_{SC}$  and FF. To attain a higher  $V_{OC}$ , instead of MDMO-PPV, another polymer could be used featuring a higher distance between the polymers' HOMO and the CIS LUMO.

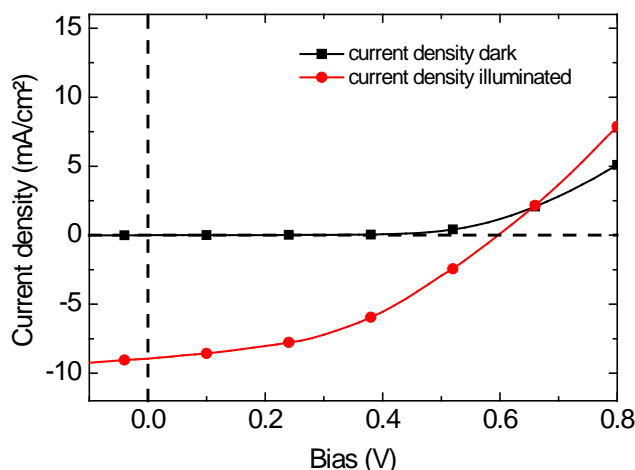


Figure 5-11: Current-density-voltage characteristics of a typical MDMO-PPV:CIS nanocomposite solar cell under AM1.5G illumination at  $100 \text{ mW/cm}^2$ .

### 5.2.9 IPCE Characteristics

Absorption measurements revealed a significant broadening of the absorption width for MDMO-PPV:CIS nanocomposite layers in comparison to the pristine polymer. To investigate if the observed broadening of the absorption characteristics also reflects itself in the photocurrent generation IPCE measurements were performed. With respect to this, it is of particular interest if CIS in combination with MDMO-PPV constitutes just a proper electron acceptor material, or if it contributes to photocurrent generation as well – especially at wavelengths above the absorption edge of the polymer (600 nm – 800 nm). The IPCE characteristics of device presented above as well as the absorption characteristics of MDMO-PPV and CIS are depicted in Figure 5-12. As can be observed, photocurrent is generated over the whole range of the visible spectrum from 400 nm to 800 nm. Within this range two distinct regimes can be identified. The first can be found roughly between 400 nm and 575 nm where the EQE is clearly dominated by the polymer absorption. Yet more importantly, in the second regime between 575 nm and 800 nm the photocurrent generation can be attributed exclusively to light absorbed by CIS. The EQE maximum can be found around at a wavelength of 433 nm and is 14%. These results finally evidence that a considerable contribution to photocurrent generation is made by CIS (c.f. Figure 5-12).

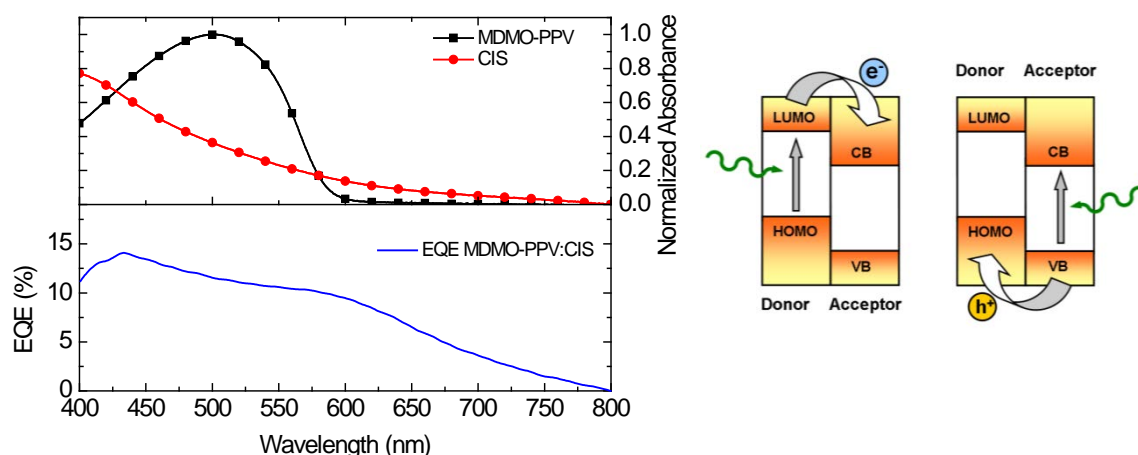


Figure 5-12 left: Comparison of absorption and emission characteristics of MDMO-PPV and CIS (Top) to the IPCE characteristics of a MDMO-PPV:CIS NCSC (bottom). Right: Scheme of the exciton dissociation and charge transfer process at the MDMO-PPV:CIS interface.

### 5.2.10 Conclusion

In summary it is shown in this section that a xanthate route can be applied for the fabrication of polymer:CIS NCSCs by the utilization of new highly soluble copper and indium precursors. Conversion temperatures below 200°C are compatible to thermal stability of most conjugated polymers. By the means of AFM and TEM it is shown that within the nanocomposite layer interpenetrating networks are formed. Absorption measurements reveal that the inorganic acceptor phase contributes significantly to the overall absorption of nanocomposite films and PL quenching experiments indicate an efficient exciton dissociation at the polymer:CIS interface. The presented device properties consequently result in the presentation of NCSCs with a PCE of 1.75%. Yet more important, it is evidenced by IPCE measurements, that the CIS phase significantly contributes to the photocurrent generation up to 800 nm. Particularly this contribution of the electron acceptor material is the great advantage of the presented polymer:CIS nanocomposite system compared to OSCs containing PCBM, which shows only marginal absorption for incident light. For all these facts and despite the PCE for the as presented device, which is located in the upper range for polymer:nanocrystal NCSCs, further optimizations of the system are necessary. A particular challenge for the future research work is to optimize the MDMO-PPV:CIS layer morphology. Higher PCEs will only be achieved if one is able to succeed in realizing polymer:CIS networks that allow for an efficient exciton dissociation as well as an efficient charge transport in the nanocomposite system.

### 5.3 Influence of the Bridging Atom in Donor-Acceptor Fluorene-Analogue Low-Bandgap Polymers on Morphology and Efficiency of Polymer:CIS-Nanocomposite Solar Cells

*The content of this chapter is in preparation for publication: Monika Jäger, Roman Trattnig, Markus Postl, Wernfried Haas, Birgit Kunert, Andreas Klug, Roland Resel, Ferdinand Hofer, Gregor Trimmel and Emil List, Journal of Polymer Science.*

The author of the thesis is a main author of this publication. Exclusive contributions by the author: surface morphology measurements as well as planning und supervision of the overall work. Collaborative contributions: photophysical characterization, device assembling, device characterization and discussion of the overall results. M. Jäger and the author of the thesis have written the publication. In the current chapter the publication text was expanded essentially by the author.

#### 5.3.1 Introduction

As it was mentioned in the conclusion of the last chapter (c.f. chapter 5.2.10) an optimization of the relative positions of the donor's HOMO and the acceptor's LUMO constitutes a suitable way to enhance the performance of typical heterojunction solar cells. An alternative approach is given by the use of low-bandgap polymers. As their name implies these polymers exhibit particularly low bandgaps, which result in an enhanced absorption in the red spectral region and allows for a shift of the absorption gap closer to values as predicted by the Shockley-Queisser limit. In that context polymers have already been reported that provide an absorption up to 1300 nm, however BHJ solar cells fabricated with these materials and [6,6]-phenyl-C<sub>61</sub> butyric acid methyl ester (PCBM) led only to rather low photocurrents.<sup>[423]</sup> Nevertheless, a non-negligible part of reported record solar cells was realized under the utilization of low bandgap materials.<sup>[37,361,424]</sup> One of the main influencing factors concerning the morphology of the active layer is the polymer structure.<sup>[425]</sup> For bulkheterojunction solar cells manifesting a bicontinuous polymer:fullerene network favourable morphologies and the morphological impact of the polymer already are rather well-studied.<sup>[425–428]</sup>

This chapter presents a comparative study on the morphology of NCSCs comprising two low-bandgap polymers – Poly[[9-(1-octylnonyl)-9H-carbazole-2,7-diyl]-2,5-thiophenediyl-2,1,3-benzothiadiazole-4,7-diyl-2,5-thiophenediyl] (PCDTBT, Figure 5-13)) and Poly[2,1,3-benzothiadiazole-4,7-diyl-2,5-thiophenediyl(9,9-dioctyl-9H-9-silafluorene-2,7-diyl)-2,5-thiophenediyl] (PSiF-DBT, Figure 5-13) – in combination with in-situ synthesized copper indium sulphide nanoparticles. The in-situ formation is based on the thermal decomposition of copper- and indium- xanthate within a semiconducting polymer film as presented in chapter 5.2. The obtained electron-transporting CIS nanocrystal network embedded in a hole-transporting conjugated polymer matrix results in BHJ solar cells, which exhibit high yields of photogenerated charge carriers and power conversion efficiencies up to 2.8%.<sup>[374]</sup> However, due to the thermal decomposition process with temperatures up to 200°C there is the need for hole-transporting polymers that can withstand thermal stress at least up to these temperatures. One of the first polymers reported with remarkable stability at temperatures up to 350°C under inert conditions is the low-bandgap carbazole-based polymer PCDTBT.<sup>[429]</sup> This material constitutes a “donor-acceptor” copolymer comprising of carbazole (C) and di-2-thienyl-2,1,3-benzothiadiazole (DTBT).<sup>[430]</sup> The combination of the carbazole unit and the electron-donating nitrogens leads to an increased electron density on the polymer as well as to HOMO-LUMO energy levels of 5.5 eV and 3.6 eV, respectively.<sup>[424,430–438]</sup> It has already been demonstrated that PCDTBT exhibits excellent hole transport properties even after thermal treatment.<sup>[438]</sup> A substitution of the centre nitrogen in the carbazole unit by silicon [i.e. converting the carbazole into silafluorene (SiF)], however, directly

results in the copolymer PSiF-DBT. This polymer exhibits a HOMO energy level of 5.4 eV and a LUMO energy level of 3.6 eV<sup>[439,440]</sup> and was already reported as low-bandgap polymer in nanocomposite solar cells.<sup>[374]</sup> Moreover, in earlier studies it was shown that the class of silicon bridged polymers in general features a high degree of  $\pi$ -electron delocalization leading to high carrier mobility ( $1 \times 10^{-3} \text{ cm}^2/\text{V s}$ )<sup>[440]</sup> as well as good thermal stability.<sup>[439]</sup>

The present work, however, will show that this simple substitution of the nitrogen atom by silicon leading from PCDTBT to PSiF-DBT, has a dramatic impact on the nanomorphology of corresponding polymer:CIS blends in NCSCs as well as on their fluorescence properties and device performance. In analogy to OSCs, the device efficiency is strongly determined by the polymer structures leading to a different packaging of the polymer chains and consequently to clearly dissimilar morphologies.

To evaluate the extent of the influence caused by the structural difference of the polymers the following investigations were performed: The polymer hole mobility was assessed by means of field effect investigations in OFETs. Optical properties of polymer:CIS films were investigated by absorption and PL quenching studies. In addition, the morphological and structural properties of nanocomposite layers were studied by AFM, TEM and XRD. Thereby, the size of the CIS nanoparticles as well as a probable crystallinity in the polymers was determined. The results from all these measurements as well as the performance of polymer:CIS NCSCs fabricated by the utilization of PCDTBT and PSiF-DBT, respectively, reveal clearly, that polymer structure, fluorescence and morphological properties correlate directly to the achieved device efficiency.

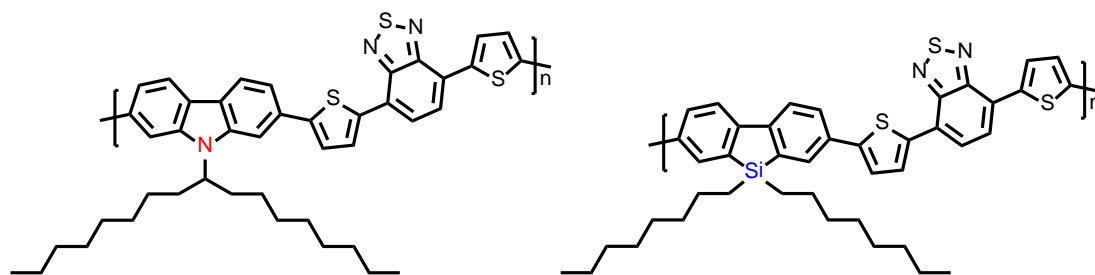


Figure 5-13: Chemical Structure of PCDTBT (left) and PSiF-DBT (right).

### 5.3.2 Experimental

Organic field-effect transistors (OFETs) were fabricated in a bottom-gate/bottom-contact architecture on highly n-doped ( $n^{++}$ )-Si substrates (used as common gate electrode) with a 200 nm thick, thermally evaporated  $\text{SiO}_2$  layer (acting as gate dielectric) provided by ams AG. The source/drain-electrodes (channel length: 25  $\mu\text{m}$ , channel width: 2.85 mm) were structured via photolithographic lift-off processing, using AZ® nLOF-2035 photoresist, AZ® 826 MIF developer and 1-methyl-2-pyrrolidone (NMP)/TechniStrip® NI555 remover from MicroChemicals and including UV-exposure with an EVG-620 mask-aligner as well as thermal evaporation ( $p < 5 \times 10^{-6}$  mbar) of a 2 nm chromium adhesion layer and a 50 nm gold layer. The OFETs were completed by spin-casting of polymer films from chlorobenzene solutions (5 mg/ml) in argon and drying them at 80°C for 1h in high vacuum ( $p < 1 \times 10^{-5}$  mbar). Afterwards each sample consisting of 12 PCDTBT- or PSiF-DBT-devices was annealed at 200°C for 25 min in a tube furnace under vacuum ( $p < 0.2$  mbar). Electrical characterization of the OFETs before and after the high-temperature bake was performed with an Agilent B1500A parameter analyzer in argon atmosphere.

### 5.3.3 Morphology Studies on PCDTBT:CIS and PSiF-DBT:CIS Nanocomposite Films

In order to evaluate the influence of the two different polymers on the nanocomposite morphology, AFM measurements were performed on polymer:CIS films with various CIS content. Therefore, NC films with different CIS-content (weight ratio: 1:5, 1:7 and 1:10) were spin-cast on glass substrates from polymer:xanthate solutions in chlorobenzene and annealed at 200°C in vacuum. Figure 5-15 shows the corresponding AFM topography images. The PCDTBT:CIS blend with a polymer:CIS ratio of 1:5 displays a network of heightened, partially connected regions above a continuous ground (Figure 5-15d). For this film and a surface roughness of 6.4 nm could be determined.

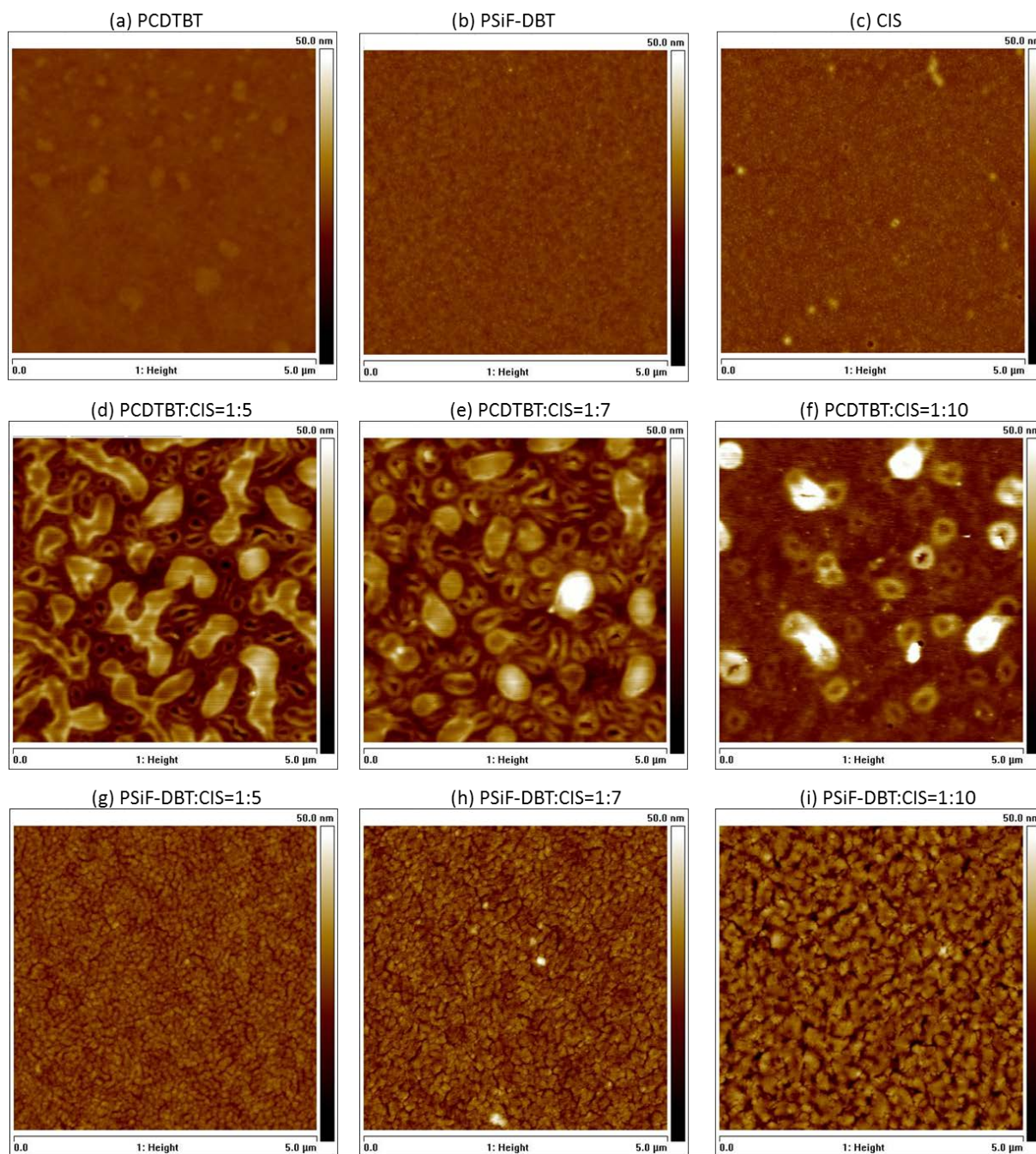
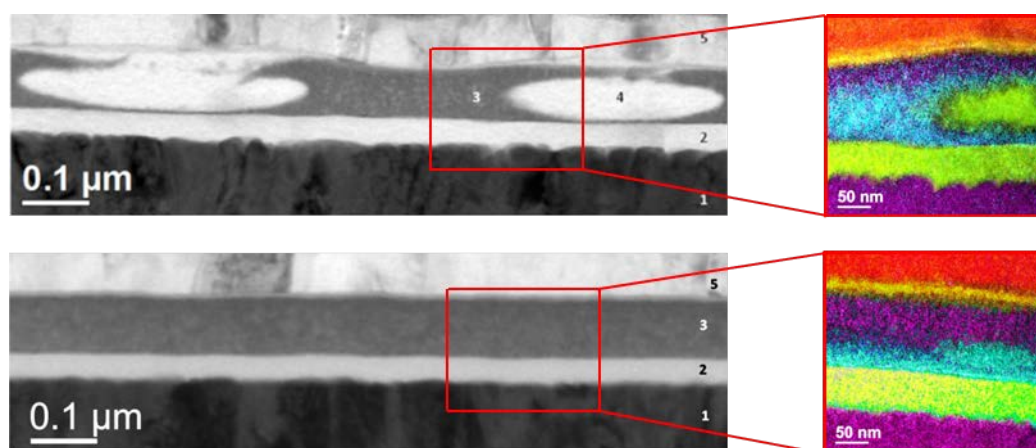


Figure 5-14: AFM height images of pristine PCDTBT, PSiF-DBT and CIS films (top) as well as of PCDTBT:CIS (center) and PSiF-DBT:CIS (bottom) nanocomposite films containing different weight ratios of CIS.

Upon increasing the CIS concentration to a ratio of 1:7 and 1:10, respectively, it can be observed that the network is disrupted and individual islands with a diameter in the range of 300 nm to 400 nm are formed (Figure 5-14e). Obviously, these islands become significantly less numerous at higher fractions of the inorganic component. This morphological change naturally also reflects itself in a higher surface roughness and thus an  $R_q$  of 6.8 nm and 7.1 nm was found for polymer:CIS concentrations of 1:7 and 1:10, respectively. Figure 5-15(g-i) shows the AFM topography images of the PSiF-DBT:CIS blends. It can be seen that, in comparison to NC layers containing PCDTBT, these layers exhibit a much more homogeneous surface topography. The NC film with a polymer:CIS ratio of 1:5 is characterized by a grainy structure with a surface roughness of only 2.4 nm. As Figure 5-14 (g-i) show, an increase of the fraction of the inorganic component leads to the development of distinctive cracks in the surface, which become more pronounced for higher CIS ratio. This development leads to elevated roughness values of 3.5 nm and 5.0 nm for polymer:CIS ratios of 1:7 and 1:10, respectively. However, no signs for agglomerates can be detected in the PSiF-DBT:CIS nanocomposite layers.

The fact that in PCDTBT:CIS films the number of islands or agglomerates, respectively, decreases with increasing CIS content leads to the assumption that the observed islands consist of polymer agglomerates. Thus, in order to determine the actual composition of these agglomerates TEM measurements were performed. Therefore, NCSCs were assembled in a standard sandwich geometry ITO/PEDOT:PSS/polymer:CIS/Al, which was sectioned and thinned again using the FIB lift-out specimen preparation technique.<sup>[393]</sup> The cross section image of a PCDTBT:CIS nanocomposite solar cell (Figure 5-15, top left) shows the layered structure of this system. It can be observed that the polymer:CIS blend is enclosed by an aluminum layer on the top and a PEDOT:PSS layer on bottom. Furthermore, the blend obviously contains some large lens shaped embeddings surrounded by a homogenous phase. An energy filtered transmission electron microscopy (EFTEM) analysis of these embeddings revealed that they indeed consist of polymer agglomerates surrounded by a nanocomposite matrix phase (Figure 5-15). The picture in the bottom left part of Figure 5-15 shows a TEM image of the cross section of the PSiF-DBT:CIS system. In comparison to the PCDTBT:CIS blend the PSiF-DBT:CIS system exhibits a homogeneous bulk-morphology and no agglomerates are detected. EFTEM revealed a nanocomposite layer comprising CIS nanoparticles embedded in a PSiF-DBT polymer matrix.



**Figure 5-15:** TEM images (left) and EFTEM analyses (right) of the active layers of PCDTBT:CIS (top) and PSiF-DBT:CIS (bottom) solar cells. The structure of the individual layers can be clearly seen: 1. ITO; 2. PEDOT:PSS; 3. nanocomposite layer; 4. polymer agglomerate without nanoparticles; 5. Aluminum. Elemental colors for EFTEM: Al – red, C – green, Cu – blue, In – magenta, O – yellow.



### 5.3.4 X-Ray Diffraction

In order to determine the dependence of the polymers morphology on their molecular arrangement, which might lead either to an amorphous or to a semicrystalline conformation, X-ray measurements were performed on pristine and CIS blended PCDTBT and PSiF-DBT films. For the investigations the corresponding chlorobenzene solutions were deposited on Si-wafer substrates under inert atmosphere and annealed in vacuum at 200°C. The diffraction patterns of pristine films are depicted in the top left part of Figure 5-16. The pattern of PCDTBT shows two peaks located at  $2\theta = 21^\circ$  and  $2\theta = 4.6^\circ$ . The  $2\theta = 21.2^\circ$  peak is assigned to a typical polymer correlation peak which according to Bragg's law (equation (3.21)) indicates a mean distance between disordered polymer chains of 4.2 Å. The long range peak at  $2\theta = 4.6^\circ$  corresponds to a distance of 19.2 Å and is related to the spacing between adjacent chains determined by the branched side chains of the polymer. These results allow for the conclusion that PCDTBT shows pure amorphous structure and, since no additional peaks can be found, it is evident that no crysallite formation is caused due to the thermal treatment even when the film was annealed significantly above the glass transition temperature for PCDTBT of 130°C.<sup>[441]</sup>

The diffraction pattern of PSiF-DBT (Figure 5-16), however, presents some slight dissimilarities compared to PCDTBT. For this polymer again two main peaks can be detected at  $2\theta = 4.6^\circ$  and at  $2\theta = 20^\circ$  and in addition a small feature can be found at  $2\theta = 9.3^\circ$ . While the two known peaks again correspond to a spacing between disordered chains of 19.2 Å and between adjacent chains of 4.4 Å the additional characteristic is attributed to the formation a mid-range ordering in the material and correlates to a distance between polymer side chains of 9.5 Å. Furthermore, in comparison to PCDTBT, in the pattern of PSiF-DBT the correlation peak between  $2\theta = 10^\circ$ - $30^\circ$  is significantly lower in intensity. This finding, in conjunction with the additional diffraction feature at  $9.3^\circ$ , is a clear indication for the development of a mid-range order in PSiF-DBT. Thus, in contrast to PCDTBT, PSiF-DBT not only exhibits an amorphous structure but also shows a certain semicrystallinity.

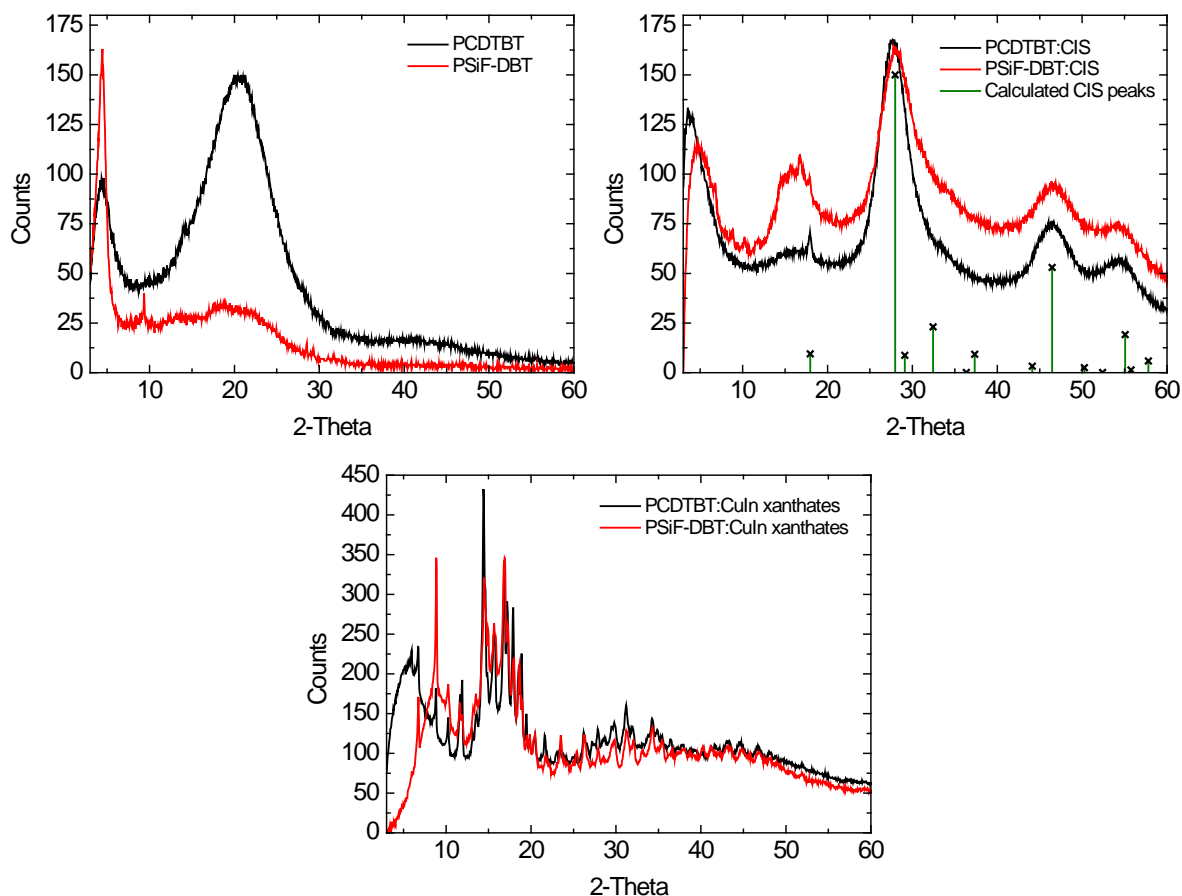


**Figure 5-16: XRD-profiles of pristine PCDTBT and PSiF-DBT films prepared (top, left), of PCDTBT:CIS and PSiF-DBT:CIS films annealed with 220°C (top, right) as well as of non-converted PCDTBT:xanthate and PSiF-DBT:xanthate films.**

The top right part of Figure 5-16 depicts the diffraction patterns of PCDTBT:CIS and PSiF-DBT:CIS NC films. For both polymer:CIS nanocomposites broad reflections appear at  $2\theta = 18^\circ$ ,  $2\theta = 28^\circ$ ,  $2\theta = 46^\circ$  and  $2\theta = 55^\circ$  which are assigned to stem from CIS in a chalcopyrite structure of. The location of these features is in good agreement with the Joint Committee on Powder Diffraction Standards (JCPDS) for the corresponding bulk phases.<sup>[33,442]</sup> It is important to note, that both diffraction patterns exhibit some spikes in the range of  $2\theta = 10^\circ$  to  $2\theta = 20^\circ$ . These spikes are in accordance with diffraction peaks typically observed in patterns of polymer:xanthate blends which contain the non-converted precursor material (Figure 5-16).

The size of the CIS nanoparticles was calculated using the Scherrer relation (equation (3.22)) and was determined to be in the range of 2 nm in both, the PSiF-DBT:CIS as well as PCDTBT:CIS nanocomposite film.

### 5.3.5 Photophysical properties of PCDTBT:CIS and PSiF-DBT:CIS Nanocomposite Films

One of the main advantages of nanocomposite devices compared to OSCs is that they combine the light-harvesting properties of inorganic semiconductor nanoparticles – preferably for photon energies below the absorption edge of the conjugated polymer – as well as those of the organic semiconductor, which results in an enhanced overall absorption width.<sup>[374]</sup> Figure 5-17 shows the absorption characteristics of pristine PCDTBT and PSiF-DBT films, a pristine CIS film and of polymer:CIS films with increasing CIS concentration. For both polymers two prominent absorption bands are detected,

one ranging from 350 nm to 450 nm with a maximum of 400 nm and the other one between 480 and 700 nm with its peak at 580 nm. According to Giesecking et al.,<sup>[435]</sup> these peaks can be assigned to the different constituent parts in the copolymers and their respective functionality. In particular, the absorption bands are attributed to the absorption of the carbazole or silafluorene, respectively, and to a charge transfer state formed by these moieties and the adjacent benzothiadiazole units, respectively. In contrast to these basic characteristics of PCDTBT and PSiF-DBT, a blending of the polymers with CIS results in significantly altered absorption characteristics. In analogy to MDMO-PPV:CIS nanocomposite films (c.f. chapter 5.2.7), this is particularly valid in the range between 300 nm to 450 nm as well as between 650 nm to 800 nm, where a significant enhancement of absorption is caused by CIS. The obtained spectra again resemble a superposition of the semiconducting polymers and the inorganic phase. This fact clearly evidences that both components of the nanocomposite layers significantly contribute to the NC layer absorption.

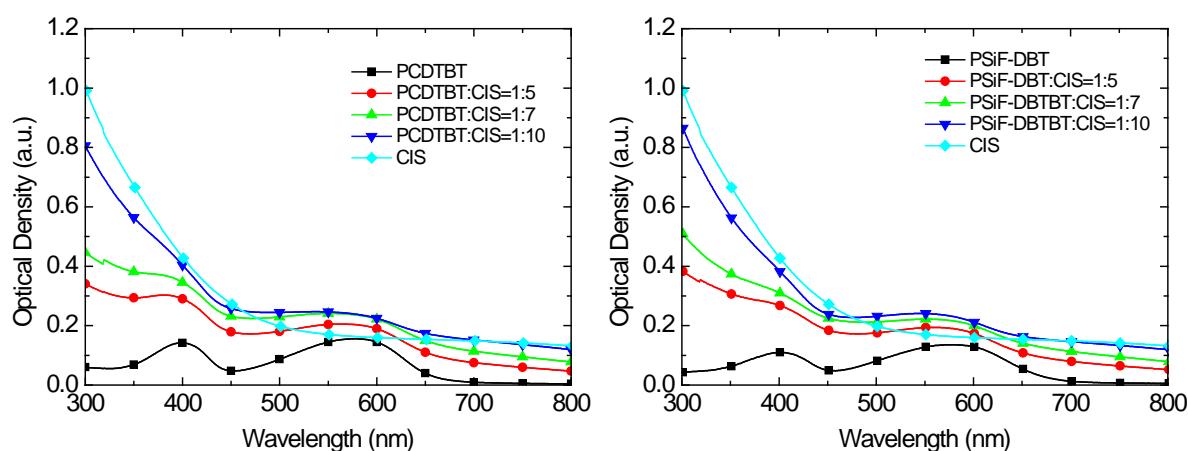


**Figure 5-17: Absorption characteristics of pristine polymer films, a pristine CIS-film and of polymer:CIS blends with various polymer:CIS ratios in PCDTBT (left) and PSiF-DBT (right).**

The efficiency of an electron transfer and subsequent exciton dissociation at the interface between donor and acceptor material strongly correlate to the energetic difference between the donor and acceptor LUMO levels. It is widely accepted that in order to achieve an efficient charge separation, the corresponding energy level offset at least needs to be higher than the exciton binding energy, which depending on the material can range between 0.3 eV and 1 eV.<sup>[443,444]</sup> Hence, in case of polymer:CIS NCSCs, an appropriate selection of the donor polymers, which are compatible to the energy levels of the CIS acceptor (HOMO = 5.6 eV, LUMO = 4.1 eV), is essential. With respect to that, the energy levels of PCDTBT (HOMO = 5.5 eV, LUMO = 3.6 eV) and PSiF-DBT (HOMO = 5.4 eV; LUMO = 3.6 eV) obviously theoretically match with those of CIS.<sup>[33,432,433,440]</sup> To obtain an indication for the exciton dissociation efficiency in the investigated NC systems, again PL quenching studies of nanocomposite films with different polymer:nanoparticle ratio were performed. The corresponding PL spectra as well as the integrated absolute PL intensity relative to the pure polymer as a function of the CIS volume fraction are shown in Figure 5-18.

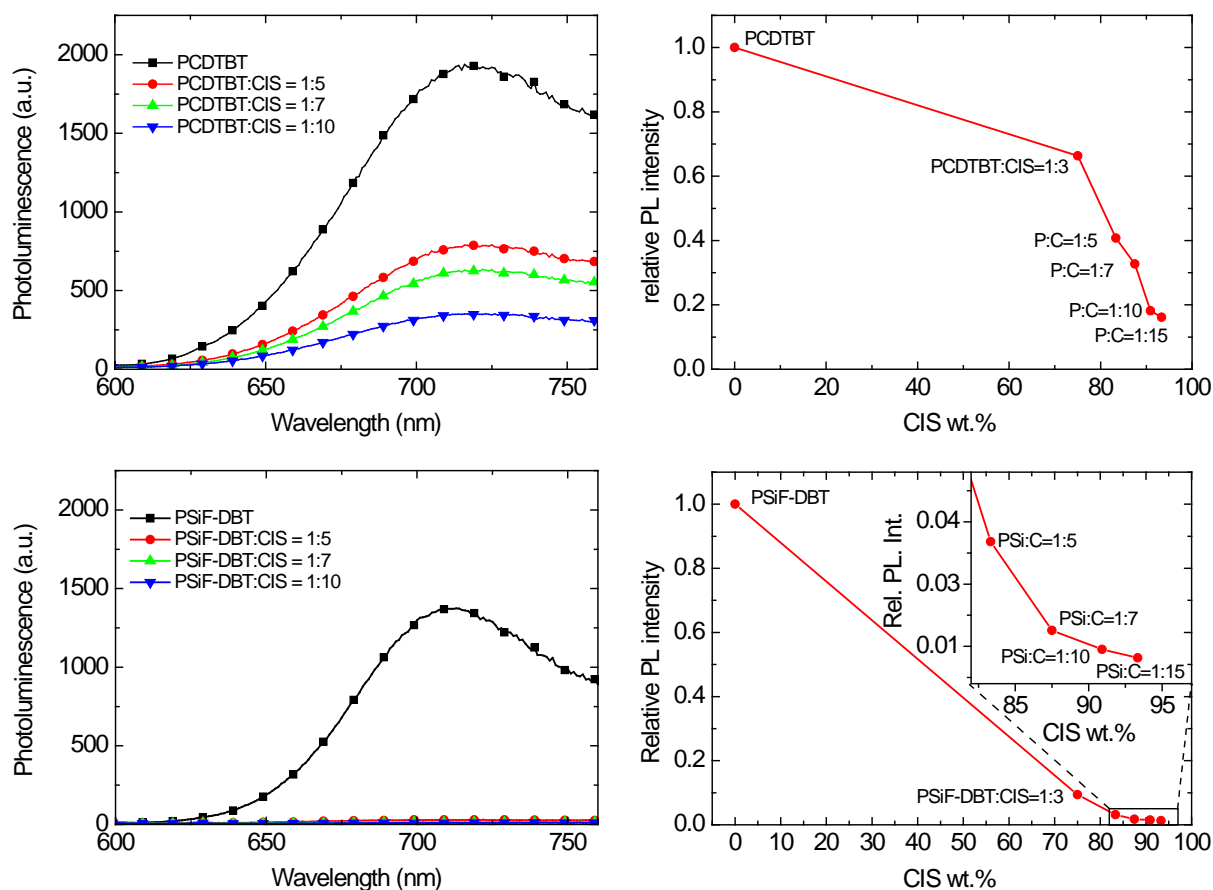


**Figure 5-18: PL spectra (left) of pristine polymers and polymer:CIS blends with various CIS content and corresponding integrated PL intensity as a function of CIS volume fraction (right) for PCDTBT:CIS (top) and PSiF-DBT:CIS (bottom) films.**

The upper part of Figure 5-18 shows the results of the PL measurements for pristine PCDTBT and PCDTBT:CIS NC layers. Optical excitation of a pristine PCDTBT film at the absorption maximum (580 nm) results in the appearance of an emission band with its maximum intensity located at 720 nm. Upon blending the polymer with CIS nanoparticles the radiative recombination of excitons decreases. However, the luminescence of the PCDTBT is quenched to a much lower extent than expected considering a LUMO-LUMO distance of 0.5 eV between the polymer and CIS. For a weight ratio of 1:10 (90 wt.% CIS) the PL intensity still achieves 18% of the initial intensity and even for a ratio of 1:15 (93 wt.% CIS) 16% of the PL intensity remain. This result suggests that no efficient electron transfer occurs in the PCDTBT:CIS system. The PL spectra of pristine PSiF-DBT and PSiF-DBT:CIS films, in comparison, are shown in the lower part of Figure 5-18. Optical excitation of a pristine PSiF-DBT film at 580 nm results in the appearance of an emission band located at 713 nm. However, in PSiF-DBT:CIS film, the PL of the polymer is quenched significantly. Already at a PSiF-DBT:CIS weight ratio of 1:5, the PL emission from PSiF-DBT is quenched dramatically to only 3.2% (PSiF-DBT:CIS = 1:5; 83 wt.%) of the original level and a further increase of the CIS content to 88 wt.% (PSiF-DBT:CIS = 1:7) or higher results in a PL intensity below 1.8%. This evidences an effective PL quenching by the CIS nanoparticles.

A comparison of the results for both polymers yields that the PL-quenching in PSiF-DBT:CIS films is 7 times stronger in a blend with 75 wt.% CIS ratio and even 12 times higher in a blend with 90 wt.% CIS content compared to PCDTBT-based NC films containing the same amount of the inorganic compound. Thus, the PL quenching in the in-situ formed PSiF-DBT:CIS nanocomposite layer is obviously much more effective than the PL quenching efficiency in PCDTBT:CIS films.

### 5.3.6 Field Effect Charge Carrier Mobility

In order to gain a deeper insight into the thermal stability of the two polymers as semiconductors for their prospective use in NCSCs, organic field-effect transistors based on PCDTBT and PSiF-DBT were fabricated and characterized before and after annealing at 200°C. Figure 5-19 a - c depict the square root of the channel current  $I_D$  vs. gate voltage  $V_G$  and semi logarithmic transfer curves of two typical devices before and after the high-temperature annealing step, exhibiting reasonable OFET-performance comparable to literature values,<sup>[438,440]</sup> also considering the applied bottom-contact architecture. Table 7 summarizes the relevant OFET parameters before and after annealing. Regarding the on/off-current ratio, for PCDTBT it increased from  $6.5 \times 10^3$  to  $2.4 \times 10^4$  and for PSiF-DBT from  $1.3 \times 10^3$  to  $6.5 \times 10^3$ . The field-effect mobility was derived at a  $V_G$  of -60 V and a source-drain voltage  $V_D$  of -100 V using a well-established model based on the gradual channel approximation.<sup>[445]</sup> It showed a slight increase after annealing at 200°C for both, the PCDTBT-based (from  $1.2 \times 10^{-3}$  cm<sup>2</sup>/Vs to  $1.7 \times 10^{-3}$  cm<sup>2</sup>/Vs) and the PSiF-DBT-OFET (from  $3.2 \times 10^{-4}$  cm<sup>2</sup>/Vs to  $8.0 \times 10^{-4}$  cm<sup>2</sup>/Vs). This effect is tentatively assigned to reduced trap densities within the semiconductor or at the semiconductor/dielectric interface,<sup>[446]</sup> also supported by a slight shift of the switch-on voltages to more positive values.

Figure 5-19 e and f show the corresponding output characteristics after the high-temperature bake. While both devices exhibit distinct current saturation, the absence of a linear channel-current behavior at low drain voltages indicates the presence of significant contact resistance associated with high injection barriers at the Au/semiconductor interfaces,<sup>[447]</sup> considering also the rather high HOMO levels of the polymers and the most probably reduced Au work function (below 5 eV) due to hydrocarbon adsorption in air.<sup>[448]</sup>

In general, compared to P3HT, a well-established polymer in BHJ devices – both, OSCs<sup>[449]</sup> and NCSCs<sup>[383]</sup> – with a noticeable current density (over 10 mA/cm<sup>2</sup>) as well as in OFETs,<sup>[450]</sup> which exhibits degradation of the field-effect mobility by more than two orders of magnitude after exposure to 200°C,<sup>[438]</sup> the obtained OFET-results for PCDTBT and PSiF-DBT indicate an excellent thermal stability for the two polymers.

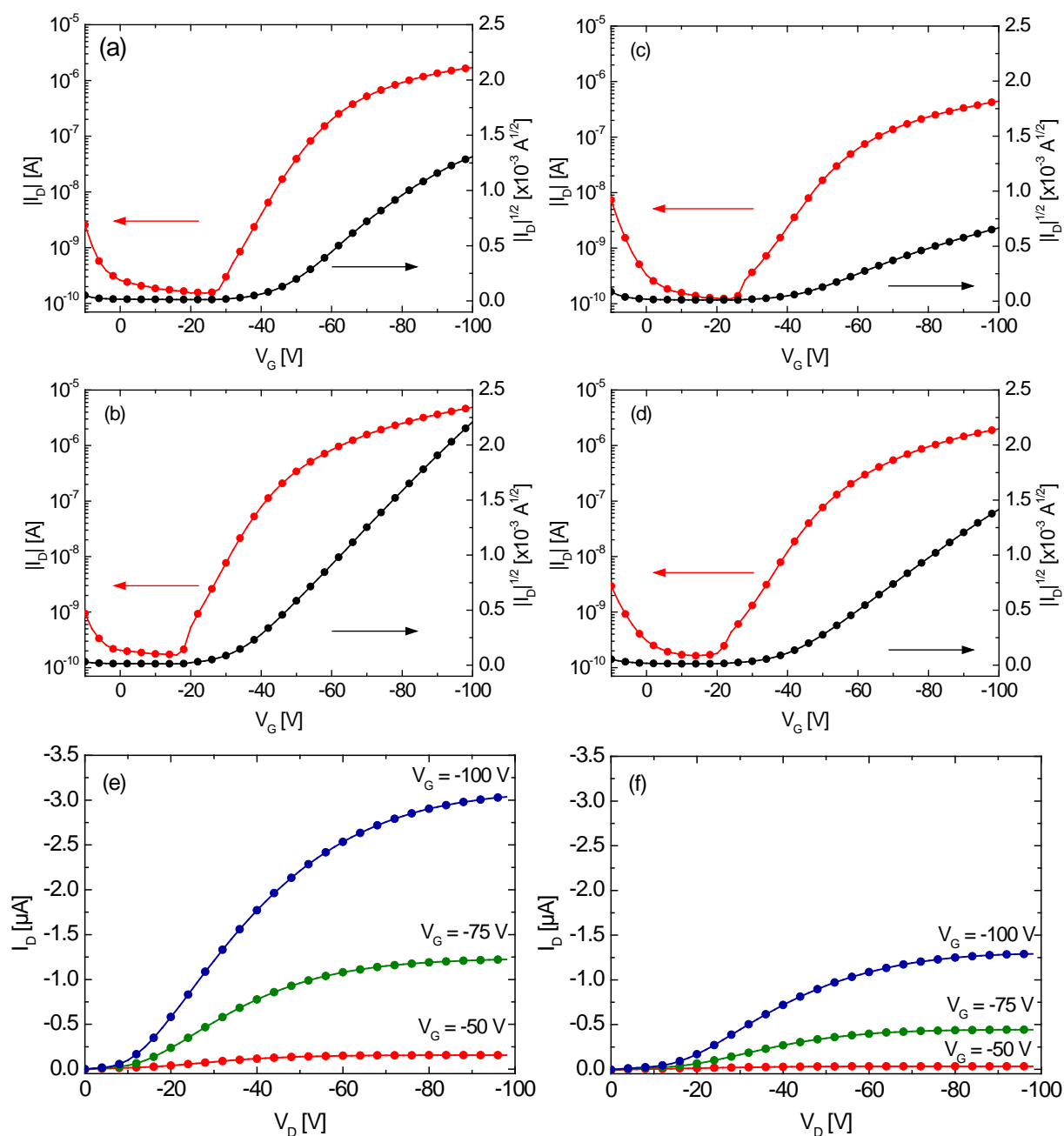
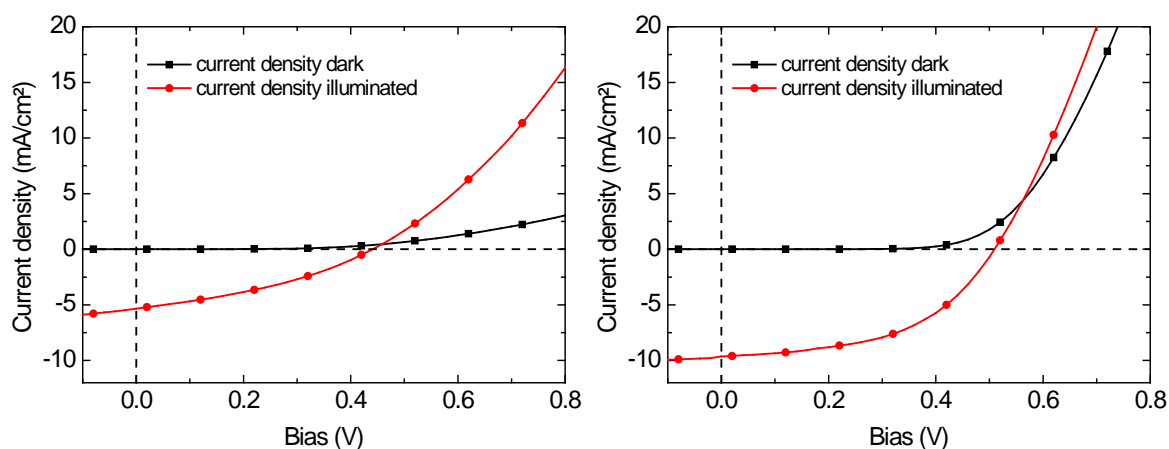


Figure 5-19: Characteristics of OFETs based on PCDTBT (left) and PSiF-DBT (right): square root of the channel current  $I_D$  vs. gate voltage and semi logarithmic transfer curves at  $V_D = -75$  V before (a, c) and after annealing (b, d) at  $200^\circ\text{C}$ ; corresponding output characteristics after annealing at  $200^\circ\text{C}$  (e, f).

### 5.3.7 PCDTBT:CIS and PSiF-DBT:CIS Nanocomposite Solar Cells

The results from structural, optical and mobility investigations of PCDTBT:CIS and PSiF-DBT:CIS films, reveal that considerable differences exist in the morphology between the nanocomposites fabricated from these polymers, which have a dramatic impact on the optical properties of the respective layers. To assess to what extent the differences, caused by a different structural conformation of the polymer molecules, correlate to the performance of polymer:CIS NCSCs, devices were fabricated in the standard sandwich geometry ITO/PEDOT:PSS/PCDTBT:CIS, PSiF-DBT:CIS/Al. The nanocomposite layers thereby exhibited a polymer:CIS ratio of 1:8.5 and the Cu:In ratio was 1:2.2. Current density-voltage characteristics of the respective solar cells are presented in Figure 5-20

and all relevant device parameters are summarized in Table 7. The PCDTBT based device exhibited a short-circuit current density of  $6.9 \text{ mA/cm}^2$ , an open circuit voltage of  $0.44 \text{ V}$ , a fill factor of  $41\%$  and consequently a PCE of  $1.2\%$ . In comparison, the PSiF-DBT:CIS solar cell showed an enhancement for all device related parameters achieving a  $V_{OC}$  of  $0.5 \text{ V}$ , a  $J_{SC}$  of  $9.6 \text{ mA/cm}^2$  and a FF of  $51\%$  leading to a PCE of  $2.5\%$ . Thus, the electrical characterization of the NCSCs reveals a drastic increase in  $J_{SC}$  of more than  $40\%$  as well as in FF of  $24\%$  for PSiF-DBT:CIS solar cells in comparison to PCDTBT:CIS devices. These dramatic differences in the device performance, however, can actually be explained perfectly by the observed morphological dissimilarities. AFM- and TEM investigations as well as the PL-quenching experiments confirm, polymer agglomerates in PCDTBT:CIS films with dimensions up to more than  $100 \text{ nm}$  are formed. As a result a non-negligible fraction of photogenerated excitons created in these particles are not able to reach the polymer-CIS interface *via* exciton migration and to dissociate to independent charge carriers.<sup>[444]</sup> Consequently, they recombine radiatively or non-radiatively in the polymer and therefore are lost for charge carrier generation. In contrast to that, totally different conditions are found for PSiF-DBT:CIS films. As morphological investigations unveil the silicon-bridged polymer has a certain tendency to crystallize, which apparently leads to more favorable phase segregation and domain sizes for both, the CIS nanoparticles and the polymer. This improved phase segregation enables a more effective electron transfer from PSiF-DBT to CIS, which results in a stronger PL-quenching compared to PCDTBT:CIS blends. Due to the diminished recombination of excitons in PSiF-DBT, combined with an elevated charge transfer to CIS,  $J_{SC}$  as well as FF are significantly enhanced. Compared to these device parameters, the  $V_{OC}$  seems to be much less dependent on the morphology and hence to the nature of the polymers.<sup>[451]</sup> The presented device data therefore display well that one of the key parameters determining  $J_{SC}$  and FF is given by the nanocomposite morphology, which is directly related to the polymer's structure.



**Figure 5-20: Current density-voltage characteristics of PCDTBT:CIS (left) and PSiF-DBT:CIS (right) solar cells.**

To actually assess the impact of dissimilar nanomorphologies on the photocurrent generation efficiency at the particular wavelengths of the incident light IPCE measurements were performed. Figure 5-21 presents the EQE characteristics for a PCDTBT based as well as for PSiF-DBT based NCSC. It can clearly be observed from both EQE spectra that, just as in case of the MDMO-PPV:CIS system, the polymers as well as the nanocrystals in the nanocomposite layers contribute significantly to photocurrent generation. Thus, the EQE spectra are formed more or less by a superposition of the absorption characteristics of CIS and PCDTBT or PSiF-DBT, respectively. This particularly can be concluded from the fact that the absorption maximum of PCDTBT as well as of PSiF-DBT around  $600 \text{ nm}$  is clearly reflected in the IPCE data and the onset of the photocurrent generation at approximately  $900 \text{ nm}$  is attributable to the absorption onset of the CIS phase. An EQE of  $45\%$  is

achieved at 460 nm for PSiF-DBT:CIS devices which constitutes a two-fold higher value than for PCDTBT:CIS devices with a maximum of 25% (280 nm). The in general higher EQE in the nanocomposite system utilizing the silafluorene based copolymer, thus perfectly corroborates all findings presented above. Moreover, it underlines once more the importance of the formation of a suitable nanomorphology in order to realize efficient nanocomposite solar cells.

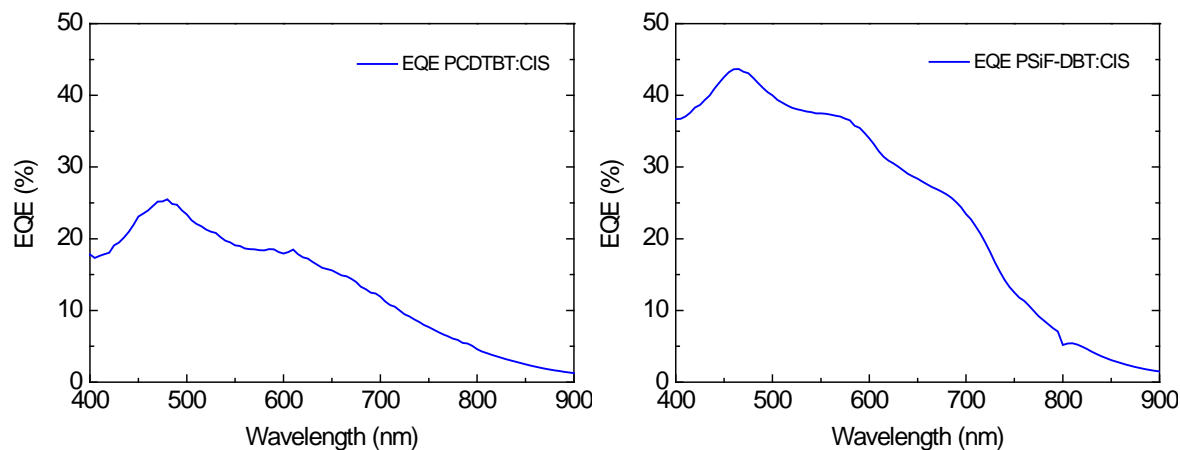


Figure 5-21: IPCE characteristics (bottom) of PCDTBT:CIS (left) and PSiF-DBT:CIS (right) solar cells.

Table 7: Characteristic solar cell parameters under standard AM 1.5G conditions and relevant device parameters as achieved from OFET characterization.

Polymer	$V_{oc}$ [mV]	$J_{sc}$ [mA/cm <sup>2</sup> ]	FF [%]	PCE [%]	EQE [%]	$\mu^a$ [cm <sup>2</sup> /Vs]		on-off current ratio	
						before	after	before	after
						annealing <sup>b</sup>		annealing <sup>b</sup>	
PCDTBT	440	6.9	41	1.2	25	$1.2 \times 10^3$	$1.7 \times 10^3$	$6.5 \times 10^3$	$2.4 \times 10^4$
PSiF-DBT	500	9.6	51	2.5	45	$3.2 \times 10^4$	$8.0 \times 10^4$	$1.3 \times 10^3$	$6.5 \times 10^3$

<sup>a</sup>  $V_G = 60$  V;  $V_D = 100$  V; <sup>b</sup> 200°C in vacuum.

### 5.3.8 Conclusion

In summary, in this chapter the effects of the molecular structure of highly similar conjugated polymers on the nanomorphology formation in nanocomposite films and its impact on their photophysical properties as well as on the performance of polymer:CIS NCSCs was investigated. Structural studies thereby reveal that the simple exchange of the nitrogen atom at the bridging position of carbazole to silicon, i.e. a change from PCDTBT to PSiF-DBT, yields a certain semicrystallinity for the latter while the former proved to be completely amorphous. Interestingly, despite the semicrystalline packing of PSiF-DBT, OFET mobility measurements evidenced a higher mobility in PCDTBT. Yet, the structural modification of the polymer backbone (Si vs. N heteroatom), displayed to exhibit a tremendous impact on the morphology of polymer:CIS nanocomposite films. Polymer agglomerates with lateral dimensions of up to several hundred nanometers formed in the PCDTBT:CIS films facilitate radiative recombination in the polymer for excitons that are not able to reach the heterojunction interface and thus the PL quenching was rather inefficient. PSiF-DBT:CIS films, in contrast, displayed a more favorable nanomorphology which in association with the



semicrystalline arrangement of PSiF-DBT enables effective PL-quenching and efficient exciton dissociation. Device related results obtained from polymer:CIS nanocomposite solar cells further confirm that in the PSiF-DBT:CIS system, in contrast to the amorphous constitution of PCDTBT, the conversion of excitons to mobile charges is more efficient resulting in a comparably elevated photocurrent generation. The observed enhancement of the PCE from 1.2% to 2.5%, upon an exchange of the carbazole-based PCDTBT with the silicon-bridged analogue PSiF-DBT, was found to correlate directly to the distinctively dissimilar nanomorphology of the respective CIS blended films, leading to an enhanced overall device efficiency for PSiF-DBT:CIS solar cells.

As a conclusion from all these findings it can be stated that despite charge carrier mobility doubtlessly constitutes an important parameter for the realization of efficient solar cells, the formation of a suitable nanomorphology in the nanocomposite system proves to be a key factor with even higher impact. Thus, for further works on polymer:nanocrystallite solar cells it will be one of the main tasks to find polymers as well as the respective processing parameters that allow for the realization of NC systems exhibiting highly efficient photocurrent generation. Only then the required prerequisites are met that enable to exploit the nanocomposite approach for efficient hybrid solar cells.

## 5.4 Conclusions – Organic Photovoltaics

The second part of this thesis is dedicated to a novel strategy for the realization of polymer:CIS nanocomposite solar cells via an in-situ nanoparticle formation approach. The basic photo-physical properties, the surface and bulk morphology and the opto-electronic characteristics of nanocomposite films fabricated in that manner are investigated by means of absorbance and photoluminescence spectroscopy, AFM and TEM studies, X-ray diffraction as well as by evaluating the optoelectrical characteristics of hybrid solar cells fabricated with the presented approach.

In chapter 5.2 at first the underlying principle of nanoparticle formation *via* a thermal decomposition of highly soluble metal xanthate precursor molecules is presented and it is shown that a mild thermal annealing step with annealing temperatures in the range of 200°C is sufficient to convert the metal salts to CIS nanoparticles. As a first polymer, the well-known PPV derivative MDMO-PPV is used as corresponding matrix polymer for the fabrication of polymer:CIS nanocomposite films. Absorption and fluorescence quenching studies on the one hand reveal a significant contribution of the inorganic phase in the NC films to the overall absorption and the pronounced PL quenching suggests efficient charge carrier transfer at the polymer:nanoparticle interface. These findings are corroborated by the performance of as fabricated MDMO-PPV solar cells and the corresponding IPCE measurements. The solar cells achieved power conversion efficiencies of 1.75% and IPCE characteristics reveal a distinct contribution of the inorganic phase to photocurrent generation. This contribution, however, constitutes the main advantage of the organic-inorganic hybrid concept compared to classical polymer:fullerene bulkheterojunction solar cells, since it allows for an effective broadening of the overall absorption width in nanocomposite solar cells.

Chapter 5.3 presents detailed analyses of the interplay between polymer structure, nanomorphology and device performance for polymer:CIS NCSCs. In particular, the impact of different bridging atoms in the molecular structure of the thermally highly stable low bandgap polymers PCDTBT and PSiF-DBT is assessed. XRD studies on thin films of both polymers reveal that despite the significant molecular similarity both polymers exhibit a considerably different conformation. While PSiF-DBT shows semicrystallinity, PCDTBT is completely amorphous. Nevertheless, interestingly a higher field effect hole mobility is measured for PCDTBT. The difference in the molecular structure naturally also bears a tremendous impact on the nanomorphology formation in polymer:CIS nanocomposite films. The appearance of polymer agglomerates in PCDTBT:CIS NC films leads to a decreased PL quenching and, as shown by IPCE measurements, to a considerably lower photocurrent generation in the respective solar cells, compared to PSiF-DBT:CIS films which exhibit a homogenous polymer:CIS nanomorphology. The corresponding NCSC show a PCE of only 1.2% for PCDTBT:CIS and of 2.5% for PSiF-DBT:CIS.

## 6 Outlook

In this thesis possible ways to enhance the luminous efficiency of blue emitting PLEDs and DLEDs via solution processed multilayer structures have been shown on the examples of pyrene-based polymers and dendrimers. Yet, besides the presented technique, for future works also other strategies to enhance the light generation or extraction efficiencies should be addressed. A possible way to further enhance devices luminous efficiency may be realized by the exploitation of surface plasmons at organic-metal interfaces. This can be done by an effect called “metal enhanced fluorescence”, where the incorporation of gold or silver nanoparticles modifies the photophysical properties of fluorophores like absorption, radiative and nonradiative decay rate in such a way that light emitting diodes with fluorescence efficiencies of almost 100% can be realized.<sup>[452]</sup> Strategies to enhance the light outcoupling efficiency of the devices are given for example by texturing the OLED spherically which leads to an outcoupling of waveguided and substrate modes<sup>[453]</sup> or by matching the refractive index of the light emitting materials to the supporting substrate which as well leads to an reduction of trapped light within the device.<sup>[454]</sup>

In addition to these device improving techniques, novel assembling strategies allowing for the exploitation of large scale OLED fabrication are under development. Here one particular challenge is the realization of thin and uniform layers via inkjet printing, which makes great demands for the applied device-<sup>[455]</sup> as well as for inkjet printer design.<sup>[456]</sup> Another way towards the fabrication of low-cost large area devices is the manufacturing of large-area emissive devices with low-cost roll-to-roll coating methods like slot-die coating.<sup>[457]</sup>

Concerning the future developments of OSCs, even though small molecule based devices already reached PCEs of 12% and those based on polymers are in the range of 10%, the challenges are similar to those found for OLEDs. As presented in this thesis, an enhancement of the PCE can be addressed by NCSCs, which exhibit an enhanced absorption width in the visible region compared to entirely organic solar cells. Yet, this technology is still in its infants and more efforts need to be put into it in order to realize devices with similar performance as their purely organic counterparts. This is especially valid regarding on the one hand the understanding of the interplay between the molecular structure of the organic materials and the nanomorphology of the formed nanocomposite and on the other hand regarding the physical processes governing the charge generation and charge separation efficiencies between organic material and inorganic nanocrystals.

However, in order to enhance the PCE, also in organic photovoltaics the exploitation of surface plasmons is an intensively studied topic.<sup>[458–460]</sup>

Finally, large area-production of organic solar cells is also already under investigation utilizing again inkjet-printing<sup>[461]</sup> as well as roll-to-roll fabrication techniques.<sup>[462]</sup>

## 7 References

- [1] Riordan M., Hoddeson L.; "Invention of the First Transistor", <http://www.aps.org/publications/apsnews/200011/history.cfm> (accessed Oct1, 2012).
- [2] Bardeen J., Brattain W.; "The transistor, a semi-conductor triode" *Physical Review* **1948**, *74*, 230–231.
- [3] Shockley W.; "The theory of pn junctions in semiconductors and pn junction transistors" *Bell Syst. Tech. J* **1949**, *28*, 435–489.
- [4] Pope M., Kallmann H. P., Magnante P.; "Electroluminescence in Organic Crystals" *The Journal of Chemical Physics* **1963**, *38*, 2042.
- [5] Helfrich W., Schneider W. G.; "Recombination Radiation in Anthracene Crystals" *Physical Review Letters* **1965**, *14*, 229–232.
- [6] Chiang C. K., Fincher jr. C. R., Park Y. W., Heeger A. J., Shirakawa H., Louis E. J., Gau S. C., MacDiarmid A. G.; "Electrical conductivity in doped polyacetylene" *Physical Review Letters* **1977**, *39*, 1098–1101.
- [7] Braun D., Heeger A. J.; "Visible light emission from semiconducting polymer diodes" *Applied Physics Letters* **1991**, *58*, 1982.
- [8] Koezuka H., Tsumura A., Ando T.; "Field-effect transistor with polythiophene thin film" *Synthetic Metals* **1987**, *18*, 699–704.
- [9] Garnier F., Hajlaoui R., Yassar A., Srivastava P.; "All-polymer field-effect transistor realized by printing techniques." *Science* **1994**, *265*, 1684–6.
- [10] Sariciftci N. S., Smilowitz L., Heeger A. J., Wudl F.; "Photoinduced electron transfer from a conducting polymer to buckminsterfullerene." *Science* **1992**, *258*, 1474–6.
- [11] Granström M., Petritsch K., Arias A.; "Laminated fabrication of polymeric photovoltaic diodes" *Nature* **1998**, *395*, 257–260.
- [12] Yu G., Gao J., Hummelen J. C., Wudl F., Heeger A. J.; "Polymer Photovoltaic Cells: Enhanced Efficiencies via a Network of Internal Donor-Acceptor Heterojunctions" *Science* **1995**, *270*, 1789–1791.
- [13] Yu G., Wang J., McElvain J., Heeger A. J.; "Large-Area, Full-Color Image Sensors Made with Semiconducting Polymers" *Advanced Materials* **1998**, *10*, 1431–1434.
- [14] Mills A., Lepre A.; "Controlling the Response Characteristics of Luminescent Porphyrin Plastic Film Sensors for Oxygen" *Analytical Chemistry* **1997**, *69*, 4653–4659.
- [15] Amao Y., Asai K., Miyashita T., Okura I.; "Novel optical oxygen sensing material: platinum porphyrin-fluoropolymer film" *Polymers for Advanced Technologies* **2000**, *11*, 705–709.
- [16] Ouyang J., Chu C.-W., Szmanda C. R., Ma L., Yang Y.; "Programmable polymer thin film and non-volatile memory device." *Nature Materials* **2004**, *3*, 918–22.
- [17] Wan Han K., Ho Lee M., Whan Kim T., Yeol Yun D., Woo Kim S., Wook Kim S.; "Electrical characteristics and operating mechanisms of nonvolatile memory devices fabricated utilizing core-shell CuInS<sub>2</sub>-ZnS quantum dots embedded in a poly(methyl methacrylate) layer" *Applied Physics Letters* **2011**, *99*, 193302.
- [18] Tang C. W., Vanslyke S. A.; "Organic electroluminescent diodes" *Applied Physics Letters* **1987**, *51*, 913–915.
- [19] Burroughes J. H., Bradley D. D. C., Brown A. R., Marks R. N., Mackay K., Friend R. H., Burns P. L., Holmes A. B.; "Light-emitting diodes based on conjugated polymers" *Nature* **1990**, *347*, 539–541.
- [20] Hung L. ., Chen C. .; "Recent progress of molecular organic electroluminescent materials and devices" *Materials Science and Engineering: R: Reports* **2002**, *39*, 143–222.
- [21] Friend R., Gymer R., Holmes A., Burroughes J. H., Marks R. N., Taliani C., Bradley D. D. C., Dos Santos D. A., Brédas J.-L., Lögdlund M., Salaneck W. R.; "Electroluminescence in conjugated polymers" *Nature* **1999**, *397*, 121–128.
- [22] Kido J., Kimura M., Nagai K.; "Multilayer white light-emitting organic electroluminescent device." *Science* **1995**, *267*, 1332–4.
- [23] Tasch S., List E. J. W., Ekström O., Graupner W., Leising G., Schlichting P., Rohr U., Geerts Y., Scherf U., Müllen K.; "Efficient white light-emitting diodes realized with new processable blends of conjugated polymers" *Applied Physics Letters* **1997**, *71*, 2883.

- [24] Pochettino A.; "Sul comportamento foto-elettrico dell' antracene" *Acad. Lincei Rendus* **1906**, *15*, 355–368.
- [25] Kearns D., Calvin M.; "Photovoltaic Effect and Photoconductivity in Laminated Organic Systems" *The Journal of Chemical Physics* **1958**, *29*, 950.
- [26] Tang C. W.; "Two-layer organic photovoltaic cell" *Applied Physics Letters* **1986**, *48*, 183.
- [27] Hiramoto M., Fukusumi H., Yokoyama M.; "Organic solar cell based on multistep charge separation system" *Applied Physics Letters* **1992**, *61*, 2580.
- [28] Sariciftci N., Smilowitz L., Heeger A. J., Wudl F.; "Semiconducting polymers (as donors) and buckminsterfullerene (as acceptor): photoinduced electron transfer and heterojunction devices" *Synthetic Metals* **1993**, *59*, 333–352.
- [29] Hiramoto M., Fujiwara H., Yokoyama M.; "Three-layered organic solar cell with a photoactive interlayer of codeposited pigments" *Applied Physics Letters* **1991**, *58*, 1062.
- [30] Tada K., Onoda M., Nakayama H., Yoshino K.; "Photocell with heterojunction of donor/acceptor polymers" *Synthetic Metals* **1999**, *102*, 982–983.
- [31] Halls J. J. M., Arias A. C., MacKenzie J. D., Wu W., Inbasekaran M., Woo E. P., Friend R. H.; "Photodiodes Based on Polyfluorene Composites: Influence of Morphology" *Advanced Materials* **2000**, *12*, 498–502.
- [32] Arici E., Hoppe H., Schäffler F., Meissner D., Malik M. A., Sariciftci N. S.; "Hybrid solar cells based on inorganic nanoclusters and conjugated polymers" *Thin Solid Films* **2004**, *451-452*, 612–618.
- [33] Arici E., Sariciftci N., Meissner D.; "Hybrid Solar Cells Based on Nanoparticles of CuInS<sub>2</sub> in Organic Matrices" *Advanced Functional Materials* **2003**, *13*, 165–171.
- [34] Arici E., Hoppe H., Reuning A., Sariciftci N. S., Meissner D.; "CIS plastic solar cells" *17th European Photovoltaic Solar Energy Conference Proceedings* **2002**, 61–64.
- [35] Dang X., Yi H., Ham M.-H., Qi J., Yun D. S., Ladewski R., Strano M. S., Hammond P. T., Belcher A. M.; "Virus-templated self-assembled single-walled carbon nanotubes for highly efficient electron collection in photovoltaic devices." *Nature Nanotechnology* **2011**, *6*, 377–84.
- [36] He Z., Zhong C., Su S., Xu M., Wu H., Cao Y.; "Enhanced power-conversion efficiency in polymer solar cells using an inverted device structure" *Nature Photonics* **2012**, *6*, 593–597.
- [37] Green M. A., Emery K., Hishikawa Y., Warta W., Dunlop E. D.; "Solar cell efficiency tables (version 39)" *Progress in Photovoltaics: Research and Applications* **2012**, *20*, 12–20.
- [38] Rohr S.; "Neuer Weltrekord für organische Solarzellen: Heliatek behauptet sich mit 12 % Zelleffizienz als Technologieführer", [http://www.heliatek.com/wp-content/uploads/2013/01/130116\\_PM\\_Heliatek-erzielt-Weltkordeffizienz-fuer-OPV.pdf](http://www.heliatek.com/wp-content/uploads/2013/01/130116_PM_Heliatek-erzielt-Weltkordeffizienz-fuer-OPV.pdf) (accessed Jan27, 2013).
- [39] Konarka Technologies; "Power Plastic", <http://www.konarka.com/index.php/power-plastic/about-power-plastic/> (accessed Oct17, 2012).
- [40] Grizzi I., Crankshaw M., Forsythe D., Williams G.; "62.3: Fundamental Issues with IJP P-OLED Devices: Identification and Corrective Actions" *SID Symposium Digest of Technical Papers* **2011**, *42*, 932–934.
- [41] Nikam M., Singh R., Bhise S.; "Organic Light Emitting Diodes: Future of Displays" *IJCA Proceedings on International Conference on Advances in Communication and Computing Technologies 2012* **2012**, 31–34.
- [42] Heitler W., London F.; "Wechselwirkung neutraler Atome und homöopolare Bindung nach der Quantenmechanik" *Zeitschrift für Physik A: Hadrons and Nuclei* **1927**, *472*, 1–19.
- [43] Pauling L.; "The nature of the chemical bond. Application of results obtained from the quantum mechanics and from a theory of paramagnetic susceptibility to the structure of molecules" *Journal of the American Chemical Society* **1931**, *53*, 1367–1400.
- [44] Bruce P. Y.; "Organic Chemistry", <http://wps.prenhall.com/wps/media/objects/724/741576/> (accessed Oct27, 2012).
- [45] Heeger A. J.; "Semiconducting and metallic polymers: the fourth generation of polymeric materials" *Synthetic Metals* **2001**, *125*, 23–42.
- [46] Leo K.; "What are organic semiconductors?", [www.orgworld.de](http://www.orgworld.de) (accessed Oct28, 2012).
- [47] Collon M.; "Energy Transfer from Conjugated Polymers to Novel Lanthanide Complexes and its Application in Organic Light Emitting Devices", Diploma Thesis, Graz University of Technology, **2002**.

- [48] Zojer E., Shuai Z., Leising G., Brédas J. L.; "From molecular states to band structure: Theoretical investigation of momentum dependent excitations in phenylene based organic materials" *The Journal of Chemical Physics* **1999**, *111*, 1668.
- [49] Weaire D., Thorpe M.; "Electronic Properties of an Amorphous Solid. I. A Simple Tight-Binding Theory" *Physical Review B* **1971**, *4*, 2508–2520.
- [50] Coté M.; "Electronic Properties of Polymers: A Microscopic View" *Physics in Canada* **2003**, *59*, 121.
- [51] Knoester J., Mostovoy M.; Disorder and Solitons in Trans-Polyacetylene. In *Semiconducting Polymers*; Georges H., van Hutten P. F., Eds.; Wiley-VCH: Weinheim, **2000**.
- [52] Brédas J., Thémans B., Fripiat J., André J., Chance R.; "Highly conducting polyparaphenylene, polypyrrole, and polythiophene chains: An ab initio study of the geometry and electronic-structure modifications upon doping" *Physical Review B* **1984**, *29*, 6761–6773.
- [53] Peierls R. E.; "*Quantum Theory of Solids*"; Clarendon Press: Oxford, **1955**.
- [54] Peierls R. E.; "*More surprises in Theoretical Physics*"; Princeton University Press: Princeton, **1991**.
- [55] Su W. P., Schrieffer J. R., Heeger A. J.; "Solitons in Polyacetylene" *Physical Review Letters* **1979**, *42*, 1698–1701.
- [56] Su W., Schrieffer J., Heeger A.; "Soliton excitations in polyacetylene" *Physical Review B* **1980**, *22*, 2099–2111.
- [57] Hudson B. S., Kohler B. E., Schulten K.; Linear Polyene Electronic Structure and Potential Surfaces. In *Excited States*; Lim E. C., Ed.; Academic Press Inc: New York, NY, **1982**; pp. 1–95.
- [58] Hudson B., Kohler B.; "Electronic structure and spectra of finite linear polyenes" *Synthetic Metals* **1984**, *9*, 241–253.
- [59] Hubbard J.; "Electron Correlations in Narrow Energy Bands" *Proceedings of the Royal Society A: Mathematical, Physical and Engineering Sciences* **1963**, *276*, 238–257.
- [60] Hubbard J.; "Electron Correlations in Narrow Energy Bands. III. An Improved Solution" *Proceedings of the Royal Society A: Mathematical, Physical and Engineering Sciences* **1964**, *281*, 401–419.
- [61] Livioiti E., Ubertini F., Erdös P.; "Bond configurations in the Peierls–Hubbard model of small ring-shaped molecules" *The Journal of Chemical Physics* **1999**, *111*, 2392.
- [62] Baldenebro-López J., Castorena-González J., Flores-Holguín N., Almaral-Sánchez J., Glossman-Mitnik D.; "Density functional theory (DFT) study of triphenylamine-based dyes for their use as sensitizers in molecular photovoltaics." *International journal of molecular sciences* **2012**, *13*, 4418–32.
- [63] Jacquemin D., Wathélet V., Perpète E. A., Adamo C.; "Extensive TD-DFT Benchmark: Singlet-Excited States of Organic Molecules" *Journal of Chemical Theory and Computation* **2009**, *5*, 2420–2435.
- [64] Ichikawa H., Ebisawa Y.; "Hartree-Fock MO theoretical approach to aromaticity. Interpretation of Hückel resonance energy in terms of kinetic energy of pi electron" *Journal of the American Chemical Society* **1985**, *107*, 1161–1165.
- [65] Brédas J. L., Calbert J. P., Da Silva Filho D., Cornil J.; "Organic semiconductors: a theoretical characterization of the basic parameters governing charge transport." *Proceedings of the National Academy of Sciences of the United States of America* **2002**, *99*, 5804–9.
- [66] Figueira-Duarte T. M., Del Rosso P. G., Trattnig R., Sax S., List E. J. W., Müllen K.; "Designed suppression of aggregation in polypyrene: toward high-performance blue-light-emitting diodes." *Advanced Materials* **2010**, *22*, 990–3.
- [67] Cornil J., Beljonne D., Calbert J.-P., Brédas J.-L.; "Interchain Interactions in Organic  $\pi$ -Conjugated Materials: Impact on Electronic Structure, Optical Response, and Charge Transport" *Advanced Materials* **2001**, *13*, 1053–1067.
- [68] Roth S., Carroll D. L.; "*One-Dimensional Metals*"; 2nd Edn.; Wiley-VCH: Weinheim, **2003**.
- [69] Frenkel Y.; "On the absorption of light and the trapping of electrons and positive holes in crystalline dielectrics" *Physikalische Zeitschrift der Sowjetunion* **1936**, *9*, 158.
- [70] Mott N. F.; "Conduction in polar crystals. II. The conduction band and ultra-violet absorption of alkali-halide crystals" *Transactions of the Faraday Society* **1938**, *34*, 500.
- [71] Wannier G.; "The Structure of Electronic Excitation Levels in Insulating Crystals" *Physical Review* **1937**, *52*, 191–197.
- [72] Franck J., Dymond E. G.; "Elementary processes of photochemical reactions" *Transactions of the Faraday Society* **1926**, *21*, 536.

- [73] Condon E.; "Nuclear Motions Associated with Electron Transitions in Diatomic Molecules" *Physical Review* **1928**, *32*, 858–872.
- [74] Henderson B., Imbusch G. F.; "*Optical Spectroscopy of Inorganic Solids*"; Oxford University Press: Oxford, **1989**.
- [75] Huang K., Rhys A.; "Theory of Light Absorption and Non-Radiative Transitions in F-Centres" *Proceedings of the Royal Society A: Mathematical, Physical and Engineering Sciences* **1950**, *204*, 406–423.
- [76] Kasha M.; "Characterization of electronic transitions in complex molecules" *Discussions of the Faraday Society* **1950**, *9*, 14.
- [77] Stokes G. G.; "On the Change of Refrangibility of Light" *Philosophical Transactions of the Royal Society of London* **1852**, *142*, 463–562.
- [78] Heimel G., Daghofer M., Gierschner J., List E. J. W., Grimsdale A. C., Müllen K., Beljonne D., Brédas J.-L., Zojer E.; "Breakdown of the mirror image symmetry in the optical absorption/emission spectra of oligo(para-phenylene)s." *The Journal of chemical physics* **2005**, *122*, 54501.
- [79] Wilson J. S., Dhoot A. S., Seeley A. J., Khan M. S., Köhler A., Friend R. H.; "Spin-dependent exciton formation in pi-conjugated compounds." *Nature* **2001**, *413*, 828–31.
- [80] Niedermair F., Trattnig R., Mereiter K., Schmuck M., Sax S., List E. J. W., Slugovc C.; "Red electrophosphorescent platinum(II) quinolinolate complexes" *Monatshefte für Chemie - Chemical Monthly* **2010**, *141*, 847–858.
- [81] Kappaun S., Eder S., Sax S., Mereiter K., List E. J. W., Slugovc C.; "Organoiridium Quinolinolate Complexes: Synthesis, Structures, Thermal Stabilities and Photophysical Properties" *European Journal of Inorganic Chemistry* **2007**, *2007*, 4207–4215.
- [82] Baldo M., Adachi C., Forrest S.; "Transient analysis of organic electrophosphorescence. II. Transient analysis of triplet-triplet annihilation" *Physical Review B* **2000**, *62*, 10967–10977.
- [83] Partee J., Frankevich E., Uhlhorn B., Shinar J., Ding Y., Barton T.; "Delayed Fluorescence and Triplet-Triplet Annihilation in  $\pi$ -Conjugated Polymers" *Physical Review Letters* **1999**, *82*, 3673–3676.
- [84] Lakowicz J. R.; "*Principles of Fluorescence Spectroscopy*"; 4th Edn.; Springer: New York, NY, **2010**.
- [85] Wohlgenannt M., Tandon K., Mazumdar S., Ramasesha S., Vardeny Z. V.; "Formation cross-sections of singlet and triplet excitons in pi-conjugated polymers." *Nature* **2001**, *409*, 494–7.
- [86] Reufer M., Walter M., Lagoudakis P.; "Spin-conserving carrier recombination in conjugated polymers" *Nature Materials* **2005**, *4*.
- [87] Sirringhaus H., Brown P. J., Friend R. H., Nielsen M. M., Bechgaard K., Langeveld-Voss B. M. W., Spiering A. J. H., Janssen R. A. J., Meijer E. W., Herwig P., De Leeuw D. M.; "Two-dimensional charge transport in self-organized, high-mobility conjugated polymers" *Nature* **1999**, *401*, 685–688.
- [88] Logan R., Peters A.; "Impurity effects upon mobility in silicon" *Journal of Applied Physics* **1960**, *31*, 122.
- [89] Pienn M.; "Application of Blue-Emitting Ladder-Type Poly(para-phenylene)s for Solid State Lighting: Efficiency Improvement and Colour Tuning", Diploma Thesis, Graz University of Technology, **2009**.
- [90] Marcus R. A.; "On the Theory of Electron-Transfer Reactions. VI. Unified Treatment for Homogeneous and Electrode Reactions" *The Journal of Chemical Physics* **1965**, *43*, 679.
- [91] Förster T.; "Zwischenmolekulare Energiewanderung und Fluoreszenz" *Annalen der Physik* **1948**, *437*, 55–75.
- [92] Dexter D. L.; "A Theory of Sensitized Luminescence in Solids" *The Journal of Chemical Physics* **1953**, *21*, 836.
- [93] Lane P., Palilis L., O'Brien D., Giebeler C., Cadby A., Lidzey D., Campbell A., Blau W., Bradley D.; "Origin of electrophosphorescence from a doped polymer light emitting diode" *Physical Review B* **2001**, *63*, 235206.
- [94] Sudhakar M., Djurovich P. I., Hogen-Esch T. E., Thompson M. E.; "Phosphorescence quenching by conjugated polymers." *Journal of the American Chemical Society* **2003**, *125*, 7796–7.
- [95] Mott N. F.; "The Theory of Crystal Rectifiers" *Proceedings of the Royal Society A: Mathematical, Physical and Engineering Sciences* **1939**, *171*, 27–38.
- [96] Schottky W.; "Abweichung vom Ohmschen Gesetz in Halbleitern" *Physikalische Zeitschrift* **1940**, *41*, 570–573.

- [97] Chassé T., Wu C.-I., Hill I. G., Kahn A.; "Band alignment at organic-inorganic semiconductor interfaces:  $\alpha$ -NPD and CuPc on InP(110)" *Journal of Applied Physics* **1999**, *85*, 6589.
- [98] Koch N., Kahn A., Ghijsen J., Pireaux J.-J., Schwartz J., Johnson R. L., Elschner A.; "Conjugated organic molecules on metal versus polymer electrodes: Demonstration of a key energy level alignment mechanism" *Applied Physics Letters* **2003**, *82*, 70.
- [99] Koch N.; "Organic electronic devices and their functional interfaces." *Chemphyschem: a European journal of chemical physics and physical chemistry* **2007**, *8*, 1438–55.
- [100] Ishii H., Sugiyama K., Ito E., Seki K.; "Energy Level Alignment and Interfacial Electronic Structures at Organic/Metal and Organic/Organic Interfaces" *Advanced Materials* **1999**, *11*, 605–625.
- [101] Scott J. C.; "Metal-organic interface and charge injection in organic electronic devices" *Journal of Vacuum Science & Technology A: Vacuum, Surfaces, and Films* **2003**, *21*, 521.
- [102] Braun S., Salaneck W. R., Fahlman M.; "Energy-Level Alignment at Organic/Metal and Organic/Organic Interfaces" *Advanced Materials* **2009**, *21*, 1450–1472.
- [103] Beljonne D., Cornil J., Muccioli L., Zannoni C., Brédas J.-L., Castet F.; "Electronic Processes at Organic–Organic Interfaces: Insight from Modeling and Implications for Opto-electronic Devices" *Chemistry of Materials* **2011**, *23*, 591–609.
- [104] Scott J. C., Malliaras G. G.; "Charge injection and recombination at the metal–organic interface" *Chemical Physics Letters* **1999**, *299*, 115–119.
- [105] Tengstedt C., Osikowicz W., Salaneck W. R., Parker I. D., Hsu C.-H., Fahlman M.; "Fermi-level pinning at conjugated polymer interfaces" *Applied Physics Letters* **2006**, *88*, 053502.
- [106] Richardson O. W.; "LXVII. The distribution of the molecules of gas in a field of force, with applications to the theory of electrons" *Philosophical Magazine Series 6* **1914**, *28*, 633–647.
- [107] Dushman S.; "Electron Emission from Metals as a Function of Temperature" *Physical Review* **1923**, *21*, 623–636.
- [108] Fowler R. H., Nordheim L.; "Electron Emission in Intense Electric Fields" *Proceedings of the Royal Society A: Mathematical, Physical and Engineering Sciences* **1928**, *119*, 173–181.
- [109] Arkhipov V., Emelianova E.; "Charge injection into light-emitting diodes: Theory and experiment" *Journal of applied physics* **1998**, *84*, 848–856.
- [110] Arkhipov V., Emelianova E., Adriaenssens G., Bäessler H.; "Equilibrium carrier mobility in disordered organic semiconductors" *Journal of Non-Crystalline Solids* **2002**, *299-302*, 1047–1051.
- [111] Wolf U., Arkhipov V., Bäessler H.; "Current injection from a metal to a disordered hopping system. I. Monte Carlo simulation" *Physical Review B* **1999**, *59*, 7507–7513.
- [112] Van Woudenberg T., Blom P., Vissenberg M. C., Huijberts J. N.; "Temperature dependence of the charge injection in poly-dialkoxy-p-phenylene vinylene" *Applied Physics Letters* **2001**, *79*, 1697.
- [113] Flämmich M.; "Optical Characterization of OLED Emitter Properties by Radiation Pattern Analyses", Dissertation, Friedrich-Schiller-Universität Jena, **2011**.
- [114] Nowy S., Krummacher B. C., Frischeisen J., Reinke N. A., Brütting W.; "Light extraction and optical loss mechanisms in organic light-emitting diodes: Influence of the emitter quantum efficiency" *Journal of Applied Physics* **2008**, *104*, 123109.
- [115] Meerheim R., Furno M., Hofmann S., Lüssem B., Leo K.; "Quantification of energy loss mechanisms in organic light-emitting diodes" *Applied Physics Letters* **2010**, *97*, 253305.
- [116] Purcell E. M., Pound R. V.; Theory of Magnetic Resonance Absorption by Nuclear Moments in Solids. In *Proceedings of the American Physical Society*; **1946**; Vol. 69, p. 680.
- [117] Kropp J. L., Dawson W. R., Windsor M. W.; "Radiative and radiationless processes in aromatic molecules. Pyrene" *The Journal of Physical Chemistry* **1969**, *73*, 1747–1752.
- [118] Hofmann S., Thomschke M., Lüssem B., Leo K.; "Top-emitting organic light-emitting diodes" *Optics Express* **2011**, *19*, A1250.
- [119] Marks R. N., Halls J. J. M., Bradley D. D. C., Friend R. H., Holmes A. B.; "The photovoltaic response in poly(p-phenylene vinylene) thin-film devices" *Journal of Physics: Condensed Matter* **1994**, *6*, 1379–1394.
- [120] Morel D. L., Ghosh A. K., Feng T., Stogryn E. L., Purwin P. E., Shaw R. F., Fishman C.; "High-efficiency organic solar cells" *Applied Physics Letters* **1978**, *32*, 495.
- [121] Peumans P., Bulović V., Forrest S. R.; "Efficient photon harvesting at high optical intensities in ultrathin organic double-heterostructure photovoltaic diodes" *Applied Physics Letters* **2000**, *76*, 2650.



- [122] Halls J. J. M., Walsh C. A., Greenham N. C., Marseglia E. A., Friend R. H., Moratti S. C., Holmes A. B.; "Efficient photodiodes from interpenetrating polymer networks" *Nature* **1995**, 376, 498–500.
- [123] Halls J. J. M., Pichler K., Friend R. H., Moratti S. C., Holmes A. B.; "Exciton diffusion and dissociation in a poly(p-phenylenevinylene)/C60 heterojunction photovoltaic cell" *Applied Physics Letters* **1996**, 68, 3120.
- [124] Halls J. J. M., Friend R. H.; "The photovoltaic effect in a poly(p-phenylenevinylene)/perylene heterojunction" *Synthetic Metals* **1997**, 85, 1307–1308.
- [125] Braun C. L.; "Electric field assisted dissociation of charge transfer states as a mechanism of photocarrier production" *The Journal of Chemical Physics* **1984**, 80, 4157.
- [126] Onsager L.; "Initial Recombination of Ions" *Physical Review* **1938**, 54, 554–557.
- [127] Hoppe H., Arnold N., Meissner D., Sariciftci N. S.; "Modeling of optical absorption in conjugated polymer/fullerene bulk-heterojunction plastic solar cells" *Thin Solid Films* **2004**, 451-452, 589–592.
- [128] Martin S., Bradley D., Lane P., Mellor H., Burn P.; "Linear and nonlinear optical properties of the conjugated polymers PPV and MEH-PPV" *Physical Review B* **1999**, 59, 15133–15142.
- [129] Koeppel R., Bossart O., Calzaferri G., Sariciftci N.; "Advanced photon-harvesting concepts for low-energy gap organic solar cells" *Solar Energy Materials and Solar Cells* **2007**, 91, 986–995.
- [130] Jeong J.; "PHOTOVOLTAICS: Measuring the "Sun"", <http://www.laserfocusworld.com/articles/2009/05/photovoltaics-measuring-the-sun.html> (accessed Nov21, 2012).
- [131] Rohde R. A.; "Solar Radiation Spectrum", [http://en.wikipedia.org/wiki/Air\\_mass\\_\(solar\\_energy\)](http://en.wikipedia.org/wiki/Air_mass_(solar_energy)) (accessed Nov21, 2012).
- [132] Parker C. A., Rees W. T.; "Correction of fluorescence spectra and measurement of fluorescence quantum efficiency" *The Analyst* **1960**, 85, 587.
- [133] Crosby G. A., Demas J. N.; "Measurement of photoluminescence quantum yields. A Review" *The Journal of Physical Chemistry* **1971**, 75, 991–1024.
- [134] Nau S.; "Efficiency and Stability of Poly(indenofluorene)-based Homo- and Copolymers", Master Thesis, Graz University of Technology, **2011**.
- [135] Melhuish W. H.; "Quantum efficiencies of fluorescence of organic substances: effect of solvent and concentration of the fluorescent solute" *Journal of Physical Chemistry* **1961**, 65, 229–235.
- [136] Dellepiane G., Cuniberti C., Comoretto D., Musso G., Figari G., Piaggi A., Borghesi A.; "Long-lived photoexcited states in symmetrical polydicarbazolyldiacetylene" *Physical Review B* **1993**, 48, 7850–7856.
- [137] Epshtein O., Nakhmanovich G., Eichen Y., Ehrenfreund E.; "Dispersive dynamics of photoexcitations in conjugated polymers measured by photomodulation spectroscopy" *Physical Review B* **2001**, 63, 2–7.
- [138] Petritsch K.; "Optical modulation spectroscopy in organic and inorganic semiconductors", Diploma Thesis, Graz University of Technology, **1996**.
- [139] Einstein A.; "Über einen die Erzeugung und Verwandlung des Lichtes betreffenden heuristischen Gesichtspunkt" *Annalen der Physik* **1905**, 322, 132–148.
- [140] Schlaf R.; "Calibration of Photoemission Spectra and Work Function Determination", <http://rsl.eng.usf.edu/Documents/Tutorials/PEScalibration.pdf> (accessed Dec4, 2012).
- [141] Scherrer P.; "Bestimmung der Grösse und der inneren Struktur von Kolloidteilchen mittels Röntgenstrahlen" *Nachrichten von der Königl. Gesellschaft der Wissenschaften zu Göttingen* **1918**, 2, 98–100.
- [142] Patterson A.; "The Scherrer Formula for X-Ray Particle Size Determination" *Physical Review* **1939**, 56, 978–982.
- [143] Jones J. E.; "On the Determination of Molecular Fields. II. From the Equation of State of a Gas" *Proceedings of the Royal Society A: Mathematical, Physical and Engineering Sciences* **1924**, 106, 463–477.
- [144] Wang P.-W., Liu Y., Devadoss C., Bharathi P., Moore J. S.; "Electroluminescent diodes from a single component emitting layer of dendritic macromolecules" *Advanced Materials* **1996**, 8, 237–241.
- [145] Halim M., Pillow J. N. G., Samuel I. D. W., Burn P. L.; "Conjugated Dendrimers for Light-Emitting Diodes: Effect of Generation" *Advanced Materials* **1999**, 11, 371–374.
- [146] Lane P. A., Kushto G. P., Kafafi Z. H.; "Efficient, single-layer molecular organic light-emitting diodes" *Applied Physics Letters* **2007**, 90, 023511.

- [147] Duan L., Chin B. D., Yang N. C., Kim M.-H., Kim H. D., Lee S. T., Chung H. K.; "Multilayer blue polymer light-emitting devices with spin-coated interlayers" *Synthetic Metals* **2007**, *157*, 343–346.
- [148] Thomschke M., Hofmann S., Olthof S., Anderson M., Kleemann H., Schober M., Lüsse B., Leo K.; "Improvement of voltage and charge balance in inverted top-emitting organic electroluminescent diodes comprising doped transport layers by thermal annealing" *Applied Physics Letters* **2011**, *98*, 083304.
- [149] Gu G., Bulović V., Burrows P. E., Forrest S. R., Thompson M. E.; "Transparent organic light emitting devices" *Applied Physics Letters* **1996**, *68*, 2606.
- [150] Gather M. C., Jin R., Mello J., Bradley D. D. C., Meerholz K.; "Highly-efficient solution-processed phosphorescent multi-layer organic light-emitting diodes investigated by electromodulation spectroscopy" *Applied Physics B* **2009**, *95*, 113–124.
- [151] Hebner T. R., Wu C. C., Marcy D., Lu M. H., Sturm J. C.; "Ink-jet printing of doped polymers for organic light emitting devices" *Applied Physics Letters* **1998**, *72*, 519.
- [152] Lee T.-W., Zaumseil J., Bao Z., Hsu J. W. P., Rogers J. A.; "Organic light-emitting diodes formed by soft contact lamination." *Proceedings of the National Academy of Sciences of the United States of America* **2004**, *101*, 429–33.
- [153] Kim C., Burrows P. E., Forrest S. R.; "Micropatterning of Organic Electronic Devices by Cold-Welding" *Science* **2000**, *288*, 831–833.
- [154] Gu G., Shen Z., Burrows P. E., Forrest S. R.; "Transparent flexible organic light-emitting devices" *Advanced Materials* **1997**, *9*, 725–728.
- [155] Greenham N. C., Friend R. H., Bradley D. D. C.; "Angular Dependence of the Emission from a Conjugated Polymer Light-Emitting Diode: Implications for efficiency calculations" *Advanced Materials* **1994**, *6*, 491–494.
- [156] Scherf U., List E. J. W.; "Semiconducting Polyfluorenes—Towards Reliable Structure-Property Relationships" *Advanced Materials* **2002**, *14*, 477–487.
- [157] Heise.de; "Verkaufsstart für Sonys OLED-TV", <http://www.heise.de/newsticker/meldung/Verkaufsstart-fuer-Sonys-OLED-TV-751913.html> (accessed Dec8, 2012).
- [158] SAMSUNG; "SAMSUNG Smartphones", <http://www.samsung.com/at/consumer/mobile-phone/mobile-phone/smartphones> (accessed Dec8, 2012).
- [159] OSRAM GmbH; "ORBEOS Komponenten", [http://www.osram.de/osram\\_de/produkte/led-technologie/oled-lichtgestaltung/orbeos/index.jsp](http://www.osram.de/osram_de/produkte/led-technologie/oled-lichtgestaltung/orbeos/index.jsp) (accessed Dec8, 2012).
- [160] Philips Electronics; "Lumiblade OLEDs", <http://www.lighting.philips.com/main/lightcommunity/trends/oled/> (accessed Dec8, 2012).
- [161] Duggal A. R., Heller C. M., Shiang J. J., Liu J., Lewis L. N.; "Solution-Processed Organic Light-Emitting Diodes for Lighting" *Journal of Display Technology* **2007**, *3*, 184–192.
- [162] Kim J., Beardslee R.; "Fluorescence lifetimes of pyrene monomer and excimer at high pressures" *Journal of chemical physics* **1969**, *51*, 2761–2762.
- [163] Kalyanasundaram K., Thomas J. K.; "Environmental effects on vibronic band intensities in pyrene monomer fluorescence and their application in studies of micellar systems" *Journal of the American Chemical Society* **1977**, *99*, 2039–2044.
- [164] Johnson P. C.; "Pyrene fluorescence in ethanol and cyclohexane under pressure" *The Journal of Chemical Physics* **1973**, *59*, 801.
- [165] Pope M., Swenberg C. E.; "*Electronic Processes in Organic Crystals and Polymers*"; 2nd ed.; Oxford University Press, **1999**.
- [166] Birks J. B., Dyson D. J., Munro I. H.; "'Excimer' Fluorescence. II. Lifetime Studies of Pyrene Solutions" *Proceedings of the Royal Society A: Mathematical, Physical and Engineering Sciences* **1963**, *275*, 575–588.
- [167] Snavely B. B.; "Flashlamp-excited organic dye lasers" *Proceedings of the IEEE* **1969**, *57*, 1374–1390.
- [168] Guldi D. M., Rahman G. M. A., Sgobba V., Ehli C.; "Multifunctional molecular carbon materials--from fullerenes to carbon nanotubes." *Chemical Society reviews* **2006**, *35*, 471–87.
- [169] Thomas K. R. J., Lin J. T., Tao Y.-T., Ko C.-W.; "Novel Green Light-Emitting Carbazole Derivatives: Potential Electroluminescent Materials" *Advanced Materials* **2000**, *12*, 1949–1951.
- [170] Moorthy J. N., Natarajan P., Venkatakrishnan P., Huang D.-F., Chow T. J.; "Steric inhibition of pi-stacking: 1,3,6,8-tetraarylpyrenes as efficient blue emitters in organic light emitting diodes (OLEDs)." *Organic letters* **2007**, *9*, 5215–8.

- [171] Mikroyannidis J. A., Fenenko L., Adachi C.; "Synthesis and photophysical characteristics of 2,7-fluorenevinylene-based trimers and their electroluminescence." *The journal of physical chemistry. B* **2006**, *110*, 20317–26.
- [172] Figueira-Duarte T. M., Simon S. C., Wagner M., Druzhinin S. I., Zachariasse K. A., Müllen K.; "Polypyrene dendrimers." *Angewandte Chemie* **2008**, *47*, 10175–8.
- [173] Otsubo T., Aso Y., Takimiya K.; "Functional oligothiophenes as advanced molecular electronic materials" *Journal of Materials Chemistry* **2002**, *12*, 2565–2575.
- [174] Wu K.-C., Ku P.-J., Lin C.-S., Shih H.-T., Wu F.-I., Huang M.-J., Lin J.-J., Chen I.-C., Cheng C.-H.; "The Photophysical Properties of Dipyrenylbenzenes and Their Application as Exceedingly Efficient Blue Emitters for Electroluminescent Devices" *Advanced Functional Materials* **2008**, *18*, 67–75.
- [175] Xing Y., Xu X., Zhang P., Tian W., Yu G., Lu P., Liu Y., Zhu D.; "Carbazole–pyrene-based organic emitters for electroluminescent device" *Chemical Physics Letters* **2005**, *408*, 169–173.
- [176] Thomas K. R. J., Velusamy M., Lin J. T., Chuen C. H., Tao Y.-T.; "Hexaphenylphenylene dendronised pyrenylamines for efficient organic light-emitting diodes" *Journal of Materials Chemistry* **2005**, *15*, 4453.
- [177] Hancock J. M., Gifford A. P., Tonzola C. J., Jenekhe S. A.; "High-Efficiency Electroluminescence from New Blue-Emitting Oligoquinolines Bearing Pyrenyl or Triphenyl Endgroups" *Journal of Physical Chemistry C* **2007**, *111*, 6875–6882.
- [178] Tao S. L., Peng Z. K., Zhang X. H., Wang P. F., Lee C.-S., Lee S.-T.; "Highly Efficient Non-Doped Blue Organic Light-Emitting Diodes Based on Fluorene Derivatives with High Thermal Stability" *Advanced Functional Materials* **2005**, *15*, 1716–1721.
- [179] Tang C., Liu F., Xia Y.-J., Xie L.-H., Wei A., Li S.-B., Fan Q.-L., Huang W.; "Efficient 9-alkylphenyl-9-pyrenylfluorene substituted pyrene derivatives with improved hole injection for blue light-emitting diodes" *Journal of Materials Chemistry* **2006**, *16*, 4074.
- [180] Tang C., Liu F., Xia Y.-J., Lin J., Xie L.-H., Zhong G.-Y., Fan Q.-L., Huang W.; "Fluorene-substituted pyrenes—Novel pyrene derivatives as emitters in nondoped blue OLEDs" *Organic Electronics* **2006**, *7*, 155–162.
- [181] Sotoyama W., Sato H., Kinoshita M., Takahashi T., Matsuura A., Kodama J., Sawatari N., Inoue H.; "45.3: Tetra-Substituted Pyrenes: New Class of Blue Emitter for Organic Light-Emitting Diodes" *SID Symposium Digest of Technical Papers* **2003**, *34*, 1294.
- [182] Bisri S. Z., Takahashi T., Takenobu T., Yahiro M., Adachi C., Iwasa Y.; "Ambipolar Field-Effect Transistor of High Photoluminescent Material Tetraphenylpyrene (TPPy) Single Crystal" *Japanese Journal of Applied Physics* **2007**, *46*, L596–L598.
- [183] Oyamada T., Uchiuzou H., Akiyama S., Oku Y., Shimoji N., Matsushige K., Sasabe H., Adachi C.; "Lateral organic light-emitting diode with field-effect transistor characteristics" *Journal of Applied Physics* **2005**, *98*, 074506.
- [184] Oyamada T., Sasabe H., Oku Y., Shimoji N., Adachi C.; "Estimation of carrier recombination and electroluminescence emission regions in organic light-emitting field-effect transistors using local doping method" *Applied Physics Letters* **2006**, *88*, 093514.
- [185] Oh H., Lee C., Lee S.; "Efficient blue organic light-emitting diodes using newly-developed pyrene-based electron transport materials" *Organic Electronics* **2009**, *10*, 163–169.
- [186] Ammerer L., Zinke A.; "Untersuchungen über Perylen und seine Derivate" *Monatshefte für Chemie - Chemical Monthly* **1953**, *84*, 25–31.
- [187] Fatiadi A. J.; "Novel, facile preparation of 1, 1'-bipyrene" *The Journal of Organic Chemistry* **1967**, *32*, 2903–2904.
- [188] Von Der Haar T., Hebecker A., Il'ichev Y., Jiang Y.-B., Kühnle W., Zachariasse K. A.; "Excited-state intramolecular charge transfer in donor/acceptor-substituted aromatic hydrocarbons and in biaryls. The significance of the redox potentials of the D/A subsystems" *Recueil des Travaux Chimiques des Pays-Bas* **2010**, *114*, 430–442.
- [189] Baumgarten M., Gherghel L., Friedrich J., Jurczok M., Rettig W.; "Electronic Decoupling in Ground and Excited States of Asymmetric Biaryls" *The Journal of Physical Chemistry A* **2000**, *104*, 1130–1140.
- [190] Bargon J., Mohmand S., Waltman R. J.; "Electrochemical Synthesis of Electrically Conducting Polymers from Aromatic Compounds" *IBM Journal of Research and Development* **1983**, *27*, 330–31.
- [191] Hino S., Iwasaki K., Matsumoto K.; "Ultraviolet photoelectron spectra of electropolymerized polymers: polyazulene, polypyrene and polycarbazole" *Synthetic Metals* **1994**, *64*, 259–264.

- [192] Qu L., Shi G.; "Crystalline oligopyrene nanowires with multicolored emission." *Chemical Communications* **2004**, 2800–1.
- [193] Sakamoto Y., Ichimura M., Kashiwabara M., Tamura S.; "Organic electroluminescent device" Pat.Nr.: **US 7,244,516 B1**.
- [194] Rivera E., Belletête M., Xia Zhu X., Durocher G., Giasson R.; "Novel polyacetylenes containing pendant 1-pyrenyl groups: synthesis, characterization, and thermal and optical properties" *Polymer* **2002**, *43*, 5059–5068.
- [195] Mikroyannidis J. A.; "Luminescent monomer of substituted tetrastylpyrene and poly(p-phenylenevinylene) derivative with pyrene segments: Synthesis and photophysics" *Synthetic Metals* **2005**, *155*, 125–129.
- [196] Mikroyannidis J. A., Persephonis P. G., Giannetas V. G.; "Poly(fluorene)s and poly(p-phenylene)s with pyrenyltriazine segments: synthesis and photophysics" *Synthetic Metals* **2005**, *148*, 293–299.
- [197] Kawano S., Yang C., Ribas M., Balushev S., Baumgarten M., Müllen K.; "Blue-Emitting Poly(2,7-pyrenylene)s: Synthesis and Optical Properties" *Macromolecules* **2008**, *41*, 7933–7937.
- [198] Lu G., Shi G.; "Electrochemical polymerization of pyrene in the electrolyte of boron trifluoride diethyl etherate containing trifluoroacetic acid and polyethylene glycol oligomer" *Journal of Electroanalytical Chemistry* **2006**, *586*, 154–160.
- [199] Miura Y., Yamano E., Tanaka A., Yamauchi J.; "Generation, Isolation, and Characterization of N-(Arylthio)-7-tert-butyl- and N-(Arylthio)-2,7-di-tert-butyl-1-pyrenylaminyl Radicals" *The Journal of Organic Chemistry* **1994**, *59*, 3294–3300.
- [200] Yamamoto T.; "Synthesis of  $\pi$ -Conjugated Polymers Bearing Electronic and Optical Functionalities by Organometallic Polycondensations. Chemical Properties and Applications of the  $\pi$ -Conjugated Polymers" *Synlett* **2003**, 0425–0450.
- [201] Pogantsch A., Wenzl F. P., List E. J. W., Leising G., Grimsdale A. C., Müllen K.; "Polyfluorenes with Dendron Side Chains as the Active Materials for Polymer Light-Emitting Devices" *Advanced Materials* **2002**, *14*, 1061.
- [202] Jacob J., Sax S., Piok T., List E. J. W., Grimsdale A. C., Müllen K.; "Ladder-type pentaphenylenes and their polymers: efficient blue-light emitters and electron-accepting materials via a common intermediate." *Journal of the American Chemical Society* **2004**, *126*, 6987–95.
- [203] Grimsdale A. C., Leclère P., Lazzaroni R., MacKenzie J. D., Murphy C., Setayesh S., Silva C., Friend R. H., Müllen K.; "Correlation Between Molecular Structure, Microscopic Morphology, and Optical Properties of Poly(tetraalkylindenofluorene)s" *Advanced Functional Materials* **2002**, *12*, 729–733.
- [204] Tu G., Zhou Q., Cheng Y., Wang L., Ma D., Jing X., Wang F.; "White electroluminescence from polyfluorene chemically doped with 1,8-naphthalimide moieties" *Applied Physics Letters* **2004**, *85*, 2172.
- [205] Craig M. R., De Kok M. M., Hofstraat J. W., Schenning A. P. H. J., Meijer E. W.; "Improving color purity and stability in a blue emitting polyfluorene by monomer purification" *Journal of Materials Chemistry* **2003**, *13*, 2861.
- [206] List E. J. W., Guentner R., Scanducci de Freitas P., Scherf U.; "The Effect of Keto Defect Sites on the Emission Properties of Polyfluorene-Type Materials" *Advanced Materials* **2002**, *14*, 374.
- [207] Sax S., Rugen-Penkalla N., Neuhold A., Schuh S., Zojer E., List E. J. W., Müllen K.; "Efficient blue-light-emitting polymer heterostructure devices: the fabrication of multilayer structures from orthogonal solvents." *Advanced Materials* **2010**, *22*, 2087–91.
- [208] Shih H.-M., Lin C.-J., Tseng S.-R., Lin C.-H., Hsu C.-S.; "Synthesis of New Blue Anthracene-based Conjugated Polymers and Their Applications in Polymer Light-Emitting Diodes" *Macromolecular Chemistry and Physics* **2011**, *212*, 1100–1108.
- [209] Castanheira E. M. S., Martinho J. M. G.; "Solvatochromic shifts of pyrene excimer fluorescence" *Chemical Physics Letters* **1991**, *185*, 319–323.
- [210] Jurczok M., Plaza P., Rettig W., Martin M. M.; "Ultrafast electron transfer in acceptor substituted bianthryl derivatives" *Chemical Physics* **2000**, *256*, 137–148.
- [211] List E., Scherf U., Müllen K., Graupner W., Kim C.-H., Shinar J.; "Direct evidence for singlet-triplet exciton annihilation in  $\pi$ -conjugated polymers" *Physical Review B* **2002**, *66*, 1–5.
- [212] Fogel Y., Kastler M., Wang Z., Andrienko D., Bodwell G. J., Müllen K.; "Electron-deficient N-heteroaromatic linkers for the elaboration of large, soluble polycyclic aromatic hydrocarbons and their use in the synthesis of some very large transition metal complexes." *Journal of the American Chemical Society* **2007**, *129*, 11743–9.

- [213] Yang C.-H., Guo T.-F., Sun I.-W.; "Highly efficient greenish blue-emitting organic diodes based on pyrene derivatives" *Journal of Luminescence* **2007**, *124*, 93–98.
- [214] Malliaras G. G., Scott J. C.; "The roles of injection and mobility in organic light emitting diodes" *Journal of Applied Physics* **1998**, *83*, 5399.
- [215] Tamoto N., Adachi C., Nagai K.; "Electroluminescence of 1,3,4-Oxadiazole and Triphenylamine-Containing Molecules as an Emitter in Organic Multilayer Light Emitting Diodes" *Chemistry of Materials* **1997**, *9*, 1077–1085.
- [216] Figueira-Duarte T. M., Simon S. C., Wagner M., Druzhinin S. I., Zachariasse K. A., Müllen K.; "Polypyrene Dendrimers" *Angewandte Chemie* **2008**, *120*, 10329–10332.
- [217] List E. J. W., Scherf U.; Blue emitting poly(para-phenylene) type polymers. In *Handbook of Conducting Polymers*; Skrotheim T. A., Reynolds J. R., Eds.; CRC Press: Boca Raton, Fla., **2007**.
- [218] List E., Kim C.-H., Naik A., Scherf U., Leising G., Graupner W., Shinar J.; "Interaction of singlet excitons with polarons in wide band-gap organic semiconductors: A quantitative study" *Physical Review B* **2001**, *64*, 155204.
- [219] Scheiber H.; "Structure to Property Relationships in Blue Light Emitting Conjugated Polymers", PhD Thesis, Graz University of Technology, **2008**.
- [220] Langelaar J., Rettschnik R. P., Hoijtink G. J.; "Studies on Triplet Radiative Lifetimes, Phosphorescence, and Delayed Fluorescence Yields of Aromatic Hydrocarbons in Liquid Solutions" *The Journal of Chemical Physics* **1971**, *54*, 1.
- [221] Burrows H. D., Seixas de Melo J., Serpa C., Arnaut L. G., Miguel M. d. G., Monkman a. P., Hamblett I., Navaratnam S.; "Triplet state dynamics on isolated conjugated polymer chains" *Chemical Physics* **2002**, *285*, 3–11.
- [222] Pogantsch A., Gadermaier C., Cerullo G., Lanzani G., Scherf U., Grimsdale A. C., Müllen K., List E. J. W.; "Photophysics of poly(fluorenes) with dendronic side chains" *Synthetic Metals* **2003**, *139*, 847–849.
- [223] Hoffmann M., Hotze E. M., Wiesner M. R.; Reactive oxygen species generation on nanoparticulate material. In *Environmental Nanotechnology: Applications and Impacts of Nanomaterials*; Bottero J.-Y., Wiesner M. R., Eds.; McGraw-Hill Professional: New York, NY, **2007**.
- [224] Shen Y., Hosseini A. R., Wong M. H., Malliaras G. G.; "How to make ohmic contacts to organic semiconductors." *Chemphyschem: A European journal of chemical physics and physical chemistry* **2004**, *5*, 16–25.
- [225] Salaneck W. R.; "Photoelectron spectroscopy of polyconjugated polymer surfaces and interfaces" *Reports on Progress in Physics* **1991**, *54*, 1215–1249.
- [226] Duhm S., Heimel G., Salzmann I.; "Orientation-dependent ionization energies and interface dipoles in ordered molecular assemblies" *Nature Materials* **2008**.
- [227] Shirota Y., Kageyama H.; "Charge carrier transporting molecular materials and their applications in devices." *Chemical Reviews* **2007**, *107*, 953–1010.
- [228] Tao Y. T., Balasubramaniam E., Danel A., Tomasik P.; "Dipyrazolopyridine derivatives as bright blue electroluminescent materials" *Applied Physics Letters* **2000**, *77*, 933.
- [229] Gamerith S., Nothofer H.-G., Scherf U., List E. J. W.; "Identification of Emissive Interface-Related Defects in Polyfluorene-Based Light Emitting Devices" *Japanese Journal of Applied Physics* **2004**, *43*, L891–L893.
- [230] Chang C.-H., Chen C.-C., Wu C.-C., Yang C.-H., Chi Y.; "Efficient iridium(III) based, true-blue emitting phosphorescent OLEDs employing both double emission and double buffer layers" *Organic Electronics* **2009**, *10*, 1364–1371.
- [231] Chang C.-H., Chang K. K.-Y., Lo Y.-J. Y., Chang S. S.-J., Chang H. H.-H.; "Fourfold power efficiency improvement in organic light-emitting devices using an embedded nanocomposite scattering layer" *Organic Electronics* **2012**, *13*, 1073–1080.
- [232] Kim H., Schulte N., Zhou G., Müllen K., Laquai F.; "A high gain and high charge carrier mobility indenofluorene-phenanthrene copolymer for light amplification and organic lasing." *Advanced Materials* **2011**, *23*, 894–7.
- [233] Wen G.-A., Xin Y., Zhu X.-R., Zeng W.-J., Zhu R., Feng J.-C., Cao Y., Zhao L., Wang L.-H., Wei W., Peng B., Huang W.; "Hyperbranched triazine-containing polyfluorenes: Efficient blue emitters for polymer light-emitting diodes (PLEDs)" *Polymer* **2007**, *48*, 1824–1829.

- [234] Lee K. H., Kang L. K., Kwon Y. S., Lee J. Y., Kang S., Kim G. Y., Seo J. H., Kim Y. K., Yoon S. S.; "Blue electroluminescent materials based on 2,7-distyrylfluorene for organic light-emitting diodes" *Thin Solid Films* **2010**, *518*, 5091–5097.
- [235] Trattnig R., Figueira-Duarte T. M., Lorbach D., Wiedemair W., Sax S., Winkler S., Vollmer A., Koch N., Manca M., Loi M. A., Baumgarten M., List E. J. W., Müllen K.; "Deep blue polymer light emitting diodes based on easy to synthesize, non-aggregating polypyrene" *Optics Express* **2011**, *19*, A1281.
- [236] Ding J., Tao Y., Day M., Roovers J., D Iorio M.; "Electrochemical and fluorescent properties of alternating copolymers of 9,9-dioctylfluorene and oxadiazole as blue electroluminescent and electron transport materials" *Journal of Optics A: Pure and Applied Optics* **2002**, *4*, S267–S272.
- [237] Scheiber H., Graf M., Plank H., Zojer E., Slugovc C., Kappaun S., Galbrecht F., Scherf U., List E. J. W.; "The Influence of UV Irradiation on Ketonic Defect Emission in Fluorene-Based Copolymers" *Advanced Functional Materials* **2008**, *18*, 2480–2488.
- [238] Gong X., Moses D., Heeger A. J., Xiao S.; "Excitation energy transfer from polyfluorene to fluorenone defects" *Synthetic Metals* **2004**, *141*, 17–20.
- [239] Duan L., Hou L., Lee T.-W., Qiao J., Zhang D., Dong G., Wang L., Qiu Y.; "Solution processable small molecules for organic light-emitting diodes" *Journal of Materials Chemistry* **2010**, *20*, 6392.
- [240] Lin W.-C., Wang W.-B., Lin Y.-C., Yu B.-Y., Chen Y.-Y., Hsu M.-F., Jou J.-H., Shyue J.-J.; "Migration of small molecules during the degradation of organic light-emitting diodes" *Organic Electronics* **2009**, *10*, 581–586.
- [241] Zuniga C. A., Barlow S., Marder S. R.; "Approaches to Solution-Processed Multilayer Organic Light-Emitting Diodes Based on Cross-Linking" *Chemistry of Materials* **2011**, *23*, 658–681.
- [242] Li W., Wang Q., Cui J., Chou H., Shaheen S. E., Jabbour G. E., Anderson J., Lee P., Kippelen B., Peyghambarian N., Armstrong N. R., Marks T. J.; "Covalently Interlinked Organic LED Transport Layers via Spin-Coating/Siloxane Condensation" *Advanced Materials* **1999**, *11*, 730–734.
- [243] Niu Y.-H., Liu M. S., Ka J.-W., Bardeker J., Zin M. T., Schofield R., Chi Y., Jen A. K.-Y.; "Crosslinkable Hole-Transport Layer on Conducting Polymer for High-Efficiency White Polymer Light-Emitting Diodes" *Advanced Materials* **2007**, *19*, 300–304.
- [244] Cheng Y.-J., Liu M. S., Zhang Y., Niu Y., Huang F., Ka J.-W., Yip H.-L., Tian Y., Jen A. K.-Y.; "Thermally Cross-Linkable Hole-Transporting Materials on Conducting Polymer: Synthesis, Characterization, and Applications for Polymer Light-Emitting Devices" *Chemistry of Materials* **2008**, *20*, 413–422.
- [245] Huang F., Wu H., Cao Y.; "Water/alcohol soluble conjugated polymers as highly efficient electron transporting/injection layer in optoelectronic devices." *Chemical Society Reviews* **2010**, *39*, 2500–21.
- [246] Kim J.-S., Friend R. H., Grizzi I., Burroughes J. H.; "Spin-cast thin semiconducting polymer interlayer for improving device efficiency of polymer light-emitting diodes" *Applied Physics Letters* **2005**, *87*, 023506.
- [247] Tseng S.-R., Li S.-Y., Meng H.-F., Yu Y.-H., Yang C.-M., Liao H.-H., Horng S.-F., Hsu C.-S.; "High-efficiency blue multilayer polymer light-emitting diode based on poly(9,9-dioctylfluorene)" *Journal of Applied Physics* **2007**, *101*, 084510.
- [248] Redecker M., Bradley D. D. C., Inbasekaran M., Wu W. W., Woo E. P.; "High Mobility Hole Transport Fluorene-Triarylamine Copolymers" *Advanced Materials* **1999**, *11*, 241–246.
- [249] Deng X. Y., Lau W. M., Wong K. Y., Low K. H., Chow H. F., Cao Y.; "High efficiency low operating voltage polymer light-emitting diodes with aluminum cathode" *Applied Physics Letters* **2004**, *84*, 3522.
- [250] Niu Y.-H., Ma H., Xu Q., Jen A. K.-Y.; "High-efficiency light-emitting diodes using neutral surfactants and aluminum cathode" *Applied Physics Letters* **2005**, *86*, 083504.
- [251] Huang F., Niu Y.-H., Zhang Y., Ka J.-W., Liu M. S., Jen A. K.-Y.; "A Conjugated, Neutral Surfactant as Electron-Injection Material for High-Efficiency Polymer Light-Emitting Diodes" *Advanced Materials* **2007**, *19*, 2010–2014.
- [252] Su W.-F., Chen R.-T., Chen Y.; "Thermally crosslinkable hole-transporting poly(fluorene-co-triphenylamine) for multilayer polymer light-emitting diodes" *Journal of Polymer Science Part A: Polymer Chemistry* **2011**, *49*, 352–360.
- [253] Xu X., Han B., Chen J., Peng J., Wu H., Cao Y.; "2,7-Carbazole-1,4-phenylene Copolymers with Polar Side Chains for Cathode Modifications in Polymer Light-Emitting Diodes" *Macromolecules* **2011**, *44*, 4204–4212.

- [254] Liu M. S., Niu Y.-H., Ka J.-W., Yip H.-L., Huang F., Luo J., Kim T.-D., Jen A. K.-Y.; "Thermally Cross-Linkable Hole-Transporting Materials for Improving Hole Injection in Multilayer Blue-Emitting Phosphorescent Polymer Light-Emitting Diodes" *Macromolecules* **2008**, *41*, 9570–9580.
- [255] Yan H., Lee P., Armstrong N. R., Graham A., Evmenenko G. a, Dutta P., Marks T. J.; "High-performance hole-transport layers for polymer light-emitting diodes. Implementation of organosiloxane cross-linking chemistry in polymeric electroluminescent devices." *Journal of the American Chemical Society* **2005**, *127*, 3172–83.
- [256] Choulis S. A., Choong V.-E., Mathai M. K., So F.; "The effect of interfacial layer on the performance of organic light-emitting diodes" *Applied Physics Letters* **2005**, *87*, 113503.
- [257] Trattnig R.; "Organic Light Emitting Devices based on Phosphorescent Organometallic Complexes in Blend- and Onchain Polymer Systems", Diploma thesis, Graz University of Technology, **2009**.
- [258] Hild W., Opitz A., Schaefer J. A., Scherge M.; "The effect of wetting on the microhydrodynamics of surfaces lubricated with water and oil" *Wear* **2003**, *254*, 871–875.
- [259] Hwang J., Kim E., Liu J., Bredas J.-L., Duggal A., Kahn A.; "Photoelectron Spectroscopic Study of the Electronic Band Structure of Polyfluorene and Fluorene-Arylamine Copolymers at Interfaces" *Journal of Physical Chemistry C* **2007**, *111*, 1378–1384.
- [260] Heibel G., Salzmann I., Duhm S., Rabe J. P., Koch N.; "Intrinsic Surface Dipoles Control the Energy Levels of Conjugated Polymers" *Advanced Functional Materials* **2009**, *19*, 3874–3879.
- [261] Beamson G., Briggs D.; "*High Resolution XPS of Organic Polymers*"; John Wiley and Sons: Chichester, **1992**.
- [262] Kim J.-S., Ho P. K. H., Murphy C. E., Seeley A. J. A. B., Grizzi I., Burroughes J. H., Friend R. H.; "Electrical degradation of triarylamine-based light-emitting polymer diodes monitored by micro-Raman spectroscopy" *Chemical Physics Letters* **2004**, *386*, 2–7.
- [263] Tseng S.-R., Meng H.-F., Yeh C.-H., Lai H.-C., Horng S.-F., Liao H.-H., Hsu C.-S., Lin L.-C.; "High-efficiency blue multilayer polymer light-emitting diode fabricated by a general liquid buffer method" *Synthetic Metals* **2008**, *158*, 130–134.
- [264] Huang C.-W., Peng K.-Y., Liu C.-Y., Jen T.-H., Yang N.-J., Chen S.-A.; "Creating a Molecular-scale Graded Electronic Profile in a Single Polymer to Facilitate Hole Injection for Efficient Blue Electroluminescence" *Advanced Materials* **2008**, *20*, 3709–3716.
- [265] Percec V., Glodde M., Bera T. K., Miura Y., Shiyonovskaya I., Singer K. D., Balagurusamy V. S. K., Heiney P. a, Schnell I., Rapp a, Spiess H.-W., Hudson S. D., Duan H.; "Self-organization of supramolecular helical dendrimers into complex electronic materials." *Nature* **2002**, *419*, 384–7.
- [266] Lo S.-C., Burn P. L.; "Development of dendrimers: macromolecules for use in organic light-emitting diodes and solar cells." *Chemical Reviews* **2007**, *107*, 1097–1116.
- [267] Grayson S. M., Fréchet J. M. J.; "Convergent Dendrons and Dendrimers: from Synthesis to Applications" *Chemical Reviews* **2001**, *101*, 3819–3868.
- [268] Adronov A., Fréchet J. M. J.; "Light-harvesting dendrimers" *Chemical Communications* **2000**, 1701–1710.
- [269] Hecht S., Fréchet J.; "Dendritic encapsulation of function: applying nature's site isolation principle from biomimetics to materials science" *Angewandte Chemie International Edition* **2001**, *40*, 74–91.
- [270] Wang J.-L., Yan J., Tang Z.-M., Xiao Q., Ma Y., Pei J.; "Gradient shape-persistent pi-conjugated dendrimers for light-harvesting: synthesis, photophysical properties, and energy funneling." *Journal of the American Chemical Society* **2008**, *130*, 9952–62.
- [271] Furuta P., Brooks J., Thompson M. E., Fréchet J. M. J.; "Simultaneous light emission from a mixture of dendrimer encapsulated chromophores: a model for single-layer multichromophoric organic light-emitting diodes." *Journal of the American Chemical Society* **2003**, *125*, 13165–72.
- [272] Thelakkat M.; "Star-Shaped, Dendrimeric and Polymeric Triarylamine as Photoconductors and Hole Transport Materials for Electro-Optical Applications" *Macromolecular Materials and Engineering* **2002**, *287*, 442.
- [273] Qin T., Zhou G., Scheiber H., Bauer R. E., Baumgarten M., Anson C. E., List E. J. W., Müllen K.; "Polytriphenylene dendrimers: a unique design for blue-light-emitting materials." *Angewandte Chemie International Edition* **2008**, *47*, 8292–6.
- [274] Dawson W. R., Windsor M. W.; "Fluorescence yields of aromatic compounds" *The Journal of Physical Chemistry* **1968**, *72*, 3251–3260.

- [275] Medinger T., Wilkinson F.; "Concentration dependence of quantum yield of triplet-state production of pyrene in ethanol" *Transactions of the Faraday Society* **1966**, *62*, 1785.
- [276] Langenegger S. M., Häner R.; "Excimer formation by interstrand stacked pyrenes." *Chemical Communications* **2004**, 2792–3.
- [277] Bernhardt S., Kastler M., Enkelmann V., Baumgarten M., Müllen K.; "Pyrene as chromophore and electrophore: encapsulation in a rigid polyphenylene shell." *Chemistry* **2006**, *12*, 6117–28.
- [278] Venkataramana G., Sankararaman S.; "Synthesis, Absorption, and Fluorescence-Emission Properties of 1,3,6,8-Tetraethynylpyrene and Its Derivatives" *European Journal of Organic Chemistry* **2005**, *2005*, 4162–4166.
- [279] Chojnacki H., Laskowski Z., Lewanowicz A., Ruziewicz Z., Wandas R.; "Reinvestigation of the absorption spectrum of triphenylene: Vibronic structure of the S1 ← S0 transition and location of higher excited singlet states" *Chemical Physics Letters* **1986**, *124*, 478–482.
- [280] Markovitsi D., Germain A., Millie P., Lecuyer P., Gallos L., Argyrakis P., Bengs H., Ringsdorf H.; "Triphenylene Columnar Liquid Crystals: Excited States and Energy Transfer" *The Journal of Physical Chemistry* **1995**, *99*, 1005–1017.
- [281] Park Y. H., Rho H. H., Park N. G., Kim Y. S.; "Theoretical investigation of tetra-substituted pyrenes for organic light emitting diodes" *Current Applied Physics* **2006**, *6*, 691–694.
- [282] Kim H. M., Lee Y. O., Lim C. S., Kim J. S., Cho B. R.; "Two-photon absorption properties of alkynyl-conjugated pyrene derivatives." *The Journal of organic chemistry* **2008**, *73*, 5127–30.
- [283] Brown T. M., Cacialli F.; "Contact optimization in polymer light-emitting diodes" *Journal of Polymer Science Part B: Polymer Physics* **2003**, *41*, 2649–2664.
- [284] Burn P. L., Lo S.-C., Samuel I. D. W.; "The Development of Light-Emitting Dendrimers for Displays" *Advanced Materials* **2007**, *19*, 1675–1688.
- [285] Mitschke U., Bäuerle P.; "The electroluminescence of organic materials" *Journal of Materials Chemistry* **2000**, *10*, 1471–1507.
- [286] Ho M.-H., Balaganesan B., Chu T.-Y., Chen T.-M., Chen C. H.; "A morphologically stable host material for efficient phosphorescent green and red organic light emitting devices" *Thin Solid Films* **2008**, *517*, 943–947.
- [287] Förster T., Kasper K.; "Ein Konzentrationsumschlag der Fluoreszenz." *Zeitschrift für Physikalische Chemie* **1954**, *1*, 275–277.
- [288] Tao Y., Wang Q., Ao L., Zhong C., Qin J., Yang C., Ma D.; "Molecular design of host materials based on triphenylamine/oxadiazole hybrids for excellent deep-red phosphorescent organic light-emitting diodes" *Journal of Materials Chemistry* **2010**, *20*, 1759.
- [289] Duan L., Qiao J., Sun Y., Qiu Y.; "Strategies to design bipolar small molecules for OLEDs: donor-acceptor structure and non-donor-acceptor structure." *Advanced Materials* **2011**, *23*, 1137–44.
- [290] Zhang Y., Zuniga C., Kim S., Cai D., Barlow S., Salman S., Coropceanu V., Brédas J.-L., Kippelen B., Marder S.; "Polymers with Carbazole-Oxadiazole Side Chains as Ambipolar Hosts for Phosphorescent Light-Emitting Diodes" *Chemistry of Materials* **2011**, *23*, 4002–4015.
- [291] Matsusue N., Suzuki Y., Naito H.; "Charge Carrier Transport in Neat Thin Films of Phosphorescent Iridium Complexes" *Japanese Journal of Applied Physics* **2005**, *44*, 3691–3694.
- [292] Kido J., Hongawa K., Okuyama K., Nagai K.; "Bright blue electroluminescence from poly(N-vinylcarbazole)" *Applied Physics Letters* **1993**, *63*, 2627.
- [293] Zhang Q., Hu Y. F., Cheng Y. X., Su G. P., Ma D. G., Wang L. X., Jing X. B., Wang F. S.; "Carbazole-based hole-transporting materials for electroluminescent devices" *Synthetic Metals* **2003**, *137*, 1111–1112.
- [294] Kremser G., Hofmann O. T., Sax S., Kappaun S., List E. J. W., Zojer E., Slugovc C.; "Synthesis and Photophysical Properties of 3,6-Diphenyl-9-hexyl-9H-carbazole Derivatives Bearing Electron Withdrawing Groups" *Monatshefte für Chemie - Chemical Monthly* **2008**, *139*, 223–231.
- [295] Wang Y., Hua Y., Wu X., Zhang L., Hou Q., Guan F., Zhang N., Yin S., Cheng X.; "High-efficiency and multi-function blue fluorescent material for organic electroluminescent devices" *Organic Electronics* **2008**, *9*, 692–698.
- [296] Tao Y., Wang Q., Yang C., Wang Q., Zhang Z., Zou T., Qin J., Ma D.; "A simple carbazole/oxadiazole hybrid molecule: an excellent bipolar host for green and red phosphorescent OLEDs." *Angewandte Chemie International Edition* **2008**, *47*, 8104–7.



- [297] Yamada T., Suzuki F., Goto A., Sato T., Tanaka K., Kaji H.; "Revealing bipolar charge-transport property of 4,4'-N,N'-dicarbazolylbiphenyl (CBP) by quantum chemical calculations" *Organic Electronics* **2011**, *12*, 169–178.
- [298] Ting H.-C., Chen Y.-M., You H.-W., Hung W.-Y., Lin S.-H., Chaskar A., Chou S.-H., Chi Y., Liu R.-H., Wong K.-T.; "Indolo[3,2-b]carbazole/benzimidazole hybrid bipolar host materials for highly efficient red, yellow, and green phosphorescent organic light emitting diodes" *Journal of Materials Chemistry* **2012**, *22*, 8399.
- [299] Rausch D., Lambert C.; "Synthesis and spectroscopic properties of a hexapyrenylbenzene derivative." *Organic letters* **2006**, *8*, 5037–40.
- [300] Lee H., Harvey R. G.; "Synthesis of 2,7-dibromopyrene" *The Journal of Organic Chemistry* **1986**, *51*, 2847–2848.
- [301] Liu Y., Nishiura M., Wang Y., Hou Z.; "Pi-conjugated aromatic enynes as a single-emitting component for white electroluminescence." *Journal of the American Chemical Society* **2006**, *128*, 5592–3.
- [302] Driver M. S., Hartwig J. F.; "A Second-Generation Catalyst for Aryl Halide Amination: Mixed Secondary Amines from Aryl Halides and Primary Amines Catalyzed by (DPPF)PdCl<sub>2</sub>" *Journal of the American Chemical Society* **1996**, *118*, 7217–7218.
- [303] Wolfe J. P., Wagaw S., Buchwald S. L.; "An Improved Catalyst System for Aromatic Carbon–Nitrogen Bond Formation: The Possible Involvement of Bis(Phosphine) Palladium Complexes as Key Intermediates" *Journal of the American Chemical Society* **1996**, *118*, 7215–7216.
- [304] Nakashima H., Sachiko K., Satoko S., Satoshi S.; "Aromatic amine compound, and light emitting element, light emitting device, and electronic device using aromatic amine compound" Pat.Nr.: **US 2007/0096639 A1**.
- [305] Jankus V., Winscom C., Monkman A. P.; "The photophysics of singlet, triplet, and degradation trap states in 4,4'-N,N'(C)-dicarbazolyl-1,1'(C)-biphenyl." *The Journal of Chemical Physics* **2009**, *130*, 074501.
- [306] Zhang Q., Chen J., Cheng Y., Wang L., Ma D., Jing X., Wang F.; "Novel hole-transporting materials based on 1,4-bis(carbazolyl)benzene for organic light-emitting devices" *Journal of Materials Chemistry* **2004**, *14*, 895.
- [307] Krotkus S., Kazlauskas K., Miasojedovas A., Gruodis A., Tomkeviciene A., Grazulevicius J. V., Jursenas S.; "Pyrenyl-Functionalized Fluorene and Carbazole Derivatives as Blue Light Emitters" *The Journal of Physical Chemistry C* **2012**, *116*, 7561–7572.
- [308] Lee T.-W., Noh T., Shin H.-W., Kwon O., Park J.-J., Choi B.-K., Kim M.-S., Shin D. W., Kim Y.-R.; "Characteristics of Solution-Processed Small-Molecule Organic Films and Light-Emitting Diodes Compared with their Vacuum-Deposited Counterparts" *Advanced Functional Materials* **2009**, *19*, 1625–1630.
- [309] You J.-D., Tseng S.-R., Meng H.-F., Yen F.-W., Lin I.-F., Horng S.-F.; "All-solution-processed blue small molecular organic light-emitting diodes with multilayer device structure" *Organic Electronics* **2009**, *10*, 1610–1614.
- [310] Wang Z., Lu P., Chen S., Gao Z., Shen F., Zhang W., Xu Y., Kwok H. S., Ma Y.; "Phenanthro[9,10-d]imidazole as a new building block for blue light emitting materials" *Journal of Materials Chemistry* **2011**, *21*, 5451.
- [311] Qian L., Bera D., Holloway P. H.; "Electrophosphorescence from triplet excimers in poly-(N-vinylcarbazole)" *Applied Physics Letters* **2007**, *90*, 103511.
- [312] Hu B., Yang Z., Karasz F. E.; "Electroluminescence of pure poly(N-vinylcarbazole) and its blends with a multiblock copolymer" *Journal of Applied Physics* **1994**, *76*, 2419.
- [313] Qin T., Wiedemair W., Nau S., Trattnig R., Sax S., Winkler S., Vollmer A., Koch N., Baumgarten M., List E. J. W., Müllen K.; "Core, shell, and surface-optimized dendrimers for blue light-emitting diodes." *Journal of the American Chemical Society* **2011**, *133*, 1301–3.
- [314] Zhu Y.-C., Zhou L., Li H.-Y., Xu Q.-L., Teng M.-Y., Zheng Y.-X., Zuo J.-L., Zhang H.-J., You X.-Z.; "Highly efficient green and blue-green phosphorescent OLEDs based on iridium complexes with the tetraphenylimidodiphosphinate ligand." *Advanced Materials* **2011**, *23*, 4041–6.
- [315] Ulbricht C., Beyer B., Friebe C., Winter A., Schubert U. S.; "Recent Developments in the Application of Phosphorescent Iridium(III) Complex Systems" *Advanced Materials* **2009**, *21*, 4418–4441.
- [316] Clar E.; "Aromatic Sextet"; John Wiley and Sons: New York, NY, **1972**.
- [317] Rieger R., Müllen K.; "Forever young: polycyclic aromatic hydrocarbons as model cases for structural and optical studies" *Journal of Physical Organic Chemistry* **2010**, n/a–n/a.

- [318] Buess C. M., Lawson D. D.; "The Preparation, Reactions, and Properties of Triphenylenes." *Chemical Reviews* **1960**, *60*, 313–330.
- [319] Pérez D., Guitián E.; "Selected strategies for the synthesis of triphenylenes" *Chemical Society Reviews* **2004**, *33*, 274–83.
- [320] Billard J., Dubois J. C., Tinh N. H., Zann A.; "Mesophase of disc-like molecules" *Nouveau Journal de Chimie* **1978**, *2*, 535–540.
- [321] Kumar S.; "Recent developments in the chemistry of triphenylene-based discotic liquid crystals" *Liquid Crystals* **2004**, *31*, 1037–1059.
- [322] Laschat S., Baro A., Steinke N., Giesselmann F., Hägele C., Scalia G., Judele R., Kapatsina E., Sauer S., Schreivogel A., Tosoni M.; "Discotic liquid crystals: from tailor-made synthesis to plastic electronics." *Angewandte Chemie International Edition* **2007**, *46*, 4832–87.
- [323] Markovitsi D., Lécuyer I., Lianos P., Malthête J.; "One-dimensional singlet energy migration in the columnar liquid crystal of a triphenylene derivative" *Journal of the Chemical Society, Faraday Transactions* **1991**, *87*, 1785.
- [324] Adam D., Schuhmacher P., Simmerer J., Häussling L., Siemensmeyer K., Etzbach K. H., Ringsdorf H., Haarer D.; "Fast photoconduction in the highly ordered columnar phase of a discotic liquid crystal" *Nature* **1994**, *371*, 141–143.
- [325] Henderson P., Kumar S., Rego J. A., Ringsdorf H., Schuhmacher P.; "The synthesis of alkoxybromotriphenylenes: new discotic liquid crystals and valuable precursors to "mixed tail" discotics" *Journal of the Chemical Society, Chemical Communications* **1995**, 1059.
- [326] Zemtsova O. V., Zheleznov K. N.; "Synthesis and specific features of mesomorphic behavior of new polysubstituted triphenylenes" *Russian Chemical Bulletin* **2004**, *53*, 1743–1748.
- [327] Kumar S.; "Triphenylene-based discotic liquid crystal dimers, oligomers and polymers" *Liquid Crystals* **2005**, *32*, 1089–1113.
- [328] Saleh M., Baumgarten M., Mavrinskiy A., Schäfer T., Müllen K.; "Triphenylene-Based Polymers for Blue Polymeric Light Emitting Diodes" *Macromolecules* **2010**, *43*, 137–143.
- [329] Hao Q., Xie X., Lei W., Xia M., Wang F., Wang X.; "Electrochemical Polymerization and Properties of Poly(triphenylene), an Excellent Blue-Green-Light Emitter" *The Journal of Physical Chemistry C* **2010**, *114*, 9608–9617.
- [330] McKenna M. D., Barberá J., Marcos M., Serrano J. L.; "Discotic liquid crystalline poly(propylene imine) dendrimers based on triphenylene." *Journal of the American Chemical Society* **2005**, *127*, 619–25.
- [331] Wendorff J. H., Christ T., Glüsen B., Greiner A., Kettner A., Sander R., Stümpflen V., Tsukruk V. V.; "Columnar discotics for light emitting diodes" *Advanced Materials* **1997**, *9*, 48–52.
- [332] Seguy I., Destruel P., Bock H.; "An all-columnar bilayer light-emitting diode" *Synthetic Metals* **2000**, *111-112*, 15–18.
- [333] Freudenmann R., Behnisch B., Hanack M.; "Synthesis of conjugated bridged triphenylenes and application in OLEDs" *Journal of Materials Chemistry* **2001**, *11*, 1618–1624.
- [334] Boden B. N., Abdolmaleki A., Ma C. T.-Z., MacLachlan M. J.; "New diformyldihydroxyaromatic precursors for luminescent Schiff base macrocycles: Synthesis, characterization, and condensation studies" *Canadian Journal of Chemistry* **2008**, *86*, 50–64.
- [335] Wang D., Hsu J. F., Bagui M., Dusevich V., Wang Y., Liu Y., Holder A. J., Peng Z.; "Synthesis and self-assembly of a triphenylene-containing amphiphilic conjugated macrocycle" *Tetrahedron Letters* **2009**, *50*, 2147–2149.
- [336] Li J., He Z., Gopee H., Cammidge A. N.; "Synthesis of crown ether-linked discotic triphenylenes." *Organic Letters* **2010**, *12*, 472–5.
- [337] Kaller M., Deck C., Meister A., Hause G., Baro A., Laschat S.; "Counterion effects on the columnar mesophases of triphenylene-substituted [18]crown-6 ethers: is flatter better?" *Chemistry* **2010**, *16*, 6326–37.
- [338] Rego J. A., Kumar S., Ringsdorf H.; "Synthesis and Characterization of Fluorescent, Low-Symmetry Triphenylene Discotic Liquid Crystals: Tailoring of Mesomorphic and Optical Properties" *Chemistry of Materials* **1996**, *8*, 1402–1409.
- [339] Levell J. W., Ruseckas A., Henry J. B., Wang Y., Stretton A. D., Mount A. R., Galow T. H., Samuel I. D. W.; "Fluorescence enhancement by symmetry breaking in a twisted triphenylene derivative." *Journal of Physical Chemistry A* **2010**, *114*, 13291–5.

- [340] Simpson C. D., Wu J., Watson M. D., Müllen K.; "From graphite molecules to columnar superstructures - an exercise in nanoscience" *Journal of Materials Chemistry* **2004**, *14*, 494.
- [341] Pisula W., Menon A., Stepputat M., Lieberwirth I., Kolb U., Tracz A., Siringhaus H., Pakula T., Müllen K.; "A Zone-Casting Technique for Device Fabrication of Field-Effect Transistors Based on Discotic Hexa-peri-hexabenzocoronene" *Advanced Materials* **2005**, *17*, 684–689.
- [342] Lee Y. Z., Chen X., Chen S.-A., Wei P. K., Fann W. S.; "Soluble electroluminescent poly(phenylene vinylene)s with balanced electron- and hole injections." *Journal of the American Chemical Society* **2001**, *123*, 2296–307.
- [343] Sung H.-H., Lin H.-C.; "Novel Alternating Fluorene-Based Conjugated Polymers Containing Oxadiazole Pendants with Various Terminal Groups" *Macromolecules* **2004**, *37*, 7945–7954.
- [344] Li Z., Lieberman M.; "Axial Reactivity of Soluble Silicon(IV) Phthalocyanines" *Inorganic Chemistry* **2001**, *40*, 932–939.
- [345] Meier H., Rose B.; "Dehydrotriphenylene zum Aufbau gewinkelter molekularer Bandstrukturen" *Journal für Praktische Chemie/Chemiker-Zeitung* **1998**, *340*, 536–543.
- [346] Bhatt M. V.; "Quinone studies—I" *Tetrahedron* **1964**, *20*, 803–821.
- [347] Yamamoto T.; "Electrically conducting and thermally stable  $\pi$ -conjugated poly(arylene)s prepared by organometallic processes" *Progress in Polymer Science* **1992**, *17*, 1153–1205.
- [348] Yamamoto T.; " $\pi$ -Conjugated Polymers Bearing Electronic and Optical Functionalities. Preparation by Organometallic Polycondensations, Properties, and Their Applications." *Bulletin of the Chemical Society of Japan* **1999**, *72*, 621–638.
- [349] Pisula W., Tomović Ž., Simpson C., Kastler M., Pakula T., Müllen K.; "Relationship between Core Size, Side Chain Length, and the Supramolecular Organization of Polycyclic Aromatic Hydrocarbons" *Chemistry of Materials* **2005**, *17*, 4296–4303.
- [350] Becker R. S., Singh I. Sen, Jackson E. a.; "Comprehensive Spectroscopic Investigation of Polynuclear Aromatic Hydrocarbons. I. Absorption Spectra and State Assignments for the Tetracyclic Hydrocarbons and their Alkyl-Substituted Derivatives" *The Journal of Chemical Physics* **1963**, *38*, 2144.
- [351] Saleh M., Park Y.-S., Baumgarten M., Kim J.-J., Müllen K.; "Conjugated Triphenylene Polymers for Blue OLED Devices." *Macromolecular Rapid Communications* **2009**, *30*, 1279–83.
- [352] Bagui M., Melinger J. S., Chakraborty S., Keightley J. A., Peng Z.; "Synthesis and optical properties of triphenylene-based conjugated dendrons" *Tetrahedron* **2009**, *65*, 1247–1256.
- [353] Masson G., Latour M., Biancardi D.; "*Global Market Outlook for Photovoltaics until 2016*"; Brussels, Belgium, **2012**.
- [354] Yu G., Pakbaz K., Heeger A. J.; "Semiconducting polymer diodes: Large size, low cost photodetectors with excellent visible-ultraviolet sensitivity" *Applied Physics Letters* **1994**, *64*, 3422.
- [355] Goetzberger A., Hebling C., Schock H.-W.; "Photovoltaic materials, history, status and outlook" *Materials Science and Engineering: R: Reports* **2003**, *40*, 1–46.
- [356] Voigt M. M., Mackenzie R. C. I., Yau C. P., Atienzar P., Dane J., Keivanidis P. E., Bradley D. D. C., Nelson J.; "Gravure printing for three subsequent solar cell layers of inverted structures on flexible substrates" *Solar Energy Materials and Solar Cells* **2011**, *95*, 731–734.
- [357] Krebs F. C. F.; "Fabrication and processing of polymer solar cells: a review of printing and coating techniques" *Solar Energy Materials and Solar Cells* **2009**, *93*, 394–412.
- [358] NREL; "Research Cell efficiency Records", <http://www.nrel.gov/ncpv/> (accessed Jan15, 2013).
- [359] Shockley W., Queisser H. J.; "Detailed Balance Limit of Efficiency of p-n Junction Solar Cells" *Journal of Applied Physics* **1961**, *32*, 510.
- [360] Baumann A.; "Charge Transport and Recombination Dynamics in Organic Bulk Heterojunction Solar Cells", PhD Thesis, Julius-Maximilians-Universität Würzburg, **2011**.
- [361] Deibel C., Dyakonov V.; "Polymer–fullerene bulk heterojunction solar cells" *Reports on Progress in Physics* **2010**, *73*, 096401.
- [362] Zhou Y., Eck M., Krüger M.; "Bulk-heterojunction hybrid solar cells based on colloidal nanocrystals and conjugated polymers" *Energy & Environmental Science* **2010**, *3*, 1851.
- [363] Helgesen M., Søndergaard R., Krebs F. C.; "Advanced materials and processes for polymer solar cell devices" *Journal of Materials Chemistry* **2010**, *20*, 36.
- [364] Saunders B. R., Turner M. L.; "Nanoparticle-polymer photovoltaic cells." *Advances in Colloid and Interface Science* **2008**, *138*, 1–23.

- [365] Lira-Cantu M., Khoda Siddiki M., Muñoz-Rojas D., Amade R., González-Pech N. I.; "Nb-TiO<sub>2</sub>/polymer hybrid solar cells with photovoltaic response under inert atmosphere conditions" *Solar Energy Materials and Solar Cells* **2010**, *94*, 1227–1234.
- [366] Ravirajan P., Haque S. A., Durrant J. R., Bradley D. D. C., Nelson J.; "The Effect of Polymer Optoelectronic Properties on the Performance of Multilayer Hybrid Polymer/TiO<sub>2</sub> Solar Cells" *Advanced Functional Materials* **2005**, *15*, 609–618.
- [367] Reeja-Jayan B., Manthiram A.; "Influence of polymer–metal interface on the photovoltaic properties and long-term stability of nc-TiO<sub>2</sub>-P3HT hybrid solar cells" *Solar Energy Materials and Solar Cells* **2010**, *94*, 907–914.
- [368] Beek W. J. E., Wienk M. M., Janssen R. A. J.; "Hybrid Solar Cells from Regioregular Polythiophene and ZnO Nanoparticles" *Advanced Functional Materials* **2006**, *16*, 1112–1116.
- [369] Beek W. J. E., Wienk M. M., Janssen R. A. J.; "Efficient Hybrid Solar Cells from Zinc Oxide Nanoparticles and a Conjugated Polymer" *Advanced Materials* **2004**, *16*, 1009–1013.
- [370] Olson D. C., Piris J., Collins R. T., Shaheen S. E., Ginley D. S.; "Hybrid photovoltaic devices of polymer and ZnO nanofiber composites" *Thin Solid Films* **2006**, *496*, 26–29.
- [371] Ren S., Chang L.-Y., Lim S.-K., Zhao J., Smith M., Zhao N., Bulović V., Bawendi M., Gradecak S.; "Inorganic-organic hybrid solar cell: bridging quantum dots to conjugated polymer nanowires." *Nano letters* **2011**, *11*, 3998–4002.
- [372] Maier E., Fischereder A., Haas W., Mauthner G., Albering J., Rath T., Hofer F., List E. J. W., Trimmel G.; "Metal sulfide–polymer nanocomposite thin films prepared by a direct formation route for photovoltaic applications" *Thin Solid Films* **2011**, *519*, 4201–4206.
- [373] Dowland S., Lutz T., Ward A., King S. P., Sudlow A., Hill M. S., Molloy K. C., Haque S. a.; "Direct growth of metal sulfide nanoparticle networks in solid-state polymer films for hybrid inorganic-organic solar cells." *Advanced Materials* **2011**, *23*, 2739–44.
- [374] Rath T., Edler M., Haas W., Fischereder A., Moscher S., Schenk A., Trattng R., Sezen M., Mauthner G., Pein A., Meischler D., Bartl K., Saf R., Bansal N., Haque S. a., Hofer F., List E. J. W., Trimmel G.; "A Direct Route Towards Polymer/Copper Indium Sulfide Nanocomposite Solar Cells" *Advanced Energy Materials* **2011**, *1*, 1046–1050.
- [375] Maier E., Rath T., Haas W., Werzer O., Saf R., Hofer F., Meissner D., Volobujeva O., Bereznev S., Mellikov E., Amenitsch H., Resel R., Trimmel G.; "CuInS<sub>2</sub>–Poly(3-(ethyl-4-butanoate)thiophene) nanocomposite solar cells: Preparation by an in situ formation route, performance and stability issues" *Solar Energy Materials and Solar Cells* **2011**, *95*, 1354–1361.
- [376] Seo J., Cho M. J., Lee D., Cartwright A. N., Prasad P. N.; "Efficient heterojunction photovoltaic cell utilizing nanocomposites of lead sulfide nanocrystals and a low-bandgap polymer." *Advanced Materials* **2011**, *23*, 3984–8.
- [377] Celik D., Krueger M., Veit C., Schleiermacher H. F., Zimmermann B., Allard S., Dumsch I., Scherf U., Rauscher F., Niyamakom P.; "Performance enhancement of CdSe nanorod-polymer based hybrid solar cells utilizing a novel combination of post-synthetic nanoparticle surface treatments" *Solar Energy Materials and Solar Cells* **2012**, *98*, 433–440.
- [378] Jeltsch K. F., Schädel M., Bonekamp J., Niyamakom P., Rauscher F., Lademann H. W. A., Dumsch I., Allard S., Scherf U., Meerholz K.; "Efficiency Enhanced Hybrid Solar Cells Using a Blend of Quantum Dots and Nanorods" *Advanced Functional Materials* **2012**, *22*, 397–404.
- [379] Albero J., Zhou Y., Eck M., Rauscher F., Niyamakom P., Dumsch I., Allard S., Scherf U., Krüger M., Palomares E.; "Photo-induced charge recombination kinetics in low bandgap PCPDTBT polymer:CdSe quantum dot bulk heterojunction solar cells" *Chemical Science* **2011**, *2*, 2396.
- [380] Yang Y., Zhong H., Bai Z., Zou B., Li Y., Scholes G. D.; "Transition from Photoconductivity to Photovoltaic Effect in P3HT/CuInSe<sub>2</sub> Composites" *The Journal of Physical Chemistry C* **2012**, *116*, 7280–7286.
- [381] Cui D., Xu J., Zhu T., Paradee G., Ashok S., Gerhold M.; "Harvest of near infrared light in PbSe nanocrystal-polymer hybrid photovoltaic cells" *Applied Physics Letters* **2006**, *88*, 183111.
- [382] Saunders B. R.; "Hybrid polymer/nanoparticle solar cells: preparation, principles and challenges." *Journal of colloid and interface science* **2012**, *369*, 1–15.
- [383] Leventis H. C., King S. P., Sudlow A., Hill M. S., Molloy K. C., Haque S. A.; "Nanostructured hybrid polymer-inorganic solar cell active layers formed by controllable in situ growth of semiconducting sulfide networks." *Nano Letters* **2010**, *10*, 1253–8.

- [384] Talapin D. V, Lee J.-S., Kovalenko M. V, Shevchenko E. V; "Prospects of colloidal nanocrystals for electronic and optoelectronic applications." *Chemical Reviews* **2010**, *110*, 389–458.
- [385] Rhodes R., Horie M., Chen H., Wang Z., Turner M. L., Saunders B. R.; "Aggregation of zinc oxide nanoparticles: from non-aqueous dispersions to composites used as photoactive layers in hybrid solar cells." *Journal of Colloid and Interface Science* **2010**, *344*, 261–71.
- [386] Rhodes R., O'Brien P., Saunders B. R.; "Triggered aggregation of PbS nanocrystal dispersions; towards directing the morphology of hybrid polymer films using a removable bilinker ligand." *Journal of Colloid and Interface Science* **2011**, *358*, 151–9.
- [387] Gur I., Fromer N. A., Alivisatos A. P.; "Controlled assembly of hybrid bulk-heterojunction solar cells by sequential deposition." *The Journal of Physical Chemistry B* **2006**, *110*, 25543–6.
- [388] Gur I., Fromer N. A., Chen C.-P., Kanaras A. G., Alivisatos A. P.; "Hybrid solar cells with prescribed nanoscale morphologies based on hyperbranched semiconductor nanocrystals." *Nano Letters* **2007**, *7*, 409–14.
- [389] Peng X., Manna L., Yang W., Wickham J., Scher E., Kadavanich A., Alivisatos A. P.; "Shape control of CdSe nanocrystals" *Nature* **2000**, *404*, 59–61.
- [390] Huynh W. U., Dittmer J. J., Alivisatos A. P.; "Hybrid nanorod-polymer solar cells" *Science* **2002**, *295*, 2425–7.
- [391] Dayal S., Kopidakis N., Olson D. C., Ginley D. S., Rumbles G.; "Photovoltaic devices with a low band gap polymer and CdSe nanostructures exceeding 3% efficiency." *Nano Letters* **2010**, *10*, 239–42.
- [392] Nozik A. J.; "Exciton multiplication and relaxation dynamics in quantum dots: applications to ultrahigh-efficiency solar photon conversion." *Inorganic Chemistry* **2005**, *44*, 6893–9.
- [393] Schaffer B., Mitterbauer C., Schertel A., Pogantsch A., Rentenberger S., Zojer E., Hofer F.; "Cross-section analysis of organic light-emitting diodes." *Ultramicroscopy* **2004**, *101*, 123–8.
- [394] Arici E., Sariciftci N., Meissner; "Hybrid solar cells". *Encyclopedia of nanoscience and nanotechnology* **2008**.
- [395] Franzman M., Brutchey R.; "Solution-Phase Synthesis of Well-Defined Indium Sulfide Nanorods" *Chemistry of Materials* **2009**, 1790–1792.
- [396] Rogach A. L., Kotov N. A., Koktysh D. S., Susa A. S., Caruso F.; "II–VI semiconductor nanocrystals in thin films and colloidal crystals" *Colloids and Surfaces A: Physicochemical and Engineering Aspects* **2002**, *202*, 135–144.
- [397] Martínez-Ferrero E., Albero J., Palomares E.; "Materials, Nanomorphology, and Interfacial Charge Transfer Reactions in Quantum Dot/Polymer Solar Cell Devices" *The Journal of Physical Chemistry Letters* **2010**, *1*, 3039–3045.
- [398] Zhou Y., Riehle F. S., Yuan Y., Schleiermacher H.-F., Niggemann M., Urban G. A., Krüger M.; "Improved efficiency of hybrid solar cells based on non-ligand-exchanged CdSe quantum dots and poly(3-hexylthiophene)" *Applied Physics Letters* **2010**, *96*, 013304.
- [399] Zhou Y., Eck M., Veit C., Zimmermann B., Rauscher F., Niyamakom P., Yilmaz S., Dumsch I., Allard S., Scherf U.; "Efficiency enhancement for bulk-heterojunction hybrid solar cells based on acid treated CdSe quantum dots and low bandgap polymer PCPDTBT" *Solar Energy Materials and Solar Cells* **2011**, *95*, 1232–1237.
- [400] Albero J., Martínez-Ferrero E., Ajuria J., Waldauf C., Pacios R., Palomares E.; "Photo-induced electron recombination dynamics in CdSe/P3HT hybrid heterojunctions." *Physical chemistry chemical physics: PCCP* **2009**, *11*, 9644–7.
- [401] Huynh W. U., Peng X., Alivisatos A. P.; "CdSe Nanocrystal Rods/Poly(3-hexylthiophene) Composite Photovoltaic Devices" *Advanced Materials* **1999**, *11*, 923–927.
- [402] Sun B., Snaith H. J., Dhoot A. S., Westenhoff S., Greenham N. C.; "Vertically segregated hybrid blends for photovoltaic devices with improved efficiency" *Journal of Applied Physics* **2005**, *97*, 014914.
- [403] Oosterhout S. D., Wienk M. M., Van Bavel S. S., Thiedmann R., Koster L. J. A., Gilot J., Loos J., Schmidt V., Janssen R. A. J.; "The effect of three-dimensional morphology on the efficiency of hybrid polymer solar cells." *Nature Materials* **2009**, *8*, 818–24.
- [404] Liao H.-C., Chen S.-Y., Liu D.-M.; "In-Situ Growing CdS Single-Crystal Nanorods via P3HT Polymer as a Soft Template for Enhancing Photovoltaic Performance" *Macromolecules* **2009**, *42*, 6558–6563.
- [405] Watt A. A. R., Blake D., Warner J. H., Thomsen E. A., Tavenner E. L., Rubinsztein-Dunlop H., Meredith P.; "Lead sulfide nanocrystal: conducting polymer solar cells" *Journal of Physics D: Applied Physics* **2005**, *38*, 2006–2012.

- [406] Dayal S., Kopidakis N., Olson D. C., Ginley D. S., Rumbles G.; "Direct synthesis of CdSe nanoparticles in poly(3-hexylthiophene)." *Journal of the American Chemical Society* **2009**, *131*, 17726–7.
- [407] Yue W., Han S., Peng R., Shen W., Geng H., Wu F., Tao S., Wang M.; "CuInS<sub>2</sub> quantum dots synthesized by a solvothermal route and their application as effective electron acceptors for hybrid solar cells" *Journal of Materials Chemistry* **2010**, *20*, 7570.
- [408] Yordanov N. D., Gancheva V., Mladenova B., Grampp G.; "Kinetic studies on the reaction between copper(II) ions and some dithiocarbonates using stopped-flow technique" *Inorganic Chemistry Communications* **2003**, *6*, 54–57.
- [409] Dutta D. P., Sharma G., Ghoshal S., Kushwah N. P., Jain V. K.; "Synthesis and Characterization of Indium Xanthates and Their use for the Preparation of  $\beta$ -In<sub>2</sub>S<sub>3</sub> Nanoparticles" *Journal of Nanoscience and Nanotechnology* **2006**, *6*, 6.
- [410] Park B. M., Chang H. J.; "Preparation and Characterization of White Polymer Light Emitting Diodes Using PVK:PFO:MDMO-PPV Emission Layer" *Molecular Crystals and Liquid Crystals* **2012**, *563*, 230–237.
- [411] Von Malm N., Schmechel R., Von Seggern H.; "Electronic Traps in Polymeric Semiconductors" *SID Symposium Digest of Technical Papers* **2003**, *34*, 1072.
- [412] Wienk M. M., Kroon J. M., Verhees W. J. H., Knol J., Hummelen J. C., Van Hal P. A., Janssen R. A. J.; "Efficient methano[70]fullerene/MDMO-PPV bulk heterojunction photovoltaic cells." *Angewandte Chemie International Edition* **2003**, *42*, 3371–5.
- [413] Baek W.-H., Yang H., Yoon T.-S., Kang C. J., Lee H. H., Kim Y.-S.; "Effect of P3HT:PCBM concentration in solvent on performances of organic solar cells" *Solar Energy Materials and Solar Cells* **2009**, *93*, 1263–1267.
- [414] Li G., Yao Y., Yang H., Shrotriya V., Yang G., Yang Y.; "'Solvent Annealing' Effect in Polymer Solar Cells Based on Poly(3-hexylthiophene) and Methanofullerenes" *Advanced Functional Materials* **2007**, *17*, 1636–1644.
- [415] Li G., Shrotriya V., Yao Y., Yang Y.; "Investigation of annealing effects and film thickness dependence of polymer solar cells based on poly(3-hexylthiophene)" *Journal of Applied Physics* **2005**, *98*, 043704.
- [416] Boland P., Sunkavalli S. S., Chennuri S., Foe K., Abdel-Fattah T., Namkoong G.; "Investigation of structural, optical, and electrical properties of regioregular poly(3-hexylthiophene)/fullerene blend nanocomposites for organic solar cells" *Thin Solid Films* **2010**, *518*, 1728–1731.
- [417] Montanari I., Nogueira A. F., Nelson J., Durrant J. R., Winder C., Loi M. A., Sariciftci N. S., Brabec C.; "Transient optical studies of charge recombination dynamics in a polymer/fullerene composite at room temperature" *Applied Physics Letters* **2002**, *81*, 3001.
- [418] Yang X., Loos J.; "Toward High-Performance Polymer Solar Cells: The Importance of Morphology Control" *Macromolecules* **2007**, *40*, 1353–1362.
- [419] Haugeneder A., Neges M., Kallinger C., Spirkel W., Lemmer U., Feldmann J., Scherf U., Harth E., Gügel A., Müllen K.; "Exciton diffusion and dissociation in conjugated polymer/fullerene blends and heterostructures" *Physical Review B* **1999**, *59*, 15346–15351.
- [420] Kruszynska M., Knipper M., Kolny-Olesiak J., Borchert H., Parisi J.; "Charge transfer in blends of P3HT and colloiddally prepared CuInS<sub>2</sub> nanocrystals" *Thin Solid Films* **2011**, *519*, 7374–7377.
- [421] Yang J., You J., Chen C.-C., Hsu W.-C., Tan H., Zhang X. W., Hong Z., Yang Y.; "Plasmonic polymer tandem solar cell." *ACS nano* **2011**, *5*, 6210–7.
- [422] Liang Y., Xu Z., Xia J., Tsai S.-T., Wu Y., Li G., Ray C., Yu L.; "For the bright future-bulk heterojunction polymer solar cells with power conversion efficiency of 7.4%." *Advanced Materials* **2010**, *22*, E135–8.
- [423] Gong X., Tong M., Xia Y., Cai W., Moon J. S., Cao Y., Yu G., Shieh C.-L., Nilsson B., Heeger A. J.; "High-detectivity polymer photodetectors with spectral response from 300 nm to 1450 nm." *Science* **2009**, *325*, 1665–7.
- [424] Park S. H., Roy A., Beaupré S., Cho S., Coates N., Moon J. S., Moses D., Leclerc M., Lee K., Heeger A. J.; "Bulk heterojunction solar cells with internal quantum efficiency approaching 100%" *Nature Photonics* **2009**, *3*, 297–302.
- [425] Morana M., Azimi H., Dennler G., Egelhaaf H.-J., Scharber M., Forberich K., Hauch J., Gaudiana R., Waller D., Zhu Z., Hingerl K., Van Bavel S. S., Loos J., Brabec C. J.; "Nanomorphology and Charge Generation in Bulk Heterojunctions Based on Low-Bandgap Dithiophene Polymers with Different Bridging Atoms" *Advanced Functional Materials* **2010**, *20*, 1180–1188.

- [426] Hoppe H., Sariciftci N. S.; "Morphology of polymer/fullerene bulk heterojunction solar cells" *Journal of Materials Chemistry* **2006**, *16*, 45.
- [427] Liu F., Gu Y., Jung J. W., Jo W. H., Russell T. P.; "On the morphology of polymer-based photovoltaics" *Journal of Polymer Science Part B: Polymer Physics* **2012**, *50*, 1018–1044.
- [428] Hoppe H., Glatzel T., Niggemann M., Schwinger W., Schaeffler F., Hinsch A., Lux-Steiner M. C., Sariciftci N. S.; "Efficiency limiting morphological factors of MDMO-PPV:PCBM plastic solar cells" *Thin Solid Films* **2006**, *511-512*, 587–592.
- [429] Zhou H., Yang L., You W.; "Rational Design of High Performance Conjugated Polymers for Organic Solar Cells" *Macromolecules* **2012**, *45*, 607–632.
- [430] Banerji N., Cowan S., Leclerc M., Vauthey E., Heeger A. J.; "Exciton Formation, Relaxation, and Decay in PCDTBT." *Journal of the American Chemical Society* **2010**, 17459–17470.
- [431] Aïch R. B., Blouin N., Bouchard A., Leclerc M.; "Electrical and Thermoelectric Properties of Poly(2,7-Carbazole) Derivatives" *Chemistry of Materials* **2009**, *21*, 751–757.
- [432] Blouin N., Michaud A., Leclerc M.; "A Low-Bandgap Poly(2,7-Carbazole) Derivative for Use in High-Performance Solar Cells" *Advanced Materials* **2007**, *19*, 2295–2300.
- [433] Blouin N., Michaud A., Gendron D., Wakim S., Blair E., Neagu-Plesu R., Belletête M., Durocher G., Tao Y., Leclerc M.; "Toward a rational design of poly(2,7-carbazole) derivatives for solar cells." *Journal of the American Chemical Society* **2008**, *130*, 732–42.
- [434] Chu T.-Y., Alem S., Verly P. G., Wakim S., Lu J., Tao Y., Beaupré S., Leclerc M., Bélanger F., Désilets D., Rodman S., Waller D., Gaudiana R.; "Highly efficient polycarbazole-based organic photovoltaic devices" *Applied Physics Letters* **2009**, *95*, 063304.
- [435] Gieseck B., Jäck B., Preis E., Jung S., Forster M., Scherf U., Deibel C., Dyakonov V.; "Excitation Dynamics in Low Band Gap Donor-Acceptor Copolymers and Blends" *Advanced Energy Materials* **2012**, *2*, 1477–1482.
- [436] Seo J. H., Cho S., Leclerc M., Heeger A. J.; "Energy level alignments at poly[N-9''-hepta-decanyl-2,7-carbazole-alt-5,5-(4',7'-di-2-thienyl-2',1',3'-benzothiadiazole)] on metal and polymer interfaces" *Chemical Physics Letters* **2011**, *503*, 101–104.
- [437] Tong M., Coates N. E., Moses D., Heeger A. J.; "Charge carrier photogeneration and decay dynamics in the poly(2,7-carbazole) copolymer PCDTBT and in bulk heterojunction composites with PC70BM" *Physical Review B* **2010**, *81*, 1–6.
- [438] Cho S., Seo J. H., Park S. H., Beaupré S., Leclerc M., Heeger A. J.; "A thermally stable semiconducting polymer." *Advanced Materials* **2010**, *22*, 1253–7.
- [439] Hou J., Chen H.-Y., Zhang S., Li G., Yang Y.; "Synthesis, characterization, and photovoltaic properties of a low band gap polymer based on silole-containing polythiophenes and 2,1,3-benzothiadiazole." *Journal of the American Chemical Society* **2008**, *130*, 16144–5.
- [440] Wang E., Wang L., Lan L., Luo C., Zhuang W., Peng J., Cao Y.; "High-performance polymer heterojunction solar cells of a polysilafuorene derivative" *Applied Physics Letters* **2008**, *92*, 033307.
- [441] Beiley Z. M., Hoke E. T., Noriega R., Dacuña J., Burkhard G. F., Bartelt J. A., Salleo A., Toney M. F., McGehee M. D.; "Morphology-Dependent Trap Formation in High Performance Polymer Bulk Heterojunction Solar Cells" *Advanced Energy Materials* **2011**, *1*, 954–962.
- [442] Czekelius C., Hilgendorff M., Spanhel L., Bedja I., Lerch M., Müller G., Bloeck U., Su D., Giersig M.; "A Simple Colloidal Route to Nanocrystalline ZnO/CuInS<sub>2</sub> Bilayers" *Advanced Materials* **1999**, *11*, 643–646.
- [443] Campbell I., Hagler T., Smith D., Ferraris J.; "Direct Measurement of Conjugated Polymer Electronic Excitation Energies Using Metal/Polymer/Metal Structures" *Physical Review Letters* **1996**, *76*, 1900–1903.
- [444] Knupfer M.; "Exciton binding energies in organic semiconductors" *Applied Physics A: Materials Science & Processing* **2003**, *77*, 623–626.
- [445] Horowitz G., Hajlaoui R., Bouchriha H., Bourguiga R., Hajlaoui M.; "The Concept of "Threshold Voltage" in Organic Field-Effect Transistors" *Advanced Materials* **1998**, *10*, 923–927.
- [446] Chua L.-L., Zaumseil J., Chang J.-F., Ou E. C.-W., Ho P. K.-H., Sirringhaus H., Friend R. H.; "General observation of n-type field-effect behaviour in organic semiconductors." *Nature* **2005**, *434*, 194–9.
- [447] Natali D., Caironi M.; "Charge injection in solution-processed organic field-effect transistors: physics, models and characterization methods." *Advanced Materials* **2012**, *24*, 1357–87.

- [448] Rentenberger S., Vollmer A., Zojer E., Schennach R., Koch N.; "UV/ozone treated Au for air-stable, low hole injection barrier electrodes in organic electronics" *Journal of Applied Physics* **2006**, *100*, 053701.
- [449] Dennler G., Scharber M. C., Brabec C. J.; "Polymer-Fullerene Bulk-Heterojunction Solar Cells" *Advanced Materials* **2009**, *21*, 1323–1338.
- [450] Klug A., Meingast A., Wurzinger G., Blümel A., Schmoltner K., Scherf U., List E. J. W.; Organic field-effect transistors: a combined study on short-channel effects and the influence of substrate pre-treatment on ambient stability. In *Proceedings of SPIE (Proc. SPIE)*; Shinar R., Kymissis I., Eds.; **2011**; Vol. 8118, pp. 811809–811809–15.
- [451] Van Duren J. K. J., Yang X., Loos J., Bulle-Lieuwma C. W. T., Sieval A. B., Hummelen J. C., Janssen R. A. J.; "Relating the Morphology of Poly(p-phenylene vinylene)/Methanofullerene Blends to Solar-Cell Performance" *Advanced Functional Materials* **2004**, *14*, 425–434.
- [452] Kumar A., Srivastava R., Mehta D. S., Kamalasanan M. N.; "Surface plasmon enhanced blue organic light emitting diode with nearly 100% fluorescence efficiency" *Organic Electronics* **2012**, *13*, 1750–1755.
- [453] Reboud V., Kehagias N., Kehoe T., Leveque G., Mavidis C., Kafesaki M., Sotomayor Torres C. M.; "Nanoimprinted plasmonic crystals for light extraction applications" *Microelectronic Engineering* **2010**, *87*, 1367–1369.
- [454] Mladenovski S., Neyts K., Pavicic D., Werner A., Rothe C.; "Exceptionally efficient organic light emitting devices using high refractive index substrates." *Optics express* **2009**, *17*, 7562–70.
- [455] Seki S., Uchida M., Sonoyama T., Ito M., Watanabe S., Sakai S., Miyashita S.; "40.1: Invited Paper: Current Status of Printing OLEDs" *SID Symposium Digest of Technical Papers* **2009**, *40*, 593.
- [456] Bruner S., Xu D., Phillips C.; "54.3: Drop Landing Accuracy Improvements in Inkjet Printed OLED Displays" *SID Symposium Digest of Technical Papers* **2007**, *38*, 1611.
- [457] Sandström A., Dam H. F., Krebs F. C., Edman L.; "Ambient fabrication of flexible and large-area organic light-emitting devices using slot-die coating." *Nature communications* **2012**, *3*, 1002.
- [458] Atwater H. A., Polman A.; "Plasmonics for improved photovoltaic devices." *Nature materials* **2010**, *9*, 205–13.
- [459] Catchpole K. R., Pillai S.; "Surface plasmons for enhanced silicon light-emitting diodes and solar cells" *Journal of Luminescence* **2006**, *121*, 315–318.
- [460] Pillai S., Green M. A.; "Plasmonics for photovoltaic applications" *Solar Energy Materials and Solar Cells* **2010**, *94*, 1481–1486.
- [461] Teichler A., Perelaer J., Schubert U. S.; "Inkjet printing of organic electronics – comparison of deposition techniques and state-of-the-art developments" *Journal of Materials Chemistry C* **2013**, *1*, 1910.
- [462] Søndergaard R. R., Hösel M., Krebs F. C.; "Roll-to-Roll fabrication of large area functional organic materials" *Journal of Polymer Science Part B: Polymer Physics* **2013**, *51*, 16–34.



## Curriculum Vitae

<b>DI Roman Trattnig</b>	
<b>Personal Details</b>	
<i>Date and Place of Birth</i>	21/02/1979, Klagenfurt/Austria
<b>Education</b>	
<i>10/2009 – 04/2013</i>	PhD student (Doctoral studies, Technical Physics) at the Graz University of Technology
<i>18/05/2009</i>	Graduation to Diplom-Ingenieur (MSc.) in Technical Physics at the Graz University of Technology Diploma Thesis: “Organic Light Emitting Devices based on Phosphorescent Organometallic Complexes in Blend- and Onchain Polymer Systems”
<i>10/2007-10/2009</i>	Student of Psychology at University of Graz
<i>10/1998-5/2009</i>	Student of Technical Physics at the Graz University of Technology
<i>10/1998</i>	Enrolment at the Graz University of Technology
<i>06/1997</i>	A-levels (Matura) (with excellence)
<i>1989-1997</i>	Grammar school: BG/BRG Ingeborg Bachmann Klagenfurt
<b>Career History</b>	
<i>since 06/2009</i>	Key researcher at the NanoTecCenter Weiz Forschungsgesellschaft mbH
<i>01/2009 – 05/2009</i>	Technical Research Assistant at the NanoTecCenter Weiz Forschungsgesellschaft mbH
<i>11/2007 – 12/2008</i>	Junior researcher at the Institute of Solid State Physics, Graz University of Technology
<i>07/2002 – 09/2004</i>	Student trainee in the field of product engineering, process engineering, project management and technology transfer, Infineon Technologies Austria AG
<i>06/2001– 09/2001</i>	Student trainee in the field of product and process engineering, Infineon Technologies Austria AG
<i>07/2000 – 09/2000</i>	Trainee in the field of product engineering, Infineon Technologies Austria AG
<b>Other important Career-Related Activities</b>	
<i>Dissimination and Exploitation of Scientific Results</i>	10 publications in „peer-reviewed journals“, 2 conference contributions, 2 patents submitted
<i>Additional training</i>	Participant of advanced training courses and executive trainings on leadership and communication at WINTERHELLER management
<i>10/2004 – 10/2005</i> <i>10/2000 – 10/2002</i>	Spokesman for the students council of the Akademikerhilfe, Graz Untere Schönbrunngrasse
<i>10/1999 – 8/2009</i>	Elected member of the students council of the Akademikerhilfe, Graz Untere Schönbrunngrasse
<b>Languages</b>	
	<ul style="list-style-type: none"> <li>• German: mother tongue</li> <li>• English: fluent</li> <li>• Italian: elementary (4 years school Italian)</li> </ul>